Open Access Dissertations   Electronic Theses and Dissertations

2007-12-21

Development Of A Delivery System And Optical-Thermal Model For Laser Interstitial Thermotherapy Of Breast Tumors

Nelson Salas
University of Miami, nsalas@med.miami.edu

Follow this and additional works at: https://scholarlyrepository.miami.edu/oa_dissertations

UNIVERSITY OF MIAMI

DEVELOPMENT OF A DELIVERY SYSTEM AND OPTICAL-THERMAL MODEL
FOR LASER INTERSTITIAL THERMOTHERAPY OF BREAST TUMORS

By

Nelson Salas

A DISSERTATION

Submitted to the Faculty
of the University of Miami
in partial fulfillment of the requirements for
the degree of Doctor of Philosophy

Coral Gables, Florida

December 2007

UNIVERSITY OF MIAMI

A dissertation submitted in partial fulfillment of
the requirements for the degree of
Doctor of Philosophy

DEVELOPMENT OF A DELIVERY SYSTEM AND OPTICAL-THERMAL MODEL
FOR LASER INTERSTITIAL THERMOTHERAPY OF BREAST TUMORS

Nelson Salas

Approved:

_____   _____
Dr. Fabrice Manns   Dr. Terri A. Scandura
Associate Professor of   Dean of the Graduate School
Biomedical Engineering and
Ophthalmology

_____   _____
Dr. Ozcan Ozdamar   Dr. Jean-Marie Parel
Professor and Chair of   Research Associate Professor of
Biomedical Engineering   Ophthalmology and
                                           Biomedical Engineering

_____   _____
Dr. Peter Milne   Dr. David S. Robinson
Research Associate Professor   Surgical Oncologist
Rosenstiel School of Marine and   Coral Springs, FL
Atmospheric Science

_____
Dr. Fotios Andreopoulos
Assistant Professor of
Biomedical Engineering and Surgery

SALAS, NELSON   (Ph.D., Biomedical Engineering)
Development Of A Delivery System   (December 2007)
And Optical Thermal Model For Laser
Interstitial Thermotherapy Of Breast Tumors

Abstract of a dissertation at the University of Miami.

Dissertation supervised by Professor Fabrice Manns.
No. of pages in text. (241)

The purpose of this project was to develop a delivery system optimized for laser interstitial thermotherapy of small tumors of the breast. The proposed approach is to combine laser interstitial thermotherapy with stereotactic imaging for fiber guidance and treatment monitoring. The goals of the dissertation were to design a fiber insertion system for cylindrical diffusing tip optical fibers and to derive optimal laser parameters for coagulation of 1 cm tumor plus a surrounding 1 cm thick rim of healthy tissue. A fiber insertion system compatible with a high resolution stereotactic digital X-ray biopsy system was designed to guide the fiber into the tumor site in similar fashion to the insertion of the biopsy needle. An optical-thermal model consisting of a radiation model, a thermal model, and a coagulation model was developed and validated using *ex-vivo* porcine tissue. A single integrating sphere optical property measurement system and an inverse Monte Carlo algorithm were developed to measure the optical properties of *ex-vivo* porcine tissue at 830, 940, and 980 nm. An experimental method was developed to determine the parameters of the Arrhenius model (frequency factor (A) and activation energy (E_a)). The optical-thermal model was validated by comparing the predicted temperature and coagulation to results of laser irradiation experiments at 830, 940, and 980 nm. Using published values of the optical properties of the breast, the model

predicts that a 3 cm coagulation size can be produced without vaporization in 10 min with 10.4 W at 980 and 940 nm and 13.2 W at 830 nm. The same outcome can be achieved in 20 min with 4.5 W at 980 and 940 nm and 6.1 W at 830 nm.

DEDICATION

I dedicate this dissertation to two individuals closest to me:

The first person is to my mother, Rosario Parron. She is a person that has showed strength and resiliency above adversity. She was and still is the rock, a pillar of the family when I needed one to lean on. She raised me with nothing short of unconditional love that went beyond her own self. Without her, I would not be the person I am today. May the Lord allow me to be at least half the parent that she was and still is to me today.

The second person is to Mariela Aguilar, the love of my life and best friend. She lifted me up through the worst of times and celebrated with me through the best of times. When I wanted to quit, she reminded me of the reasons for staying. When I wanted to let go, she gave me the strength to hang on. Her love, patience, and endurance have been my anchor. She reminds me everyday of how blessed I am and of all the things that I can achieve in life. She has and continues to make me a better person everyday.

ACKNOWLEDGEMENTS

PREFACE

The following are publications, proceedings, presentations, and posters that were submitted within the duration of this project:

Peer-Reviewed Publications:

N Salas, Jr., F Manns, P Milne, D Denham, A Minhaj, JM Parel, DS Robinson; "Thermal Analysis Of Laser Interstitial Thermotherapy In Ex-Vivo Fibro-Fatty Tissue Using Exponential Functions"; *Physics in Medicine and Biology* **49**(9), 1609-1624 , 2004.

A Minhaj, F Manns, P Milne, D Denham, N Salas, Jr., I Nose, K Damgaard-Iversen, JM Parel, DS Robinson; "Laser Interstitial Thermotherapy (LITT) Monitoring Using High-Resolution Digital Mammography: theory and experimental studies"; *Physics in Medicine and Biology*; **47,** 2987-2999, 2002

Conference Proceedings:

N Salas, Jr., Manns F, Parel JM, Milne P, Denham DB, Robinson DS; "Predictions Of Tissue Denaturation During Experimental Laser Interstitial Thermotherapy For Breast Tumors"; *Lasers in Surgery: Advanced Characterization, Therapeutics, and Systems XIII*; LS Bass, *et al.*, ed.; Proc. SPIE Vol.4949, p.444-449, 2003.

N Salas, Jr.**,** F Manns, JM Parel, PJ Milne, M Figueroa, DB Denham, DS Robinson; "Experimental Laser Interstitial Thermotherapy In Ex-Vivo Porcine Tissue At 940 nm"; *Lasers in Surgery: Advanced Characterization. Therapeutics, and Systems XII*; RR Anderson, et al., ed.; SPIE Proceedings vol. 4609, p.398-403, 2002.

TABLE OF CONTENTS

1. AIMS

1.1 Introduction

According to the American Cancer Society, breast cancer is the most common form of cancer amongst women and the second leading cause of cancer death in women. The American Cancer Society estimated that approximately 212,920 women in the United States were diagnosed with an invasive form of breast cancer in 2006. There are approximately over 2 million women currently living in the United States that have been treated for breast cancer. Current clinical treatment include either total removal of the breast or removal of the tumor plus a surrounding portion of healthy tissue, depending on the size of both the tumor and the breast. Minimally-invasive procedures, such as cryotherapy, high intensity focused ultrasound, radiofrequency, and laser interstitial thermotherapy have been tested for the treatment of small tumors of the breast. Laser interstitial thermotherapy is the minimally-invasive procedure of choice due to its feasible tunability, which in turn would allow a complete treatment of different tumor sizes up to 3 cm with minimal collateral damage. In laser interstitial thermotherapy, the tumor plus a surrounding rim of healthy tissue is treated by the absorption of near-infrared laser irradiation that is emitted by an optical fiber inserted into the tumor site.

1.2 Project goal

The goal of this project is to develop a delivery system and treatment planning algorithm for laser interstitial thermotherapy of small tumors of the breast. The delivery system includes a fiber-insertion system to be used under stereotactic guidance, and an

www.manaraa.com

optical-thermal model that will predict the optimal laser parameters (laser wavelength, output power, and irradiation time) for a large range of coagulation sizes.

The aims of this study are:

a) Develop and test an optical-thermal model that will predict the light propagation, temperature distribution, and the coagulation zone in the breast tissue during laser irradiation with a diffusing tip optical fiber

b) Develop and test in breast models a fiber-guidance assembly for the insertion of the optical fiber into the breast tumor under stereotactic X-ray guidance.

2. BACKGROUND AND SIGNIFICANCE

2.1. Introduction

The light distribution in tissue during laser interstitial thermotherapy depends on the absorbing and scattering properties of the tissue, which, in turn, depend on the structural composition and vascular system of the tissue. The female mammary gland, or breast, is a heterogeneous organ whose structure varies not only amongst different individuals, but also during menstruation, pregnancy, and menopause. Knowledge of the tissue structure is imperative to both accurately predict the light dosimetry in the tissue and choose an appropriate tissue phantom that would closely mimic the laser interaction with the targeted tissue.

2.2 Human female breast anatomy and physiology

2.2.1 General anatomy and physiology

The mammary, or breast, gland is a structurally heterogeneous tissue designed for the function of milk production during and shortly after pregnancy. The average adult breast is generally 10 to 12 cm in diameter and approximately 5 to 7 cm thick. The general anatomy of the breast is shown in Figure 2.1 (Thompson and Tatman 1998, Osborne 1996, Baum *et al* 1994). The breast gland consists of the parenchyma, which comprises the ductal system, and the surrounding stroma.

The adult breast tissue parenchyma itself consists of 15 to 20 lobes or segments. Each segment or lobe consists of many ductal branches that begin with the breast lobules. These lobules vary in range from 0.5 to between 3 and 5 mm in size during the menstrual

3

cycle and consist of a convoluted network of tubular ductules, or acini plus a small portion of the terminal ductule (Figure 2.1) (Thompson and Tatman 1998). These, in turn, drain into the lactiferous duct, lactiferous sinus, and a collecting duct at the nipple (Tavassoli 1999, Osborne 1996, Baum *et al* 1994) (Figure 2.1). The mammary ducts consist of an epithelial cell layer surrounded by a myoepithelial cell layer (Tavassoli 1999). These are surrounded by a basal lamina layer and enveloped by one or more "delimiting fibroblasts" (Figure 2.2).

There are two fascia layers that together envelope the breast. The superficial pectoral fascia lies between the skin and the breast gland and is composed of a thin film of fibrous tissue. The deep pectoral fascia is a thicker, more fibrous film and lies between the breast gland and the pectoral muscles. Bands of collagenous, fibrous ligaments, called Cooper's ligaments, network throughout the breast gland and extend from the superficial to the deep pectoral fascias. These ligaments support the breast. A thin band of adipose tissue between the skin and the breast gland forms a network throughout the glandular tissue. Various amounts of adipose tissue are also intermixed within the glandular breast, depending on the patient's weight, age, heritage, and general habits (Thomsen and Tatman 1998).

While the ductal system comprises the functional unit of the breast, the fibro-adipose tissue surrounding the ducts, or the stroma, accounts for the major bulk of the breast (Tavassoli 1999). The stroma can be divided into the intralobular and interlobular stroma. The intralobular stroma, which surrounds the entire ductal system but is especially pronounced around the lobules, is an ellipsoid volume of loose, fibrous connective tissue (Thomsen and Tatman 1998). The interlobular stroma, which

surrounds the lobes of the breast, consists of fat, connective tissue, blood vessels, and lymphatics (Tavassoli 1999, Osborne 1996). Because of the changes in the ductal system during pregnancy and menopause, the more cellular intralobular stroma is more sensitive to hormonal changes than the interlobular stroma.
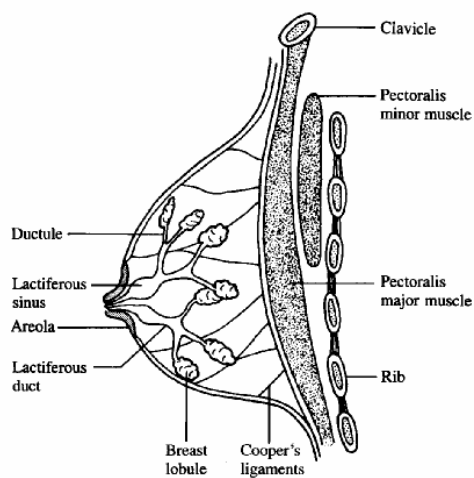
Figure 2.1: Anatomy of the human female mammary gland (Baum 1994)
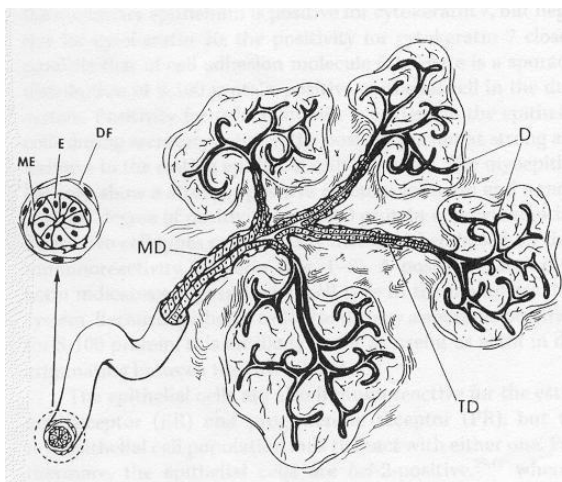
Figure 2.2: The epithelial cell layer(E), myoepithelial cell layer(ME), basal lamina, and the deliminating fibroblasts (DF)of the mammary gland ductal system (Tavassoli 1999). The ductal structure in this figure consist of the ductules (D), the terminal ducts (TD), and the major ducts (MD)

The mammary gland is highly vascular, with more blood vessels found in the glandular breast than in the fibrous and adipose stroma. The main blood supply to the breast is from the branches of the internal mammary artery, which accounts for 60% of the breast blood supply (medial and central portions), and the branches of the lateral thoracic artery, which accounts for 30% of the breast blood supply (upper,outer portion) (Figure 2.3) (Tavassoli 1999, Osborne 1996).

The lymphatic system is considered to be the major route for the spread of carcinoma. The lymphatic vessels stemming from the nipple and surrounding areola are connected with those branching from the ductal system. The lymph flows centrifugally from the connected nipple and ductal region outward toward the internal mammary lymph nodes, located from the second intercostals space in the ribs downward, and the axillary lymph nodes, located in the axillary or upper quadrant of the breast tissue (Figure 2.4). Approximately 3% of the mammary lymph flows to the internal mammary chain, while the other 97% flows to the axillary nodes. For this reason, the axillary nodes are investigated as the major route for the spread of carcinoma (Tavassoli 1999, Thomsen and Tatman 1998, Osborne 1996, Baum *et al* 1994).
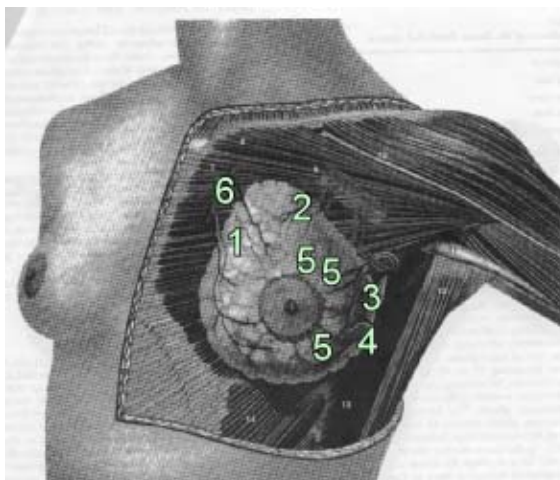
Figure 2.3: The blood supply to the female breast (Osborne 1996). The blood supply in this figure include the (1) perforating branches of the internal mammary artery and vein, (2) pectoral branches from the thoracoacromial artery and vein, (3) external mammary branch of the lateral thoracic artery, (4) branches from subscapular and thoracodorsal arteries and veins, (5) lateral branches of third, fourth, and fifth intercostals arteries and veins, and (6) internal mammary arteries and veins.
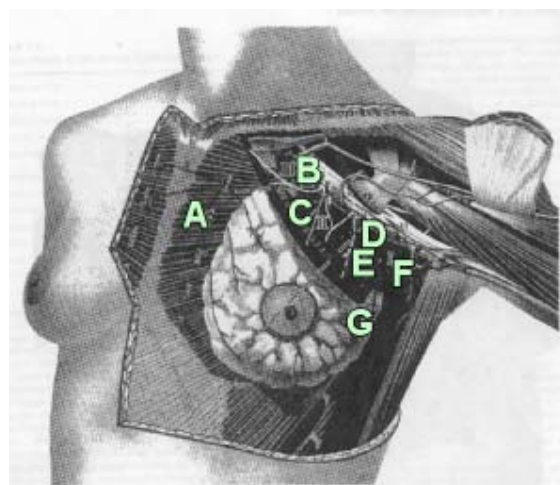
Figure 2.4: The lymphatic system of the breast (Osborne 1996). This system in this figure includes the (A) Internal mammary lymph nodes chain and (B-G) the axillary lymph nodes

2.2.2 Breast transformation: menstruation, pregnancy, and menopause

The breast is a complex organ whose morphology varies in composition amongst different individuals having different age, hormonal status, weight, and genetic heritage.

However, breast composition also changes during the menstrual cycle, pregnancy, and menopause (Thomsen and Tatman 1998). Throughout the female menstruation cycle, the breast undergoes fluctuations in stromal density, size and mitosis of epithelial cells, and ductal lumen dilation (Tavassoli 1999, Thomsen and Tatman 1998). Blood flow may increase up to 50% at the time of ovulation and remain that way until menstruation (Thomsen and Tatman 1998). Women may, therefore, suffer up to a 20% enlargement of their breast.

During pregnancy, enlargement continues due to the expansion of the lobules from the accumulation of secretory material and fat droplets in the epithelial cells, while the stroma becomes inconspicuous. Some time after lactation, the lobules decrease in size followed by an increase in the quantity of fibrous and fatty tissue (Tavassoli 1999).

During menopause, the parenchymal structures of the breast suffer involution, which is characterized by apoptotic cell death and tissue remodeling (Osborne 1996). The epithelial components of the lobules suffer complete atrophy, and both the lobules and surrounding, lobular stroma become transparent and granule free (hyalinized). The number of ductules decreases from 25-35% of the total volume at 35 years of age to less than 5% after 60 years of age. Alterations in the elastic and collagen fibers in the stroma result in the loss of connective tissue, while the adipose tissue increases and eventually becomes predominant after 60 years of age (Tavassoli 1999, Thomsen and Tatman 1998).

Therefore, the composition of the breast constantly varies throughout the woman's life up to the end of menopause. Since the breast composition varies slightly, the optical properties of the breast and the light distribution in the breast during laser irradiation will vary amongst different women and at different stages of menstruation and menopause

within the same breast. For this project we focus on the structure of the women's breast at menopause, for they comprise the highest percentage of women with breast cancer.

2.3 Breast Tumors

2.3.1 Benign breast tumors

Benign tumors are abnormal growths of tissue that neither spread beyond their site of origin nor metastasize to the surrounding tissue within the same organ and/or other organs in the body (Thomsen and Tatman 1998, Baum *et al* 1994). Most benign tumor types have excellent prognosis and sometimes are not even treated unless they either cause deformation, pressure against important surrounding tissue, or psychological stress to the patient (Baum *et al* 1994). Benign breast tumors include fibroadenomas, cysts, lipomas, and epithelial hyperplasias. A summary of these benign tumor types is given in Table 2.1.

2.3.2 Malignant breast tumors

Breast cancer tumors are abnormal growths of cells due to genetic mutations that, unlike benign tumors, will invade into the surrounding tissue and / or metastasize to other organs in the body (Thomsen and Tatman 1998, Baum *et al* 1994). Even though the exact causes of breast cancer are still under investigation, there are some risk factors that have been outlined. These risk factors include age, geographical variation, age at menarche or menopause, age at pregnancy, family history, benign breast disease history, obesity after menopause, age of oral contraceptive use, hormonal replacement therapy,

and breast asymmetry and volume (Boyle 2005, McPherson *et al* 2000, Scutt *et al* 1997, Baum *et al* 1994).

Malignant breast tumors are classified according to their type and stage. The stage of a breast cancer tumor ranges from stage 0 to stage IV (Table 2.2), depending on its size and the extent to which the cancer has spread to the lymph nodes and / or metastasized to other organs. Breast carcinomas fall under two types: infiltrating, or invasive, and pre-invasive, in-situ carcinoma (Table 2.3).

Table 2.1: The types, description, and rate of occurrence of benign tumors of the breast. These types include fibroadenomas (Baum et al 1994, Schnitt and Connolly 2000), Cysts (Thomsen and Tatman 1998, Baum et al 1994, Schnitt and Connolly 2000), Lipomas (Baum et al 1994, Thomsen and Tatman 1998), and epithelial hyperplasias (Baum et al 1994, Schnitt and Connolly 2000)

BENIGN BREAST TUMOR TYPES	
TYPE	**DESCRIPTION**
Fibroadenomas	Most common of benign breast tumors. Consist of various degrees of epithelial duct-like spaces, stromal components with collagenous connective tissue, and adipose tissue. (Baum *et al* 1994, Schnitt and Connolly 2000) Develops as well-defined, painless lump.
Cysts	Closed cavities lined by epithelium containing liquid or semi-solid material (Thomsen and Tatman 1998, Baum *et al* 1994). Usually develops in the lobules Vary sin size from microscopic to grossly evident (Schnitt and Connolly 2000)
Lipomas	Adipose cells that form a lump within the breast (Baum *et al* 1994, Thomsen and Tatman 1998). Painless and harmless
Epithelial Hyperplasias	Abnormal growths of the epithelial cells lining the ducts (Baum *et al* 1994) Accounts for 12-17% of biopsies due to microcalcifications found on mammographic screenings (Schnitt and Connolly 2000) Are easily mistaken for and carry risk of becoming a cancer tumor.

Infiltrating carcinomas have neoplastic cells that invade from their origin to the surrounding stroma of the breast tissue and eventually metastasize to other organs if left untreated (Schnitt and Guidi 2000). These tumors arise from the epithelial cells of the ductal system and mostly originate from the lobular units (Tavassoli 1999). The majority of invasive breast tumors fall under two types according to their growth patterns and cytological features: invasive ductal carcinomas - not otherwise specified (IDC-NOS) and invasive lobular carcinomas (ILC).

In-situ, or pre-invasive, carcinomas are tumors that are confined to the ductal or lobular system and have the potential of becoming invasive. Because they are confined within the ducts and lobules, no lumps are detected, and the only method of detection is through either screening, symptoms such as nipple discharge, or detection either during surgery or by pathology of the surgically excised lesion. Most invasive breast carcinomas have components of in-situ carcinoma within them, the extent of them being variable (Schnitt and Guidi 2000). It is uncertain which ones of them will become or how long it would take for them to become invasive (Baum *et al* 1994). They may extend through a large area of the ductal system without any stromal invasion (Tavassoli 1999). The two types of in-situ carcinomas seen in breast cancer patients are ductal carcinoma *in-situ* (DCIS) and lobular carcinoma *in-situ* (LCIS) (Baum *et al* 1994). These infiltrative and pre-invasive carcinoma types are described in Table 2.3.

2.3.3 Tumors targeted for LITT

Any tumor with questionable margins will pose difficulty in optical fiber placement and total treatment without residual tumor. The ideal tumors for our procedure are those

in which the margins of the tumor are well-delineated. Those include fibroadenomas and infiltrating ductal carcinomas-NOS with little or no carcinoma in-situ.

2.4 Breast tumor diagnostic methods

2.4.1 Breast imaging

Since the 1950's, women have been screened for breast tumors using a non-invasive imaging modality. Women who are targeted for screening are those with age greater than 40 due to increased risk with menopause and those that suffer a lump, nipple discharge, pain, or some other form discomfort in their breast. The current clinical imaging modalities for breast tumor screening are X-ray mammography, ultrasound, and MRI.

Table 2.2: The different stages of breast cancer and the description of each stage

Stage	Description
0	This is a cancer that has not spread beyond the ductal system. These cancers are known as in-situ cancers. The two most common types are lobular carcinoma in-situ and ductal carcinoma in-situ
I	The tumor is 2 cm or less and has not spread to the lymph nodes
IIA	The tumor is between 2 to 5 cm and has not spread to the lymph nodes
IIB	Either the tumor is between 2 to 5 cm and has spread to the lymph nodes, or the tumor is greater than 5 cm and has not spread to the lymph nodes
IIIA	Breast cancer larger than 5 cm that has spread to the axillary lymph nodes and the axillary tissue
IIIB	Breast cancer of any size that has attached itself to the chest wall and has spread to the pectoral (chest) lymph nodes or has attached to the skin
IV	The cancer has spread out to other parts of the body

Table 2.3: The types, description, and rate of occurrence of malignant tumors of the breast. These types include invasive ductal carcinoma (Schnitt and Guidi 2000, Baum et al 1994, Molland et al 2004), invasive lobular carcinomas (Schnitt and Guidi 2000, Molland et al 2004), ductal carcinoma in-situ (Baum et al 1994, Tavassoli 1999, Allred 2002, Morrow et al 2000), and lobular carcinoma in-situ (Baum et al 1994, Morrow and Schnitt 2000)

MALIGNANT BREAST TUMOR TYPES		
TYPE	**DESCRIPTION**	**RATE OF OCCURRENCE**
Invasive Ductal Carcinoma (IDC-NOS)	Heterogeneous group of cells (NOS = not of specific type) (Schnitt and Guidi 2000) Most common malignant type (Mullond *et al* 2004, Baum *et al* 1994) Stellate, speculated, or well-rounded palpable lump (Tavassoli 1999)	85-90%
Invasive Lobular Carcinoma (ILC)	Small cells that invade stroma either alone or in single-file pattern (Molland *et al* 2004, Schnitt and Guidi 2000) True margins difficult to assess, thus total excision difficult to achieve (Molland *et al* 2004, Schnitt and Guidi 2000)	5.8-15%
Ductal Carcinoma In-Situ (DCIS)	Unifocal (Morrow *et al* 2000, Page and Rogers 2002, Lippman 2002) 28% of cases suffer an invasive disease, mostly IDC-NOS (Morrow *et al* 2000)	20%
Lobular Carcinoma In-Situ (LCIS)	Multicentric (Morrow and Schnitt 2000) Low proliferative rate and calcification content (Morrow and Schnitt 2000) 21-29% of cases suffer an invasive disease, mostly IDC-NOS (Morrow and Schnitt 2000)	0.5-3.6%

<u>X-Ray Mammography:</u>   Since its introduction in 1956, X-ray mammography has remained the most widely used modality for non-invasive detection and investigation of breast tumors.   Tumors appear in mammographic images as a lighter-colored mass (Figure 2.5).   Despite its popularity, mammography still presents the following limitations (Benson *et al* 2004, Jarlman *et al* 1996, Baum *et al* 1994):

a)   Limited ability to detect small and lobular breast cancers,

b)   Poor resolution in dense breasts,

c)   Lack of significant improvement in detection of breast cancer over the years despite latest advances in digital mammography, and

d)   Detection of non-invasive carcinomas that do not have microcalcifications.

<u>Ultrasound:</u>   With the advancement of ultrasound technology since the late 1990's, ultrasound, once relegated to a minor role, has become as sensitive as X-ray mammography in detecting invasive breast cancer (Benson *et al* 2004).   Tumors appear as a darker mass within the breast (Figure 2.6).   The advantage of ultrasound is the lack of radiation, maintenance of resolution for dense breast, and quick, real-time image acquisition (Benson *et al* 2004, Pfleiderer *et al* 2002, Baum *et al* 1994).   However, due to its limited ability to detect microcalcifications or pre-invasive carcinomas, the combination of ultrasound with X-ray mammography for breast tumor screening has become common practice (Benson *et al* 2004, Baum *et al* 1994).

<u>Magnetic resonance imaging (MRI):</u> MRI used with the contrasting agent gadolinium and fat suppression methods has been proven to be the most sensitive modality for

showing the presence and extent of breast tumors (Kopans 2000). MRI has shown to have sensitivity over 90% (Hall-Craggs 2000) and can detect tumors as small as 4 mm in diameter (Pfleiderer *et al* 2002). Breast tumors appear as an enhanced, white mass (Figure 2.7). However, because of cost, limited access, and moderate to low specificity, MRI is reserved mainly for searching for tumors, assessing the extent of disease, evaluation of postlumpectomy margins, and detecting recurrence (Smith *et al* 2001, Kopans 2000). MRI is also used for localization and biopsy of tumors that cannot be viewed by other modalities or can be used in conjunction with ultrasound (Smith *et al* 2001).
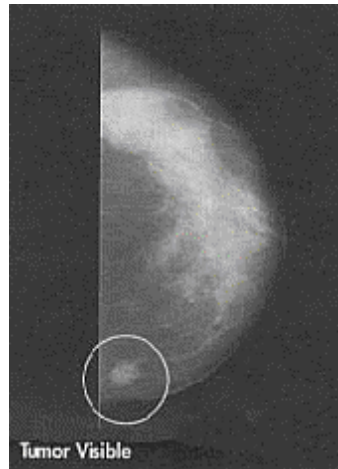
Figure 2.5: A mammographic image of a breast cancer tumor
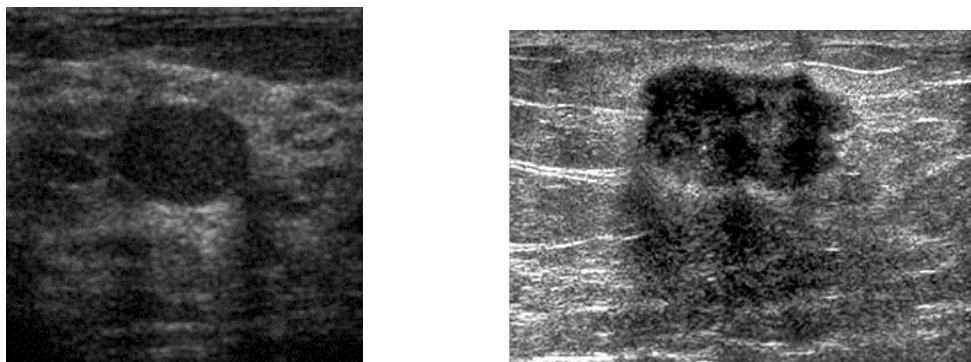
Figure 2.6: Ultrasound images of a cyst (left) and a solid cancer mass (right) as dark spots
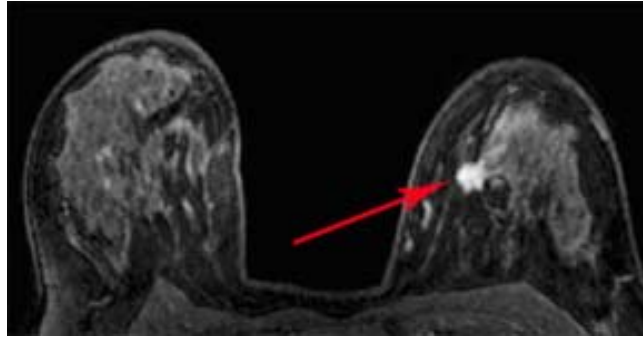
Figure 2.7: MRI image of a breast cancer tumor

2.4.2 Breast biopsies

There is no imaging modality that is 100% accurate in determining the breast tumor type. In cases of uncertainty, a biopsy, which is the removal and examination of tissue to establish a precise diagnosis, is performed. With the advancement of breast imaging sensitivity during the mid 1980's, minimally-invasive fine-needle aspiration (FNA) and core-needle (CN) biopsy techniques replaced open excision biopsies as common practice (Caleffi *et al* 2004, Bloom *et al* 2001). Fine needle aspiration uses a 20 gauge (0.902 mm OD, 0.584 mm ID) to 22 gauge (0.711 mm OD, 0.394 mm ID) needle attached to a syringe to extract either tumor cells for cytology from solid tumors or fluid from cysts. Core needle biopsies use 11 gauge (3.0 mm OD, 2.34 mm ID) to 14 gauge (2.08 mm OD, 1.55 mm ID) cutting needles to remove sections of tissue for histology. Core needles have a much lower inadequate sampling rate than FNA and, unlike FNA, can differentiate between in-situ and invasive carcinomas (Venta 2000).

Core and fine needle biopsies can be performed under ultrasound or stereotactic guidance. Stereotactic guidance uses the principle of parallax to determine the three-dimensional location of the tumor in the breast. Three X-ray images of the breast (one at

0° and one at $\pm15^o$ from the normal to the breast) are taken and sent to a computer which generates the three-dimensional coordinates of the tumor within the breast through a computer algorithm using the principles of parallax. The biopsy needle is then positioned by the stereotactic system according to those coordinates (Venta 2000). Two types of core-needle biopsies are employed under stereotactic guidance: a rapid-fire, spring-loaded biopsy gun and the directional, vacuum-assisted biopsy instrument. The directional, vacuum-assisted biopsy is preferred when larger amounts of tissue are required since they do not have to be removed from the breast to collect a sample.

Despite its localizations being accurate only to within 1 mm, the ultrasound guidance is preferred by the patient to stereotactic guidance because it takes less time to perform and does not require breast compression. However, stereotactic biopsies are preferred when the lesions are not visualized by the ultrasound modality (limited imaging of microcalcifications and in-situ carcinomas) and when large amount of samples are needed.

2.5 Breast tumor treatment methods

2.5.1 Open excision procedures

Even though there were different variations of the procedure dating back to 1867, William Stewart Halsted was credited for performing the first radical mastectomy procedure in 1898, which involved the total removal of the breast tissue, including the skin, pectoralis major and minor muscles, and the axillary lymph nodes (Sakorafas 2001). Lymph nodes act as a filter for the lymph, and cancer had already been found to spread through the lymphatic system. The axillary lymph nodes are removed and analyzed for

metastasis, since most of the lymph within the breast passes through these nodes. Patients who underwent the Halsted mastectomy treatment suffered a sharp decrease in recurrence. Thus, this mastectomy procedure gained wide acceptance through the first three quarters of the twentieth century (Sakorafas 2001).

In 1948, Patey proposed a modified radical mastectomy, which preserves the pectoralis major. Auchincloss and Madden further modified it by preserving both the pectoralis major and minor muscles (Sakorafas 2001). Because the pectoralis minor is not removed, only the lowermost axillary lymph are removed for analysis (Baum *et al* 1994). By 1982, practicing surgeons concluded that there was no change in the local control and survival rate between the classical Halsted and the modified mastectomy approach. Up to the present time, almost all mastectomies are performed through this modified radical approach (Sakorafas 2001, Baum *et al* 1994), which, up to the 1990's, was the main treatment for malignant breast lesions (Tavassoli 1999, Osborne 1996).

In the early stages of breast imaging, only larger tumor masses were visualized, and the patient would be forced to undergo radical treatment procedures. The advancement of imaging technology allowed the detection of smaller breast tumors. The results of various studies pushed the National Institutes of Health in 1990 to issue the Consensus Development Conference Statement, which acknowledged that breast conservation therapy of early stage breast cancer followed by adjuvant radiation therapy had equivalent outcomes to mastectomy, and therefore was recommended for early stage breast cancers. This led to the development of lumpectomy, which calls for the removal of the breast tumor plus approximately 1 cm of surrounding healthy tissue (Kacher and Jolesz 2004), followed by adjuvant radiation therapy and/or chemotherapy depending on

the outcome of the sentinel lymph node biopsy and/or axillary lymph node analysis. While most breast centers prefer to perform lumpectomies on small tumors less than 2 cm in diameter, others, with the use of radiation therapy or chemotherapy, prefer to treat tumors up to stage II (2-5 cm in diameter) (Sakorafas *et al* 2001).

2.5.2 Minimally Invasive Techniques

Even though lumpectomy allows the woman to retain her breast, the procedure may still be traumatic and disfiguring to the patient depending on the size of the tumor mass and the size of the woman's breast. Therefore, minimally-invasive techniques are being investigated and designed to replace lumpectomy as a breast conserving technique. As in lumpectomy, these procedures are designed at present to treat small, stage I to II tumors, approximately 1 to 2 cm in diameter, plus some degree of surrounding tissue. Since these procedures are designed to treat tumors within the breast, they rely heavily on imaging modalities used to not only guide the treatment probe to the tumor site but to effectively monitor the treatment. These procedures are, therefore, best suited for breast tumors whose margins are well-delineated and visible, such as those of infiltrating ductal carcinomas-not otherwise specified with little or no *in-situ* disease along the ducts. These minimally-invasive or non-invasive procedures are currently experimental for treatment of breast carcinomas and are currently thermal (hypothermic or hyperthermic) treatments.

Hypothermic techniques include cryotherapy, in which a ball of ice is formed inside the tumor. Cells closest to the cryogenic probe are frozen quickly, resulting in the formation of intracellular ice. Cells farther away are frozen more slowly, creating a hypertonic environment around the cell. This creates an osmotic shift, from which the

cell suffers dehydration, cellular membrane rupture, and eventual cell death (Caleffi *et al* 2004, Kaufman *et al* 2004). Subfreezing temperatures also cause damage to the epithelial cells of the capillaries, leading to leakage, thrombosis, and anoxia (Kaufman *et al* 2004).

The degree of damage observed during hyperthermia depends on the temperature induced and the duration of the hyperthermia. Below 50-60°C, the cells suffer damage to the organelles and enzymes inside the cell with some amount of rupture of the nucleic and cell membrane within minutes to hours. However, the repair mechanism of the cell may not be totally destroyed within this temperature range even at such long irradiation time, allowing the cells the possibility of survival (Pearce 1995). Above 50-60°C, the proteins begin to denature within the cells and in the connective tissue outside the cells. The repair mechanism within the cells is permanently destroyed and the cell and nucleic membranes are completely ruptured. The blood vessels also coagulate, thus cutting off the blood supply for those cells, inducing hypoxia. This latest chain of events is called tissue coagulation, and is desired for complete destruction of the tumor and surrounding tissue (Bloom *et al* 2001, Pearce 1995, Thomsen 1995).

Hypothermic minimally-invasive techniques to treat small tumors of the breast include cryotherapy (Caleffi *et al* 2004, Kaufman *et al* 2004, Pfleiderer *et al* 2002). Hyperthermic minimally-invasive or non-invasive techniques include radiofrequency (Izzo *et al* 2001, Elliot *et al* 2002, Hayashi *et al* 2003), focused ultrasound (Gianfellice *et al* 2003, Wu *et al* 2003), and laser interstitial thermotherapy (Downlatshahi *et al* 2000, Halls-Craggs *et al* 2000, Basu *et al* 1999, Akimov *et al* 1998, Downlatshahi *et al* 1996, Mumtaz *et al* 1996, Harries *et al* 1994, Steger *et al* 1989).

Cryoablation: Cryoablation employs a cyclic freezing-thawing technique to induce an ice ball that encompasses the tumor plus a certain amount of surrounding, healthy breast tissue. Ultracold temperatures down to approximately $-160^{o}C$ are achieved through the expansion of Argon gas from high to low pressure through a constricted orifice within the inserted probe at the tumor site (Figure 2.8) (Caleffi *et al* 2004, Kaufman *et al* 2004). The probe acts as a heat exchanger, forming an ice ball inside the tumor within the vicinity of the probe. After the treatment is completed, helium gas, which has the opposite effect, is used to warm the probe to facilitate its removal after freezing (Caleffi *et al* 2004, Kaufman *et al* 2004). Ultrasound has been used both for guidance of the probe into the tumor site and for treatment monitoring. The ice ball induced in the tissue is highly echogenic and well delineated in the ultrasound images (Caleffi et al 2004, Pfleiderer *et al* 2002).

The forming ice ball produces an anesthetic effect to the patient during the procedure, yet local anesthesia is still required. Ecchymia, discomfort, edema, and mild to moderate swelling were common one to two days after the procedure. Minor side effects of this procedure include pain during and after procedure, hematomas, breast abscess, edema, and transient mild thermal skin injury, some followed by hypopigmentation (Caleffi *et al* 2004, Kaufman *et al* 2004, Pfleiderer *et al* 2002). Skin injury usually resulted from the tumor or the probe tip itself being very near or touching the skin. Therefore, skin protection at the incision site was required.
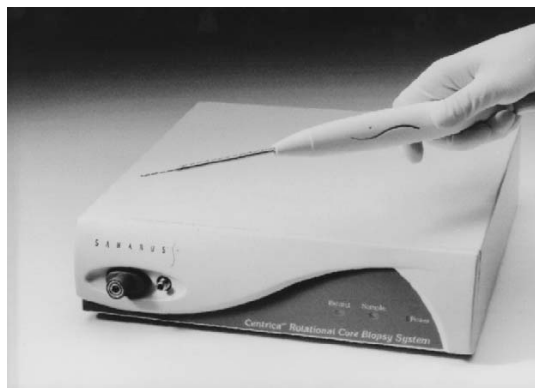
Figure 2.8: The Sanarus Visica cryoablation treatment system with cryoprobe (Caleffi et al 2004)

At present, cryotherapy has been approved for fibroadenomas, but is still being investigated for breast cancer tumors. Kaufman *et* al 2004 reported that 50% of palpable fibroadenomas less than 2.5 cm in diameter became non-palpable after 6 months, where as 94% of palpable fibroadenomas greater than 2.5 cm in diameter remained palpable after 6 months (Kaufman *et* al 2004). Caleffi *et* al 2004 reported that 84% of palpable fibroadenomas less than 2.5 cm in diameter became non-palpable after 12 months (Caleffi *et al* 2004). Pfleiderer *et al* reported only a 19% ablation rate of invasive carcinomas, where approximately 60% of those tumors less than 16 mm were treated successfully (Pfleiderer *et al* 2002). Therefore, these results indicate that, for those tumors greater than 2.5 cm, cryotherapy has a large potential for leaving residual tumor at the treatment site. Further studies must be conducted to improve the ablation rate for both benign and malignant tumors (Caleffi *et al* 2004).

Radiofrequency: In the radiofrequency (RF) treatment procedure, a needle probe is inserted into the tumor site, usually through ultrasonographic (Izzo *et al* 2001) or stereotactic guidance (Elliot *et al* 2002). The needle probes are coupled into a

radiofrequency generator. Two grounding pads are placed on each thigh to complete the current path. Once placed inside the tumor, tines are deployed from the probe tip into the tissue (Figure 2.9). Different needle probe diameters and number of tines are used depending on the size of the tumor. After deployment of the tines, a high-frequency alternating current is sent from the electrode into the tissue. Due to the tissue impedance, heating is induced within the tissue. The coagulation is detected when the tissue impedance suddenly increases and the power delivered to the tissue automatically drops. After treatment, the tines are retracted, and the probe is removed. Only the tissue through which the RF current passes through directly is heated above a cytotoxic temperature (Izzo *et al* 2001).

Ultrasound has been investigated as the imaging modality for both fiber insertion and treatment monitoring. The thermal lesions appear in the images as ill-developed hyperechoic zones. The size of the lesions is hard to measure through the images due to ultrasonographic shadowing from the hyperechoic region (Izzo *et al* 2001). MRI is not a good imaging modality for RF due to the requirement for metallic probes (Hall-Craggs 2000).

Figure 2.9: Different radiofrequency probe sizes with different amount of tines depending on the size of the lesion (Izzo et al 2001)

According to Izzo *et al*, 25 out of 26 tumors with mean average of 16 mm showed no remnant viable tumor cells (Izzo *et al* 2001). Elliott *et al* reported results on one patient with a 16 mm diameter invasive tumor in whom radiofrequency treatment was performed for 20 minutes. No viable tumor was observed in the breast tissue after being excised approximately 1 month after treatment (Elliot *et al* 2002). However, other studies have found residual tumor tissue at the ablation zone boundary (Huston and Simmons 2005). A major complication of RF ablation is full thickness burns of the skin, especially for tumors close to the skin (Izzo *et al* 2001). The deployed tines also have a tendency to bend in more dense breasts during treatment (Huston and Simmons 2005). This may lead to either a fracture of the tines within the breast or a higher risk of residual tumor.

Focused ultrasound: In the focused ultrasound treatment procedure, a specially designed transducer emits focused ultrasound into the tissue through the skin. The transducer probe is positioned such that the focal spot resides in the tumor (Figure 2.10). The ultrasound focal spot has been reported to encompass a tissue volume as small as a few cubic millimeters (Gianfelice *et al* 2003) and as large as 16.7 mm^3 (Wu *et al* 2003). The intensity of this specific focal spot ranges from 5000 to 15000 W·cm^{-2} (Wu *et al* 2003). Heat is induced at the focal spot by the absorption of the ultrasound until that area has been thermally treated. The focal spot is then scanned along the expanse of the tumor tissue until the entire tumor is treated. The scanning speed ranges from 1-3 mm·s^{-1}, with the irradiation time ranging from 45 min to 2.5 hours. This could be a considerably long time for the patient to remain immobile under local anesthesia. Movement of the patient may result in the target area moving out of the small focal spot of the ultrasound (Hall-

Craggs 2000). Usually, these procedures are done either with MRI (Gianfelice *et al* 2003) or ultrasound (Wu *et al* 2003) guidance and monitoring. According to Wu *et al*, hyperechoic images correspond well with the size of the necrotic region (Wu *et al* 2003).

Wu *et al* also reported successfully treating entire tumors plus a surrounding area of normal healthy tissue ranging in thickness from 1.5 to 2.2 cm for 48 patients investigated without any residual tumor. Patients have experienced mild local pain, warmth, and a sensation of heaviness in the breast, most likely due to the hardening of the tissue after hyperthermia. One patient suffered minimal skin burns. There was no bleeding or infection of the treated breast (Wu *et al* 2003). This procedure is still experimental and requires further investigations before being considered for clinical use.

<u>Laser interstitial thermotherapy:</u> Laser interstitial thermotherapy (LITT) was first introduced by Bown in 1983 (Bown 1983). The use of LITT in breast tumors was first published by Steger *et al* in 1989 (Steger *et al* 1989*)*. LITT is a minimally-invasive therapeutic procedure, in which the tumor is treated with near-infrared laser radiation (wavelength=800-1100nm) that is emitted from either a bare, spherical diffusing, or cylindrical diffusing tip optical fiber (Figure 2.11) (Ritz *et al* 2007, Dossing *et al* 2006, Mohammed and Verhey 2005, Vogl *et al* 2004, Mack *et al* 2004, Verhey *et al* 2003, Prudhomme *et al* 2003, Nikfarjam and Christophi 2003). The optical fiber is inserted into the breast tumor site either through ultrasound, CT, or MRI guidance (Bloom *et al* 2001, Dowlatshahi *et al* 2000, Basu *et al* 1999, Akimov *et al* 1998, Dowlatshahi *et al* 1996, Mumtaz *et al* 1996, Harries *et al* 1994, Steger *et al* 1989). Near-infrared radiation provides a good compromise between the absorption of water (Figure 2.12) and blood

(Figure 2.13), thus inducing a sufficient temperature increase while allowing a larger penetration depth into the tumor. During irradiation, heat is induced in the tissue by both the absorption of the near-infrared radiation by the tissue and the diffusion of the heat to the surrounding areas. Within seconds to minutes above $60^{o}C$, depending on the tissue, photocoagulation and cell death occur (Figure 2.11).
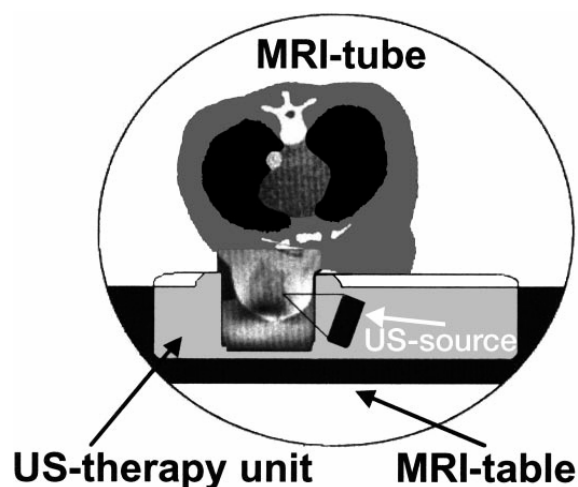
Figure 2.10: A focused ultrasound system being used to treat a breast tumor under MRI guidance

Figure 2.11: An optical fiber inside the liver during laser interstitial thermotherapy (Neimz M; Laser-Tissue Interactions; Springer-Verlag, Berlin 1996)
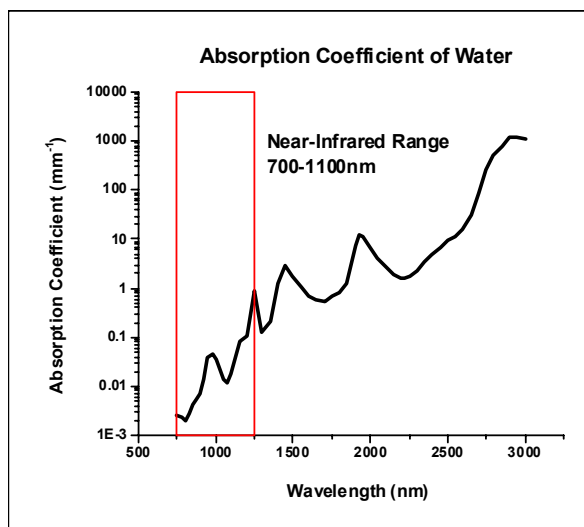
Figure 2.12: The absorption spectrum of water from the visible to the mid-infrared range (Hale and Querry 1973)
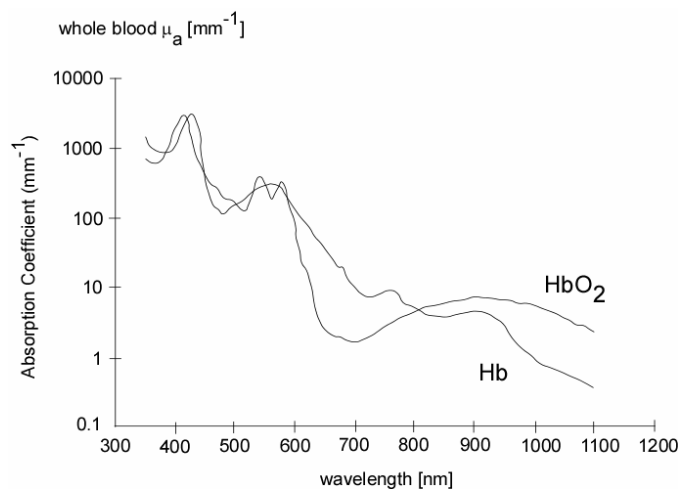
Figure 2.13: The absorption spectrum of blood in the visible and near-infrared (Roggan et al 1995)

Several preliminary clinical studies of LITT for the treatment of small localized breast tumors were performed with either a CW or pulsed Nd:YAG (1064 nm) laser (Basu *et al* 1999, Akimov *et al* 1998, Steger *et al* 1989) or with diode laser systems (805 nm) (Dowlatshahi *et al* 2000, Mumtaz *et al* 1996, Dowlatshahi *et al* 1996, Harries *et al*

1994). Laser energy was delivered through one or multiple precharred or clean bare optical fibers (Basu *et al* 1999, Akimov *et al* 1998, Mumtaz *et al* 1996, Harries *et al* 1994, Steger *et al* 1989), or optical fibers with spherical diffusing tips (Dowlatshahi *et al* 2000, Dowlatshahi *et al* 1996). These studies used ultrasound (Basu *et al* 1999, Akimov *et al* 1998, Mumtaz *et al* 1996, Harries *et al* 1994, Steger *et al* 1989) or a stereotactic biopsy device (Dowlatshahi *et al* 1996) for guidance, and invasive temperature probes (Dowlatshahi *et al* 2000, Akimov *et al* 1998, Dowlatshahi *et al* 1996), ultrasound (Basu *et al* 1999, Harries *et al* 1994, Steger *et al* 1989), or X-ray Computed Tomography (CT) (Harries *et al* 1994) for treatment monitoring.

Follow up to a maximum of 64 months (Akimov *et al* 1998) showed few reported cases of recurrence when the tumor was completely treated (tumors $\leq$ 4 cm in diameter) (Basu *et al* 1999, Harries *et al* 1994). Minor side effects included pain and sensation of warmth during the procedure (Basu *et al* 1999, Mumtaz *et al* 1996, Harries *et al* 1994, Steger *et al* 1989), mild discharge and bleeding (Basu *et al* 1999, Harries *et al* 1994), skin burns and epithelial breakdown of the skin at the puncture site (Basu *et al* 1999, Akimov *et al* 1998), transient fever, nausea, and anxiety (Akimov *et al* 1998). According to investigations in which the breast was removed some time after treatment, there was no sign of infection before and after removal of the breast (Dowlatshahi *et al* 2000, Basu *et al* 1999).

2.6. Optimization of LITT for breast tumor therapy

The advantage of laser interstitial thermotherapy over the other minimally-invasive techniques is its tunability. Unlike the other techniques, LITT has the potential to locally

treat a variety of tumor sizes with minimal collateral damage and surgical time by modifying the laser parameters used, particularly the wavelength. Other adjustable laser parameters include the laser output power out of the optical fiber, laser irradiation time, laser wavelength, and optical fiber tip geometry.

Unfortunately, clinical studies of LITT for breast cancer have focused on demonstrating the feasibility of LITT for breast tumors using delivery systems that were not optimized (Dowlatshahi *et al* 2000, Basu *et al* 1999, Akimov *et al* 1998, Mumtaz *et al* 1996, Dowlatshahi *et al* 1996, Harries *et al* 1994). Optimization of the delivery system requires the following steps:

1. Selection of efficient optical fibers and fiber insertion: Previously published investigations used bare tip and spherical diffusing tip optical fibers. There has been no extensive investigation on the use of cylindrical diffusing tip optical fibers, which have a larger emitting length and may be more suitable for breast tumor treatment. The insertion techniques into the tumor site also need to be improved.

2. Implementation of the optimal laser parameters necessary to treat breast tumors of different sizes: The laser parameters used in previous studies were empirically determined with no prior knowledge of the effect of the laser wavelength, irradiation time, and output power on the induced thermal lesions in the breast tissue. Therefore, the laser parameters used by these investigations were not specifically chosen for breast tumors. The optimal laser parameters necessary to completely treat a breast tumor of a certain size may be obtained by understanding the correlation between the laser parameters used during LITT and the coagulation size induced in the breast tissue.

The correlation between the laser parameters and the coagulation size can be obtained by creating an optical-thermal model that would calculate:

1. the light distribution in the tissue during laser irradiation as a function of the laser parameters and the optical properties of the breast tissue,

2. the temperature distribution in the tissue as a function of the light distribution during laser irradiation, and

3. the coagulation size in the tissue as a function of the temperature increase in the tissue during and shortly after irradiation.

The light distribution in the tissue during LITT is dependent on both the optical properties of the tissue and the laser parameters. The light distribution can be expressed by the radiative transfer equation (Tuchin 2000, Niemz 1995, Welch *et al* 1995):

$$\frac{dL(\mathbf{r},\hat{\mathbf{s}})}{ds} = -(\mu_a + \mu_s)L(\mathbf{r},\hat{\mathbf{s}}) - \mu_s \int_{4\pi} p(\hat{\mathbf{s}},\hat{\mathbf{s}}')L(\mathbf{r},\hat{\mathbf{s}}')d\omega' + \varepsilon(\mathbf{r},\hat{\mathbf{s}}) \qquad \text{Eq. 2.1}$$

where $L(\mathbf{r},\hat{\mathbf{s}})$ is the radiance ($W \cdot m^{-2} \cdot sr^{-1}$) at the location $\mathbf{r}$ in the tissue and in the $\hat{\mathbf{s}}$ direction, μ_s is the scattering coefficient of the tissue, which is the inverse of the mean path length between scattering events (m^{-1}), $p(\hat{\mathbf{s}}, \hat{\mathbf{s}}')$ is the scattering phase function, which is the probability density function of the light scattering in the direction of unit vector $\hat{\mathbf{s}}'$ from an incident direction of unit vector $\hat{\mathbf{s}}$, $d\omega'$ is the unit solid angle, and $\varepsilon(\mathbf{r},\hat{\mathbf{s}})$ is the radiance of the optical fiber source at the location $\mathbf{r}$ in the tissue and in the $\hat{\mathbf{s}}$ direction ($W \cdot m^{-2} \cdot sr^{-1}$). The fluence rate (in $W\ mm^{-2}$) of light within the tissue can be calculated from the radiance by using the following equation:

$$\phi(\mathrm{r}) = \int_0^{4\pi} L(\mathbf{r},\hat{\mathbf{s}})d\Omega \qquad \text{Eq. 2.2}$$

where $\phi(\mathbf{r})$ is the fluence rate at a location $\mathbf{r}$ from the source and $d\Omega$ is the infinitesimal solid angle. The fluence rate determines the temperature increase due to the irradiation.

The temperature increase in the tissue during laser irradiation is dependent on the thermal properties of the tissue (heat conductivity and specific heat capacity) and the fluence rate of light within the tissue during laser irradiation. The temperature distribution can be expressed by the bio-heat equation (Orr and Eberhart 1995):

$$\rho c \frac{\partial T(r,t)}{\partial t} = k\nabla^2 T(\mathbf{r},t) + \rho_b c_b \omega_b (T_{art}(\mathbf{r},t) - T(\mathbf{r},t)) + S(\mathbf{r},t) \qquad \text{Eq.2.3}$$

where $T(\mathbf{r},t)$ is the temperature as a function of location and time, ρ is the density of the tissue (kg m^{-3}), ρ_b is the density of blood, c is the specific heat (kJ·kg^{-1}·K^{-1}), c_b is the specific heat of blood, ω_b is the tissue average volumetric blood perfusion rate, k is the thermal conductivity (W·m^{-1}·K^{-1}), $T_{art}(\mathbf{r},t)$ is the temperature of the arterial blood entering the tissue, and $S(\mathbf{r},t)$ is the heat source term (W·m^{-3}). The heat source term can be expressed as the following (Welch and Gardner 1997):

$$S(\mathbf{r},t) = \mu_a \phi(\mathbf{r},t) \qquad \text{Eq.2.4}$$

where μ_a is the absorption coefficient, which is the inverse of the path length between photon absorption events (m^{-1}) and $\phi(\mathbf{r},t)$ is the fluence rate (W·m^{-2}).

The amount of the photocoagulation induced in the tissue is dependent on both the temperature increase in the tissue and the heating time. The photocoagulation can be expressed by the Arrhenius equation (Diaz *et al* 2003, Pearce and Thomsen 1995, Bauer and Henle 1979):

$$\Omega = \ln(\frac{C_o}{C_f}) = A \bullet \int_0^t e^{\frac{-E_a}{RT(t)}} dt \qquad \text{Eq.2.5}$$

where Ω is the thermal damage parameter, A is the collision frequency (s^{-1}), E_a is the activation energy to achieve photocoagulation (J·mol^{-1}), R is the universal gas constant (J·mol^{-1}·K^{-1}), T is the temperature (K), [C_o] is the concentration of surviving, normal tissue, and [C_f] is the concentration of denatured tissue. With knowledge of the collision frequency and the activation energy, the percentage of coagulation can be calculated from the temperature distribution as a function of time.

The purpose of this investigation is to develop and optimize the delivery system for LITT of small tumors of the breast by completing the following tasks:

1. <u>Design of a fiber-insertion system for cylindrical diffusing optical fibers</u>

A fiber-insertion system will be developed to accurately and efficiently insert a cylindrical diffusing tip optical fiber into the breast tumor under stereotactic guidance. The design and testing of this fiber-insertion system is described in chapter 3.

2. <u>Design and validation of an optical-thermal model</u>

An optical-thermal model will be developed and validated that will calculate the coagulation sizes in the breast during laser irradiation for a range of laser parameters including output power, irradiation time, laser wavelength, and fiber geometry. This optical-thermal model will calculate the light, temperature, and coagulation distribution within the breast during laser irradiation. The optical-thermal model is described in chapter 4. The optical thermal model will be validated by first measuring the optical properties of *ex-vivo* fibro-fatty porcine mammary chain tissue, a breast tissue phantom. These measurements are described in chapter 5. The coagulation model will then be optimized to predict the coagulation in the *ex-vivo* fibro-fatty tissue during laser irradiation (chapter 6). The optical-thermal model will then be validated by comparing

the temperature and coagulation predictions of the model to temperature and coagulation zones measured during laser irradiation experiments in *ex-vivo* porcine mammary chain tissue at 830, 940, and 980 nm with a cylindrical diffusing tip optical fiber (chapter 7).

Investigation of the fiber insertion technique, treatment monitoring, and optimal laser parameters is crucial to the development of the delivery system for laser interstitial thermotherapy of breast tumors. An optimized delivery system would allow for a safe and efficient clinical application of LITT for breast tumors with minimal collateral damage and surgical time.

3. FIBER-INSERTION SYSTEM

3.1 Introduction

A minimally-invasive treatment procedure for small tumors of the breast using laser interstitial thermotherapy has been developed at the Ophthalmic Biophysics Center, Bascom Palmer Eye Institute, University of Miami (Robinson *et al* 1998, Robinson *et al* 1996). The steps of this procedure are the following (Figure 3.1).

a) The tumor is localized in the breast using stereotactic imaging.

b) A cylindrical diffusing tip optical fiber is inserted into the tumor site under stereotactic X-ray guidance.

c) The tumor is irradiated with a specific amount of laser energy necessary to coagulate the tumor. The treatment is monitored with the same stereotactic imaging system used for the optical fiber insertion.

d) After irradiation, the optical fiber is removed from the breast and the insertion site is closed.

Before this procedure can be implemented, the following must be accomplished:

a) Design, construction, and testing of a fiber-insertion system that will insert cylindrical diffusing tip optical fibers to the desired position under stereotactic guidance, and

34
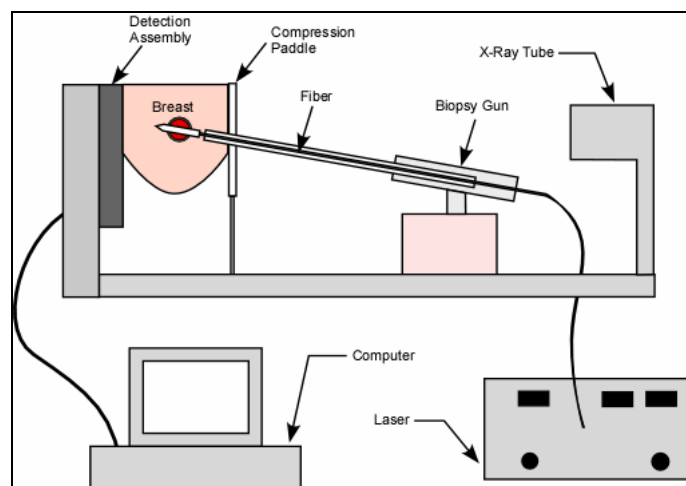
Figure 3.1: A schematic of the LITT, minimally-invasive treatment of small tumors of the breast under stereotactic guidance

b)   Development of an optical-thermal model that will calculate the fiber output power and treatment time necessary to coagulate small, different size tumors of the breast with a specific laser wavelength.

In this chapter, the following will be described:

a)   The proposed minimally-invasive procedure for stereotactic-guided LITT of small breast tumors using laser interstitial thermotherapy,

b)   The design, procedure, and testing of the fiber-insertion system.

3.2 Cylindrical diffusing tip optical fibers

Bare tip (normal and pre-charred) (Figure 3.2 and Figure 3.3) and diffusing tip (spherical) optical fibers have been clinically used for laser interstitial thermotherapy of breast tumors (Dowlatshahi *et al* 2004, Dowlatshahi *et al* 2000, Basu *et al* 1999, Akimov

et al 1998, Akimov *et al* 1997, Mumtaz *et al* 1996, Dowlatshahi *et al* 1996, Harries *et al* 1994, Steger *et al* 1989). The diffusing tip is preferred over the bare tip because of its larger light emitting surface area resulting in smaller power densities at the tip. Assuming 4 W out of the fiber, a multimode bare fiber with a 600 micron diameter circular surface area would have a power density of approximately 1415 W·cm^{-2} at the tip, while a cylindrical diffusing tip with a light emitting length of 2 cm and a tip diameter of approximately 2 mm would have a power density of approximately 3.2 W·cm^{-2} (Figure 3.3). This, in turn, leads to smaller temperature gradients within the tissue during laser irradiation and less risk of carbonization (Heisterkemp *et al* 1997). Carbonized tissue absorbs the laser radiation, preventing the transmission of light to other areas in the tissue. In addition, the cylindrical diffusing tip has a larger light-emitting area, which results in larger treatment volumes.

An ideal cylindrical diffusing tip fiber would have a scattering sleeve that is both small in diameter and resistant to high output power and extreme temperatures. A variety of commercially or custom made cylindrical diffusing tip optical fiber designs for the treatment of small tumors of the breast were tested (Salas 2001). The emission pattern and both thermal and mechanical endurance of different quartz and polymer cylindrical diffusing tip optical fibers were evaluated. A goniometric radiation system measured the emission pattern of the fiber tip by rotating a power detector around the fiber tip in the plane of the major fiber axis (Figure 3.4).
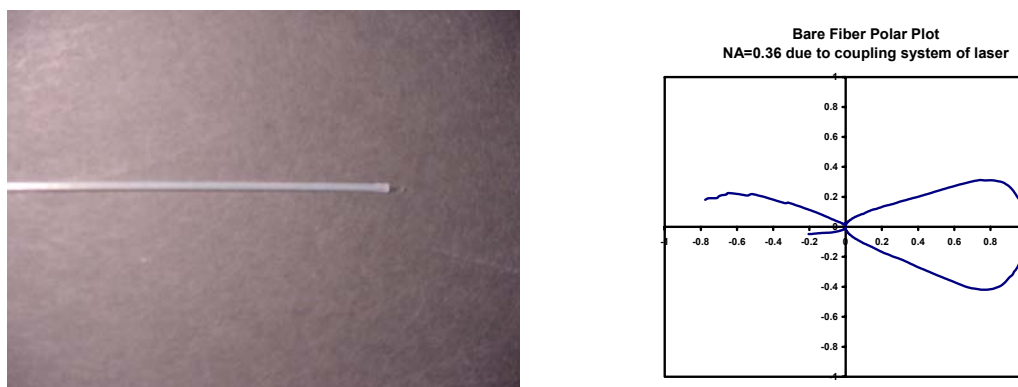
Figure 3.2: A bare tip fiber (0.39 NA 3M tecs hard clad multimode fiber, FT-600,EMT, ThorLabs, Newton, NJ) (left) and its emission pattern measured with our radiation measurement system (right)
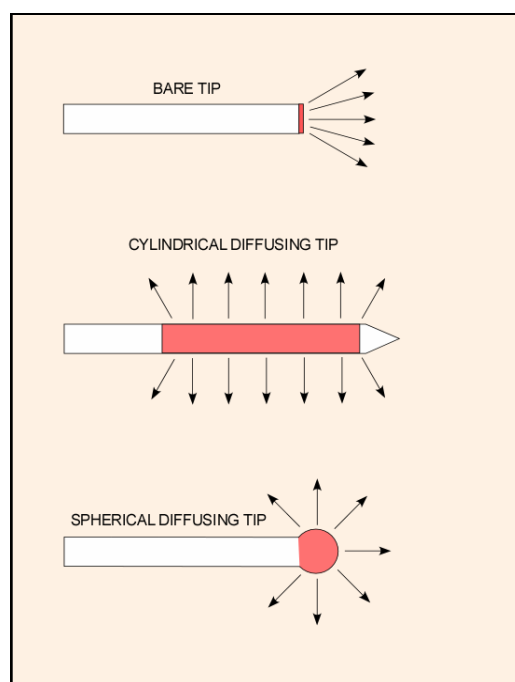
Figure 3.3: The light emitting areas and dosimetry of the bare tip (top), cylindrical diffusing tip (middle), and spherical diffusing tip (bottom) optical fibers

The best performing fibers investigated were the Indigo (Ethicon Endo-Surgery, Inc., Cincinnati, OH) and Dornier 6111 (H and D series) (Dornier MedTech, Kennesaw, GA) optical fibers. The Dornier 6111 optical fibers are bare tip fibers inserted into a quartz

sleeve that contains a diffusive material. The quartz tip has a light emitting length of 2 or 3 cm and an outer diameter of 0.9 mm (Figure 3.5). The H-series fibers were designed for coupling into the Dornier solid-state lasers, while the D-series fibers were designed for the Dornier diode lasers. The Indigo fibers consist of a bare tip fiber with a Tefzel polymer diffusing tip. This diffusing tip has a light-emitting length and an outer diameter of 16 mm and 1.8 mm, respectively (Figure 3.6). Our fiber insertion system was, thus, designed for the insertion of these two optical fiber designs.
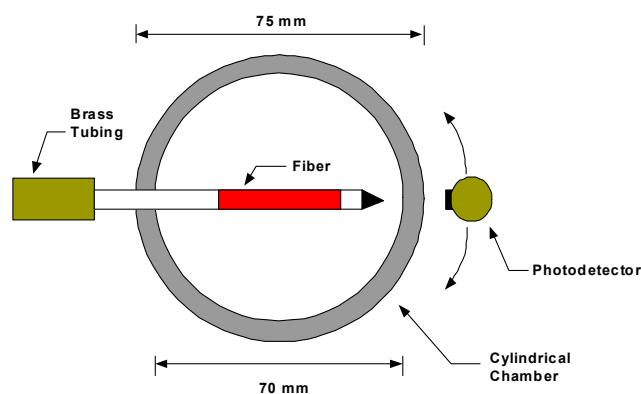
Figure 3.4: Goniometric radiation system used to measure the light emission out of the diffusing tip
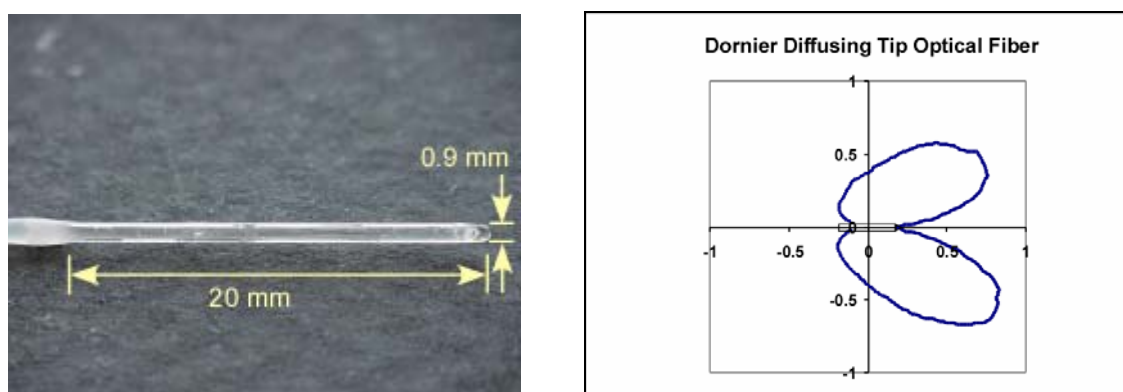
Figure 3.5: The Dornier D-Series/H-Series diffusing tip optical fiber (Dornier MedTech, Kennesaw, GA) (left) and its emission pattern measured with our goniometric radiation measurement system (right)
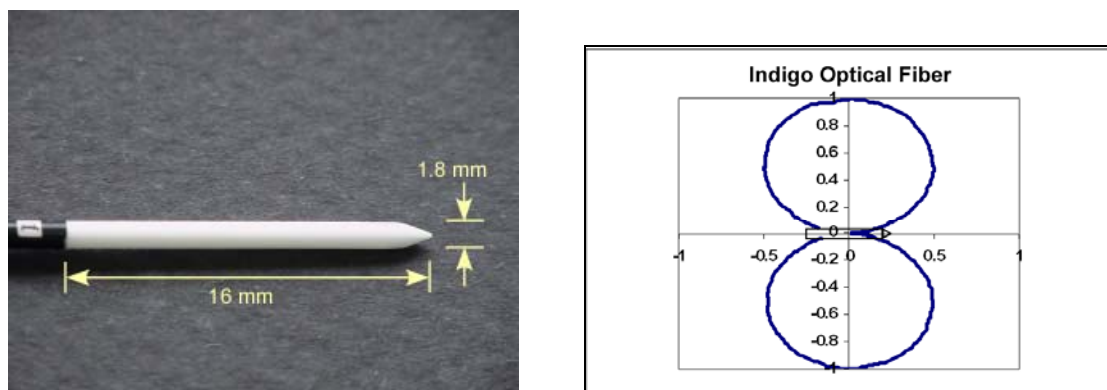
Figure 3.6: The Indigo diffusing tip optical fiber (Indigo Corp, Palo Alto, CA) (left) and its emission pattern measured with our goniometric radiation measurement system (right)

3.3 Stereotactic X-ray biopsy system

X-ray stereotactic guidance was chosen for this procedure for the following reasons:

a)   Its feasibility in locating tumors within the breast and guiding biopsy needles to the tumor site with high precision in comparison to ultrasound, and

b)   Its lower operation and maintenance cost in comparison to MRI.

Stereotactic imaging uses the principle of parallax to obtain the location of the tumor in the breast. Parallax is the shift of an object against a background due to the change in the position of the observer. During stereotactic imaging, the breast is compressed between the compression paddle and the detection system of the imaging system to prevent motion of the breast and for improved X-ray imaging. Three images are taken: one "scout" image directly facing the breast and two images at $\pm 15^{o}$ from the scout. These three images are sent to a computer, where a technician / operator locates the tumor on each of these images. The located tumors at each of these images should be aligned along the same horizontal axis. According to the information given by the technician / operator and the principle of parallax, the system uses these stereo images to

generate the three-dimensional position of the lesion using the distance between the source and image plane, the image shift between the two acquired $\pm15^{o}$ views at the image plane, and simple geometric relations (Figure 3.7) (Venta 2000, Evans 1996).

The fiber-insertion system is designed specifically for and will be tested with a Fischer Imaging Mammotest/Mammovision Plus high resolution stereotactic digital X-Ray biopsy system (Fischer Imaging Corp., Denver, CO) (Figure 3.8) (Minhaj *et al* 2002). The system consists of an X-ray tube arm containing the X-ray source, a breast compression paddle, a biopsy needle insertion system (the Autoguide system), and a digital X-Ray detection array system (bucky system) (Figure 3.8).

When a biopsy is to be performed, the patient is placed on a stereotactic biopsy table located above the CCD camera detection assembly. The breast is placed through a hole in the table and compressed between a compression paddle and the surface of the digital X-ray detection system. Once the technician / operator has taken the images at $\pm15^{o}$ and located the tumor on the computer images, the computer software calculates the location coordinates of the tumor and sends these coordinates to the Autoguide system. This system is located either between the compression and the X-ray tube or at 90° to the axis of the X-ray tube, and is equipped with the biopsy device (gun or aspiration system). The Autoguide system uses the coordinates to position the biopsy device such that the biopsy needle is fired into the tumor site with an accuracy of ±1 mm. Images are taken after insertion to confirm that the needle is within the boundaries of the tumor (Figure 3.9). If the fiber is not within the tumor, the needle is removed and the procedure is repeated. The fiber insertion system was designed to mount on the Autoguide of the stereotactic biopsy system in a similar fashion to the biopsy gun.
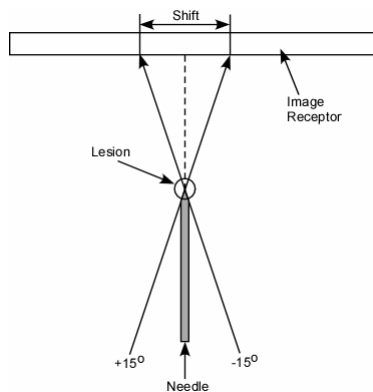
Figure 3.7: A schematic of stereotactic image location of breast lesions using the principles of parallax
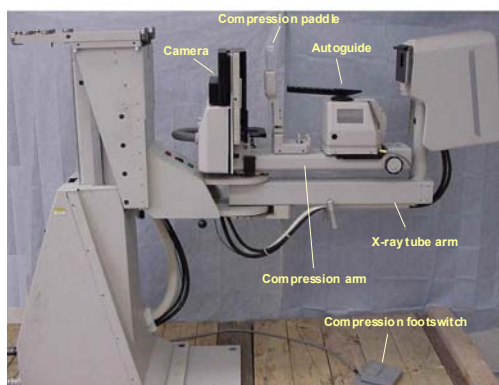
Figure 3.8: Fischer Mammotest/Mammovision Plus high resolution stereotactic digital X-Ray biopsy system (85200G-2, Fischer Imaging Corp., Denver, CO)(Minhaj et al 2002)
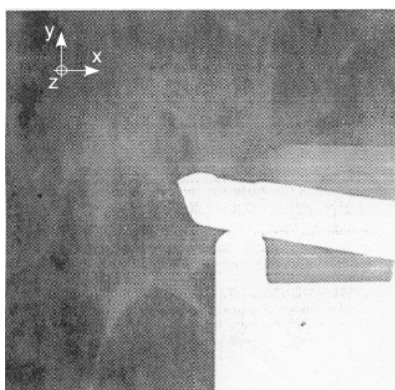
Figure 3.9: The biopsy needle stereotactically inserted into the breast tumor site (Venta 2000)

3.4 Fiber-Insertion System

3.4.1 Proposed procedure with stereotactic fiber insertion

The steps of the proposed procedure with optical fiber insertion into the tumor under stereotactic guidance are the following (Figure 3.10-12).

Step 1: Once the tumor has been located by the technician / operator with the stereotactic biopsy system, a needle and cannula similar to a biopsy needle and cannula assembly is inserted into the tumor site ±1 mm to make a track for the optical fiber. Images are taken to confirm that the needle is within the tumor site.

Step 2: The needle is removed from the breast, leaving the cannula in place for the fiber insertion.

Step 3: The optical fiber is inserted into the tumor site through the cannula up to the tip.

Step 4: The cannula is retracted prior to irradiation to expose the fiber tip to the tissue.

Step 5: The tumor is irradiated, and the treatment is monitored with the stereotactic biopsy system.

Step 6: The optical fiber is retracted through the cannula after treatment of the tumor and surrounding tissue.

Step 7: The cannula is retracted from the breast tissue after retraction of the optical fiber.

STEP 1: **The trocar and cannula of the fiber insertion system are stereotactically inserted into the tumor site**
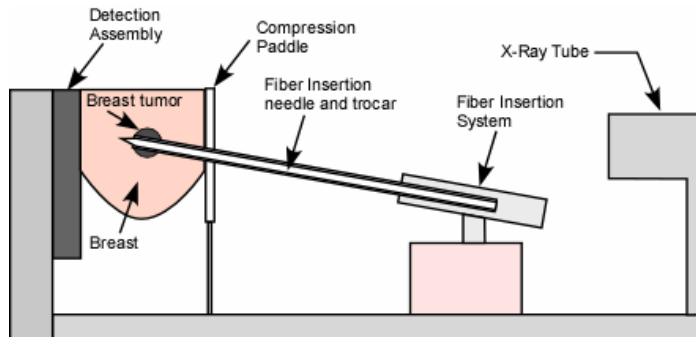
STEP 2: **The trocar is removed, leaving the cannula in the tissue as a track for the optical fiber**
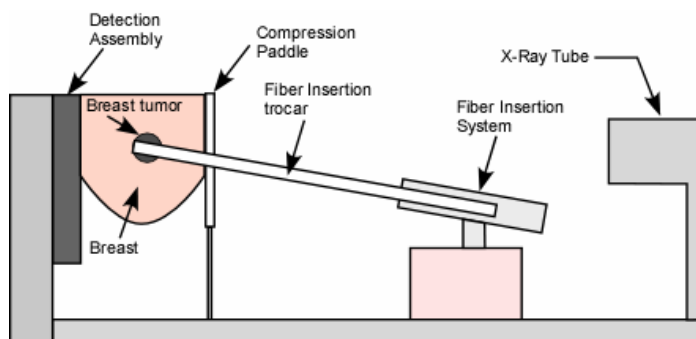
STEP 3: **The optical fiber is inserted into the tissue through the cannula up to the cannula tip**
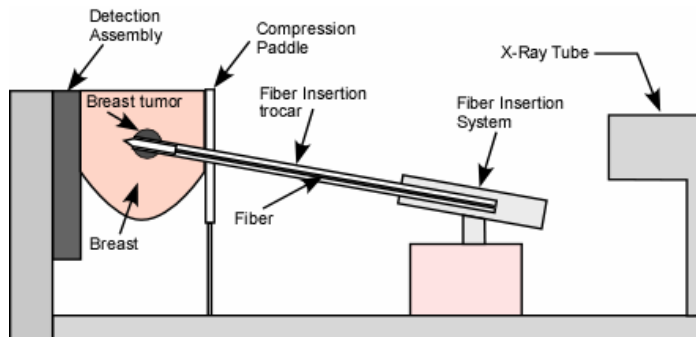
<u>Figure 3.10:</u> Steps1-3 of the proposed technique for the treatment of small tumors of the breast using laser interstitial thermotherapy.

STEP 4: **The cannula is retracted slightly to expose the fiber tip to the tissue**
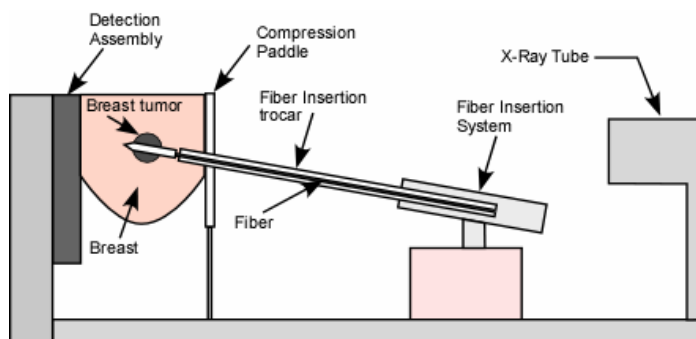
STEP 5: **The tumor is irradiated until completion of treatment**
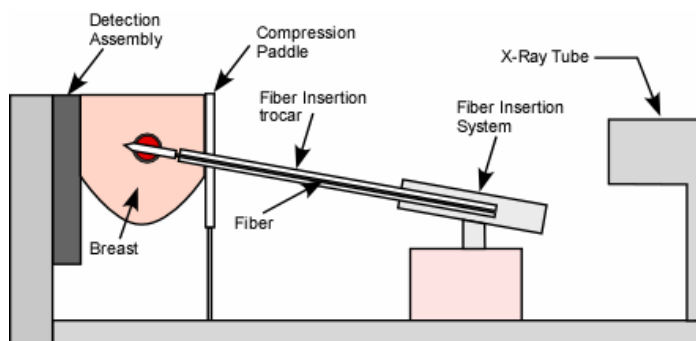
STEP 6: **The fiber is retracted out of the breast through the cannula after treatment**
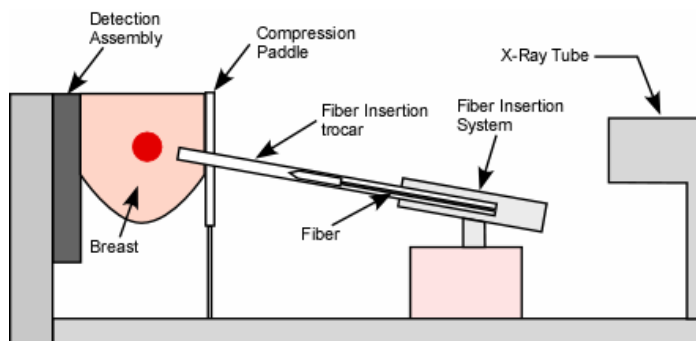
Figure 3.11: Steps4-6 of the proposed technique for the treatment of small tumors of the breast using laser interstitial thermotherapy.

STEP 7: The cannula is retracted out of the breast
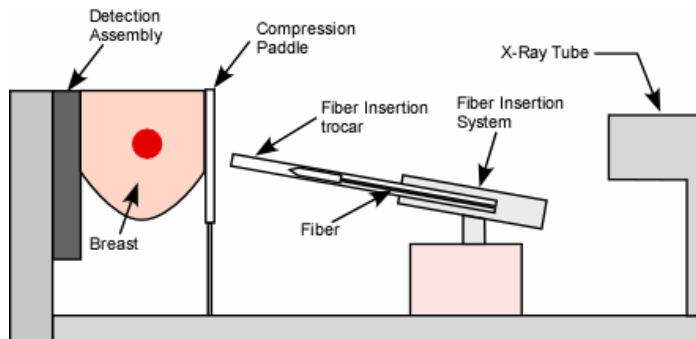
Figure 3.12: Step 7 of the proposed technique for the treatment of small tumors of the breast using laser interstitial thermotherapy.

3.4.2 Criteria for fiber-insertion system

Insertion accuracy is critical in reducing both risk of residual tumors and excess collateral damage. Therefore, there are certain criteria that the current fiber-insertion system must fulfill such that it may be both incorporated into our proposed procedure and be used with the Fisher Imaging Mammotest biopsy system. These criteria are:

a)   The fiber insertion system should be compatible with any biopsy gun holder used to mount the biopsy guns on the Fischer Imaging Autoguide system either on or perpendicular to the X-Ray tube arm.

b)   The dimensions of the housing and needles must be similar to those used for biopsies with the Fischer Imaging stereotactic system.

c)   The fiber insertion system must be able to insert a cylindrical diffusing tip optical fiber with a diffusing tip diameter of approximately 2 mm or less.

d)   The fiber insertion system must be designed to ensure that the light emitting length of the cylindrical diffusing tip is completely exposed to the tissue.

e)   The fiber insertion system must be designed to hold the fiber and cannula in place during laser irradiation.

3.4.3 Previous fiber-insertion system designs

Stereotactic fiber guidance during LITT of the breast was first clinically performed by Dowlatshahi *et al* (Dowlatshahi *et al* 2000). The fiber insertion system proposed by Dowlatshahi *et al* (US Patent# 6603988 B2, 2003) was designed for and employed by a LORAD/Trex Medical Stereoguide DSM (LORAD, Danbury, CT) stereotactic table, even though, according to the patent, it could be used with other imaging modalities. The fiber-guidance assembly is mounted on the stereotactic guidance table of the LORAD, and is comprised of the following (Figure 3.13 and 3.14):

a)   a housing containing a laser probe, a temperature probe, and probe guides extending from the housing,

b)   an alignment member attached to the housing for aligning the fiber-guidance assembly prior to insertion,

c)   an inserter member for automatically inserting the laser and temperature probe, and

d)   a control system for laser and temperature probe insertion. This system also monitors the laser source, fluid pumps, and the temperatures readings from both probes.
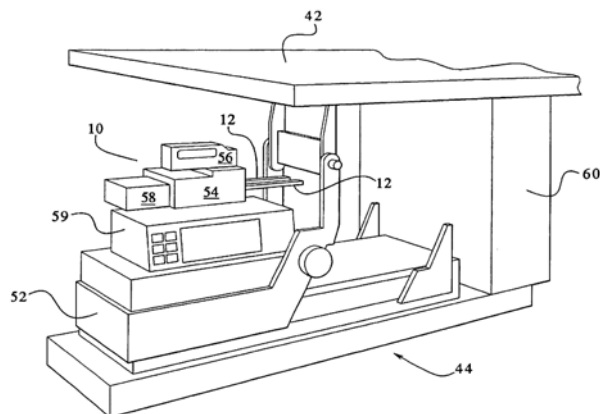
Figure 3.13: The fiber guidance system proposed by Dowlatshahi et al for the (52) LORAD/trex Medical Stereoguide DSM. The fiber insertion system includes (54) a housing for both the laser and temperature probe and the (12) probe guides, (56), an alignment member, (58)an insertion member, and (59) a control system that monitors insertion, temperature, and fluid flow (US Patent #6603988 B2, 2003).
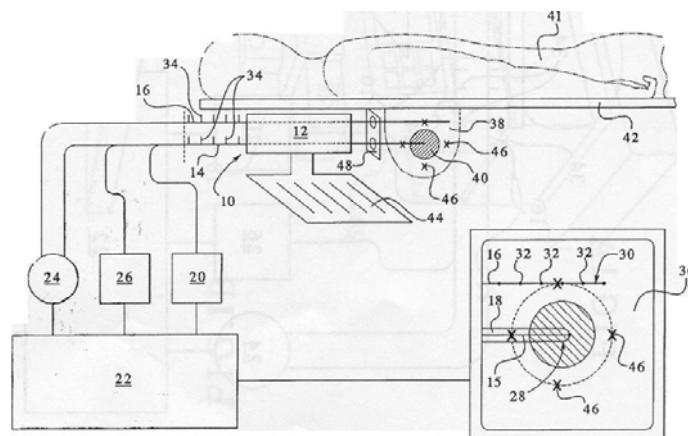
Figure 3.14: The (12) fiber guidance system proposed by Dowlatshahi et al for the (44) LORAD/trex Medical Stereoguide DSM with the (14) laser probe and the (16) temperature probe inserted into the breast of the (41) patient laying on the (42) table of the LORAD stereotactic biopsy system (US Patent #6603988 B2, 2003).

The laser probe consists of a Y-shaped connector (Qosina, Edgewood, NY) (Dowlatshai *et al* 1992, US Patent # 5222953, 1993) (Figure 3.15). One arm of the y-shaped connector contains a 16-18 gauge stainless steel cannula that served as the track for the optical fiber. A temperature sensor located on the cannula measures the

temperature of the tissue near the laser probe. The cannula also had radiopaque markers along its length so that it can be located easily in X-ray images. The second arm of the y-shaped connector is for fluid flow. The fluid flows coaxially with the optical fiber into the tumor site and serves to protect the fiber from overheating and carbonizing and to remove blood clots and debris from the fiber-tissue interface. A proximal knob located at the end of the cannula serves to clamp the fiber in place. A stylus is initially inserted in the cannula prior to fiber insertion. The stylus is used to insert the laser probe inside the breast and is removed prior to optical fiber insertion.

The temperature probe is a 16-20 gauge stainless steel needle that contains temperature sensors along the needle. These temperature sensors measure the temperature in the surrounding tumor and healthy tissue. The temperature measurements are then used to calculate the volume of coagulated tissue. Like the laser probe, the temperature probe also has radiopaque markers along its length so that it can be located easily in X-ray images.

The procedure for fiber insertion with this system is as follows.

a) The stereotactic system locates the coordinates of the tumor in the breast and positions the fiber guidance assembly for entry.

b) The laser probe containing the stylet is inserted into the tumor site of the breast using stereotactic guidance. The temperature probe is then inserted. The laser probe may be manually inserted or automatically injected. Stereotactic images are taken to confirm that the laser probe and temperature probe are within the target region.
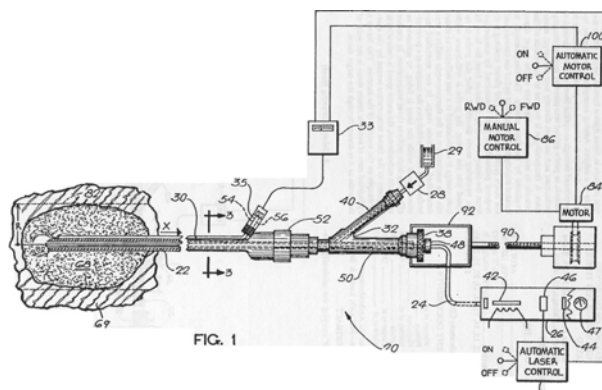
Figure 3.15: The laser probe within the housing of the fiber insertion system proposed by Dowlatshahi et al for the LORAD/trex Medical Stereoguide DSM. The probe is comprised of a (32) Y-shaped connector with (50) one arm holding the (22) cannula for fiber insertion and (40) a second arm reserved for fluid flow, (30) a temperature sensor on the cannula, and (38) a proximal knob to clamp the fiber(US Patent #5222953, 1993).

c)   The stylet is removed from the cannula after insertion, and the optical fiber is inserted through the cannula and into the tumor site. A stopper is placed on the optical fiber approximately the length of the fiber insertion system so that the physician would know when to stop the insertion.

d)   The proximal knob is then used to clamp the fiber into position. Once the fiber is in position, laser irradiation may begin.

   The main limitation of this fiber insertion system is that it was not designed for cylindrical diffusing tip optical fibers. There is no mechanism that could retract the cannula enough to completely expose the light emitting length of the diffusing tip while leaving the fiber in place.

3.4.4 Design of a fiber-insertion system for diffusing tip fibers

   Our proposed fiber-insertion system for cylindrical diffusing tip fiber insertion was designed with similar dimensions as the housing of the BARD Biopty core-needle firing

biopsy gun (BARD Biopsy System, Tempe, AZ) (Figure 3.16). The trocar and cannula of the fiber insertion system were also designed with similar dimensions to the biopsy needle and cannula of the BARD Biopty core-needle firing biopsy gun (Figure 3.17).

The final fiber-insertion system design was based on preliminary work done by Chad Pecot as a requirement for his Senior Design Project in the Department of Biomedical Engineering, University of Miami, Coral Gables, FL (Pecot 2002). The fiber-insertion system consists of the following parts (Figures 3.18-3.25):
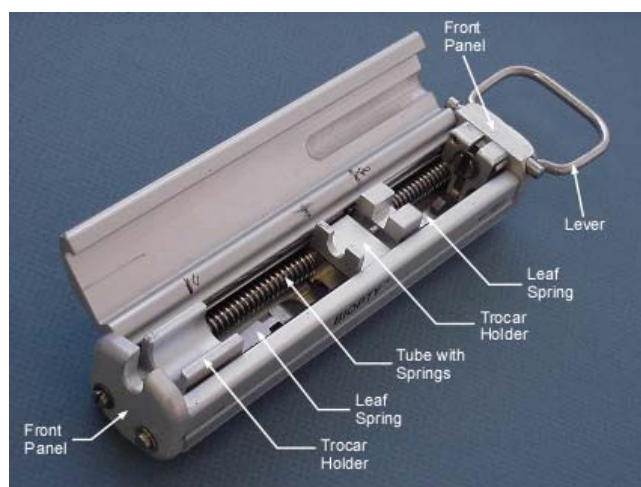
Figure 3.16: The BARD Biopty firing biopsy gun in which the fiber-insertion system is modeled (BARD Biopsy System, Tempe, AZ)
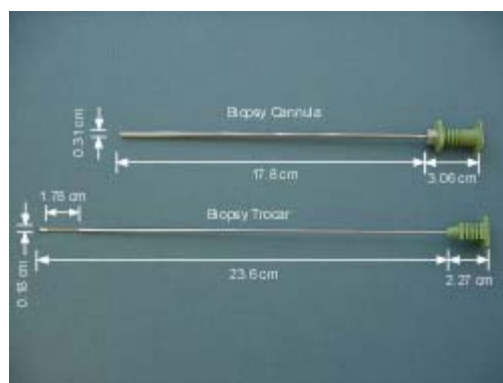
Figure 3.17: The biopsy trocar and cannula for the BARD Biopty firing biopsy gun

a)   Cannula (Figure 3.19)

b)   Trocar (Figure 3.20)

c)   Fiber clamp cannula (Figure 3.21)

d)   Cannula holder (Figure 3.22)

e)   Trocar holder (Figure 3.23)

f)   A housing that holds the cannula and trocar holder (Figure 3.24)

g)   Top lid of the housing (Figure 3.25)
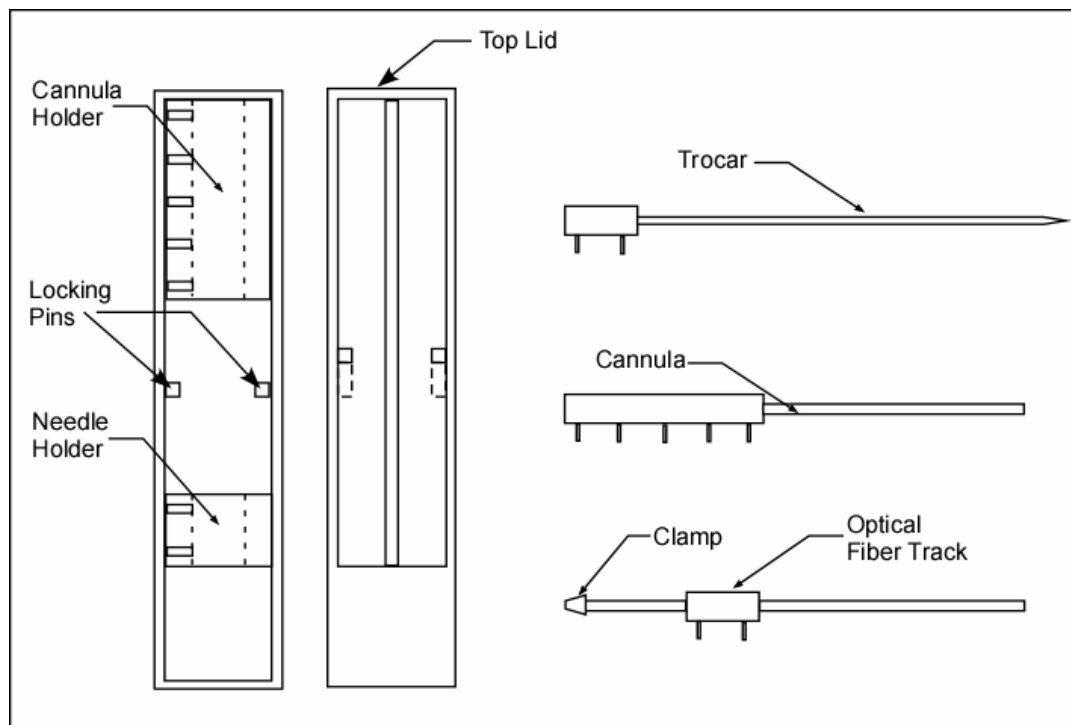
Figure 3.18: The components of the fiber-insertion system

Figure 3.19: The cannula of the fiber-insertion system consists of an aluminum cannula tube, a Plexiglas cannula handle, and six stainless steel dowel pins: five locking pins in series along the length of the handle and one rotating pin located at the edge of the cannula handle and perpendicular to the locking pins. The inner diameter of the cannula tube was chosen to allow insertion of the fiber clamp in which the optical fiber will be inserted. The locking pins were spaced such that the cannula may be retracted at 1 cm increments (Hoang M 2006).

Figure 3.20: The trocar of the fiber-insertion system consists of an aluminum trocar needle, a Plexiglas trocar handle, and four steel dowel pins (Small Parts, Miami, FL). The two pins nearest the distal end of the trocar are locking pins. The two other pins are rotating pins. The rotating pins are used to unlock / lock the trocar and retract / insert the trocar (Hoang M 2006).

Figure 3.21: The fiber clamp of the fiber insertion system consists of an aluminum fiber clamp tube, in which the optical fiber is inserted, a plexiglas fiber clamp handle, an aluminum pin vise, and four stainless steel dowel pins. The two pins nearest the distal end are locking pins. The other two pins are rotating pins. As with the trocar, these rotating pins are used to both lock / unlock the fiber clamp and retract / insert the clamp. The inner diameter of the tube was chosen to allow insertion of a 2 cm diameter diffusing tip optical fiber. The fiber clamp tube is inserted into the cannula once the trocar is removed. The optical fiber is inserted through the pin vise, which clamps the fiber after insertion.
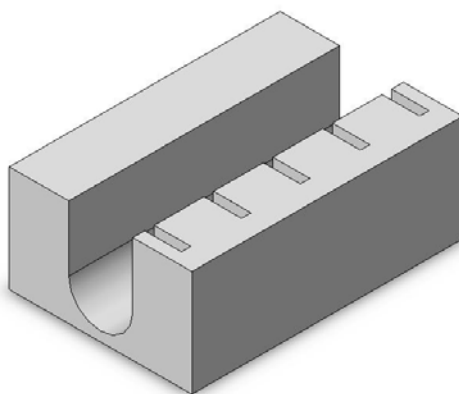
Figure 3.22: The cannula holder of the fiber insertion system is designed to mount the cannula onto the housing of the fiber insertion system. The cannula holder has a slot running along its center where the handle of the cannula is mounted during insertion. The holder has five locking pin slots along its length. These slots are designed to house the locking pins of the cannula when it is rotated to its locking position.
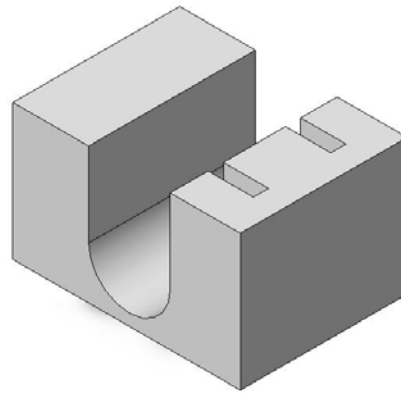
Figure 3.23: The trocar / fiber clamp holder of the fiber insertion system is designed to mount either the trocar or the fiber clamp onto the housing of the fiber insertion system. The trocar / fiber clamp holder has a 9.5 x 10 mm slot running along its length designed to house the handle of the trocar or fiber clamp during insertion. The holder has two 2 x 7.5 x 6 mm locking pin slots spaced 8 mm apart along the length of the cannula holder. These slots are designed to house the locking pins of the trocar or fiber clamp when they are rotated to their locking position.
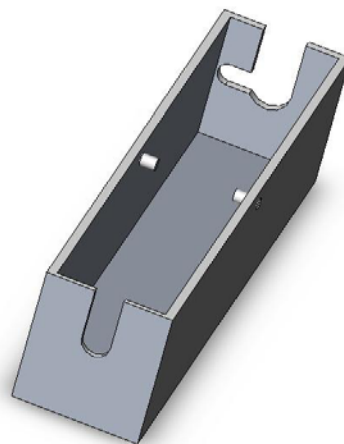
Figure 3.24: The housing of the fiber insertion system is an aluminum box with a polypropylene base. The cannula and trocar / fiber clamp holders are mounted on the propylene base. Locking pins for the top lid are located on each side of the housing. The front panel contains a rectangular opening that allows passage of the cannula and trocar. The back panel contains a rectangular opening that allows the trocar to be retracted out of the fiber insertion system and the fiber clamp to be inserted.
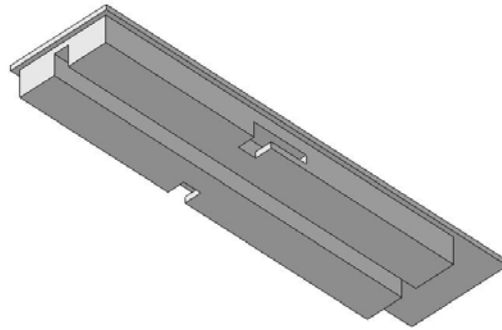
Figure 3.25: The top lid for the fiber insertion system consists of an aluminum plate screwed on to a Plexiglas base. The lid is designed to keep the cannula, trocar, and fiber clamp in their respective holders. The Plexiglas base has a square channel that runs along the length of the Plexiglas base of the lid. This channel accommodates the rotating pins of the cannula, trocar, and fiber clamp. Each side of the Plexiglas lid has an L-shaped locking pin cavity used to lock the top lid on the housing using the pins on the walls of the housing.

3.4.5 Procedure for fiber-insertion

The fiber insertion system is mounted on the Autoguide of the Fischer Imaging stereotactic biopsy system in the same manner as a biopsy gun. Initially, the trocar is inside the cannula with its point extending out of the cannula distal edge. Both are mounted onto the fiber insertion system. Once the tumor is located and the Autoguide is positioned, the procedure for fiber insertion is the following (Figure 3.26-29):

Step 1: The trocar and cannula of the fiber insertion system are inserted into the tumor by the physician. Images are taken to ensure that the needle point is within or just outside the boundary of the tumor site.

Step 2: The top lid is opened and the trocar is rotated to allow retraction.

Step 3: The trocar is retracted through the rear of the fiber insertion system, leaving the cannula in place.

Step 4: The fiber clamp is inserted into the cannula through the rear of the fiber insertion system and mounted onto the trocar holder.

Step 5: The fiber clamp is rotated and locked in place.

Step 6: The optical fiber is inserted into the fiber clamp until the distal point of the cylindrical diffusing tip optical fiber reaches the edge of the cannula. A marker placed on the optical fiber will tell the physician how far the fiber must be inserted into the cannula. The clamp is tightened to secure the fiber.

Step 7: The cannula is rotated and retracted back from its original position, exposing the light-emitting length of the diffusing tip to the tissue. After retraction, the cannula is rotated to lock it in place.

Step 8: The top lid is placed on the fiber-insertion system. Images are taken to ensure that the optical fiber is within the tumor site. If not, then the procedure has to be repeated from step 1.

At the end of the treatment, the probe is removed by first pulling the fiber out of the cannula and afterwards, extracting the cannula from the breast.
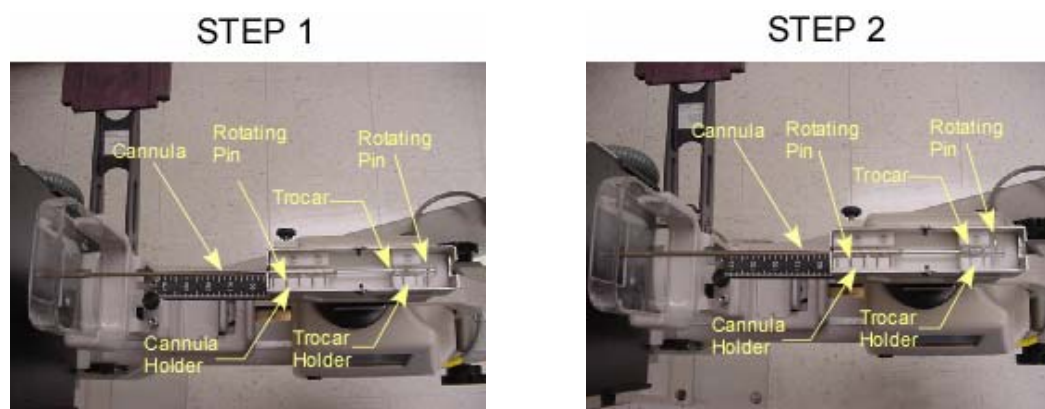
Figure 3.26: The steps 1-2 for the insertion of the optical fiber into the breast tumor under stereotactic guidance using the fiber-insertion system
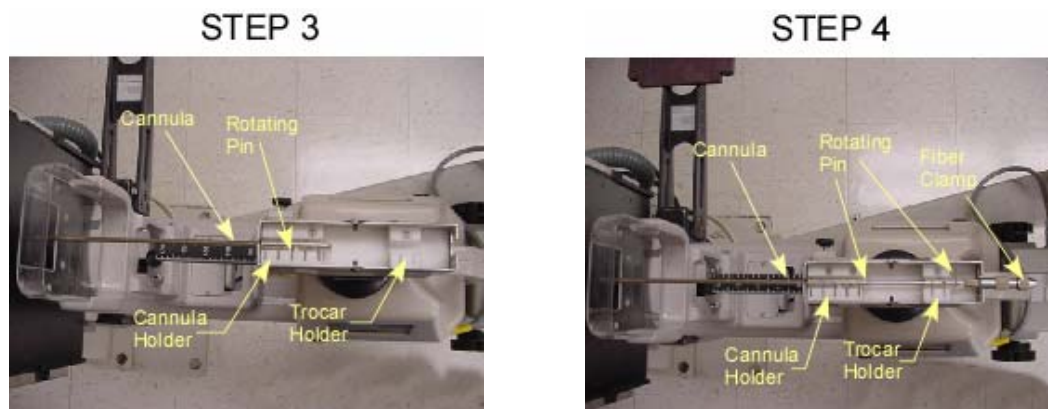
Figure 3.27: The steps 3-4 for the insertion of the optical fiber into the breast tumor under stereotactic guidance using the fiber-insertion system
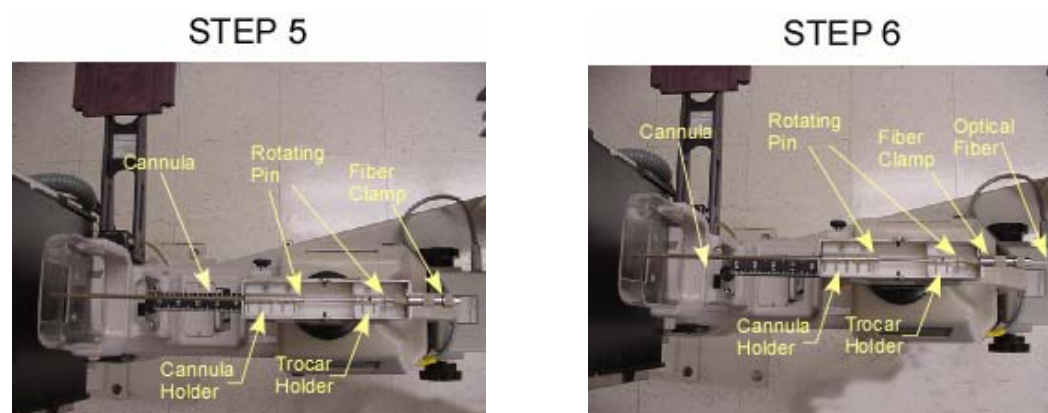
Figure 3.28: The steps 5-6 for the insertion of the optical fiber into the breast tumor under stereotactic guidance using the fiber-insertion system
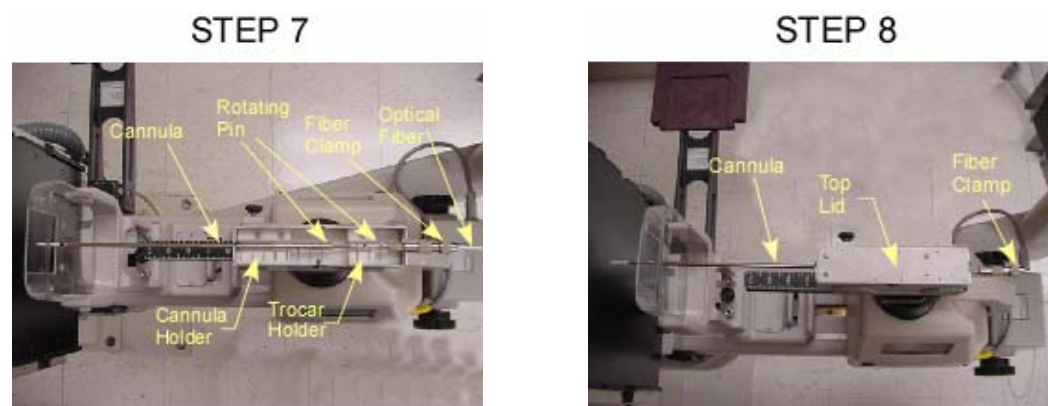
Figure 3.29: The steps 7-8 for the insertion of the optical fiber into the breast tumor under stereotactic guidance using the fiber-insertion system

3.5 Discussion

The fiber insertion system was designed for insertion of a cylindrical diffusing tip optical fiber under stereotactic guidance. To validate the approach, the following steps are required:

a)   Demonstrate the feasibility of fiber insertion into the tissue or tissue phantom,

b)   Evaluate the accuracy of the fiber insertion into the tumor under stereotactic guidance.

An eggplant was recommended to us as a model of the breast by the technicians at the Breast Center at the University of Miami Sylvester Cancer Center (UMSCC) and was used to demonstrate the feasibility of the fiber insertion system. The eggplant was mounted on the stereotactic biopy system, like the breast, between the imaging assembly and the compression paddle. The procedure for fiber insertion as described in section 3.4.5 was employed. The fiber tip could be easily inserted into the eggplant (Figure 3.30), but the following minor problems were detected during the insertion:

Figure 3.30: The insertion of the optical fiber into an eggplant using the fiber-insertion system

a)   The fiber clamp rotates while the clamp is being tightened and loosened (Step 6).

b)   The rotation, removal, and insertion of the trocar, cannula, and fiber clamp piece can be tedious because the lid must be opened.

To address these concerns, the following minor design modifications will be required in the final design:

a)   The cannula and fiber-clamp pieces will be a fixed part of the fiber insertion system. During the initial insertion (step 1), the trocar will be held in place by the fiber clamp. After its insertion, it will be retracted and replaced by the optical fiber (step 2,3, and 6). Since it will be a permanent fixture in the system, the fiber clamp will not twist during tightening and loosening.

b)   The pins will extend outside of the housing of the fiber insertion system. This will allow rotation, retraction, and locking of the cannula without having to remove the top lid of the fiber-guidance assembly.

The next phase of the investigation would have been to evaluate the accuracy of the fiber insertion by locating a 3 cm target within the eggplant. The positioning accuracy of the cylindrical diffusing fiber tip into the tumor site under stereotactic guidance could not tested because the hard drive of the stereotactic biopsy system failed prior testing.

3.6 Summary and Conclusion

A fiber-insertion system for laser interstitial thermotherapy of small tumors of the breast using cylindrical diffusing optical fibers and stereotactic guidance was designed and built. The fiber-insertion system was designed to be mounted on a Fischer Imaging Mammotest/Mammovision Plus high resolution stereotactic digital X-Ray biopsy system

(Fischer Imaging Corp., Denver, CO) and be inserted into the breast in similar fashion to a biopsy needle. When the tumor site is located by the physician, the Autoguide of the stereotactic biopsy system positions the fiber insertion system. Once the physician inserts the fiber insertion system needle into the tumor site, X-Ray images are taken to ensure that the fiber insertion needle is in the tumor site. The needle is removed, and the fiber is inserted into the tumor site through the insertion system. X-ray images are taken to ensure that the fiber is in the tumor site prior to irradiation. The feasibility of the optical fiber insertion using the fiber-insertion system was demonstrated in a model of the breast. The accuracy of the optical fiber insertion into a breast tumor site under stereotactic guidance using the fiber insertion system remains to be evaluated in a suitable model.

4. OPTICAL-THERMAL MODEL

4.1. Introduction

The goal of this part of the study is to develop an optical-thermal model that will predict the temperature distribution in fibro-fatty tissue (human breast or porcine mammary chain) during laser interstitial thermotherapy with a diffusing tip optical fiber. The model will be used to determine the laser parameters necessary to achieve a desired thermal coagulation size. The optical-thermal model will consist of three parts:

1. A radiometric model that will calculate the light distribution and the absorbed energy density in the tissue with initial knowledge of the optical properties of the tissue and irradiation geometries.

2. A thermal model that will calculate the temperature distribution in the breast tissue from the absorbed energy density.

3. A thermal coagulation model that will calculate the coagulation volume from the induced temperature increase.

4.2 General approach

The model will be developed around the Indigo cylindrical diffusing tip optical fiber (Ethicon Endo-Surgery, Inc., Cincinnati, OH) (see section 3.2). The light emitting length of these fibers is approximately 16 mm. The total fiber tip length is 18 mm, with a 2 mm long distal tip through which no light escapes. The radius of these fibers is 0.9 mm. The Indigo fibers have a uniform emission around the fiber tip (see section 3.2). In the proposed procedure (see section 3.4.1), the optical fiber is inserted into the breast tumor.

The model assumes that the fiber is located in the center of the tumor and that the tumor is located deep enough within the tissue such that all of the radiation is absorbed prior to reaching the tissue surfaces. This assumption implies that the tissue forms an inifinite medium or that the boundaries are far enough from the source to have a negligible effect. The model also assumes that there are no significant differences in the optical (Troy *et al* 1996, Peters *et al* 1990) and thermal properties of healthy and diseased breast tissue. The breast tissue is assumed to be a homogeneous medium.

To facilitate the development of the model, the emission of the cylindrical fiber will be modeled by the superposition of overlapping spherical sources which have a radius equal to the fiber radius and an isotropic emission (Figure 4.1) Since the absorbed energy density and temperature distribution are solutions of linear partial differential equations, the temperature distribution produced by this model of the cylindrical diffusing tip can be calculated by linear superposition of the temperature produced by the individual spherical sources.
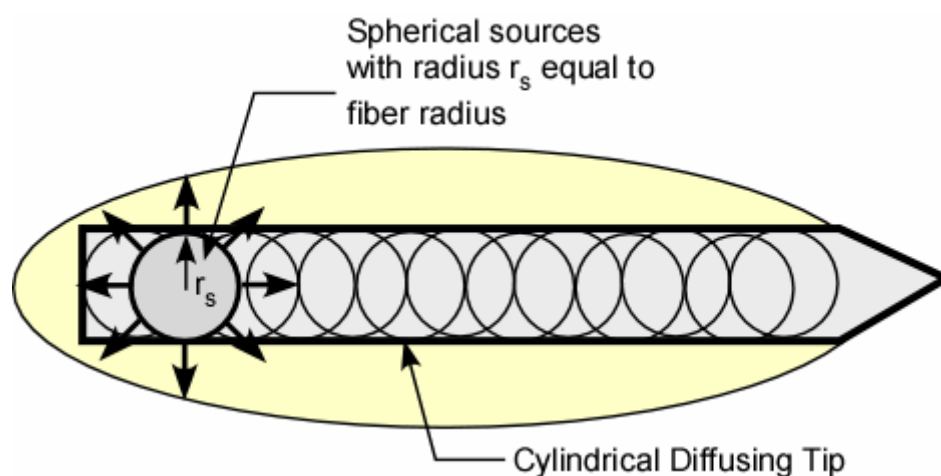
Figure 4.1: An optical fiber cylindrical diffusing tip represented as a summation of spherical sources with isotropic emission and a radius r_s equal to the radius of the fiber tip.

The calculation of the coagulation volume can then be divided into four steps:

a)   Calculation of the light distribution produced by a spherical source,

b)   Calculation of the temperature distribution induced by this light distribution,

c)   Calculation of the temperature distribution produced by the cylindrical diffusing tip using the linear superposition principle applied to the spherical sources, and

d)   Calculation of the coagulation using the Arrhenius equation applied to this temperature distribution

The main advantage of this approach is that the spherical sources produce light and temperature fields that have spherical symmetry. The spherical symmetry makes it possible to derive relatively simple analytical expressions of the temperature distribution for the optical-thermal model.

4.3 Light distribution produced by a spherical source

4.3.1 Aims

The aim of this section is to derive an analytical expression for the absorbed fluence rate produced by a spherical source. The absorbed fluence rate is the amount of light energy absorbed by the tissue per unit volume and time (Welch *et al* 1995). The absorbed fluence rate is proportional to the heat source term of the bio-heat equation (Equation 2.3). To calculate the absorbed fluence rate, a light propagation model is first developed to calculate the light distribution in the tissue as a function of the optical properties. The light propagation model is first developed for an isotropic point source (zero size). The model is then modified to simulate the emission of a spherical source of finite diameter. The output of the light propagation model is the power ($P(r)$ in W),

fluence rate ($F(r)$ in W cm^{-2}), and absorbed fluence rate ($\phi(r)$ in W cm^{-3}) as a function of the distance (r) from the center of the spherical source.

4.3.2 Selection of the light propagation model

4.3.2.1 Introduction

Biological tissue is considered to be a turbid medium. Light propagating in turbid media is attenuated by absorption and scattering of photons. The absorption and scattering of the photons and the direction in which the photons are scattered are dependent on the optical properties of the tissue. The optical properties are, in turn, dependent on the wavelength of the light and the tissue structure. At the macroscopic level, assuming that tissue is a homogeneous and isotropic medium, the optical properties that determine the light propagation are:

a) The absorption coefficient (μ_a in mm^{-1}), which determines the probability of an absorption event,

b) The scattering coefficient (μ_s in mm^{-1}), which determines the probability of an scattering event,

c) The anisotropy coefficient (g), which is the mean cosine of the angle (θ) in which the photons are scattered from their original position,

d) The refractive index (n).

A variety of numerical and analytical methods have been used to model the light propagation in biological tissue of known optical properties (Edström 2007, Chin *et al* 2006, Heiskala *et al* 2005, Yang and Miklavcic 2005, Gupta *et al* 2004, Ma *et al* 2004, Shafirstein *et al* 2004, Hayashi *et al* 2003, Verhey *et al* 2003, Iizuka *et al* 2000, Farina *et*

al 1999, Gardner *et al* 1996, Olsrud *et al* 1996, Prapavat *et al* 1996, Prahl *et al* 1993, Key *et al* 1991). The two most common methods are the diffusion approximation and the Monte Carlo technique.

4.3.2.2 Diffusion approximation

The diffusion approximation is an approximate solution to the radiation transport equation (equation 2.1):

$$\frac{dL(\mathbf{r},\hat{\mathbf{s}})}{ds} = -(\mu_a + \mu_s)L(\mathbf{r},\hat{\mathbf{s}}) - \mu_s \int_{4\pi} p(\hat{\mathbf{s}},\hat{\mathbf{s}}')L(\mathbf{r},\hat{\mathbf{s}}')d\omega' + \varepsilon(\mathbf{r},\hat{\mathbf{s}})$$ Eq. 4.1

which is valid when the tissue is highly scattering and the light scattering is almost isotropic (g almost equal to zero) (Chin *et al* 2006, Shafirstein *et al* 2004, Verhey *et al* 2003, Ishimaru 1997, Prapavat *et al* 1996). In the diffusion approximation, the average energy density of the diffuse light is the solution of the following partial differential equation (Ishimaru 1997):

$$\nabla^2 U_d(\mathbf{r}) - 3\mu_a \mu_{tr} U_d(\mathbf{r}) = -S(\mathbf{r})$$ Eq. 4.2

where $U_d(\mathbf{r})$ is the average energy density of the diffuse light at a position $\mathbf{r}$, $S(\mathbf{r})$ is a term that includes all external and internal light sources, and μ_{tr} is the attenuation transport coefficient:

$$\mu_{tr} = \mu_a + (1-g) \cdot \mu_s = \mu_a + \mu_s'$$ Eq. 4.3

where $\mu_s' = \mu_s(1-g)$ is the reduced scattering coefficient. The fluence rate, $F(\mathbf{r})$ (W cm^{-2}), is directly related to the average energy density (Ishimaru 1997).

The advantage of the diffusion approximation is that it provides a solvable analytical expression to the radiative transfer equation that can be solved either analytically in

simple cases or numerically. The main limitation of the diffusion approximation is that it breaks down at locations close to the source or close to boundaries. At these locations, the light is not totally diffuse, which is a criterion for this approximation. Therefore, this method cannot be used for thin tissue samples where the thickness is near the penetration depth of the light. Another drawback is that the partial differential equation can be difficult to solve for more complex tissue and laser irradiation geometries or in the presence of inhomogeneities.

One particular application of the diffusion approximation that is relevant to our problem is the case of an isotropic point source emitting light in a homogeneous medium. According to Ishimaru (1997), the diffuse fluence rate, $F(r)$ (in $W\ cm^{-2}$), produced by such a source in the diffusion approximation is:

$$F(r) = \frac{e^{-\mu_{eff} r}}{4\pi r^2} \left[r \cdot \mu_{eff} + 1 \right] \cdot P_o \qquad \text{Eq. 4.4}$$

where P_o (in W) is the total power emitted by the point source, and μ_{eff} is the effective attenuation coefficient (in mm^{-1}):

$$\mu_{eff} = \sqrt{3 \cdot \mu_a \cdot (\mu_a + \mu_s (1-g))} \qquad \text{Eq. 4.5}$$

4.3.2.3 Monte Carlo technique

The most common numerical method to model light propagation in turbid tissue is the Monte Carlo algorithm (Papaioannou *et al* 2004, Liu *et al* 2003, Farina *et al* 1999, Welch and Gardner 1997, Jacques and Wang 1995, Hourdakis and Perris 1995, Keys *et al* 1991, Peters *et al* 1990). The Monte Carlo numerical technique follows the probabilistic, random walk of photons after launch into the tissue until they escape through the tissue

boundaries or until they are absorbed. The path length between successive attenuation events and the angle of scatter are assigned a certain probability density function determined by the optical properties of the tissue. To determine the path length between successive attenuation events or the scattering angle, a number is randomly selected between 0 and 1. The value of the path length or scattering angle is then selected so that it gives a probability for the event that equals the randomly selected number.

Two types of Monte Carlo programs have been implemented to model the propagation of photons in tissue. The first type launches individual photons one at a time into the tissue (Farina *et al* 1999, Welch and Gardner 1997, Hourdakis and Perris 1995). In this case, the photons will travel a distance equal to the predicted path length. At this distance, the photon will either be absorbed or scattered. If the photon is absorbed, either a new photon is launched or the program terminates depending on the number of photons that have already been launched. If the photon is scattered, new random numbers are chosen to determine the angle of scatter and the new path length it will travel until the next attenuation event.

The second type launches a packet of photons rather than individual photons (Liu *et al* 2003, Papaioannou *et al* 2004, Jacques and Wang 1995, Peters *et al* 1990). The packet of photons has a weight initially equal to one. After each attenuation event, the weight is reduced by an amount determined by the optical properties to account for absorption and reflection off boundaries. Once the weight has been reduced below a set value, a "roulette" technique is used to determine if the photon packet is completely terminated or if it continues to propagate. The advantage of this approach compared to the single photon propagation technique is that it requires the launch of less photons to achieve

similar prediction accuracy. The lower number of launches significantly reduces the computation time.

Independent of the technique, the advantage of the Monte Carlo method compared to the diffusion approximation is that it can be used to simulate all kinds of applications, sample geometries, and boundary conditions. However, the accuracy of this simulation is dependent on the number of photons launched, which depends on the question being asked, the precision needed, and the spatial or temporal resolution desired (Jacques and Wang *et al* 1995). When the goal is to find the amount of light reflected and transmitted out of a thin sample, good accuracy can be achieved with a launch of approximately 10,000 photons. When the goal is to find the absorbed fluence rate, up to one million photons may be required to achieve the same accuracy. When a large number of photons are required and when the boundary conditions are complex, the computation time may be between several hours to a day.

4.3.2.4 Selection and implementation of the light propagation model

The approach that we used is the photon packet algorithm of the Monte Carlo method. This method was chosen because we are not certain that the conditions of the diffusion approximation are valid in our case. The details of the photon packet propagation algorithm have been published by Jacques and Wang (1995). The algorithm was implemented in a MATLAB program. The program calculates the light distribution in a three-dimensional rectangular slab of tissue. The dimensions of the slab and the boundary conditions are adjusted according to the experimental condition. For the simulations of LITT in breast tissue, the size of the tissue is set to 200x200x200 mm.

With these dimensions, the boundary conditions have no effect on the light propagation because, with the optical properties of fibro-fatty tissue, all photons are attenuated before they reach the boundaries. The listing of the program is included in the Appendix A.

4.3.3. Absorbed fluence rate for an isotropic point source

By definition, the absorbed fluence rate is the number of photons absorbed per unit volume. To calculate the absorbed fluence rate using the Monte Carlo method, the irradiated tissue must be divided into elementary volumes (voxels) and the total power absorbed in each voxel (ΔP_i) is recorded. The absorbed fluence rate in each voxel of volume V_i is then equal to $\Delta P_i/V_i$. With this method, there is a trade-off between the size of the voxels (resolution of the simulation) and the computation time. A large number of photons must be launched to obtain the absorbed fluence rate with good resolution because, otherwise, very few photons are captured in each voxel. In the case of an isotropic point source, which emits uniformly in all direction, the absorbed fluence rate is rotationally symmetric. The voxels can, therefore, be defined as spherical shells centered around the point source, and the number of photons absorbed in each shell can be calculated.

The volume of the i_{th} spherical shell, V_i, is given by (Figure 4.2):

$$V_i = 4 \cdot \pi \cdot r_i \cdot \Delta r \qquad \text{Eq. 4.6}$$

where r_i is the inner radius of the shell and Δr is the radial increment. If ΔP_i is the power absorbed in the i_{th} shell, then the absorbed fluence rate in that shell, ϕ_i, is (Figure 4.3):

$$\phi_i = \frac{\Delta P_i}{V_i} = \frac{\Delta P_i}{4 \cdot \pi \cdot r_i \cdot \Delta r} \qquad \text{Eq. 4.7}$$
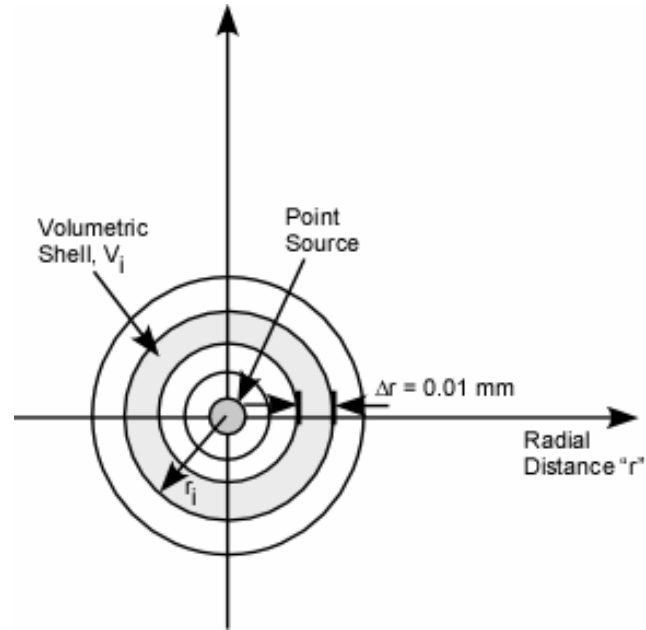
<u>Figure 4.2:</u> The voxels (left) and volumetric shells surrounding the point source (right) at radial increments of 0.01 mm away from the point source located at the origin. The photons absorbed within each of these shells are calculated using a Monte Carlo program implemented in MATLAB.

The power, P_i, remaining after the i_{th} shell is given by:

$$P_i = P_o - \sum_{j=1}^{i} \Delta P_j \qquad \text{Eq. 4.8}$$

where P_o (in W) is the power emitted by the source, which is proportional to the amount of photons launched into the tissue. By definition, the fluence rate at the i_{th} shell is equal to the power remaining divided by the surface area of the shell (Figure 4.4):

$$F_i = \frac{P_i}{4 \cdot \pi \cdot r_i^2} \qquad \text{Eq. 4.9}$$

Figure 4.3-4.6 show the number of absorbed photons, number of remaining photons, fluence rate, and the absorbed fluence rate obtained when μ_a=0.0259 mm^{-1}, μ_s=7.810 mm^{-1}, g=0.66 (corresponding to the optical properties of porcine tissue at 980 nm – see chapter 5). An increment of Δr equal to 0.01 mm was used.
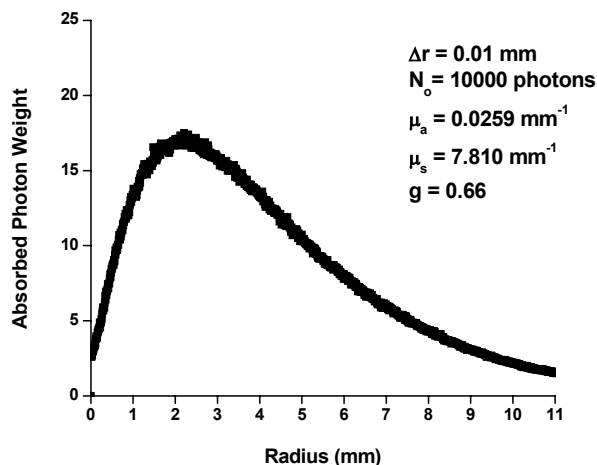
Figure 4.3: The photon weight absorbed within volumetric spherical shells surrounding a point source. The absorbed photon weight was calculated for tissue having the following optical properties: μ_a=0.0259 mm^{-1}, μ_s=7.810 mm^{-1}, g=0.66. The simulation parameters were Δr=0.01 mm and N_o=10000 photons launched.
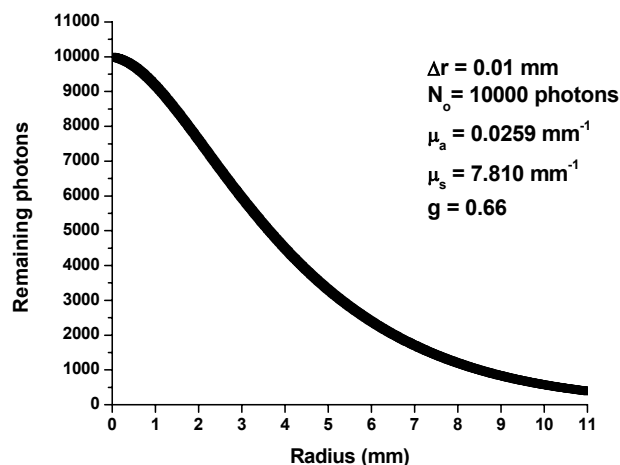
Figure 4.4: The photons remaining within volumetric spherical shells surrounding a point source. The remaining photon weight was calculated for tissue having the following optical properties: μ_a=0.0259 mm^{-1}, μ_s=7.810 mm^{-1}, g=0.66. The simulation parameters were Δr=0.01 mm and N_o=10000 photons launched.
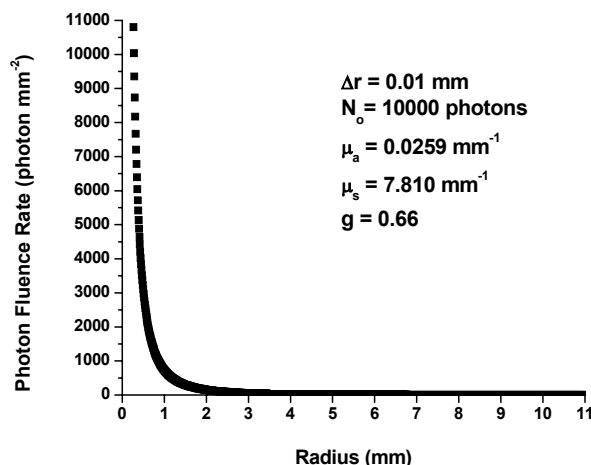
Figure 4.5: The photon fluence rate within volumetric spherical shells surrounding a point source. The photon fluence rate was calculated for tissue having the following optical properties: μ_a=0.0259 mm^{-1}, μ_s=7.810 mm^{-1}, g=0.66. The simulation parameters were Δr=0.01 mm and N_o=10000 photons launched.
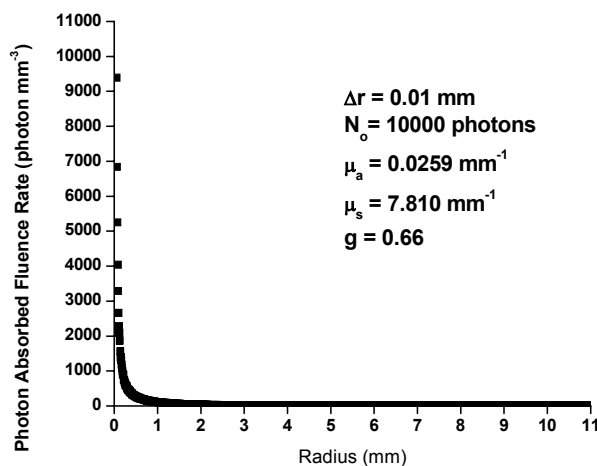
Figure 4.6: The photon absorbed fluence rate within volumetric spherical shells surrounding a point source. The absorbed photon fluence rate was calculated for tissue having the following optical properties: μ_a=0.0259 mm^{-1}, μ_s=7.810 mm^{-1}, g=0.66. The simulation parameters were Δr=0.01 mm and N_o=10000 photons launched.

4.3.4 Comparison of the Monte Carlo method with the diffusion approximation

According to Ishimaru (1997), the diffuse fluence rate for an isotropic source obtained from the solution to the diffusion approximation is given by:

$$F(r) = P_0 \cdot \left(1 + \mu_{eff} \cdot r\right) \frac{e^{-\mu_{eff} \cdot r}}{4 \cdot \pi \cdot r^2} \qquad \text{Eq. 4.10}$$

In spherical coordinates, when there is rotational symmetry, the absorbed fluence rate, $\Phi(r)$, is given by (Ishimaru 1997):

$$\Phi(\mathbf{r}) = -\operatorname{div} F(\mathbf{r}) = -\frac{1}{r^2} \frac{\partial}{\partial r}\left(r^2 F\right) \qquad \text{Eq. 4.11}$$

Combining Eqs. 4.9 and 4.10 gives the following expression for the absorbed fluence rate:

$$\Phi(\mathbf{r}) = P_0 \cdot \mu_{eff}^{\,2} \cdot \frac{e^{-\mu_{eff} \cdot r}}{4 \cdot \pi \cdot r} \qquad \text{Eq. 4.12}$$

Therefore, if the diffusion approximation applies, suitable equations to fit the fluence rate and absorbed fluence rate obtained from the Monte Carlo simulation should be:

$$F(r) = K \cdot \left(1 + m \cdot r\right) \frac{e^{-m \cdot r}}{4 \cdot \pi \cdot r^2} \qquad \text{Eq. 4.13}$$

$$\phi(r) = K \cdot m^2 \cdot \frac{e^{-m \cdot r}}{4 \cdot \pi \cdot r} \qquad \text{Eq. 4.14}$$

where K and m are the fitting parameters.

A curve fit using equation 4.13 and equation 4.14 was performed on the photon fluence rate and absorbed photon fluence rate of a point source calculated with the Monte Carlo program using the following optical properties: μ_a=0.026mm^{-1}, μ_s=7.810mm^{-1}, g=0.66, which gives μ_{eff}=0.456mm^{-1}, for r>0.9 mm. Even though the diffusion

approximation is expected to be valid only far from the source, Eqns. 4.13 and 4.14 provided an excellent fit with the Monte-Carlo simulation for all distances larger than 0.9mm. The curve fit gives $\mu_{eff} \cong 0.460$ mm^{-1}, which is similar to that calculated from the optical properties (Figure 4.7-4.8).
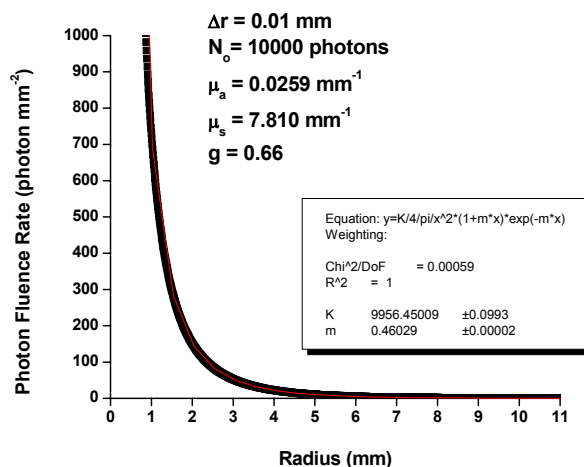
Figure 4.7: The curve fit of the photon fluence rate as a function of the radial distance away from the point source using the diffusion approximation(equation 4.12). (μ_a=0.0259 mm^{-1}, μ_s=7.810 mm^{-1}, g=0.66, Δr=0.01 mm, N$_o$=10000 photons launched)
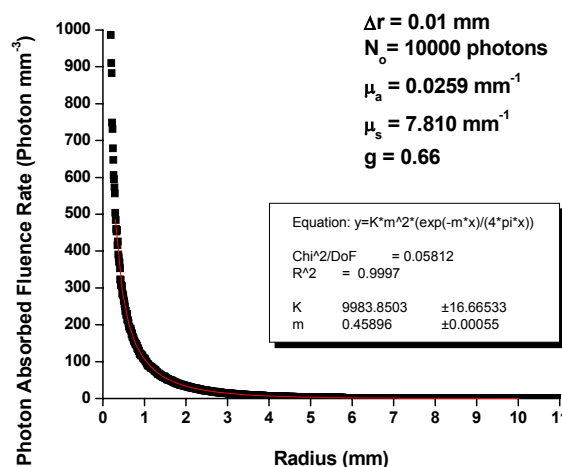
Figure 4.8: The curve fit of the absorbed photon fluence rate as a function of the radial distance away from the point source using the diffusion approximation(equation 4.12). (μ_a=0.0259 mm^{-1}, μ_s=7.810 mm^{-1}, g=0.66, Δr=0.01 mm, N$_o$=10000 photons launched)

4.3.5 Conversion to spherical source

The expression of the fluence rate and absorbed fluence rate for a point source includes a singularity at the origin (equation 4.10 and 4.12 are indefinite when r=0). To avoid this singularity, a spherical source with a finite radius can be used to model a real life isotropic source. The Monte Carlo program for the isotropic point source was modified to model such a spherical source. Photons were launched from the center of the spherical source in all directions in the same way as for the isotropic source, but the weight of the photon packets are reduced by absorption only once the photons reach the surface of the source.

The Monte Carlo program for the spherical source was run for the same parameters as with the isotropic light source (see section 4.3.2), with a source radius of 0, 2, and 4 mm (Figure 4.9). The results show that the distribution produced by the spherical source is the same as for the isotropic point source with the exception of a proportionality factor (Figure 4.9). For a spherical source of radius r_s, emitting a power P_s from its surface, the distribution of remaining power is given by:

$$P_s(r) = P_s \cdot \frac{P_0(r)}{P_0(r_s)}$$ Eq.4.15

where $P_0(r)$ is the power produced by the point source at a distance r from the source. The fluence rate, $F_s(r)$, produced by a spherical source of radius r_s is (for $r > r_s$):

$$F_s(r) = \frac{P_s(r)}{4\pi r^2}$$ Eq.4.16

Combining Eqs. 4.10, 4.15, and 4.16 gives:

$$F_s(r) = \frac{P_s}{4\pi r^2} \cdot \frac{\left(1 + \mu_{eff} \cdot r\right)}{\left(1 + \mu_{eff} \cdot r_s\right)} e^{-\mu_{eff} \cdot (r - r_s)}$$ Eq. 4.17
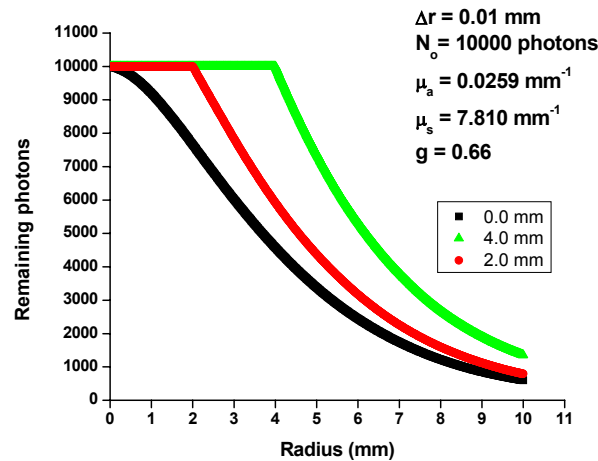
Figure 4.9: The remaining photon weight as a function of the radial distance away from a spherical source of radius equal to 0.0, 2.0, and 4.0 mm. This data was calculated for the following optical properties: μ_a=0.0259 mm^{-1}, μ_a=7.810 mm^{-1}, g=0.66. The increment of the radial distance away from the source was 0.01 mm; N_o=10000 photons launched.

where P_s is the power emitted by the spherical source and r_s is the radius of the source. Therefore, according to equation 4.11, the absorbed fluence rate is:

$$\Phi_S(\mathbf{r}) = \frac{P_S}{\left(1 + \mu_{eff} \cdot r_s\right)} \cdot \mu_{eff}^2 \cdot \frac{e^{-\mu_{eff} \cdot (r - r_s)}}{4 \cdot \pi \cdot r} \qquad \text{Eq. 4.18}$$

To confirm the validity of these equations, a curve fit using equation 4.17 was performed on the photon fluence rate of a spherical source with radius equal to 0.9 mm calculated with the Monte Carlo program using the following parameters: μ_a=0.026mm^{-1}, μ_s=7.810mm^{-1}, g=0.66 (which gives μ_{eff}=0.456mm^{-1}), Δr=0.01 mm, and P_s=10000. (Figure 4.10). The curve fit gives m=0.455mm^{-1}, which matches our optical properties, and K =10682.53, which is close to the expected value (K=10687.7 according to equation 4.17).
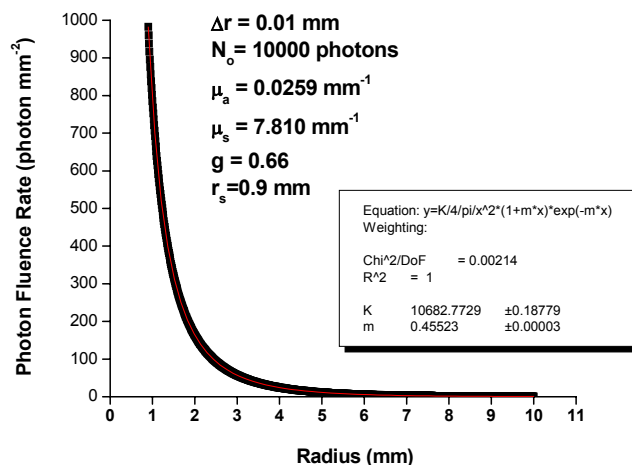
Figure 4.10: Curve fit of the fluence weight as a function of the radial distance away from a spherical source of radius equal to 0.9 mm. This data was calculated from the following parameters: μ_a=0.0259 mm^{-1}, μ_a=7.810 mm^{-1}, g=0.66, Δr=0.01 mm, 10000 photons launched.

4.3.6 Relation between spherical source power and cylindrical diffusing tip power

The emission of the cylindrical fiber will be modeled by the superposition of overlapping spherical sources with a radius equal to the fiber radius and an isotropic emission. The spherical sources all emit the same power P_s. This power must be scaled such that fluence rate at the actual fiber surface, F_{tip}, is equal to the fluence rate resulting from the summation of the spherical sources when the fiber is placed in air.

The relation of the fluence at the surface of the fiber tip, F_{tip}, and the power of the individual spherical sources, P_s, was obtained by calculating the fluence rate produced along the length of the diffusing tip by the summation of the spherical sources in air (μ_{eff}=0) (Figure 4.11).
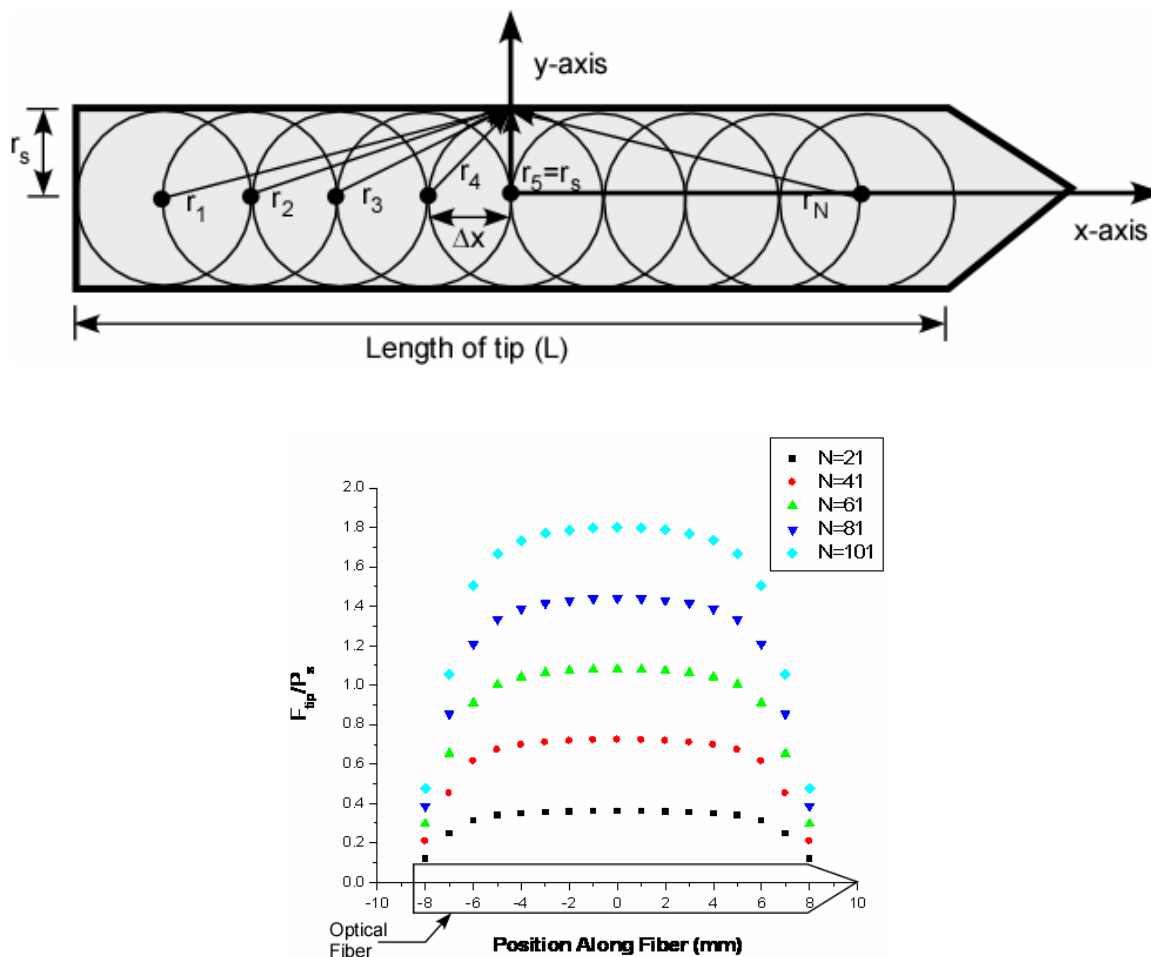
Figure 4.11: (top) Geometry and notation for the superposition of spherical sources representing the diffusing fiber tip. (bottom) The fluence rate along the surface of the cylindrical diffusing tip as a function of the number of spherical sources N when the fiber is in air (μ_{eff}=0). The number of spherical sources was N=21, 41, 61, 81, and 101. The spherical sources have a radius equal to the radius of the fiber and are separated by a distance Δx given by equation 4.22.

This calculation shows that the fluence rate along the fiber produced by the superposition of the spherical sources is approximately uniform except for the drop-out near the ends of the fiber tip. An analytical expression of the scaling factor can, therefore, be derived by calculating the relation between the fluence rate produced at the surface of the diffusing tip fiber at the mid-point (x=0, y=0.9 mm) and the power emitted

by individual spherical sources. The fluence rate, $F_s(r)$, of a spherical source of power P_s in air ($\mu_{eff}=0$) is:

$$F_s(r) = \frac{P_s}{4\pi r^2}$$

Eq. 4.19

With the notation of figure 4.11, the fluence rate produced by the superposition of N such sources at any point along the length of the fiber is given by:

$$F_{tip} = \sum_{i=1}^{N} F_s(r_i) = \sum_{i=1}^{N} \frac{P_s}{4\pi r_i^2}$$

Eq. 4.20

where r_i is the distance from the center of the i_{th} spherical source to the point of interest on the surface of the fiber tip (see Figure 4.11). If we choose the point located at the center of the fiber as a reference and use an odd number of spherical sources, the expression of r_i becomes:

$$r_i = \sqrt{r_s^2 + i^2 \Delta x^2}$$

Eq. 4.21

Where Δx is the separation between the spherical sources, which is:

$$\Delta x = \frac{L_{tip} - 2r_s}{N-1}$$

Eq. 4.22

where L_{tip} is the emitting length of the cylindrical diffusing fiber tip. Combining equations 4.20-4.22 yields the following expression for the fluence rate at the tip as a function of the power of the spherical source:

$$F_{tip} = \sum_{i=-\frac{(N-1)}{2}}^{\frac{(N-1)}{2}} \frac{P_s}{4 \cdot \pi \cdot r_s^2} \frac{1}{1 + i^2 \frac{(L_{tip} - 2r_s)^2}{r_s^2(N-1)^2}}$$

Eq. 4.23

The relation between the fluence at the surface of the fiber tip and the power emitted by the tip is:

$$F_{tip} = \frac{P_{tip}}{2 \cdot \pi \cdot r_s \cdot L_{tip}}$$

Eq. 4.24

Combining these equations shows that the power of the spherical source is given by the following equation:

$$P_s = 2 \cdot \frac{P_{tip} \cdot r_s}{L_{tip}} \cdot \frac{1}{\sum\limits_{i=-\frac{(N-1)}{2}}^{\frac{(N-1)}{2}} \frac{1}{1 + i^2 \frac{(L_{tip} - 2r_s)^2}{r_s^2 (N-1)^2}}}$$

Eq. 4.25

The ratio P_s/P_{tip} predicted from equation 4.25 is in good agreement with the results of the simulations shown in Figure 4.11 (see Figure 4.12).

4.3.7 Summary

The radiation model was developed to give an analytical solution for the absorbed fluence rate in fibro-fatty tissue with a spherical source of finite diameter equal to the diameter of the cylindrical diffusing tip. The absorbed fluence rate is proportional to the heat source term in the thermal model. A Monte Carlo model was developed to calculate the absorbed fluence rate for isotropic spherical sources. The results of the Monte Carlo model were compared to the diffusion approximation. There was an excellent agreement between the two models, which shows that the diffusion approximation can be used to model the absorbed fluence rate during LITT in fibro-fatty tissue. These calculations show that the absorbed fluence rate of a spherical source can be modeled by the following equation:
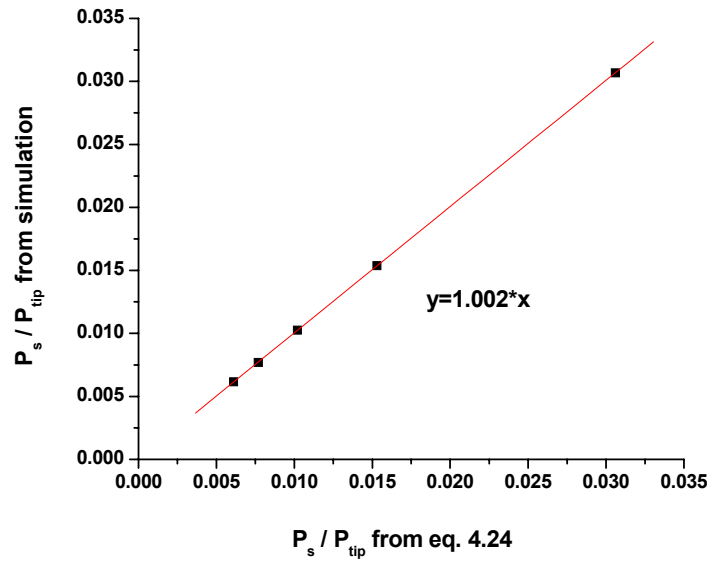
Figure 4.12: Comparison of the ratio of the power of the spherical source (P_s) over the power of the fiber tip (P_{tip}) obtained from simulations (fig. 4.11) and using equation 4.24. The simulated values were calculated by summing the fluence of each sphere comprising the cylindrical diffusing tip using MATLAB.

$$\Phi_S(r) = \frac{P_s}{\left(1 + \mu_{eff} \cdot r_s\right)} \cdot \mu_{eff}^{2} \cdot \frac{e^{-\mu_{eff} \cdot (r - r_s)}}{4 \cdot \pi \cdot r} \qquad \text{Eq. 4.26}$$

where P_s is the power of the spherical source (in W), μ_{eff} is the effective attenuation coefficient (in mm^{-1}), r_s is the radius of the spherical source, and r is the distance from the center of the spherical source. The cylindrical fiber is represented as a series of spherical sources. As more spherical sources are introduced into the cylindrical fiber, the emission of these sources overlap, resulting in a higher fluence at the surface of the fiber tip. A relationship was derived between the power of each spherical source, P_s, and the power emitted by the fiber tip, P_{tip}, and the length of the tip, L_{tip}, to produce a fluence rate at the fiber tip that matches the real-life conditions (equation 4.25).

4.4 Thermal model

4.4.1 Aims

The analytical solution of the absorbed fluence rate derived in the previous section is proportional to the heat source term of the bio-heat equation that is used to calculate the temperature increase induced by each spherical source along the length of the fiber tip. In this section, the heat equation will first be solved for an individual spherical source using an analytical approach. The temperature produced by the cylindrical diffusing tip will be calculated by summing the contribution of overlapping spherical sources.

4.4.2 Development of the thermal model for a spherical source

Since our heat source has spherical symmetry, the heat equation will be solved in a spherical coordinate system. The center of the sphere is the center of the coordinate system. To provide an analytical solution, the heat equation is solved for a finite medium bounded at the proximal end by a sphere of radius $a=r_s$ and at the distal end by a sphere of radius b. The value of b is selected to be large enough so that there is a negligible temperature increase at r=b. The boundary at r=a is assumed to be insulated and the initial temperature is assumed to be homogeneous throughout the tissue. The corresponding boundaries and initial conditions are:

$$T_s(a < r < b, t = 0) = 0$$
$$\frac{\partial T_s}{\partial r}(r = a, t) = 0 \qquad \text{Eq. 4.27}$$
$$T_s(r = b, t) = 0$$

where T_s is the temperature increase produced by a spherical source. According to Ozisik (1980), with these conditions, the solution of the heat equation is (Ozisik 1980):

$$T_s(r,t) = \frac{\alpha}{k} \cdot \frac{2}{r \cdot (b-a)} \sum_{m=1}^{\infty} e^{-\alpha \cdot \beta_m^2 \cdot t} \cdot \cos \beta_m (r-a)$$

$$\cdot \int_{\tau=0}^{t} e^{\alpha \cdot \beta_m^2 \cdot \tau} \cdot \left[\int_{r'=a}^{b} r' \cdot \cos \beta_m (r'-a) \cdot \Phi_s(r',\tau) \cdot dr' \right] \cdot d\tau$$

Eq. 4.28

where k is thermal conductivity (W cm^{-1} K^{-1}), α is the thermal diffusivity (cm^2 s^{-1}),

$\Phi_s(r,t)$ is the absorbed fluence rate (W cm^3), and:

$$\beta_m = \frac{(2m-1)\pi}{2(b-a)}$$

Eq. 4.29

For continuous wave irradiation with a duration t_p, we have:

$$\Phi_s(r',0 < \tau < t_p) = \Phi_s(r')$$

Eq. 4.30a

$$\Phi_s(r',\tau > t_p) = 0$$

Eq. 4.30b

Combining Eqs 4.28 and 4.30a,b gives:

$$T_S(r,0 < t < t_p) = \frac{\alpha}{k} \cdot \frac{2}{r \cdot (b-a)} \sum_{m=1}^{\infty} e^{-\alpha \cdot \beta_m^2 \cdot t} \cdot \cos \beta_m (r-a)$$

$$\cdot \int_{\tau=0}^{t} e^{\alpha \cdot \beta_m^2 \cdot \tau} \cdot d\tau \cdot \int_{r'=a}^{b} r' \cdot \cos \beta_m (r'-a) \cdot \Phi_s(r') \cdot dr'$$

Eq. 4.31a

$$T_S(r,t > t_p) = \frac{\alpha}{k} \cdot \frac{2}{r \cdot (b-a)} \sum_{m=1}^{\infty} e^{-\alpha \cdot \beta_m^2 \cdot t} \cdot \cos \beta_m (r-a)$$

$$\cdot \int_{\tau=0}^{t_p} e^{\alpha \cdot \beta_m^2 \cdot \tau} \cdot d\tau \cdot \int_{r'=a}^{b} r' \cdot \cos \beta_m (r'-a) \cdot \Phi_s(r') \cdot dr'$$

Eq. 4.31b

After integration of the time-dependent exponential term we obtain:

$$T(r,0 < t < t_p) = \frac{1}{k} \cdot \frac{2}{r \cdot (b-a)} \sum_{m=1}^{\infty} \left(1 - e^{-\alpha \cdot \beta_m^2 \cdot t}\right)$$

$$\cdot \frac{\cos \beta_m (r-a)}{\beta_m^2} \cdot \int_{r'=a}^{b} r' \cdot \cos \beta_m (r'-a) \cdot \Phi_s(r') \cdot dr'$$

Eq. 4.32a

$$T(r, t > t_p) = \frac{1}{k} \cdot \frac{2}{r \cdot (b-a)} \sum_{m=1}^{\infty} e^{-\alpha \cdot \beta_m^2 \cdot t} \cdot \left(e^{\alpha \cdot \beta_m^2 \cdot t_p} - 1 \right)$$

$$\cdot \frac{\cos \beta_m (r-a)}{\beta_m^2} \cdot \int_{r'=a}^{b} r' \cdot \cos \beta_m (r'-a) \cdot \Phi_S(r') \cdot dr'$$

Eq. 4.32b

With the analytical expression of the absorbed fluence rate (Eq. 4.18), a closed form expression of the integral in equation 4.32 can be found in integral tables (Schaum's Mathematical Handbook of Formulas and Tables 1999). This integration leads to the following expression:

$$T_s(r, 0 < t < t_p) = \frac{P_s}{(1 + \mu_{eff} \cdot r_s) \cdot e^{-\mu_{eff} r_s}} \cdot \frac{\mu_{eff}^2}{2 \cdot \pi \cdot k} \cdot \sum_{m=1}^{\infty} f_m(t) \cdot h_m(r)$$

Eq. 4.33a

$$T_s(r, t > t_p) = \frac{P_s}{(1 + \mu_{eff} \cdot r_s) \cdot e^{-\mu_{eff} r_s}} \cdot \frac{\mu_{eff}^2}{2 \cdot \pi \cdot k} \cdot \sum_{m=1}^{\infty} g_m(t) \cdot h_m(r)$$

Eq. 4.33b

where:

$$f_m(t) = \left(1 - e^{-\alpha \cdot \beta_m^2 \cdot t} \right) \frac{(-1)^{m+1} \cdot \beta_m \cdot e^{-\mu_{eff} \cdot b} + \mu_{eff} \cdot e^{-\mu_{eff} \cdot a}}{\beta_m^2 \cdot \left(\beta_m^2 + \mu_{eff}^2 \right)}$$

Eq. 4.34

$$g_m(t) = e^{-\alpha \cdot \beta_m^2 \cdot t} \cdot \left(e^{\alpha \cdot \beta_m^2 \cdot t_p} - 1 \right) \cdot \frac{(-1)^{m+1} \cdot \beta_m \cdot e^{-\mu_{eff} \cdot b} + \mu_{eff} \cdot e^{-\mu_{eff} \cdot a}}{\beta_m^2 \cdot \left(\beta_m^2 + \mu_{eff}^2 \right)},$$

Eq.4.35

$$h_m(r) = \frac{\cos \beta_m (r-a)}{r \cdot (b-a)},$$

Eq. 4.36

4.4.3 Thermal model for diffusing tip optical fiber

To calculate the temperature distribution produced by a diffusing tip optical fiber, we sum the temperature increase induced by all of the spherical sources comprising the optical fiber tip (Figure 4.13). The expression becomes:

$$T(x,y,z,t) = T_i + \sum_{j=1}^{N} T_s(r_j(x,y,z),t)$$

Eq. 4.37

where T_i is the initial temperature of the tissue, N is the number of spherical sources and with the coordinate system of Figure 4.13:

$$r_j(x,y,z) = \sqrt{(x-x_j)^2 + y^2 + z^2}$$

Eq. 4.38

where x_j is the x coordinate of the j_{th} spherical source. Equations 4.32a,b and 4.36 become:

$$T(x,y,z,0<t<t_p) = T_i + \frac{P_s}{(1+\mu_{eff} \cdot r_s) \cdot e^{-\mu_{eff} r_s}} \cdot \frac{\mu_{eff}^2}{2 \cdot \pi \cdot k} \cdot \sum_{m=1}^{\infty} f_m(t) \cdot \left[\sum_{j=1}^{N} h_m(r_j)\right]$$

Eq. 4.39a

$$T(x,y,z,t>t_p) = T_i + \frac{P_s}{(1+\mu_{eff} \cdot r_s) \cdot e^{-\mu_{eff} r_s}} \cdot \frac{\mu_{eff}^2}{2 \cdot \pi \cdot k} \cdot \sum_{m=1}^{\infty} g_m(t) \cdot \left[\sum_{j=1}^{N} h_m(r_j)\right]$$

Eq. 4.39b

4.4.4 Implementation

A MATLAB program was written that uses equations 4.39a and 4.39b to obtain the temperature distribution in fibro-fatty tissue. The heat equation was solved for the Indigo diffusing fiber tip. The diffusing tip was modeled with N=51 spheres of radius r_s=0.9mm

separated by Δx=0.284 mm and with b=30 mm. According to equation 4.38, the solution

of the heat equation is the sum of an infinite converging series. The minimum number of

terms that must be included in the summation to give the temperature with an acceptable

error can be determined by considering that the terms of the series are the product of two

functions $f_m(t)$ or $g_m(t)$ and $h_m(r)$. The function of $h_m(r)$ is a sinusoidal function that

modulates the functions $f_m(t)$ and $g_m(t)$, which are exponential functions. The maximum

contribution of the m_{th} term of the series to the temperature is the asymptotic value of the

function $f_m(t)$:

$$f_\infty(m) = \frac{(-1)^{m+1} \cdot \beta_m \cdot e^{-\mu_{eff} \cdot b} + \mu_{eff} \cdot e^{-\mu_{eff} \cdot a}}{\beta_m{}^2 \cdot \left(\beta_m{}^2 + \mu_{eff}{}^2\right)} \qquad \text{Eq. 4.40}$$
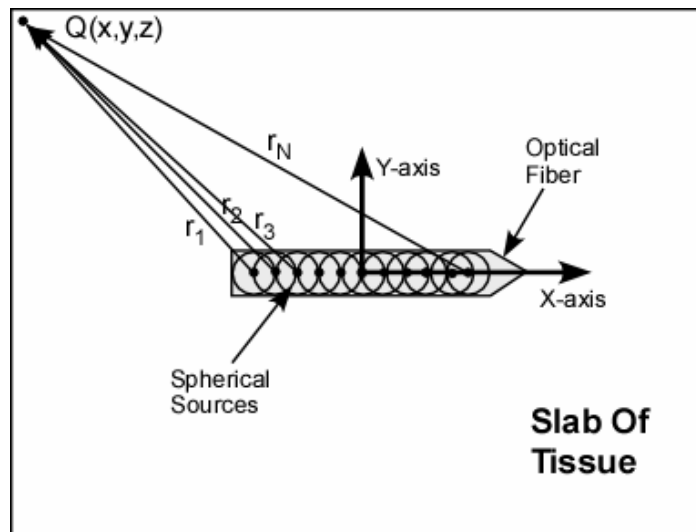
Figure 4.13: The diffusing tip optical fiber in a slab of tissue represented by a series of spherical sources of finite radius. The temperature increase at each point in the tissue will be the summation of the temperature increase induced by each of these spherical sources. The coordinate system is selected such that the center of the diffusing tip is the center of the coordinate system.

Figure 4.14 shows the function $f_m(t)$ as a function of time for m=1-6. The figure shows that the asymptotic value decreases rapidly as m increases. The value of the asymptote of the m_{th} term relative to the first term of the series is shown figure 4.15. The figure shows that the relative contribution is less than 10^{-6} after 50 terms and less than 10^{-8} after 200 terms. Based on these considerations, the summation was stopped at m=200. The MATLAB program is included in Appendix B. The validation and application of the thermal model is described in chapter 7.
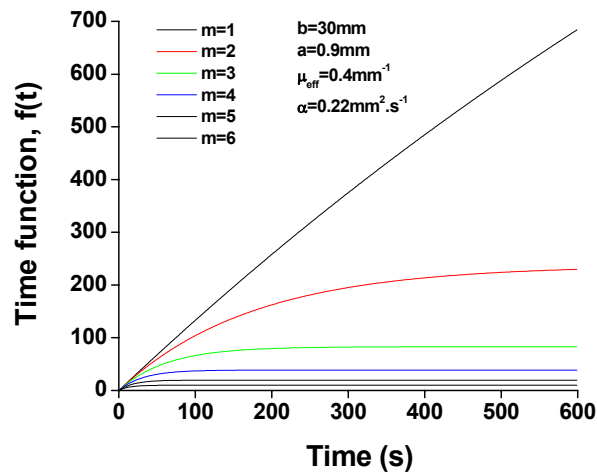
Figure 4.14: The finction $f_m(t)$ of the thermal model (see equation 4.34) as a function of time for m=1-6.
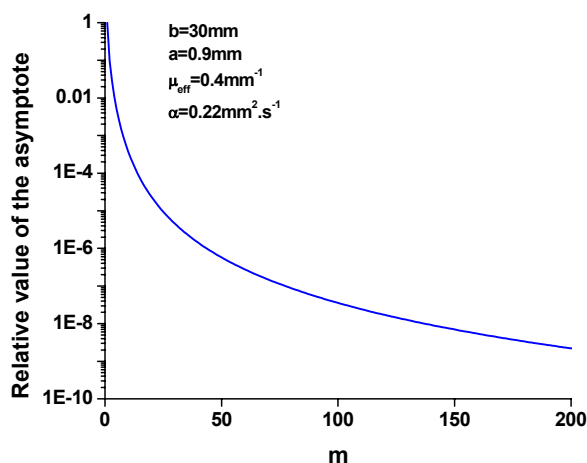
Figure 4.15: The asymptotic value of the function $f_m(t)$ as a function of m (see eq. 4.40)

4.4.5 Summary

A thermal model was developed to calculate the temperature distribution in the tissue during irradiation by an isotropic spherical source of finite radius. The heat source term is proportional to the analytical expression of the absorbed fluence rate of an isotropic spherical source obtained by the diffusion approximation. The final temperature distribution is the summation of the temperature induced by each spherical source that comprises the cylindrical diffusing tip fiber. This approach produces a relatively simple analytical expression for the temperature that can be calculated rapidly using a computer program. The model shows that the temperature is the sum of exponential functions with asymptotic values that depend on the radial coordinates. The radial dependence is the sum of cosine type functions. The validity of the model will be evaluated in chapter 7 by comparing predicted and measured temperatures during LITT in *ex-vivo* porcine tissue.

4.5 Thermal coagulation model

4.5.1 Purpose

The thermal model described above calculates the temperature increase induced at each point within the tissue as a function of both the optical properties (absorbed fluence rate) and the thermal properties (conduction of heat). Once the temperature has exceeded a certain threshold for a certain period of time, the tissue undergoes cell death and photocoagulation. In this section, the method to calculate the amount of coagulation as a function of the temperature increase using the Arrhenius equation is described.

4.5.2 Arrhenius model of thermal coagulation

The Arrhenius equation was initially used to model the kinetics of first order chemical reactions. Its use has been extended to model the temperature-dependent kinetics of tissue coagulation. This equation is given by (Pearce and Thomsen 1995):

$$\Omega(t) = \ln\left(\frac{C_N(0)}{C_N(t)}\right) = \int_0^t A e^{\frac{-E_a}{RT(\tau)}} d\tau \qquad \text{Eq. 4.41}$$

where $\Omega(t)$ is the thermal damage at time t, $C_N(0)$ is the initial concentration of native tissue, $C_N(t)$ is the remaining concentration of native tissue at time t, R is the universal gas constant (R=8.32 J mole^{-1} K^{-1}), T(t) is the temperature in Kelvin as a function of the time, E_a is an activation energy (J mol^{-1}), and A is a frequency factor (s^{-1}). If we assume that $C_N(0)=1$ (no thermal damage prior to treatment), then the concentration of coagulated tissue, $C_D(t)$, is given by:

$$C_D(t) = 1 - C_N(t) = 1 - e^{-\int_0^t A e^{\frac{-E_a}{RT(\tau)}} d\tau} \qquad \text{Eq.4.42}$$

The activation energy and the frequency factor are properties of the tissue and will vary for different tissue types and different thermal processes. The range of frequency factors and activation energies that are published in the literature is 10^{40}-10^{102} s^{-1} and 10^{5}-10^{6} J mol^{-1}, respectively (Pearce and Thomsen 1995). There are no published values for the Arrhenius parameters relevant for the coagulation of fibro-fatty tissue. The measurement of these parameters is described in chapter 6.

4.5.3 Implementation

A MATLAB program was written to solve for the coagulation in the tissue during and after laser irradiation using the temperature output by the thermal model. At each time point, the value of $C_D(t)$ is calculated by solving the integral in the exponential term of equation 4.41 numerically using the trapezoidal method (Magrab 2000). The algorithm and the program are straightforward. The program is included in Appendix C.

4.6   Summary and conclusion

An optical-thermal model was developed to calculate the temperature and thermal coagulation distribution in ex-vivo fibro-fatty tissue when irradiated with a cylindrical diffusing tip optical fiber, which is represented as a series of spherical sources. The optical-thermal model is divided into three parts: a radiometric model that calculates the light distribution in the fibro-fatty tissue for a spherical source, a thermal model that calculates the temperature distribution for the series of spherical source that make up the cylindrical diffusing tip fiber, and a coagulation model that predicts the amount of coagulation in the tissue from the predicted temperature distribution. The validation of

the optical-thermal model requires knowledge of the optical properties and of the Arrhenius equation parameters. Chapter 5 describes the optical property measurements of normal and coagulated ex-vivo fibro fatty porcine mammary chain tissue at 830, 940, and 980 nm. Chapter 6 describes the calculation of the Arrhenius equation activation energy and frequency factor constants necessary to accurately predict the coagulation in ex-vivo fibro-fatty tissue as a function of temperature and time. Chapter 7 validates the model by comparing the predicted temperature and coagulation distribution to measured values.

5. OPTICAL PROPERTY MEASUREMENTS OF PORCINE TISSUE

5.1. Introduction

Chapter 4 describes the optical thermal model that will be used to calculate the light, temperature, and coagulation distribution in the breast tissue during laser interstitial thermotherapy with a cylindrical diffusing tip optical fiber. As mentioned in chapter 4, the optical parameters of the tissue must be known to calculate the light distribution. These optical parameters include the absorption coefficient (μ_a), scattering coefficient (μ_s), the scattering anisotropy factor (g), and the refractive index (n). The absorption, scattering, and scattering anisotropy coefficients are dependent on the laser wavelength.

In this chapter, the optical properties of the *ex-vivo* porcine mammary chain tissue will be measured. Ex-vivo porcine mammary chain tissue has been used as a tissue phantom for human breast tissue (Salas *et al* 2004) and will be used to verify the predictions of the optical-thermal model. The optical properties of ex-vivo porcine tissue have been measured at wavelengths of 633 and 790 nm (Arnfield *et al* 1992, Flock *et al* 1987). No data is available at the wavelengths considered in this project (830, 940, and 980 nm).

This chapter will include the following:

a)   Review of the most common *ex-vivo* optical property measurement techniques.

b)   Description and experimental validation of the optical property measurement system used to determine the optical properties of *ex-vivo* porcine tissue.

c)   Results of optical property measurements of normal and coagulated *ex-vivo* porcine mammary chain tissue.

The results of these measurements will be used in the optical thermal model (see chapter 7). They will also help verify if the properties of *ex-vivo* porcine tissue are comparable to those of human breast tissue (Peters *et al* 1990).

5.2 Review of *ex-vivo* optical property measurement techniques

5.2.1 Introduction

Optical property measurement techniques require both an experimental set-up to measure a radiometric characteristic either in the tissue (fluence) or outside the tissue (reflection and transmission) and a light propagation model to calculate the optical properties from these measured values. These measurements are categorized into either *in-vivo* or *ex-vivo* optical property measurement techniques. Since *ex-vivo* porcine mammary chain tissue is being used in this project, only *ex-vivo* optical property measurement techniques are discussed. *Ex-vivo* optical property measurement techniques can further be categorized as direct or indirect techniques.

5.2.2 Direct *ex-vivo* optical property measurement techniques

Direct measurement techniques have been used to calculate the attenuation coefficient (μ_t), the absorption coefficient (μ_a), the scattering coefficient (μ_s), and the scattering phase function, $p(\cos\theta)$, of tissue samples. The scattering phase function is the angular distribution of scattered light for a single scattering event. The scattering anisotropy coefficient (g) is the mean value of the cosine of the scattering angle. Direct

measurements techniques require the use of thin tissue samples, where there is no more than one scattering event.

Attenuation coefficient (μ_t): The attenuation coefficient is the sum of the absorption and scattering coefficient and is found by measuring the collimated, or unscattered, transmission (Wilson 1995) of light through a thin sample (Figure 5.1). The collimated transmission is related to the attenuation coefficient by the Beer-Lambert law (Wilson 1995, Choeng *et al* 1990):

$$T_c = \frac{P_f}{P_i} = K \cdot e^{-\mu_t d} \qquad \text{Eq. 5.1}$$

where T_c is the transmission of light through the sample, μ_t is the attenuation coefficient, d is the thickness of the sample, and K accounts for the reflection or transmission losses at the sample boundaries and in the tissue holder. According to equation 5.1, the attenuation coefficient can be calculated from the collimated transmission by using the following equation:
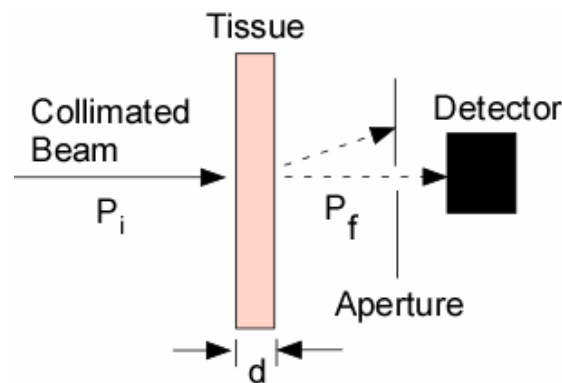
Figure 5.1: Measurement of collimated transmittance through a thin sample. The collimated transmittance is the ratio of the output power (P_f) over the input power (P_i). The aperture is used to block out any scattered light. The attenuation coefficient can be calculated from this measurement.

$$\mu_t = \frac{-\ln(\frac{T_c}{K})}{d}.$$ Eq. 5.2

The value of K can be determined either experimentally by measuring the collimated transmission for two different sample thicknesses or by using reflection and transmission formulas if the refractive indices of the tissue cell and sample are known.

Absorption coefficient (μ_a): The absorption coefficient of a thin sample can be measured by placing the sample inside an integrating sphere. The inner wall of the integrating sphere is coated with a highly diffuse reflective material that reflects light in a Lambertian (uniform) fashion with minimal absorptive loss (Figure 5.2). Integrating spheres are designed so that the irradiance on the inner wall of the sphere is uniform. Integrating spheres have one entrance port to deliver the light to the tissue sample located inside the sphere and at least one exit port that lets some of the light escape for measurements. The total power incident on the sphere inner wall can be calculated from a measurement of the light escaping through the exit port.

In the absence of tissue, the detected power, P_f, is related to the incident power, P_i, by

$$P_f = \eta \cdot P_i$$ Eq. 5.3

where η is the detection efficiency. When a tissue sample is placed inside the sphere, the detected power is reduced due to absorption by the tissue. All transmitted and scattered photons are detected. For a thin tissue sample, the detected power is given by (Wilson 1995, Cheong *et al* 1990):

$$P_f = P_i \cdot \eta \cdot e^{-\mu_a d}$$ Eq. 5.4
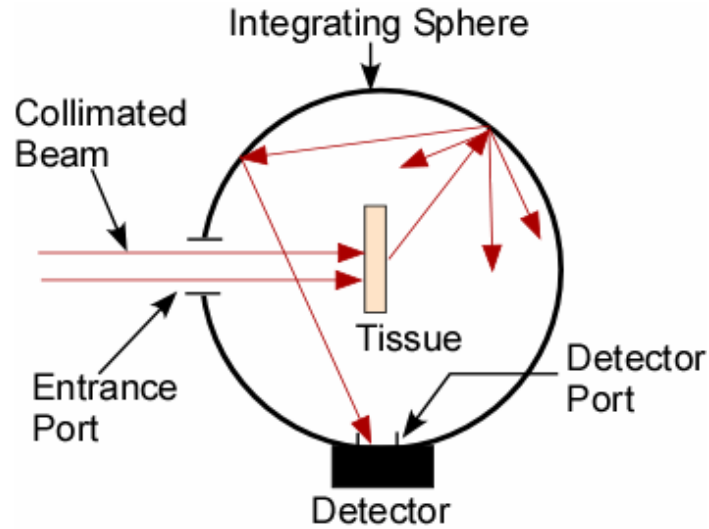
Figure 5.2: The measurement of a portion of the total transmitted light through a tissue sample using an integrating sphere. The absorption coefficient can be calculated from this measurement.

where μ_a is the absorption coefficient and d is the thickness of the tissue sample. According to equation 5.4, the absorption coefficient is given by the following equation:

$$\mu_a = -\frac{1}{d}\ln(\frac{P_f}{\eta P_i}).$$ eq. 5.5

Scattering coefficient (μ_s): The scattering coefficient of a thin tissue sample can be measured using an integrating sphere in the same manner as the absorption coefficient. To measure the scattering coefficient, an additional exit port is required to let the collimated transmission to exit the sphere (Figure 5.3). The scattering coefficient is calculated using the following formula (Wilson 1995, Choeng et al 1990):

$$\mu_s = -\frac{1}{d}\ln(1-\frac{P_f}{\eta P_i}).$$ eq. 5.6

Scattering phase function: The scattering phase function of a thin tissue sample can be measured by recording the angular dependence of the light scattered by the sample. The tissue is generally placed in a cylindrical container and irradiated with a collimated beam. A light detector is rotated around the cylinder to measure the light scattered at each angle. The cylinder is usually filled with a liquid of refractive index similar to that of the tissue to minimize refraction effects (Figure 5.4). The phase function, $p(\cos\theta)$, is proportional to the detected signal (Wilson 1995, Cheong *et al* 1990).
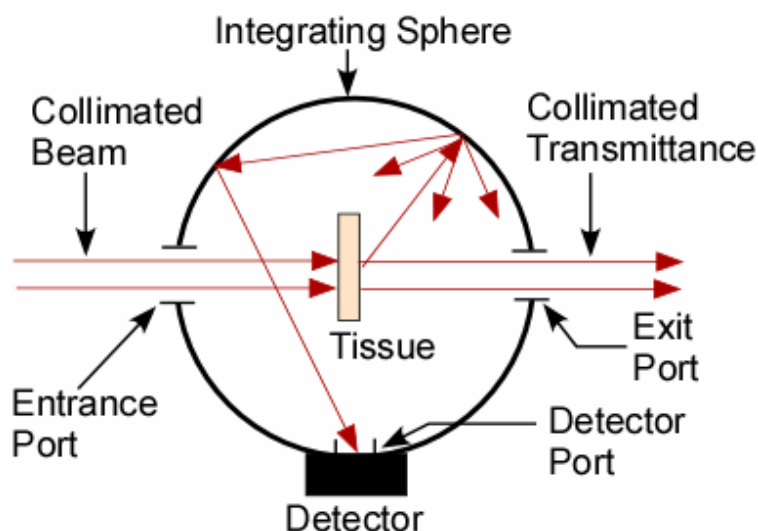
Figure 5.3: The measurement of a portion of the the scattered transmitted light through a tissue sample using an integrating sphere. The collimated transmittance is allowed to leave the integrating sphere through another exit portal hole. The scattering coefficient can be calculated with this measurement.
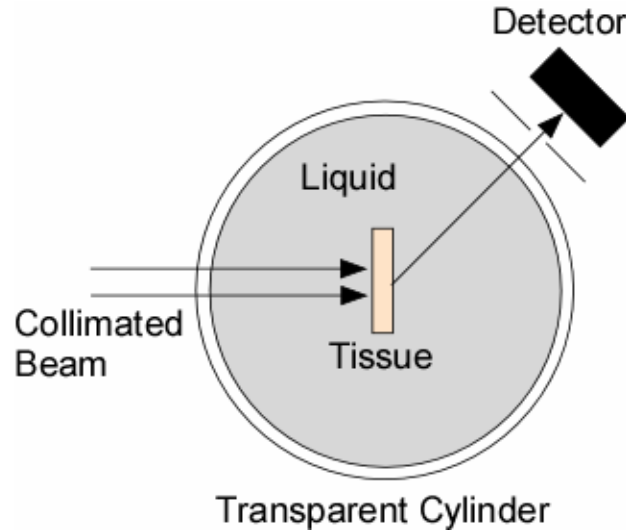
Figure 5.4: Measurement of the diffusely transmitted light at each angle around the tissue sample. The tissue sample is placed in a cylinder filled with a medium of similar refractive index to the tissue. A detector is rotated around the cylinder. An aperture is used at the detector to limit the collection angle. The scattering phase function of the tissue can be calculated from these measurements.

Discussion: The advantage of direct techniques is that the optical properties are directly related to the radiometric quantities through simple formulas.   The main drawback of these techniques is that they require thin samples, typically less than 10 µm thick, to avoid multiple scattering. In practice it is difficult to produce such samples with uniform thickness.   In addition, the present study is concerned with the treatment of a heterogeneous fibro-fatty tissue (human breast or porcine mammary chain tissue) at a scale of several millimeters.   The optical properties obtained from measurements on a micrometer scale may not be representative of the bulk tissue.

5.2.3 Indirect *ex-vivo* optical property measurement techniques

The optical properties of thick *ex-vivo* tissue samples with multiple scattering can be measured using indirect techniques.   Indirect techniques rely on measurements of the

diffuse reflectance (R_d), diffuse transmittance (T_d), and collimated transmittance (T_c) of the sample. The optical properties (μ_a, μ_s, g) are calculated from the reflectance and transmittance measurements (R_d, T_d, T_c) using an inverse method relying on either an analytical or numerical light propagation model (Bevilacqua *et al* 1997, Troy *et al* 1996, Key *et al* 1991, Peters *et al* 1990). The light propagation model is designed to simulate the experimental measurement set-up. The goal of the inverse method is to find which set of input optical properties (μ_a, μ_s, g) produces an output that corresponds to the experimental measurements (R_d, T_d, T_c) within a predetermined error. The most common technique to measure the diffuse reflectance and transmittance of thick tissue samples is to use one or two integrating spheres.

In the single integrating sphere method, the sample diffuse reflectance (R_d) and diffuse transmittance (T_d) are measured separately (Figure 5.5). For the diffuse reflectance measurements, the sample is mounted on the exit port of the integrating sphere. The incident light beam is delivered through the entrance port. The diffusely reflected light is collected by a photodiode mounted on the detector port of the integrating sphere. For the diffuse transmission measurements, the sample is mounted on the entrance port of the integrating sphere. The incident light beam is delivered through the sample. The diffusely transmitted light is collected by the integrating sphere detector. During both measurements, the collimated transmittance (T_c) can be measured by leaving the exit port open to let the unscattered photon exit the integrating sphere (Figure 5.5). To allow measurements of diffuse reflectance and transmittance without having to displace the entire sphere or dismount the sample, the integrating sphere may be rotated

around the optical axis of the system to set it up either in reflectance or transmittance mode.

The main drawback of the single integrating sphere set-up is that the diffuse reflectance and transmittance cannot be measured simultaneously. Simultaneous measurements would accelerate the data collection and allow quantification of potential dynamic changes in the tissue reflection and transmission properties during laser irradiation. This problem can be solved by using a double-integrating sphere technique, in which the tissue sample is sandwiched between two integrating spheres. One of the spheres measures the diffuse reflectance, while the other simultaneously measures the diffuse transmittance (Figure 5.6). The drawback of the double-integrating sphere method is that there is light exchange between the two integrating spheres, which makes calibration more difficult (Wilson 1995, Pickering *et al* 1993). Also, the cost of the system is higher, for there is more equipment involved. For these reasons, and since measurements of the optical properties during laser irradiation and heating were not part of the project aims, the single integrating sphere set-up was used.

5.3 Design of the optical property measurement system

5.3.1 General description

The optical properties of *ex-vivo* porcine fibro-fatty tissue were measured with an indirect technique using a single integrating sphere. The system consists of:

a)   a single integrating sphere experimental set-up that measures the diffuse reflection, diffuse transmission, and collimated transmission of light through a tissue sample, and
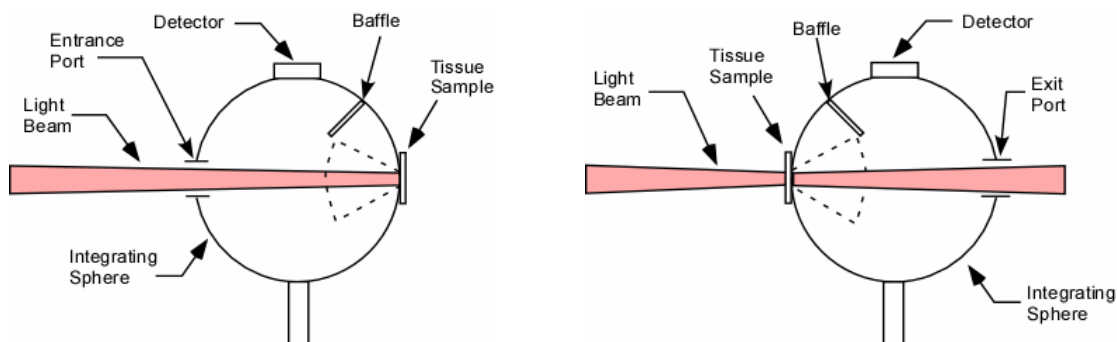
Figure 5.5: The integrating sphere positioned to measure the diffuse reflection (left) and diffuse transmission (right) of light through a tissue sample mounted on the integrating sphere
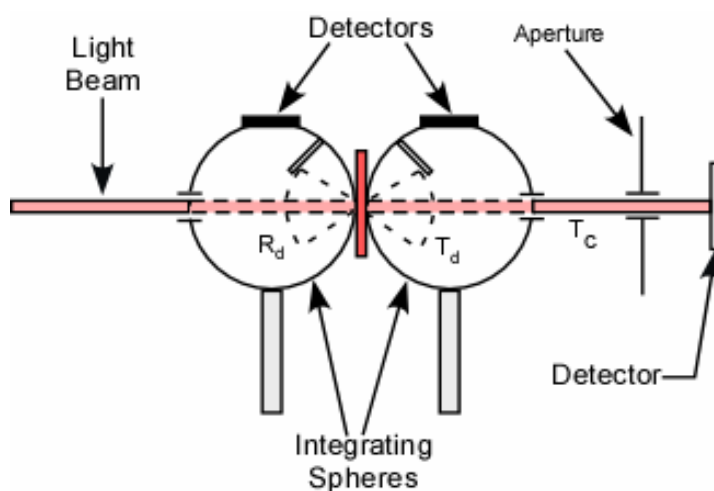
Figure 5.6: Schematic of a double integrating sphere optical property measurement system

b)   an inverse Monte-Carlo light propagation program that calculates the optical parameters of the tissue sample from the single integrating sphere measurements.

5.3.2 Single integrating sphere experimental set-up

The optical properties were measured at three different near-infrared wavelengths. Three laser systems were used to irradiate the tissue sample:

a)   a 980 nm diode laser system (AOC25, Applied Optronics, South Plainfield, NJ),

b)   an 830 nm diode laser system (Indigo830, Indigo Corp., Palo Alto, CA), and

c)   a 940 nm diode laser system (Medilas D SkinPulse, Dornier Medical Systems Inc., Kennesaw, GA).

The general principle of the experimental set-up is shown in figure 5.7. The three lasers are delivered through optical fibers terminated with standard SMA connectors at the distal end of the fiber but with different connector designs at the laser end. The distal end of these fibers was connected to a separate bare-tip optical fiber that delivered the laser beam to the integrating sphere system. The delivery fiber had a 600 μm diameter core and 0.39 numerical aperture.

The output of the fiber is imaged onto the tissue sample using a plano-convex lens (f=+50.2 mm). The optical system was designed to produce a spot diameter of 3 mm on the sample with an incidence angle of less than 1 degree. The spot diameter was selected such that it is approximately 5-10 times smaller than the diameter of the tissue port. A small focal spot to port hole diameter ratio is required to avoid the blockage of scattered photons at the edge of the port hole. A small divergence of the incident beam is required because the calibration formulas for the integrating sphere assume a nearly collimated irradiation of the sample. The small divergence of the incidence beam was reduced by placing a circular aperture between the optical fiber and the lens.

A 4 cm diameter integrating sphere (819S-IS-4, Newport Corp., Irvine, CA) was used. The integrating sphere is mounted on a rotating stage that allows the sample to be positioned at the exit port during diffuse reflection measurements and at the entrance port during diffuse transmission measurements. The light inside the integrating sphere is

measured with a photodiode detector (818-SL, Newport Corp., Irvine, CA) mounted on a 6.35 mm diameter port hole. The photodetector is coupled to a power meter (1815-C, Newport Corp., Irvine, CA). A baffle located inside the sphere ensures that light is reflected off the sphere wall prior to reaching the detector.

The collimated, unscattered light leaving the exit port of the integrating sphere is detected by an external photodiode detector (818-SL, Newport Corp., Irvine, CA) coupled to a power meter (1815-C, Newport Corp., Irvine, CA). The photodetector is placed at approximately 10 cm away from the exit port of the integrating sphere to minimize the detection of scattered photons and at the same time ensure that the beam approximately fills the detector area. In addition, a circular aperture is placed in front of the detector to further block scattered light from reaching the photodetector.

5.3.3 Experimental procedure

According to the integrating sphere theory (see derivation in Appendix D), the measurement of the diffuse reflectance (R_d) and diffuse transmittance (T_d) of a sample are given by the following equations:

$$R_d = R \cdot \frac{P_{Rcd}}{P_{Rd}} \qquad\qquad \text{Eq. 5.7}$$

$$T_d = R \cdot \frac{P_{Tcd}}{P_{Rd}} \qquad\qquad \text{Eq. 5.8}$$

where R is the reflectance of the inner sphere wall (provided by the manufacturer), P_{Rcd} is the power diffusely reflected by the sample when the incident beam is collimated, P_{Tcd} is the power diffusely transmitted by the tissue when the incident beam is collimated, and P_{Rd} is the power reflected when the tissue is irradiated diffusely. According to these

equations, three radiometric measurements are needed to obtain the diffuse transmittance and diffuse reflectance of the sample. The collimated transmittance (T_c) is calculated using equation 5.1, which is dependent on the sample thickness. A sample thickness was chosen in which there was both multiple scattering within the tissue and collimated transmission that were both measurable.

The experimental procedure for measuring diffuse transmittance (T_d), diffuse reflectance (R_d), and collimated transmittance (T_c) is the following:

a) The integrating sphere is placed in transmittance mode (Figure 5.7a).

b) The incident power (P_{ini-T}) of the laser beam is measured prior to mounting the sample onto the integrating sphere using the external photodetector (PD2).

c) The sample thickness is measured with a caliper. The sample is then mounted onto the sample mount of the integrating sphere (Figure 5.8).

d) The laser is turned on.

e) The collimated transmitted light (P_{Tc}) is measured using the external photodetector (PD2).

f) The diffuse transmitted light (P_{Tcd}) is measured using the photodetector mounted on the integrating sphere (PD1).

g) The laser is turned off.

h) The integrating sphere is rotated into the reflection mode position (Figure 5.7b).

i) The laser is turned on

j) The collimated transmitted light (P_{Rc}) is measured using the external photodetector (PD2).

(A)

(B)

(C)
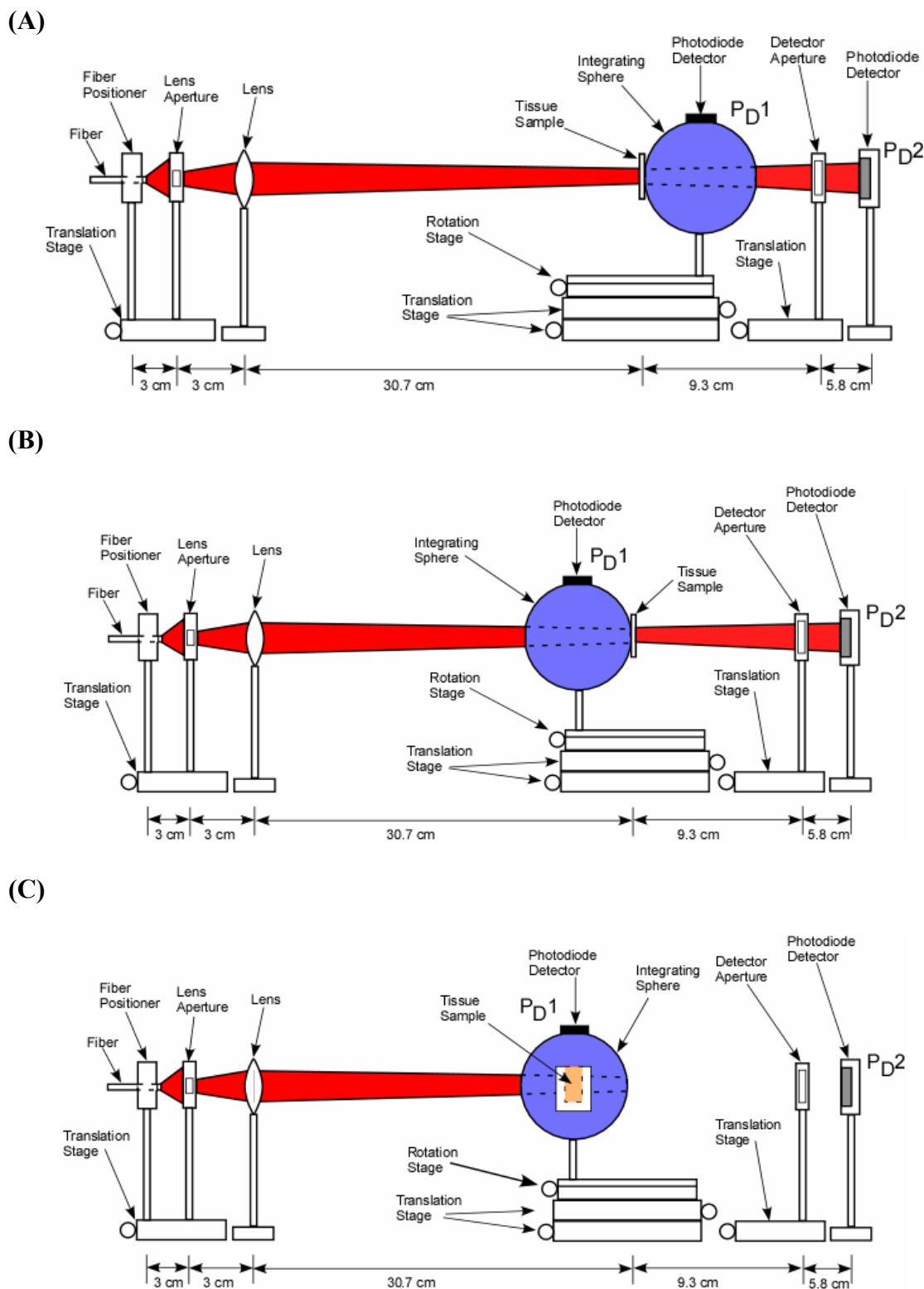
Figure 5.7: The schematic of a diffuse transmittance (A) and diffuse reflectance (B) with collimated irradiation and diffuse reflectance with diffuse irradiance (C) positions of the single integrating sphere optical property measurement system
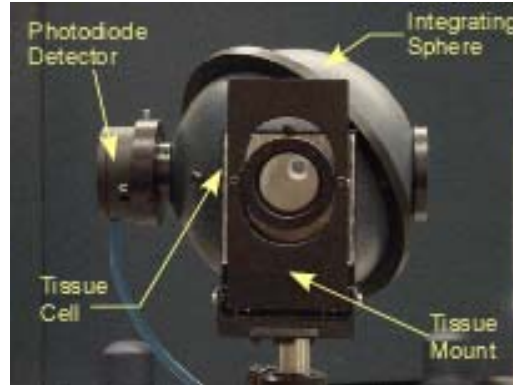
Figure 5.8: The sample mount on the integrating sphere

k)   The diffuse reflected light (P_{Rcd}) is measured using the photodetector mounted on the integrating sphere (PD1).

l)   The sample is removed from the integrating sphere.

m)   The incident power (P_{ini-R}) of the laser beam is measured using the external photodetector (PD2).

n)   The tissue sample cell is moved to the diffuse irradiation port for measurements of diffuse reflectance with diffuse irradiance (P_{Rd}) (Figure 5.7c).

o)   The original tissue sample port is closed.

p)   The laser is turned on.

q)   The diffuse reflected light (P_{Rd}) of the tissue sample with diffuse irradiation is measured with the photodetector mounted on the integrating sphere.

From these measurements, the diffuse reflectance (R_d) and diffuse transmittance (T_d) are calculated using equations 5.7 and 5.8. The collimated transmittance, T_c, is calculated by taking the average of the measurements recorded in the transmission and reflection mode:

$$T_c = \frac{\dfrac{P_{Rc}}{P_{ini-R}} + \dfrac{P_{Tc}}{P_{ini-T}}}{2} .$$
<div align="right">Eq. 5.9</div>

5.3.4 Calibration of the integrating sphere

Equations 5.7 and 5.8 provide the theoretical relation between the transmittance and reflectance of the sample and the radiometric measurements. In practice there is always some loss of light through the ports of the integrating sphere. These losses are accounted for by calibrating the integrating sphere set-up with a diffuse calibration standard. The measurements with the calibration standard are used to derive a calibration factor for the sphere. Incorporating the calibration factor, χ, into equations 5.7 and 5.8 gives the following relations (Roggan *et al* 1995):

$$R_{cd} = R \frac{P_{Rcd}}{P_{Rd}} \chi$$
<div align="right">Eq. 5.10</div>

$$T_{cd} = R \frac{P_{Tcd}}{P_{Rd}} \chi .$$
<div align="right">Eq. 5.11</div>

According to the manufacturer's specifications, the reflectance of the integrating sphere inner surface, R, is approximately 0.968, 0.966, and 0.965 at 830, 940, and 980 nm, respectively.

The integrating sphere was calibrated by measuring the diffuse reflectance of a calibration standard (99% Spectralon diffuse reflectance standard, SRS-99-010, #4911A, Labsphere Inc., North Sutton, NH) for the three laser wavelengths. Based on these measurements, the following calibration factors were used: $\chi=0.987$ at 830 nm, $\chi=0.959$ at 940 nm, and $\chi=0.973$ at 980 nm. The difference between the calibration factors at the

three wavelengths is less than 3%. This difference can be attributed to slight difference in the irradiation geometry at the three wavelengths.

5.4 Inverse Monte-Carlo program

5.4.1 Description and implementation

The Monte Carlo method (see chapter 4) can be designed to simulate the light propagation in the tissue mounted on the optical property measurement system. These simulations can be used to predict the diffuse reflectance (R_d), diffuse transmittance (T_d), and collimated transmittance (T_c) of a tissue sample of known optical properties mounted on the integrating sphere. To find the optical properties (μ_a, μ_s, g) from the diffuse reflectance, diffuse transmittance, and collimated transmittance, an inverse method is needed.

Two approaches have been used for the inverse method. In the first approach (Nilsson *et al* 1998, Peters *et al* 1990), a Monte Carlo simulation is used to calculate the reflectance and transmittance for a range of absorption, scattering, and anisotropy coefficients. The reflectance and transmittance are plotted on the same graph as a function of the optical properties. The optical properties of the tissue are the coordinates of the intersection point of the reflectance and transmittance curves (Figure 5.9).

The second approach is to use an inverse Monte Carlo method (Roggan *et al* 1995). An initial set of values is assumed for the optical properties. The resulting reflectance and transmittance are then calculated using the Monte Carlo method. These values are compared to the measured reflectance and transmittance. If the difference is larger than a desired error, the optical properties are changed and the calculation is repeated. An

iterative algorithm is used to make the reflectance and transmittance converge to the experimental values within the desired error. This second approach was used in the present study.

An inverse Monte-Carlo program was written in MATLAB specifically for our optical property measurement system (Figure 5.10 and 5.11). The algorithm is comprised of the following main steps:

a) The attenuation coefficient ($\mu_t = \mu_a + \mu_s$) is calculated from the collimated transmittance (T_c) using eq. 5.2.

b) The diffuse reflectance and diffuse transmittance are calculated for values of the scattering coefficient ranging from 0 to μ_t in increments of $\mu_t/10$ for values of g ranging from 0.5 to 1.0 in increments of 0.1. These calculations are performed using the Monte Carlo program described in chapter 4 modified to simulate the experimental conditions in the optical property measurement set-up (collimated irradiance of a tissue slab of uniform thickness contained between parallel glass slides).

c) The pair (μ_{s1}, g_1) that produces the smallest difference between the measured and simulated diffuse reflectance and transmittance is selected.

d) The second step is repeated with $\mu_{s1} - \mu_t/10 < \mu_s < \mu_{s1} + \mu_t/10$ with increments of $\mu_t/100$ and with $g_1 - 0.1 < g < g_1 + 0.1$ with increments of 0.01.

e) The pair (μ_{s2}, g_2) that produces the smallest difference between the measured and simulated diffuse reflectance and transmittance is selected.
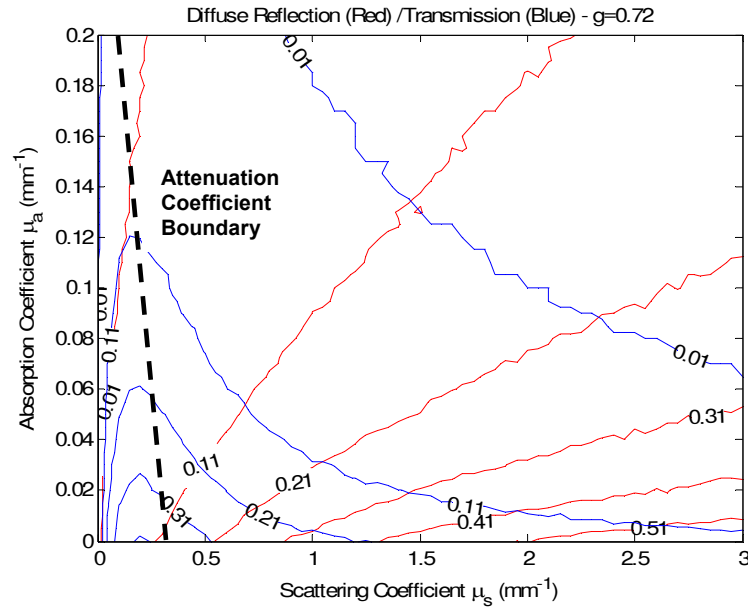
Figure 5.9: A reflection and transmission contour plot for a range of absorption and scattering coefficients for optical property measurements of Intralipid 10% at 630 nm. In this technique, the absorption and scattering coefficients are determined by finding the point of intersection of the diffuse reflectance and diffuse transmittance curves with the attenuation coefficient line.

f)   The second step is repeated with $\mu_{s2}-\mu_t/100<\mu_s<\mu_{s2}+\mu_t/100$ with increments of $\mu_t/1000$ and with $g_2-0.05<g< g_2+0.05$ in increments of 0.01.

g)   The pair (μ_{s3},g_3) that produces the smallest difference between the measured and simulated diffuse reflectance and transmittance is selected. The value g_3 is selected to be the anisotropy coefficient.

h)   The second step is repeated with $\mu_{s3}-\mu_t/1000<\mu_s<\mu_{s3}+\mu_t/1000$ with increments of $\mu_t/10000$ and a fixed value of the anisotropy coefficient ($g_4=g_3$).

i)   The pair (μ_{s4},g_4) that produces the smallest difference between the measured and simulated diffuse reflectance and transmittance is selected as the final values.
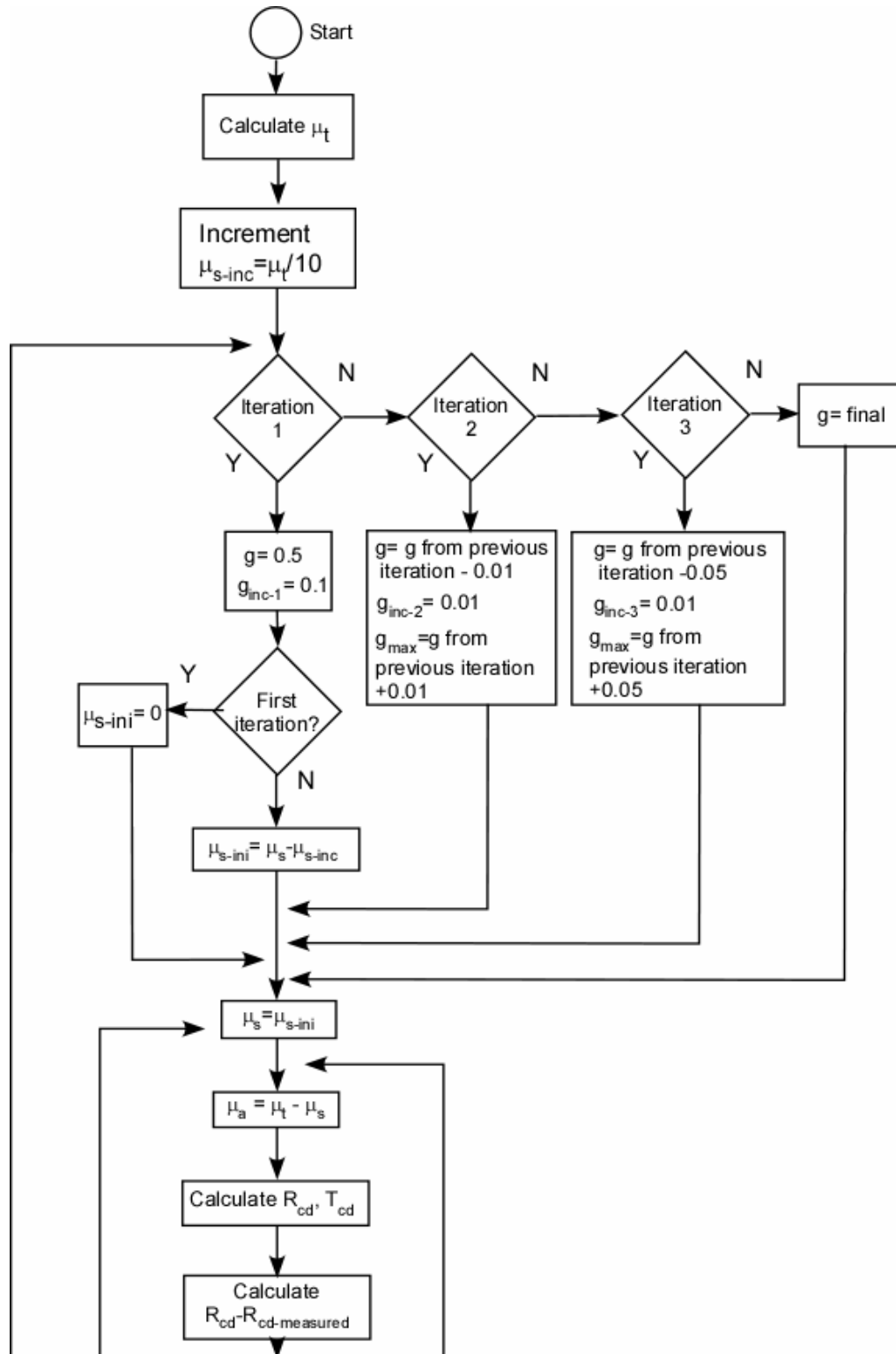
Figure 5.10: Upper half of the flow chart of the iterative inverse Monte Carlo algorithm
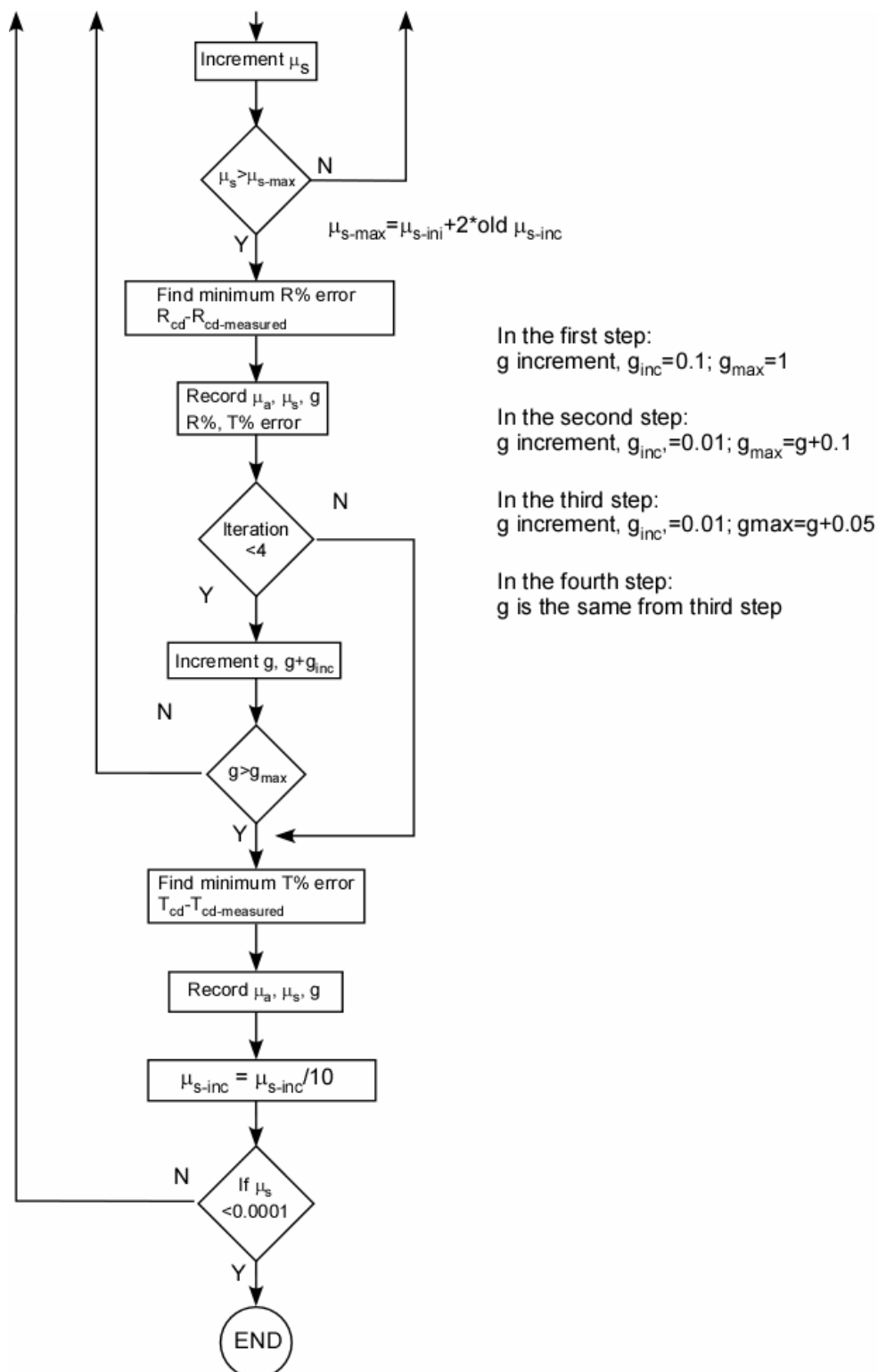
Figure 5.11: Bottom half of the flow chart of the iterative inverse Monte Carlo algorithm

5.4.2 Validation of the inverse method

The validation of the inverse Monte Carlo program consisted of two steps:

a) Validation of the Monte Carlo program that calculates R_d, T_d, and T_c for a tissue slab of known μ_a, μ_s, and g sandwiched between two glass plates (forward Monte Carlo program).

b) Validation of the inverse program

Forward Monte Carlo Program Validation

The forward Monte Carlo program was validated by comparison of its output with a set of reference data for the same tissue and irradiation geometry that was obtained using the adding-doubling method (Prahl 1995). The outputs were compared for the following ranges of input parameters:

a) optical depth = 1, 2, 4, and 8. The optical depth is defined as $\mu_t \cdot t$, where t is the tissue thickness.

b) albedos (a) = 0.6, 0.9, and 0.99. The albedo is defined as:

$$a = \frac{\mu_s}{\left(\mu_s + \mu_a\right)}$$
<div align="right">Eq. 5.12</div>

c) anisotropy coefficient (g) = 0.5 and 0.875

d) scattering coefficients (μ_s) = 0.2, 0.4, 0.6, 0.8, and 1.0 mm^{-1}

e) collimated irradiation with a beam radius of 10mm.

f) tissue refractive index: n_{sample}=1.4

In theory, the output of the Monte Carlo simulation is dependent only on the albedo, anisotropy coefficient, and the optical depth. As long as these three parameters are the same, the output should be independent of the scattering or absorption coefficient.

Comparisons were made for matched and mismatched optical boundaries. In the matched conditions, the tissue was surrounded by a medium with a refractive index of 1.4 (equal to the refractive index of the tissue). In the mismatched condition, the tissue was sandwiched between two media of refractive index n_{cell}=1.5 representing the glass cells. The mismatched boundary produces reflection losses that were taken into account in the calculations. The output of the Monte Carlo program is compared to the reference data in Tables 5.1-5.4.

For all values of the input parameters and boundary conditions, there is excellent agreement (within the rounding error) between the reference values and the output of our program. These results demonstrate the validity of the forward Monte Carlo program.

Inverse program

To validate the inverse program, the output of selected forward Monte Carlo simulations from Tables 5.3-5.4 (mismatched boundaries) that are expected to correspond to highly-scattering fibro-fatty tissue (a>0.9, g>0.5) was fed into the inverse program. The optical properties output by the inverse program were compared to the optical properties input into the forward program. The results are shown in Table 5.5. For all simulations with an optical depth of 2 or higher, the output of the inverse program is within 16% of the expected values. Since the optical depth is expected to be larger than 2 in all of our experiments, these results demonstrate the validity of the inverse program.

Table 5.1: The total reflectance of light through a collimated irradiated sample of refractive index $n_{tissue} \cong 1.4$ with no boundaries. The total reflectance calculated by the forward Monte Carlo program developed for the inverse method is compared to published data obtained using the adding doubling method (Prahl 1995).

Optical Depth	Reference Value	$\mu_s = 0.2$ mm^{-1}	$\mu_s = 0.4$ mm^{-1}	$\mu_s = 0.6$ mm^{-1}	$\mu_s = 0.8$ mm^{-1}	$\mu_s = 1.0$ mm^{-1}
Monte Carlo vs Adding Doubling Method – Reflectance Matched Boundaries
Albedo = 0.6 ; g = 0.875
1	**0.009**	0.009	0.009	0.009	0.009	0.009
2	**0.012**	0.011	0.011	0.011	0.011	0.011
4	**0.013**	0.013	0.013	0.013	0.013	0.013
8	**0.013**	0.013	0.013	0.013	0.013	0.013
Albedo = 0.9 ; g = 0.875
1	**0.024**	0.025	0.024	0.024	0.024	0.023
2	**0.042**	0.043	0.043	0.042	0.041	0.043
4	**0.066**	0.065	0.065	0.065	0.066	0.067
8	**0.083**	0.084	0.084	0.083	0.083	0.083
Albedo = 0.99 ; g = 0.875
1	**0.033**	0.033	0.034	0.034	0.034	0.033
2	**0.069**	0.069	0.071	0.069	0.070	0.069
4	**0.142**	0.140	0.140	0.142	0.139	0.144
8	**0.258**	0.260	0.257	0.260	0.262	0.255
Albedo = 0.6 ; g = 0.5
1	**0.053**	0.053	0.053	0.054	0.051	0.054
2	**0.066**	0.067	0.066	0.064	0.066	0.066
4	**0.070**	0.071	0.071	0.070	0.071	0.070
8	**0.070**	0.069	0.069	0.070	0.070	0.071
Albedo = 0.9 ; g = 0.5
1	**0.130**	0.129	0.133	0.129	0.130	0.129
2	**0.205**	0.203	0.201	0.208	0.204	0.206
4	**0.261**	0.262	0.263	0.263	0.261	0.265
8	**0.277**	0.281	0.280	0.281	0.278	0.279
Albedo = 0.99 ; g = 0.5
1	**0.171**	0.171	0.172	0.172	0.168	0.172
2	**0.305**	0.306	0.306	0.306	0.307	0.309
4	**0.470**	0.467	0.468	0.467	0.465	0.470
8	**0.600**	0.602	0.599	0.603	0.599	0.599

Table 5.2: The total transmittance through a collimated irradiated sample of refractive index $n_{tissue} \cong 1.4$ with no boundaries. The total transmittance calculated by the forward Monte Carlo program developed for the inverse method is compared to published data obtained using the adding doubling method (Prahl1995).

Optical Depth	Reference Value	$\mu_s = 0.2$ mm^{-1}	$\mu_s = 0.4$ mm^{-1}	$\mu_s = 0.6$ mm^{-1}	$\mu_s = 0.8$ mm^{-1}	$\mu_s = 1.0$ mm^{-1}
	Monte Carlo vs Adding Doubling Method – Transmittance Matched Boundaries,					
	Albedo = 0.6 ; g = 0.875					
1	**0.646**	0.644	0.647	0.643	0.642	0.647
2	**0.407**	0.406	0.407	0.406	0.409	0.402
4	**0.154**	0.153	0.153	0.153	0.154	0.155
8	**0.020**	0.019	0.020	0.019	0.020	0.020
	Albedo = 0.9 ; g = 0.875					
1	**0.870**	0.871	0.871	0.871	0.870	0.872
2	**0.743**	0.744	0.744	0.746	0.746	0.745
4	**0.521**	0.526	0.524	0.522	0.524	0.524
8	**0.234**	0.236	0.236	0.236	0.235	0.235
	Albedo = 0.99 ; g = 0.875					
1	**0.956**	0.955	0.955	0.954	0.955	0.955
2	**0.906**	0.906	0.903	0.906	0.905	0.906
4	**0.800**	0.803	0.803	0.801	0.803	0.798
8	**0.608**	0.608	0.610	0.607	0.605	0.613
	Albedo = 0.6 ; g = 0.5					
1	**0.563**	0.562	0.559	0.562	0.567	0.558
2	**0.296**	0.290	0.293	0.295	0.293	0.291
4	**0.074**	0.073	0.074	0.074	0.074	0.074
8	**0.004**	0.004	0.004	0.004	0.004	0.004
	Albedo = 0.9 ; g = 0.5					
1	**0.739**	0.741	0.737	0.743	0.740	0.740
2	**0.523**	0.526	0.529	0.521	0.525	0.525
4	**0.250**	0.253	0.253	0.252	0.254	0.251
8	**0.054**	0.055	0.055	0.055	0.057	0.055
	Albedo = 0.99 ; g = 0.5					
1	**0.815**	0.814	0.814	0.814	0.817	0.814
2	**0.660**	0.661	0.660	0.660	0.660	0.657
4	**0.453**	0.456	0.455	0.457	0.458	0.453
8	**0.244**	0.245	0.246	0.243	0.248	0.246

Table 5.3: The total reflectance of light through a collimated irradiated sample of refractive index $n_{tissue} \cong 1.4$ within a cell with wall of refractive index $n_{glass} \cong 1.5$. The total reflectance calculated by the forward Monte Carlo program developed for the inverse method is compared to published data obtained using the adding doubling method (Prahl 1995).

Optical Depth	Monte Carlo vs Adding Doubling Method – Reflectance, Mismatched Boundaries,					
	Albedo = 0.6 ; g = 0.875					
	Reference Value	$\mu_s = 0.2\ mm^{-1}$	$\mu_s = 0.4\ mm^{-1}$	$\mu_s = 0.6\ mm^{-1}$	$\mu_s = 0.8\ mm^{-1}$	$\mu_s = 1.0\ mm^{-1}$
1	**0.061**	0.060	0.060	0.060	0.060	0.060
2	**0.052**	0.052	0.051	0.051	0.052	0.051
4	**0.046**	0.046	0.046	0.046	0.046	0.047
8	**0.045**	0.046	0.045	0.046	0.045	0.045
	Albedo = 0.9 ; g = 0.875					
1	**0.090**	0.088	0.088	0.089	0.089	0.088
2	**0.094**	0.092	0.093	0.094	0.094	0.094
4	**0.092**	0.092	0.092	0.091	0.091	0.092
8	**0.082**	0.083	0.082	0.083	0.083	0.081
	Albedo = 0.99 ; g = 0.875					
1	**0.126**	0.117	0.117	0.118	0.118	0.119
2	**0.169**	0.158	0.161	0.158	0.158	0.158
4	**0.233**	0.225	0.222	0.220	0.222	0.220
8	**0.288**	0.276	0.276	0.276	0.276	0.275
	Albedo = 0.6 ; g = 0.5					
1	**0.078**	0.077	0.076	0.077	0.077	0.077
2	**0.072**	0.071	0.073	0.072	0.072	0.071
4	**0.069**	0.069	0.068	0.068	0.069	0.069
8	**0.069**	0.069	0.069	0.069	0.069	0.068
	Albedo = 0.9 ; g = 0.5					
1	**0.166**	0.161	0.159	0.159	0.159	0.160
2	**0.188**	0.186	0.184	0.186	0.183	0.185
4	**0.191**	0.187	0.190	0.186	0.187	0.189
8	**0.189**	0.187	0.189	0.187	0.188	0.185
	Albedo = 0.99 ; g = 0.5					
1	**0.255**	0.238	0.236	0.237	0.237	0.237
2	**0.348**	0.332	0.328	0.326	0.326	0.331
4	**0.434**	0.412	0.413	0.419	0.416	0.416
8	**0.497**	0.480	0.478	0.479	0.478	0.479

Table 5.4: The total transmittance of light through a collimated irradiated sample of refractive index $n_{tissue} \cong 1.4$ within a cell with wall of refractive index $n_{glass} \cong 1.5$. The total transmittance calculated by the forward Monte Carlo program developed for the inverse method is compared to published data obtained using the adding doubling method (Prahl 1995).

Optical Depth	Reference Value	$\mu_s = 0.2$ mm^{-1}	$\mu_s = 0.4$ mm^{-1}	$\mu_s = 0.6$ mm^{-1}	$\mu_s = 0.8$ mm^{-1}	$\mu_s = 1.0$ mm^{-1}
	Monte Carlo vs Adding Doubling Method – Transmittance, Mismatched Boundaries,					
	Albedo = 0.6 ; g = 0.875					
1	**0.572**	0.572	0.570	0.568	0.573	0.573
2	**0.350**	0.348	0.348	0.350	0.350	0.349
4	**0.127**	0.126	0.128	0.127	0.127	0.126
8	**0.015**	0.016	0.015	0.015	0.015	0.015
	Albedo = 0.9 ; g = 0.875					
1	**0.759**	0.760	0.758	0.757	0.758	0.760
2	**0.614**	0.614	0.617	0.613	0.613	0.614
4	**0.392**	0.394	0.391	0.392	0.391	0.392
8	**0.157**	0.159	0.159	0.159	0.158	0.160
	Albedo = 0.99 ; g = 0.875					
1	**0.850**	0.842	0.843	0.841	0.841	0.841
2	**0.779**	0.768	0.766	0.769	0.770	0.770
4	**0.652**	0.638	0.641	0.641	0.641	0.644
8	**0.477**	0.468	0.470	0.467	0.470	0.468
	Albedo = 0.6 ; g = 0.5					
1	**0.461**	0.460	0.460	0.458	0.463	0.458
2	**0.227**	0.230	0.223	0.228	0.226	0.225
4	**0.054**	0.054	0.056	0.054	0.053	0.055
8	**0.003**	0.003	0.003	0.003	0.003	0.003
	Albedo = 0.9 ; g = 0.5					
1	**0.605**	0.596	0.602	0.602	0.601	0.601
2	**0.400**	0.396	0.393	0.395	0.402	0.399
4	**0.181**	0.179	0.180	0.181	0.181	0.180
8	**0.038**	0.039	0.038	0.038	0.038	0.039
	Albedo = 0.99 ; g = 0.5					
1	**0.712**	0.693	0.696	0.695	0.694	0.695
2	**0.581**	0.561	0.566	0.567	0.567	0.562
4	**0.425**	0.413	0.412	0.407	0.409	0.410
8	**0.250**	0.237	0.242	0.239	0.240	0.240

Table 5.5: The absorption, scattering, and anisotropy coefficients calculated by the inverse Monte Carlo program in which the attenuation coefficient was obtained using the following parameters: g=0.5 and 0.875, albedo=0.9 and 0.99, and μ_s=1.0 mm^{-1}, and optical depth=1,2,4, and 8.

Inverse Monte Carlo Output – Mismatched Boundaries, $\mu_s = 1.0$ mm^{-1}			
Optical Depth	μ_a (mm^{-1})	μ_s (mm^{-1})	g
$\mu_s = 1.0$ mm^{-1}, $\mu_a = 0.111$ mm^{-1}, Albedo = 0.9 ; g = 0.875			
1	0.118	0.993	0.84
2	0.117	0.995	0.86
4	0.110	1.00	0.87
8	0.109	1.00	0.88
$\mu_s = 1.0$ mm^{-1}, $\mu_a = 0.010$ mm^{-1}, Albedo = 0.99 ; g = 0.875			
1	0.020	0.990	0.84
2	0.010	1.000	0.87
4	0.010	1.000	0.88
8	0.010	1.000	0.88
$\mu_s = 1.0$ mm^{-1}, $\mu_a = 0.111$ mm^{-1}, Albedo = 0.9 ; g = 0.5			
1	0.125	0.987	0.42
2	0.114	0.997	0.48
4	0.110	1.00	0.50
8	0.112	0.999	0.51
$\mu_s = 1.0$ mm^{-1}, $\mu_a = 0.010$ mm^{-1}, Albedo = 0.99 ; g = 0.5			
1	0.017	0.993	0.43
2	0.012	0.998	0.46
4	0.010	1.000	0.49
8	0.009	1.001	0.47

5.5 Experimental validation of the optical property measurement system

5.5.1 Purpose

The validity of the single-integrating sphere optical property measurement system combined with the inverse Monte Carlo program was evaluated by measuring the optical

properties of Intralipid 10% at different concentrations at 632.8, 830, 940, and 980 nm. The results are compared with those found in the literature.

5.5.2 Published optical properties of Intralipid 10%

Intralipid 10% (Baxter Healthcare Corp., Clintec Nutrition Division, Deerfield, IL) is a fatty emulsion that consists of soybean oil (10.0 g / 100 mL solution) miscelles that are encased in a monolayer of phospholipids (1.2 g / 100 mL solution) taken from powdered egg yolk and suspended in a glycerin-water solution (2.25 g / 100 mL solution). Intralipid 10% is a highly-scattering medium with little absorption in the visible and near-infrared wavelengths (Moes *et al* 1989, Flock *et al* 1992, Choukeife and L'Huillier 1999, Xu *et al* 2003, Autiero *et al* 2005, van Staveren *et al* 1991, Driver *et al* 1989, Flock *et al* 1987, Zhang *et al* 2004). The refractive index of Intralipid 10% is approximately 1.33, regardless of the concentration (Drakaki *et al* 2005). The published values that are used for comparison with our measurements are summarized below.

Van Staveren *et al* 1991:

Van Staveren *et* al used a combination of collimated transmittance measurement, the added absorber technique, and the principles of Mie theory to solve for the optical properties of Intralipid 10%. According to their data, the scattering coefficient increases linearly with the concentration with the following wavelength dependence:

$$\mu_S(\lambda) = 0.0152 \cdot c \cdot \lambda^{-2.4863} \qquad \text{Eq.5.13}$$

where $\mu_s(\lambda)$ is the scattering coefficient (mm^{-1}), c is the concentration (mL L^{-1}) and λ is the wavelength in micrometers. The scattering coefficient at 632.8, 830, 940, and 980

nm is 0.04742, 0.02416, 0.01773, and 0.01598 (mL L^{-1})$^{-1}$ mm^{-1}, respectively. The anisotropy coefficient is independent of concentration with the following wavelength dependence:

$$g(\lambda) = 1.1 - 0.58\lambda \qquad \text{Eq.5.14}$$

where λ is the wavelength in micrometers. The anisotropy coefficient at 632.8, 830, 940, and 980 nm is 0.796, 0.619, 0.555, and 0.532, respectively.

Moes *et al* 1989:

Moes *et al* used the diffusion approximation along with the added absorber technique to solve for the optical properties of Intralipid 10% at 632.8 nm. According to their measurements, the scattering, absorption, and anisotropy coefficient at 632.8 nm are 0.0386 (mL L^{-1})$^{-1}$ mm^{-1}, 0.000057 (mL L^{-1})$^{-1}$ mm^{-1}, and 0.71, respectively.

5.5.3 Experimental procedure

The optical properties of Intralipid 10% were measured at the following concentrations and wavelengths with the single integrating sphere experimental set-up described in section 5.3.2:

a)   1mL / 100 mL, 1 mL / 49 mL, and 1 mL / 32 mL water @ 632.8 nm

b)   2,4,6,8,10 mL / 200 mL water @ 830, 940, and 980 nm

Experiments were conducted with the 830, 940, and 980 nm lasers described in section 5.3.2 and with a 632.8 nm Helium-Neon laser (Metrologic Inc., West Deptford, NJ). The concentrations were selected to allow comparison with the data of van Staveren *et al*

(1991) and Moes *et al* (1989). The 830, 940, and 980 nm lasers were chosen since the optical properties of the porcine tissue will be obtained at these wavelengths.

The different solutions were produced by diluting Intralipid 10% in distilled water. The solutions were stirred using a magnetic mixer to ensure homogeneity. The refractive index measured with an Abbe refractometer was found to be approximately 1.33 regardless of the concentration. A sample of each solution was collected with a pipette and injected into a 10 mm thick Plexiglas cell (Figure 5.12). The Plexiglas cell was mounted onto the integrating sphere. The diffuse reflectance, diffuse transmittance, and collimated transmittance were measured according to the protocol described in section 5.3. The inverse Monte Carlo program was used to calculate the optical properties. The refractive index of the Plexiglas was assumed to be equal to 1.50 (Smith 2000). The refractive index of the Intralipid 10% solution was assumed to be 1.33. The cell thickness was assumed to be 10 mm. The program was run for collimated irradiance with a beam radius of 0.5 mm.
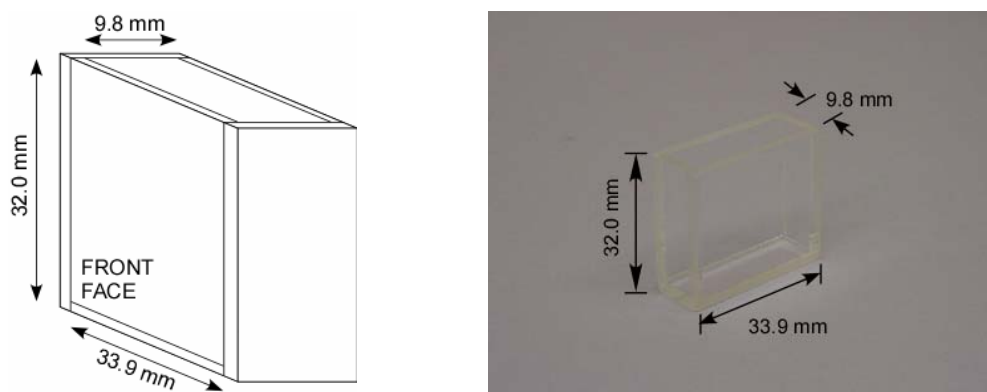
Figure 5.12: The schematic and actual picture of the sample cell used for the optical property measurements of Intralipid 10%. The cell was designed to cover the 22 mm diameter portal hole of the integrating sphere so that no light can escape out of the portal hole without propagating through the sample. The cell is made of plexiglass with inner dimensions of 33.9 x 32 x 9.8 mm. The wall thickness is approximately 2.86 mm.

To calculate the attenuation coefficient (μ_t) from the collimated transmittance, the transmission losses (K, see equation 5.2) of the Plexiglass cell must be input to the program. The value of K was determined from measurements of the collimated transmittance of the cell filled with purely absorbing (no scattering) solutions of known absorption coefficient and refractive index. The solutions were dilutions of Nigrosin ink (Sigma-Aldrich, product #N4763, St. Louis, MO) and distilled water. Based on these measurements, the value of K was assumed to be 0.750 for all wavelengths (the difference between the values obtained at the three wavelengths was less than 3 %).

Three solutions were prepared and measured at each concentration. One transmittance and reflectance measurement was performed on each solution. A preliminary experiment on two solutions demonstrated that the variability of repeated reflectance and transmittance measurements on the same solution is less than 1%.

5.5.4 Results

The absorption and scattering coefficient of Intralipid 10% solution increase with concentration. A linear regression of the scattering coefficient as a function of concentration gives a slope of 39.08, 22.54, 19.21, 17.86 mm^{-1} (mL L^{-1})$^{-1}$ at 632.8, 830, 940, and 980 nm, respectively (Figure 5.13, Table 5.6). For the absorption coefficient, the slopes of the linear regressions are 0.128, 0.407, 0.375 mm^{-1} (mL L^{-1})$^{-1}$ at 830, 940, and 980 nm, respectively (Figure 5.13, Table 5.6). At 632.8 nm, the absorption coefficient was negligible. The scattering anisotropy coefficient was independent of concentration, with values of 0.70±0.01 at 632.8 nm, 0.66±0.10 at 830 nm, 0.61±0.15 at 940 nm, and 0.61±0.09 at 980 nm.

Table 5.6: Results of the experiments at 632.8, 830, 940, and 980 nm. The reflectance and transmittance values are the average of measurements obtained on three different samples. The absorption and scattering coefficient increases with concentration. The scattering anisotropy coefficient was independent of concentration, with average values of 0.70±0.01 at 632.8 nm, 0.66±0.10 at 830 nm, 0.61±0.15 at 940 nm, and 0.61±0.09 at 980 nm

INTRALIPID 10% IN DISTILLED WATER AT 632.8, 830, 940, AND 980 nm						
632.8 nm						
Conc. mL/mL	Rcd	Tcd	Tc	μ_a (mm^{-1})	μ_s (mm^{-1})	g
1 / 100	0.1277	0.3162	0.0141	0.004	0.401	0.71
1 / 49	0.2545	0.2125	0.0000	0.007	0.849	0.70
1 / 32	0.3438	0.1750	0.0000	0.007	1.135	0.69
830 nm						
Conc mL/200mL	Rcd	Tcd	Tc	μ_a (mm^{-1})	μ_s (mm^{-1})	g
2	0.1090	0.3553	0.0665	0.0007	0.250	0.67
4	0.1965	0.2698	0.0053	0.003	0.502	0.66
6	0.2812	0.2088	0.0004	0.005	0.768	0.63
8	0.3499	0.1795	0.0001	0.006	0.918	0.80
10	0.3896	0.1615	0.0001	0.008	0.939	0.52
940 nm						
Conc mL/200mL	Rcd	Tcd	Tc	μ_a (mm^{-1})	μ_s (mm^{-1})	g
2	0.0847	0.2882	0.1200	0.009	0.182	0.54
4	0.1388	0.2446	0.0204	0.013	0.359	0.85
6	0.2047	0.1850	0.0026	0.016	0.567	0.58
8	0.2468	0.1486	0.0003	0.017	0.782	0.62
10	0.3016	0.1323	0.0001	0.015	0.902	0.44
980 nm						
Conc mL/200mL	Rcd	Tcd	Tc	μ_a (mm^{-1})	μ_s (mm^{-1})	g
2	0.0573	0.1951	0.1060	0.034	0.170	0.53
4	0.0901	0.1650	0.0200	0.041	0.333	0.77
6	0.1323	0.1168	0.0037	0.041	0.502	0.57
8	0.1647	0.0858	0.0005	0.045	0.708	0.60
10	0.1896	0.0691	0.0001	0.048	0.842	0.58
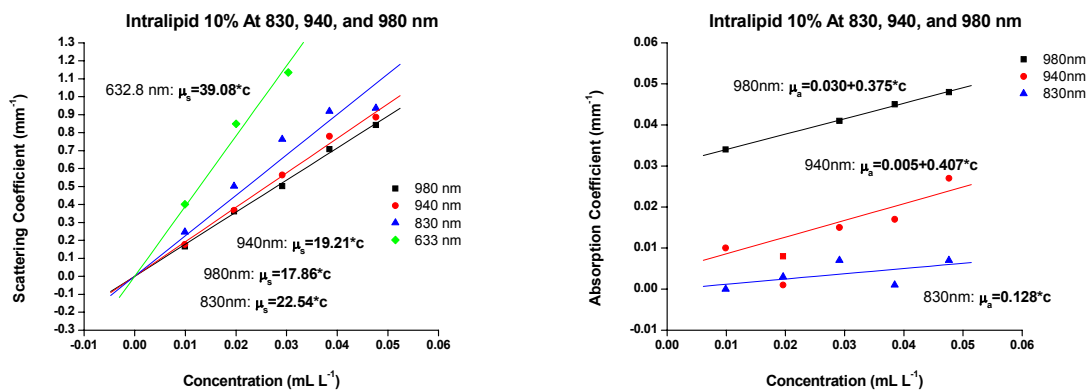
Figure 5.13: Scattering (left) and absorption coefficient(right) at 632.8, 830, 940, and 980 nm as a function of the concentration of Intralipid 10% in distilled water. The absorption coefficient at 632.8 nm is not shown (right) because absorption at 632.8 nm is negligible.

5.5.5 Discussion

The optical properties of Intralipid 10% solutions measured with our system are in good agreement with the values published by van Staveren *et al* (1991) and by Moes *et al* (1989) (Table 5.7 and 5.8). As in their studies, we find that the absorption and scattering coefficient increase linearly with the concentration and the scattering anisotropy coefficient is independent of concentration. There is close agreement of the value of the scattering coefficients as a function of concentration in mm^{-1} $(mL\ L^{-1})^{-1}$. The difference between their values of the scattering anisotropy coefficient and our values is less than 0.02. The difference in the absorption coefficient is larger, particularly at 632.8 and 940 nm. The larger error at 632.8 nm is due to the extremely small value of the absorption coefficient at 632.8 nm. The larger difference at 940 nm is caused by a larger fluctuations of the power output of the 940 nm laser compared to the other lasers. The power fluctuations make it more difficult to precisely measure the collimated transmittance. The measurement error will introduce a larger relative error on the

absorption coefficient than on the scattering coefficient because of the small value of the absorption coefficient.

Even though Intralipid 10% is often used as a tissue phantom to validate optical property measurement systems, we did not expect the values of the optical properties to exactly match the published values. There is a large variation in the published values of the optical properties of the Intralipid 10% in the literature. For instance, according to Flock *et al* (1992), the attenuation, reduced scattering, absorption, and scattering anisotropy coefficient at 632.8 nm from different publications ranged from 344 to 550 cm^{-1}, 60 to 185 cm^{-1}, 0.0029 to 0.57 cm^{-1}, and 0.55 to 0.83, respectively. This variability is due in part to differences in the composition of Intralipid 10% solution available from different suppliers, which may affect the optical properties. Our values of the scattering coefficient and anisotropy scattering coefficient are within the expected range. The accuracy of the calculated absorption coefficient is more difficult to evaluate.

In theory, the absorption coefficient at low concentrations of Intralipid 10%, such as the ones used in this experiment, should be approximately equal to the absorption coefficient of water. The absorption coefficient of water at 632.8 nm is essentially zero. The absorption coefficients at 830nm, 940nm, and 980nm are 0.003, 0.032, and 0.043 mm^{-1}, respectively. The values obtained for the absorption coefficient of Intralipid 10% at the four highest concentrations at 980 nm are close to the absorption coefficient of water (0.041 to 0.048 mm^{-1}). At 940 nm, the values obtained at the four highest concentrations (0.013-0.017 mm^{-1}) are lower than expected. At 830 nm, the values for the four highest concentrations ranged from 0.003 to 0.008 mm^{-1}. These results suggest that the inverse

program gives a reliable value of the absorption coefficient as long as the scattering coefficient is high (large albedo).

5.6 Optical property measurements of ex-vivo porcine tissue

5.6.1 Purpose

The purpose of this part of the study was to measure the optical properties of ex-vivo porcine tissue. The optical properties will be input into the optical-thermal model developed in chapter 4 to predict the temperature and coagulation zone produced during laser interstitial thermotherapy in ex-vivo fibro-fatty tissue (see chapter 6). The results of these simulations will be compared to experimental data to validate the optical-thermal model. The following studies were conducted:

a)   Measurement of the optical properties of native ex-vivo fibro-fatty porcine mammary chain tissue.

Table 5.7: Comparison of the optical properties of Intralipid 10% solutions measured at 632.8, 830, 940, and 980 nm with the values published by van Staveren et al 1991:

Wavelength (nm)	Optical Properties	Van Staveren	Current Study
830	μ_a mm^{-1} (mL L^{-1})$^{-1}$	0.14	0.13
	μ_s mm^{-1} (mL L^{-1})$^{-1}$	24.2	22.5
	g	0.62	0.66
940	μ_a mm^{-1} (mL L^{-1})$^{-1}$	0.24	0.41
	μ_s mm^{-1} (mL L^{-1})$^{-1}$	17.7	19.2
	g	0.55	0.61
980	μ_a mm^{-1} (mL L^{-1})$^{-1}$	0.29	0.38
	μ_s mm^{-1} (mL L^{-1})$^{-1}$	16.0	17.9
	g	0.53	0.61
632.8	μ_a mm^{-1} (mL L^{-1})$^{-1}$	NA	NA
	μ_s mm^{-1} (mL L^{-1})$^{-1}$	47.4	39.1
	g	0.80	0.70

Table 5.8: Comparison of the optical properties of Intralipid 10% solution measured at 632.8 nm at three different concentrations with the values published by Moes et al 1989.

INTRALIPID 10% WITH DISTILLED WATER AT 632.8 nm: Comparison with data from Moes *et al* 1989						
Conc / 100 mL	μ_s (mm^{-1}) Lit	μ_s (mm^{-1}) Calc	μ_a (mm^{-1}) Lit	μ_a (mm^{-1}) Calc	g Lit	G Calc
1	**0.386**	0.401	**0.000**	0.004	**0.71**	0.71
2.04	**0.788**	0.849	**0.001**	0.007	**0.71**	0.70
3.13	**1.206**	1.135	**0.002**	0.007	**0.71**	0.69

b)   Measurement of the effect of refrigeration and freezing on the optical properties of

the tissue

c)   Measurement of the effect of thermal coagulation on the optical properties of the

tissue.

5.6.2 Measurement of the optical properties of native tissue

5.6.2.1 Experimental procedure

The single integrating sphere set-up described in the previous sections was used to

measure the optical properties of homogenized ex-vivo porcine mammary chain tissue.

Ex-vivo porcine mammary chain fibro-fatty tissue samples were obtained from six

euthanized pigs at the University of Miami Division of Veterinary Resources as part of a

tissue sharing protocol. These tissue specimens are comprised of a top layer of muscle, a

middle layer consisting of the glandular fatty mammary chain tissue, and a thin, bottom

layer of skin. The thickness of the fibro-fatty tissue layer is approximately 1-1.5 cm.

After dissection from the euthanized pig, the tissue was stored in a freezer at -25°C for a

total time ranging from 3 to 8 months. The effect of freezing on the optical properties is discussed in section 5.6.3.

Prior to an experiment, the tissue is thawed at room temperature. A 3 cm x 3 cm square sample is cut out and divided into smaller pieces to facilitate the preparation. The muscle and skin layers are removed from each piece. The remaining glandular fibro-fatty tissue is ground using a manual meat grinder to be able to create tissue samples of a desired size and uniform thickness. The processed samples are placed in jars and stored in a refrigerator at 11°C for up to 9 days.

Before the experiment, the ground tissue is removed from the jars and placed in a 1 mm thick glass cell (Figure 5.14) using the following protocol:

a)   A 1mm thick vinyl spacer is glued onto a 50 x 50 mm glass slide (B351, Eastman Kodak, Rochester, NY) while taking care to remove any excess glue. The spacer forms a square rim that will contain the tissue in its center.

b)   The homogenized tissue is placed on the glass slide within the vinyl rim.

c)   A second glass slide is then placed on top of the rim to sandwich the tissue. The cell is slighty compressed to ensure that there is good contact between the spacer and the glass slides. This step ensures that the sample has uniform thickness.

d)   Excess tissue escaping through the top of the cell during compression is removed with a blade.

e)   The glass slides are bonded together using commercial tape.

f)   The thickness of the cell is measured with a caliper.
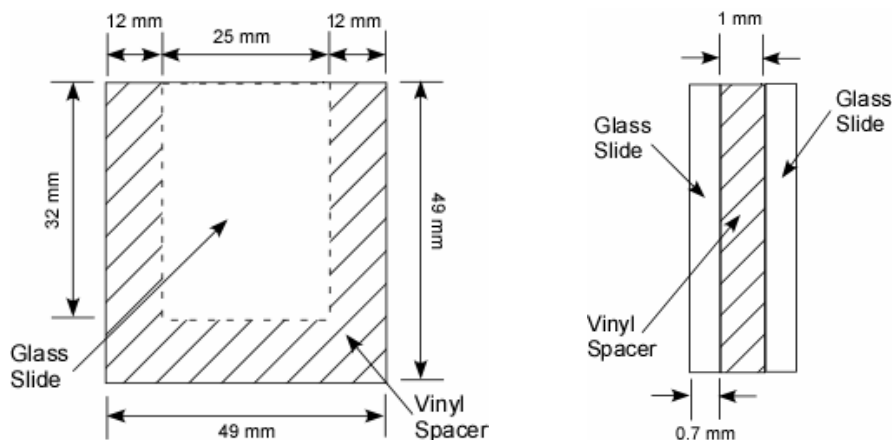
Figure 5.14: The front view (left) and the side view (right) of the tissue sample cell. The cell consists of a 49 x 49 x 1 mm thick clear vinyl sheet (US Plastics Corp, Lima, OH) sandwiched between two 49 x 49 x 0.7 mm glass cover slides (Eastman Kodak, Rochester, NY). The middle vinyl sheet acts as a spacer ensuring that the tissue thickness is 1 mm (±0.2 mm). The vinyl sheet has a 25 x 32 mm square cut out at the center. The tissue sample is sandwiched between the two glass slides in this square.

The cell containing the tissue is then mounted on the integrating sphere and the reflectance and transmittance are measured using the experimental protocol described in section 5.3.3. Each sample is measured once at 830, 940, and 980 nm. After measurements with the three wavelengths, the tissue is taken out of the cell. The cell is cleaned and re-used with the other samples from the same animal. A different cell was used for each animal. Three different ground tissue samples were measured for pigs 1-4, and six samples were measured for pigs 5-6.

The average value of the reflectance and transmittance are calculated for each pig and input into the inverse Monte Carlo program to calculate the optical properties. The inverse Monte Carlo program was run with the following input parameters: K=0.864 (determined from transmission measurements through the cell filled with water), beam radius=1.54 mm, refractive index of tissue = 1.4 (Tuchin 2000), refractive index of glass

slide = 1.60 (determined from transmission measurements through a glass slide), and average thickness of the samples.

5.6.2.2 Results

The average diffuse reflectance, diffuse transmittance, and collimated transmittance for each of the six pigs at each wavelength are shown in Table 5.9, together with the calculated optical properties (μ_a, μ_s, g, μ_t, μ_{eff}) (Figure 5.15-5.16). The diffuse reflectance, diffuse transmittance, and collimated transmittance were highest at 830 nm and lowest at 980 nm. The standard deviation was less than 10% of the average for all reflectance and transmittance measurements on the same animal.

On average, the absorption coefficient and effective attenuation coefficient are lowest at 830 nm and highest at 980nm. The scattering coefficient and the scattering anisotropy coefficient are approximately equal at the three wavelengths (Table 5.9, Figure 5.15). At all three wavelengths, the scattering coefficient was more than one order of magnitude larger than the absorption coefficient. The average albedo ranged from 0.996 at 980 nm to 0.999 at 830 nm. With the exception of two pigs at one wavelength (pig #3 at 830nm; pig #5 at 940nm), the variability of the optical properties between the six animals was small. The results are discussed in section 5.6.5.

5.6.3 Effect of freezing and refrigeration on the optical properties
5.6.3.1. Purpose

The whole pig tissue was stored in the freezer for up to nine months before being used in the experiments described in the previous section. The ground tissue samples

were refrigerated for up to nine days. The goal of the following experiments was to determine if freezing and refrigeration have an effect on the optical properties of the ex-vivo porcine tissue. These experiments will determine if freezing of the samples is an acceptable practice or if the samples should, in the future, be fresh prior to the optical property measurements.

5.6.3.2 Experimental procedure

One piece of mammary chain tissue obtained from one pig immediately after euthanasia was used. One half of the tissue was processed immediately (fresh tissue) using the same protocol as in the previous section and stored in a jar. To evaluate the effect of refrigeration, reflectance and transmittance measurements were recorded on six samples from the ground fresh tissue immediately after processing (no refrigeration) and after 37 hours (1.5 days) and 312 hours (13 days) of refrigeration.

To evaluate the effect of freezing, the second half of the whole tissue was frozen for three days (frozen tissue). After 3 days, the frozen tissue was thawed at room temperature and prepared using the same protocol as for the fresh tissue. The reflectance and transmittance of six samples were measured immediately (no refrigeration) and after 24, 48, 72, and 216 hours of refrigeration.

Independent two sample t-tests (ORIGIN 7.0, OriginLab, Northampton, MA) (significance at $p<0.05$) were performed to compare the reflectance and transmittance of the fresh tissue, the refrigerated tissue, and the frozen tissue.

(a)
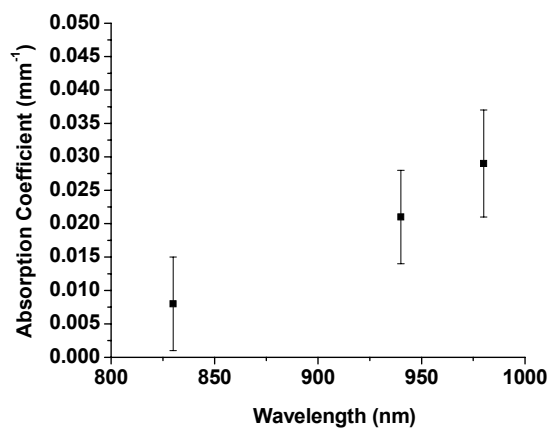
(b)
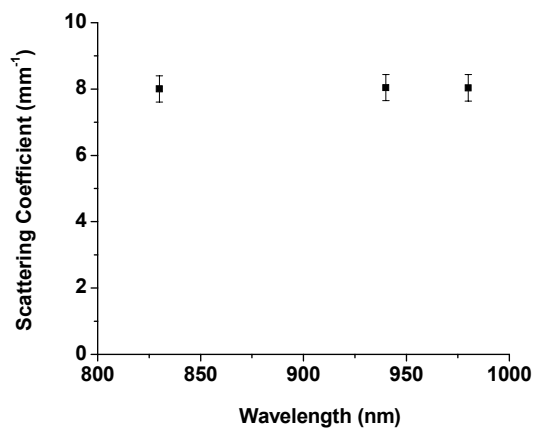
(c)
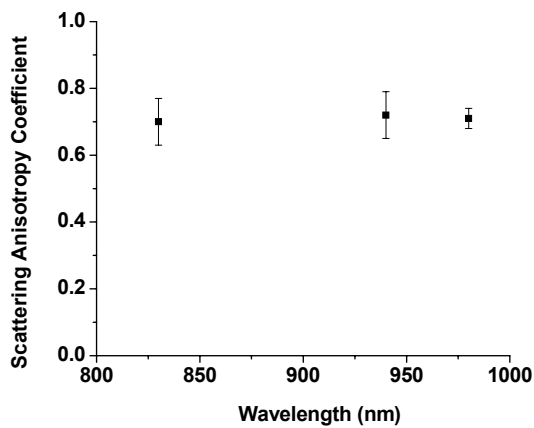
Figure 5.15: The (a) absorption, (b) scattering, and (c) scattering anisotropy coefficient of native ex-vivo porcine mammary chain tissue.

Table 5.9: The average diffuse reflectance (R$_{cd}$), diffuse transmittance (T$_{cd}$), and collimated transmittance (T$_c$) for each pig. The optical properties (μ$_a$, μ$_s$, g) were calculated for each pig from these average values using the inverse Monte Carlo program.

		Optical Properties of Native Ex-Vivo Fibro-Fatty Mammary Chain Tissue						
			830 nm					
Pig #	Rcd	Tcd	Tc	μ$_a$ (mm^{-1})	μ$_s$ (mm^{-1})	g	μ$_t$ (mm^{-1})	μ$_{eff}$ (mm^{-1})
1	0.476±0.005	0.356±0.010	0.000164±0.000003	0.005	7.785	0.62	7.790	0.220
2	0.483±0.016	0.370±0.014	0.000179±0.000012	0.002	8.000	0.64	8.002	0.126
3	0.435±0.008	0.387±0.007	0.000165±0.000002	0.021	7.361	0.70	7.382	0.377
4	0.477±0.004	0.390±0.005	0.000175±0.000003	0.004	8.501	0.80	8.505	0.135
5	0.456±0.009	0.380±0.025	0.000174±0.000011	0.005	8.257	0.68	8.262	0.207
6	0.428±0.024	0.374±0.017	0.000171±0.000009	0.012	8.110	0.76	8.122	0.261
AVG	**0.459±0.023**	**0.376±0.012**	**0.000171±0.000006**	**0.008**	**8.002**	**0.70**	**8.011**	**0.221**
STDEV				0.007	0.396	0.07	0.391	0.092
			940 nm					
1	0.427±0.021	0.352±0.04	0.000154±0.000011	0.023	7.825	0.67	7.848	0.420
2	0.435±0.0.16	0.356±0.017	0.000156±0.000006	0.020	8.112	0.67	8.132	0.398
3	0.391±0.004	0.375±0.004	0.000158±0.000003	0.018	7.402	0.74	7.420	0.320
4	0.421±0.025	0.361±0.012	0.000162±0.000007	0.021	8.561	0.69	8.582	0.408
5	0.421±0.041	0.380±0.052	0.000185±0.000049	0.013	8.190	0.85	8.203	0.219
6	0.393±0.034	0.359±0.012	0.000159±0.000007	0.034	8.157	0.71	8.191	0.494
AVG	**0.415±0.018**	**0.364±0.011**	**0.000162±0.000011**	**0.021**	**8.041**	**0.72**	**8.063**	**0.377**
STDEV				0.007	0.391	0.07	0.392	0.095
			980 nm					
1	0.420±0.002	0.344±0.006	0.000156±0.000002	0.026	7.810	0.66	7.836	0.456
2	0.420±0.022	0.370±0.019	0.000168±0.000008	0.022	8.040	0.70	8.062	0.398
3	0.384±0.008	0.380±0.004	0.000160±0.000003	0.025	7.384	0.74	7.409	0.380
4	0.421±0.005	0.366±0.010	0.000169±0.000010	0.023	8.516	0.71	8.539	0.419
5	0.387±0.012	0.355±0.020	0.000160±0.000009	0.038	8.306	0.74	8.344	0.499
6	0.378±0.033	0.354±.015	0.000161±0.000007	0.039	8.140	0.73	8.179	0.511
AVG	**0.402±0.020**	**0.362±0.013**	**0.000162±0.000005**	**0.029**	**8.033**	**0.71**	**8.062**	**0.444**
STDEV				0.008	0.398	0.03	0.400	0.054
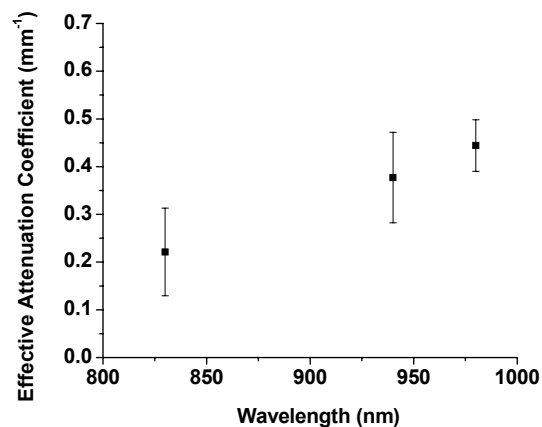
Figure 5.16: The effective attenuation coefficient of ex-vivo porcine mammary chain tissue

5.6.3.3 Results

The average diffuse reflectance, diffuse transmittance, and collimated transmittance of the fresh tissue before and after refrigeration are given in Table 5.10. Refrigeration caused a statistically significant increase in the diffuse reflectance and a statistically decrease of the diffuse and collimated transmittance at 830 and 980 nm. The same trend was observed at 940 nm, but the difference was not statistically significant, probably due to the larger variability of the data. The difference in the values measured before and after refrigeration is less than 10%. There was no statistically significant difference between the measurements recorded after 37 and 312 hours of refrigeration.

The average diffuse reflectance, diffuse transmittance, and collimated transmittance of the tissue processed after three days of freezing and measured immediately and after 1-12 days of refrigeration are given in Table 5.11. On this tissue, refrigeration had no effect on the reflectance and transmittance.

www.manaraa.com

The diffuse reflectance and transmittance of the fresh tissue and of the tissue measured after three days of freezing (with no refrigeration) are compared in Table 5.12. Freezing produced a statistically significant increase of the diffuse reflectance. The diffuse and collimated transmittance remained unchanged. The change induced by freezing was less than 10%. The results are discussed in section 5.6.5.

5.6.4. Effect of coagulation on the optical properties

5.6.4.1 Purpose

During laser interstitial thermotherapy, photocoagulation alters the structure of the tissue. These changes could have an effect on the optical properties, and thus affect both the light distribution and the thermal response of the tissue. The goal of the following experiments was to quantify the effect of coagulation on the optical properties of fibro-fatty porcine tissue.

Table 5.10: The average diffuse reflection, diffuse transmission, and collimated transmission at 830, 940, and 980 nm for fresh ex-vivo porcine mammary chain tissue refrigerated at 0, 37, and 312 hours. * signifies statistical significance.

Fresh vs Refrigerated Tissue – No Freezing			
Diffuse Reflectance (R_{cd})			
λ (nm)	0 hours	37 hours	312 hours
830	0.412±0.011	0.434±0.018 *	0.441±0.020 *
940	0.362±0.004	0.392±0.040	0.389±0.025 *
980	0.363±0.006	0.381±0.016 *	0.387±0.020 *
Diffuse Transmittance (T_{cd})			
830	0.393±0.009	0.373±0.014 *	0.388±0.027
940	0.365±0.017	0.363±0.027	0.370±0.044
980	0.378±0.007	0.360±0.013 *	0.381±0.027
Collimated Transmittance (T_c)			
830	$1.71 \times 10^{-4} \pm 4.00 \times 10^{-6}$	$1.63 \times 10^{-4} \pm 5.00 \times 10^{-6}$ *	$1.66 \times 10^{-4} \pm 1.00 \times 10^{-5}$
940	$1.61 \times 10^{-4} \pm 1.30 \times 10^{-6}$	$1.48 \times 10^{-4} \pm 6.00 \times 10^{-6}$	$1.57 \times 10^{-4} \pm 1.10 \times 10^{-5}$
980	$1.61 \times 10^{-4} \pm 3.00 \times 10^{-6}$	$1.53 \times 10^{-4} \pm 6.00 \times 10^{-6}$ *	$1.62 \times 10^{-4} \pm 1.30 \times 10^{-5}$

Table 5.11: The average diffuse reflection, diffuse transmission, and collimated transmission at 830, 940, and 980 nm for ex-vivo porcine tissue samples that were frozen for three days and thawed. The tissue was refrigerated at 0, 24, 48, 72, and 216 hours. Refrigeration after freezing and thawing did not produce any statistically significant change in the reflectance and transmittance.

Effect of Refrigeration After Freezing and Thawing					
Diffuse Reflectance (R_{cd})					
λ (nm)	0 hours	24 hours	48 hours	72 hours	216 hours
830	0.440±0.007	0.438±0.009	0.441±0.012	0.433±0.021	0.429±0.024
940	0.400±0.018	0.396±0.034	0.380±0.019	0.395±0.051	0.405±0.020
980	0.379±0.016	0.388±0.009	0.394±0.019	0.378±0.017	0.375±0.025
Diffuse Transmittance (T_{cd})					
830	0.387±0.011	0.374±0.011	0.385±0.019	0.377±0.008	0.395±0.016
940	0.383±0.040	0.364±0.030	0.350±0.023	0.381±0.031	0.392±0.040
980	0.376±0.014	0.371±0.010	0.370±0.011	0.372±0.006	0.397±0.020
Collimated Transmittance (T_c)					
830	$1.70 \times 10^{-4} \pm 8.00 \times 10^{-6}$	$1.64 \times 10^{-4} \pm 5.00 \times 10^{-6}$	$1.69 \times 10^{-4} \pm 1.40 \times 10^{-4}$	$1.63 \times 10^{-4} \pm 3.00 \times 10^{-6}$	$1.72 \times 10^{-4} \pm 7.00 \times 10^{-6}$
940	$1.68 \times 10^{-4} \pm 2.20 \times 10^{-5}$	$1.60 \times 10^{-4} \pm 8.00 \times 10^{-6}$	$1.54 \times 10^{-4} \pm 9.00 \times 10^{-6}$	$1.61 \times 10^{-4} \pm 5.00 \times 10^{-6}$	$1.70 \times 10^{-4} \pm 1.60 \times 10^{-5}$
980	$1.71 \times 10^{-4} \pm 2.60 \times 10^{-5}$	$1.61 \times 10^{-4} \pm 5.00 \times 10^{-6}$	$1.60 \times 10^{-4} \pm 6.00 \times 10^{-6}$	$1.60 \times 10^{-4} \pm 3.00 \times 10^{-6}$	$1.72 \times 10^{-4} \pm 1.20 \times 10^{-5}$

Table 5.12: The average diffuse reflection, diffuse transmission, and collimated transmission at 830, 940, and 980 nm for both fresh ex-vivo porcine tissue samples and those frozen for three days and thawed. Both tissue groups were not refrigerated prior to use. * signifies statistical significance.

Fresh vs 3 Days Frozen and Thawed – No Refrigeration		
λ (nm)	Unfrozen	Frozen
Diffuse Reflectance (R_{cd})		
830	0.412±0.011	0.440±0.007 *
940	0.362±0.004	0.400±0.018 *
980	0.363±0.006	0.379±0.016 *
Diffuse Transmittance (T_{cd})		
830	0.393±0.009	0.387±0.011
940	0.365±0.017	0.383±0.040
980	0.378±0.007	0.376±0.014
Collimated Transmittance (T_c)		
830	$1.71 \times 10^{-4} \pm 4.00 \times 10^{-6}$	$1.70 \times 10^{-4} \pm 8.00 \times 10^{-6}$
940	$1.61 \times 10^{-4} \pm 1.30 \times 10^{-5}$	$1.68 \times 10^{-4} \pm 2.20 \times 10^{-5}$
980	$1.61 \times 10^{-4} \pm 3.00 \times 10^{-6}$	$1.71 \times 10^{-4} \pm 2.60 \times 10^{-5}$

5.6.4.2 Experimental procedure

The optical properties of tissue obtained from the same six pigs that were used for the experiments of section 5.6.2 were measured after coagulation. The pig tissue was stored in the freezer between 3 months and 8 months prior to use. The pig tissue was taken out of the freezer and allowed to thaw at room temperature. After thawing, two 9 x 9 cm square samples were excised. The muscle layer of the two samples was removed with a meat slicer, leaving the skin and fibro-fatty tissue layer.

The square tissue samples are placed in a water bath and pre-heated to 37°C. The two tissue samples are placed on top of each other with the skin facing outward and compressed using a laboratory jack following a procedure described elsewhere (Salas *et al* 2004). A cylindrical diffusing tip optical fiber (Indigo #24, Indigo Corp, Palo Alto, CA) coupled to a 980 nm diode laser system (AOC25, Applied Optronics, South Plainfield, NJ) was placed in between the two samples. The tissue was irradiated at 4.0 W between 5 and 15 minutes to produce coagulation. After irradiation, the optical fiber was removed and the tissue was taken out from the water bath. Coagulated regions of the tissue detected visually by the change in structure and color were excised, processed with the meat grinder, placed in jars, and stored in the refrigerator for up to ten days.

The reflectance and transmittance of two (n=1) to six (n=4) samples were measured for each pig, depending on the amount of coagulated tissue available. The average values of the measurements for each pigs were entered in the inverse Monte Carlo program to calculate the optical properties (attenuation coefficient (μ_t), absorption coefficient (μ_a), scattering coefficient (μ_s), and anisotropy coefficient (g)) using the same input parameters

as for the experiments on the uncoagulated tissue (see section 5.6.2). A two-sample t-test was performed to compare the properties of uncoagulated and coagulated tissue.

5.6.4.3 Results

Table 5.13 and Figures 5.17 and 5.18 show a comparison between the optical properties of the native and coagulated tissue for each pig and at the three wavelengths. The following pigs were excluded from the statistical analysis due to discrepancies in the data: pig #4 at 830 nm, pig #4 at 940nm, and pig #4 and pig #3 at 980 nm. This discrepancy is seen in the absorption coefficient of these pigs. This is most likely due to the inverse Monte Carlo algorithm not providing reliable values for these coefficients at this sample thickness (Table 5.5). Coagulation produced a statistically significant increase in the scattering anisotropy coefficient at 830 and 980 nm. The same increase was observed at 940 nm, but the change was not statistically significant. There was a statistically significant decrease in the absorption and effective attenuation coefficient at 980 nm. Coagulation also produced a decrease in the value of the effective attenuation coefficient at 830 and 940 nm, but the change was not statistically significant. This decrease is expected since the effective attenuation coefficient is dependent on the scattering anisotropy coefficient, which was found to increase significantly. The results are discussed in section 5.6.5.

5.6.5 Discussion

In this chapter, our purpose was to quantify the following parameters:

a)   The optical properties of native ex-vivo porcine tissue

(a)
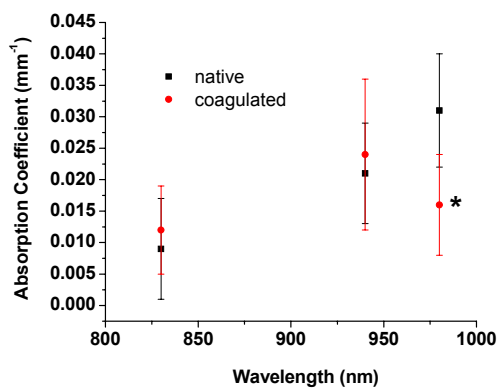
(b)
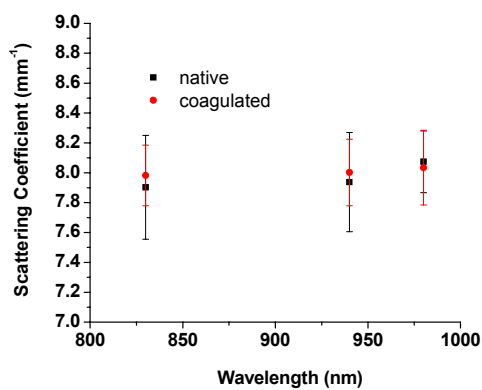
(c)
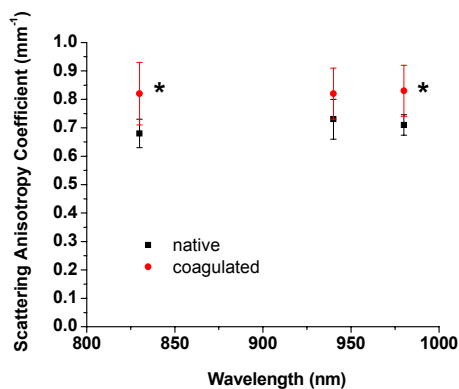
Figure 5.17: The (a) absorption, (b) scattering, and (c) scattering anisotropy coefficient of native and coagulated ex-vivo porcine tissue. * = statistical significance
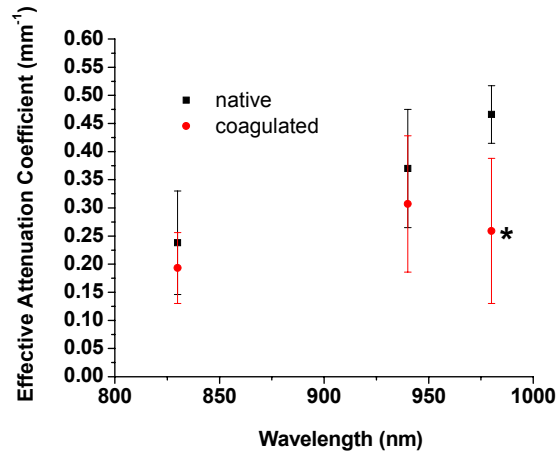
Figure 5.18: The effective attenuation coefficient of native and coagulated ex-vivo porcine tissue. * = statistical significance

b)   The effect of freezing and refrigeration on the optical properties

c)   The effect of coagulation on the optical properties

The scattering coefficient and the scattering anisotropy coefficient (μ_s and g) of ex-vivo porcine mammary chain tissue were found to be essentially the same at 830, 940 and 980 nm with average values of μ_s = 8.03 mm^{-1} and g=0.71 (see Table 5.12). The absorption coefficient was found to be 0.008 mm^{-1} at 830 nm, 0.021 mm^{-1} at 940 nm, and 0.029 mm^{-1} at 980 nm. These results suggest that differences in the light distribution in *ex-vivo* porcine tissue during LITT are only due to differences in the absorption coefficient. Since the absorption coefficient at 940 and 980 nm are similar, the light and temperature distribution during LITT should be similar at these two wavelengths. These results are consistent with the temperature distributions observed after LITT at the three wavelengths in our experimental model (Salas *et al* 2002).

Table 5.13: The scattering coefficient (mm^{-1}) of coagulated and uncoagulated ex-vivo porcine tissue at 830, 940, and 980 nm. Three simulations were performed for the average diffuse reflectance and transmittance at each wavelength and tissue type. The pigs highlighted in yellow were excluded from the analysis due to discrepancies in the absorption coefficient, which may be due to the inverse Monte Carlo program. * signifies statistical significance.

Native vs Coagulated Ex-Vivo Porcine Fibro-Fatty Tissue										
830 nm										
	μ_a (mm^{-1})		μ_s (mm^{-1})		g		μ_t (mm^{-1})		μ_{eff} (mm^{-1})	
Pig #	Native	Coagulated	Native	Coagulated	Native	Coagulated	Native	Coagulated	Native	Coagulated
1	0.005	0.002	7.785	7.679	0.62	0.73	7.790	7.681	0.220	0.108
2	0.002	0.009	8.0	8.08	0.64	0.71	8.002	8.089	0.126	0.248
3	0.021	0.015	7.361	7.868	0.7	0.81	7.382	7.883	0.377	0.262
4	0.004	0.047	8.501	7.045	0.80	0.8	8.505	7.092	0.135	0.453
5	0.005	0.019	8.257	8.131	0.68	0.94	8.262	8.150	0.207	0.172
6	0.012	0.016	8.11	8.151	0..76	0.92	8.122	8.167	0.261	0.176
AVG	0.009	0.012	7.903	7.982	0.68	0.82 *	7.912	7.994	0.238	0.193
STDEV	0.008	0.007	0.348	0.203	0.05	0.11 *	0.343	0.208	0.092	0.063
940 nm										
1	0.023	0.025	7.825	7.722	0.67	0.76	7.848	7.747	0.420	0.376
2	0.020	0.020	8.112	8.102	0.67	0.72	8.132	8.122	0.398	0.367
3	0.018	0.044	7.402	7.803	0.74	0.82	7.420	7.847	0.320	0.436
4	0.021	0.086	8.561	6.941	0.69	0.84	8.582	7.027	0.408	0.557
5	0.013	0.019	8.190	8.181	0.85	0.93	8.203	8.200	0.219	0.182
6	0.034	0.011	8.157	8.2	0.71	0.89	8.191	8.211	0.494	0.173
AVG	0.021	0.024	7.937	8.002	0.73	0.82	7.959	8.025	0.370	0.307
STDEV	0.008	0.012	0.332	0.223	0.07	0.09	0.334	0.214	0.105	0.121
980 nm										
1	0.026	0.018	7.810	7.673	0.66	0.78	7.836	7.691	0.456	0.302
2	0.022	0.027	8.040	8.062	0.70	0.73	8.062	8.089	0.398	0.420
3	0.025	0.001	7.384	7.798	0.74	0.88	7.409	7.799	0.380	0.045
4	0.023	0.217	8.516	6.87	0.71	0.61	8.539	7.087	0.419	1.374
5	0.038	0.010	8.306	8.201	0.74	0.87	8.344	8.211	0.499	0.180
6	0.039	0.010	8.140	8.201	0.73	0.93	8.179	8.211	0.511	0.132
AVG	0.031	0.016 *	8.074	8.034	0.71	0.83 *	8.105	8.051	0.466	0.259 *
STDEV	0.009	0.008	0.207	0.250	0.036	0.090	0.214	0.246	0.051	0.129

To the best of our knowledge, values of the optical properties of porcine adipose tissue have only been published at 632.8 and 789 nm (Arnfield *et al* 1992). The *ex-vivo* porcine tissue was highly scattering at 632.8 nm. Therefore, no measurements could be obtained with our optical property measurement system at 632.8 nm for the collimated and diffuse transmittance. There is no published data for 830, 940, and 980 nm. According to Arnfield *et al*, the absorption coefficients at 632.8 nm and 789 nm are 0.010 to 0.006 mm^{-1}, while the reduced scattering coefficients [$\mu_s' = \mu_s*(1-g)$] at 632.8 nm and 789 nm are 1.54 to 1.36 mm^{-1}, respectively. According to our results, the absorption coefficient and reduced scattering coefficient at 830 nm (close to 789 nm) are 0.008 and 2.4 mm^{-1}. The absorption coefficient is consistent with the value of Arnfield *et al*. The reduced scattering coefficient is approximately twice the value of Arnfield *et al*.

Ex-vivo porcine mammary chain tissue was chosen as a phantom for human breast tissue because of its high fat content. The porcine tissue was expected to have a similar composition, and therefore also similar optical properties, as adipose human breast tissue (see Chapter 2, Section 2.2). Published values of the optical properties of healthy and diseased breast tissue in the near-infrared are summarized in Table 5.14 and 5.15. According to this data, there are no significant differences in the absorption and reduced scattering coefficient between *in-vivo* and *ex-vivo* measurements. The scattering anisotropy coefficient measured *in-vivo* and *ex-vivo* are different. The reduced scattering coefficient ($\mu_s' = \mu_s*(1-g)$) is approximately constant in the near-infrared, with the exception of the data from Troy *et al*, with values ranging from 0.57 (Shah *et al* 2001) to 1.32 mm^{-1} (Peters *et al* 1990) for μ_s'. The values of μ_s' for breast tissue are comparable to the value obtained by Arnfield *et al* for adipose porcine tissue. Compared to the

published studies, except for the study of Cubeddu *et al* (2000), we find lower values of the scattering and scattering anisotropy coefficients, which result in higher values of the reduced scattering coefficient (Cubeddu *et al* 2000). The difference could be due to differences between the properties of the tissue (human breast vs porcine mammary chain tissue) or to the effect of homogenization. The published values of the absorption coefficients of breast tissue are more variable. Our results are within the range of the published data. Interestingly, our values of the scattering anisotropy coefficient agree with the values measured in-vivo by Cubeddu *et al*.

According to the model of chapter 4, the temperature distribution is determined by the effective attenuation coefficient (μ_{eff}). According to Table 5.14 and 5.15, the effective attenuation coefficient of breast tissue in the near-infrared ranges from 0.349 to 0.491 mm^{-1} at 830, 0.458 to 0.483 mm^{-1} at 940 nm, and from 0.458 to 0.636 mm^{-1} at 980 nm for ex-vivo tissue, and from 0.204 to 0.317 mm^{-1} for in-vivo tissue at these three wavelengths.   These values are within the range of the values that we find in our pig tissue (0.221 to 0.444 mm^{-1}). These findings suggest that the mammary chain porcine tissue used in our studies should produce similar temperature distributions to those obtained in human breast tissue.

The main purpose of the optical property measurements was to obtain values of the effective attenuation coefficient at 830, 940, and 980 nm that can be entered in the optical-thermal model to predict the temperature during LITT in *ex-vivo* porcine tissue. There are several factors that may affect the applicability of the measured optical properties. First, the tissue was homogenized using a manual meat grinder and frozen

before measuring the optical properties. In addition, coagulation during LITT may affect

the three optical properties.

Table 5.14: Published optical property measurements of ex-vivo human female breast tissue

Reference	Tissue Preparation	Tissue Type	Thickness (mm)	μ_a (mm^{-1})	μ_s (mm^{-1})	μ_t (mm^{-1})	g	μ_s' (mm^{-1})
			830nm (*: 836nm)					
Peters *et al*	Homogenized	Glandular	1.00	0.050	33		0.96	
Peters *et al*	Homogenized	Adipose	1.00	0.070	30		0.98	
Troy *et al*	Thick slice	Fibrous	1.00	0.067				8.1
Troy *et al**	Thick slice	Fibrous	1.00	0.011				7.3
Key *et al*	Thin frozen section	Fibrous	0.04	0.018		13	0.92	
Key *et al*	Thin frozen section	Adipose	0.04			28	0.95	
			940nm					
Peters *et al*	Homogenized	Glandular	1.00	0.07	26		0.96	
Peters *et al*	Homogenized	Adipose	1.00	0.10	30		0.98	
Key *et al*	Thin frozen section	Fibrous	0.04	0.03		12	0.92	
Key *et al*	Thin frozen section	Adipose	0.04			26	0.95	
			980nm					
Peters *et al*	Homogenized	Glandular	1.00	0.10	25		0.95	
Peters *et al*	Homogenized	Adipose	1.00	0.10	30		0.98	
Key *et al*	Thin frozen section	Fibrous	0.04	0.02		12	0.92	
Key *et al*	Thin frozen section	Adipose	0.04			26	0.95	

Table 5.15: Published optical property measurements of in-vivo human female breast tissue.

Reference	μ_a(mm^{-1})	g	μ_s'(mm^{-1})
830nm (*: 825nm)			
Cubeddu *et al*	0.009-0.014	0.68-0.72	1.20
Key *et al*	0.025		
Durduran *et al*	0.005		0.83
Shah *et al* 2001			0.57-1.02
Tromberg *et al* 2000	0.002-0.006		0.60 - 1.04
Van Veen *et al* 2004	0.015		0.300
Fantini *et al* 1998 *	0.004		1.10
940nm			
Cubeddu *et al*	0.027-0.030	0.68-0.72	1.08
Shah *et al* 2001			0.57-0.96
Tromberg *et al* 2000	0.007-0.016		0.60-0.98
Van Veen *et al* 2004	0.028		0.250
980nm			
Cubeddu *et al*	0.030-0.035	0.68-0.72	1.0
Shah *et al* 2001			0.57-0.96
Van Veen *et al* 2004	0.025		0.220

In our study, the tissue was homogenized to be able to easily produce 1 mm thick samples of uniform thickness with the required dimensions to cover the portal hole of the integrating sphere. The samples must be homogeneous and must cover the entire 22 mm diameter exit portal hole of the integrating sphere to ensure that all the light leaving the hole hits the sample. Grinding the tissue was the only technique that could produce such samples in a reproducible fashion. Homogenizing or grinding tissue is a common procedure to prepare tissue for optical property measurements (Ritz *et al* 2001a,b, Peters *et al* 1990, Flock *et al* 1987) In their study of human breast tissue, Peters *et al* (1990) compared the optical properties of three homogenized tissue samples with those of three thick slices. The difference was within the variability of the measurement. The optical properties of the ground tissue that we measured should therefore be representative of the properties of the bulk tissue.

Before measuring the optical properties, the porcine tissue was frozen. Freezing was required for logistical reasons. The availability of tissue was unpredictable and not all the tissue could be used immediately upon delivery. According to Troy *et al* (1996), freezing and thawing have no effect on the optical properties of the tissue. To confirm their findings, we measured the optical properties after freezing and refrigeration (see section 5.4). According to our measurements, freezing and refrigeration produced a statistically significant difference in the diffuse reflectance of the tissue. Even though this difference was small (less than 10%), these findings suggest that experiments ideally should be performed on fresh tissue. However, the LITT experiments on ex-vivo porcine tissue that will be used as a reference to validate the optical-thermal model were also

performed on tissue that was frozen. Therefore, the fact that the tissue was frozen before its optical properties were measured should have no effect for the validation of the model.

The optical properties of tissue may change during photocoagulation due to the denaturation of cellular and extracellular structural proteins such as collagen (Pierce and Thomsen 1995). Changes in optical properties after photocoagulation have been observed in the liver (Ritz *et al* 2001a, Ritz *et al* 2001b, Nilsson *et al* 1998, Germer *et al* 1998, Pickering *et al* 1994), brain (Yaroslavsky *et al* 2002), skin (Laufer *et al* 1998), and heart myocardium (Splinter *et al* 1991, Derbyshire *et al* 1990). With the exception of the absorption coefficient at 980 nm, our results suggest that only the anisotropy coefficient is significantly different between native and coagulated *ex-vivo* porcine tissue. There is an increase of the anisotropy coefficient which produces a slight decrease of the effective attenuation coefficient. According to the optical-thermal model of chapter 4, the absorbed fluence rate and, therefore, the temperature distribution in the tissue, are determined by the effective attenuation coefficient. Coagulation may therefore produce a change in the temperature distribution that may limit the predictability of the model. The comparison of the model prediction with the experimental results (see chapter 7) will help determine if this effect is significant.

5.6.6 Summary and conclusion

Ex-vivo porcine fibro-fatty tissue was chosen as a tissue phantom to develop the optical-thermal model for laser interstitial thermotherapy of the human breast. In this chapter, we described optical property measurements of normal and photocoagulated *ex-vivo* porcine fibro-fatty tissue at 830, 940, and 980nm using a single integrating sphere

set-up and an inverse Monte Carlo program. Our experimental set-up was validated by comparing measurements performed with different concentrations of Intralipid 10% in distilled water with published results. The key findings of this part of the study are:

a) The scattering properties of porcine tissue are approximately independent of wavelength between 830 and 980 nm with average values of μ_s = 8.03 mm^{-1} and g=0.71 (see Table 5.9).

b) The absorption coefficient is lowest at 830 nm (0.008 mm^{-1}) and approximately equal at 940 nm (0.021 mm^{-1}) and 980 nm (0.029 mm^{-1}).

c) Refrigeration and freezing have an effect on the optical properties. There is a slight change in the diffuse reflectance which suggests that the optical properties should ideally be measured on fresh tissue.

d) Coagulation produces an increase in the scattering anisotropy coefficient which produces a decrease in the effective attenuation coefficient. These changes may affect the temperature distribution in the tissue during LITT.

e) The absorption and scattering anisotropy coefficient of *ex-vivo* porcine mammary chain tissue are comparable to published values obtained on human breast tissue.

f) The effective attenuation coefficient of our fibro-fatty mammary chain porcine tissue is comparable to published values obtained on breast tissue. The temperature distribution produced in *ex-vivo* porcine tissue and *in-vivo* breast tissue should, therefore, be similar.

6. DETERMINATION OF ARRHENIUS EQUATION PARAMETERS

6.1 Purpose

The purpose of this part of the study is to determine the Arrhenius equation parameters (activation energy, E_a, and frequency factor, A) for the coagulation of *ex-vivo* porcine mammary chain fibro-fatty tissue. The Arrhenius parameters will be used in the optical-thermal model to predict the coagulation volume during LITT in porcine tissue (see chapter 7). The predictions will be compared with experimental results.

6.2 Hyperthermia and photocoagulation

When biological tissue is subjected to elevated temperatures, the tissue suffers a range of effects depending on the temperature within the tissue and the duration of heating. At approximately 42-50°C, the cellular metabolism accelerates, enzymes are inactivated, cellular membranes rupture, and organelles are distorted. These transformations induced by hyperthermia can produce cell damage. The thermal damage to the cell is non-lethal as long as the mediators for the cellular repair mechanisms are not destroyed. Lethal damage to cells may occur within a few minutes to several hours in the hyperthermic temperature range (42-50°C) depending on the cell type (Pearce and Thomsen 1995).

At temperatures above 50°C, the tissue suffers photocoagulation. Cells and organelles shrink and undergo conformational changes due to the thermal denaturation of their structural proteins and loss of water. Extracellular collagen swells and develops an

amorphous, glassy appearance. For most tissues, coagulation can be seen by the naked eye as a whitening of the tissue. Tissue that is more collagen-rich becomes more transparent. Since structural proteins are more thermally stable than cells, the thermal energy required to denature these proteins is usually also sufficient to kill all the cells within the coagulated region. Depending on the tissue type and the temperature, coagulation usually occurs within seconds to minutes.

In-vivo, the coagulated volume is usually surrounded by a ring of edematous tissue that includes coagulated blood as well as regions of hemorrhage from ruptured blood vessels (Bloom *et al* 2001, Akimov *et al* 1998). The cell death boundary may extend beyond the boundaries of coagulation (Thomsen 1995). The actual size of the region of cell death produced *in-vivo* can only be assessed accurately after cell necrosis has occurred, typically 3 to 5 days after the induction of thermal damage.

The goal of our project is to induce a 3 cm diameter coagulation zone in breast tissue during laser irradiation that encompasses the tumor plus a surrounding 1 cm thick margin of native tissue. A coagulative thermal treatment was selected since it requires less time to achieve tumor cell death than hyperthermia. We will use the Arrhenius equation

$$\Omega(t) = \ln\left(\frac{C_N(0)}{C_N(t)}\right) = \int_0^t A e^{\frac{-E_a}{RT(\tau)}} d\tau \qquad \text{Eq. 6.1}$$

to predict the extent of coagulation in fibro-fatty tissue (Zhu *et al* 2002, Germain *et al* 2001, Iizuka *et al* 2000, Purdie *et al* 2000, Olsrud *et al* 1999, Prapavat *et al* 1996, McKenzie 1990, Welch 1984).

6.3 Method to determine the coagulation parameters

Because different tissue types have different structural composition, the kinetics of coagulation vary. Published values of the frequency factor and activation energy for cell death and coagulation in biological tissue range from 1×10^{40} to 1×10^{106} s^{-1} and from 1×10^5 to 1×10^6 J mol^{-1}, respectively (Pearce and Thomsen 1995). For cell death in the hyperthermic range, the frequency factors and activation energies can be found by heating the tissue to a constant temperature for different times (He *et al* 2005, Diaz *et al* 1993, Bauer and Henle 1979). At constant cell temperature, T_c, the Arrhenius equation becomes:

$$\Omega(t) = A \cdot t \cdot e^{\frac{-E_a}{RT_c}} \ .$$

Eq. 6.2

The time necessary to achieve a specific fraction of cell death is measured as a function of the cell temperature. The Arrhenius constants can then be deduced by a simple regression analysis.

This technique is suitable to quantify cell death because it can be applied to cell cultures that can be easily heated uniformly. However, the goal of our project is to coagulate the tissue. The temperature and time range needed to coagulate the tissue is more than sufficient to induce cell death within the tissue within minutes. Since the thermal processes between coagulation and hyperthermic cell death are different, the parameters obtained from experiments with hyperthermic cell death should not be used. The technique mentioned above for cell death cannot be easily extended to quantify the kinetics of coagulation of bulk tissue because it is difficult to uniformly heat large tissue volumes in a rapid fashion. Coagulation may occur during the time it takes to reach the

target temperature, especially at higher temperatures. In addition, there will always be a temperature gradient with higher temperatures close to the heat source (He *et al* 2005).

A different method was, therefore, developed for the determination of the Arrhenius equation parameters from laser heating experiments. This method is a revised version of a method that has been applied elsewhere (Salas *et al* 2003). The steps are the following:

Step 1: A set of durations required to reach 50% coagulation are assumed for a pair of temperature values, based on experimental observations. The pair selected was 50 and 60°C. The 50% coagulation times ranged from 30 minutes to 1000 hours at 50°C and from 1 minute to 1 hour at 60°C. Coagulation is not expected at 50°C except for much longer times, while coagulation at 60°C is expected within an hour.

Step 2: The activation energy and frequency factor was calculated for each combination of the 50% coagulation times at 50 and 60°C. Only parameters that give a longer coagulation time at 50°C are considered. A total of 33 pairs of activation energy and frequency factors are obtained.

Step 3: Each pair of Arrhenius parameters was used with temperature responses measured during laser heating experiments in porcine mammary chain tissue to calculate the concentration of coagulated tissue.

Step 4: The predicted zone of coagulation was compared with the coagulation zones measured on gross anatomical sections of the laser heated tissue. The coagulated zones in laser heated tissue were measured with a ruler. The boundaries of the coagulation zone were determined by the change in the color and the texture in the tissue relative to the native tissue.

<u>Step 5</u>: Pairs where the predictions did not match the experimental findings were eliminated.

The initial 33 pairs obtained from step 1 are shown in Table 6.1. The activation energy and frequency factor were calculated from the selected 50% coagulation times using the following equations which were derived from the Arrhenius equation with constant temperature (Eq. 6.2):

$$E_a = \frac{R}{\frac{1}{T_1} - \frac{1}{T_2}} \cdot \ln\left(\frac{t_1}{t_2}\right), \qquad A = \frac{\ln 2}{\sqrt{t_1 t_2}} \cdot (\frac{t_1}{t_2})^{-0.5 \cdot \frac{T_2 + T_1}{T_2 - T_1}} \qquad \text{Eq. 6.3}$$

where (T_1, t_1) and (T_2, t_2) are the temperature-time pairs.

6.4 Temperature and coagulation measurements in ex-vivo porcine tissue

6.4.1 Purpose

The purpose of these experiments was to measure the temperature and coagulation in ex-vivo porcine tissue induced by laser irradiation. The Arrhenius equation parameters of Table 6.1 will be used with the temperature measurements to predict the coagulation at the location of the temperature measurements. The predictions will be compared to the measured coagulation zones. The set of Arrhenius parameters that gives the best match between the predicted and measured coagulation will be used to predict the coagulation in the optical-thermal model (chapter 7).

6.4.2 Experiments

Ex-vivo porcine mammary chain tissue was obtained from the University of Miami Division of Veterinary Resources and stored in a freezer until the start of the

experiments. The original porcine tissue sample is comprised of the skin (less than 1 mm thick), the mammary gland tissue (1.0-1.5 cm thick), and a layer of muscle (approximately 5 to 10 mm thick). Two 90 x 90 x 15 mm slabs are excised from the tissue. The layer of muscle is removed from the tissue slabs with a meat slicer, leaving only the skin and the fibro-fatty layer. One of the slabs (bottom slab) is placed on a lab jack inside a water bath with the skin facing down. The water bath is used to increase the temperature of the tissue to approximately $37^{o}C$ prior to laser irradiation. A cylindrical diffusing tip optical fiber (Indigo#24, Ethicon Endo-Surgery, Inc., Cincinnati, OH) is placed on top of the bottom slab. The second slab (top slab) is placed on top of the optical fiber tip and the bottom slab with the skin side facing up. The lid of the water bath is closed to slightly compress the tissue. This compression minimizes tissue movement during laser irradiation and avoids the formation of an air gap between the top and bottom slab (Figure 6.1).
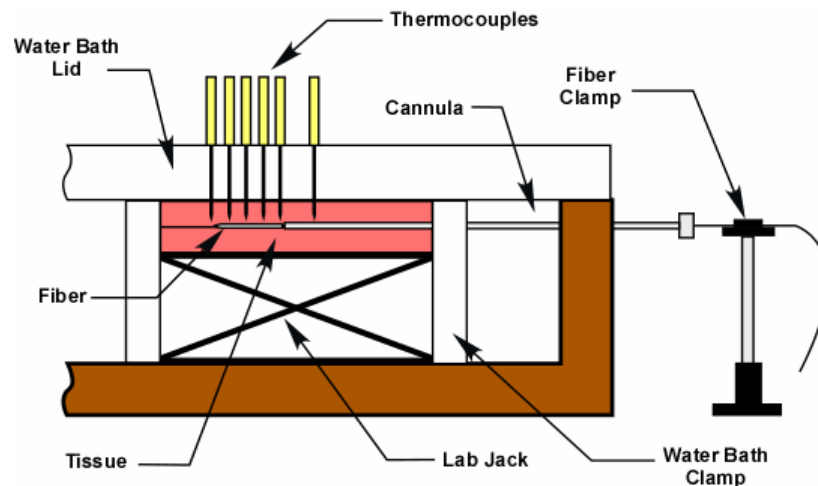
Figure 6.1: The experimental set-up for the temperature and coagulation measurements in ex-vivo porcine mammary chain fibro-fatty tissue. The experiments were performed with a cylindrical diffusing tip fiber coupled to a 980 nm diode laser system set at 4.0 W fiber output power.

Table 6.1: Activation energy and frequency factor for different sets of 50% coagulation time pairs at 50 °C and 60 °C. Coagulation times at 50 and 60°C were selected based on experimental observations. The activation energy and frequency factor were calculated from the assumed denaturation times using the Arrhenius equation.

Pair #	Time at 50°C	Time at 60°C	A (s^{-1})	E$_a$ (J mol^{-1})
1	100 hrs	1 min	1.25E+120	7.77E+05
2	100 hrs	5 min	6.63E+96	6.33E+05
3	100 hrs	10 min	6.27E+86	5.71E+05
4	100 hrs	20 min	5.92E+76	5.09E+05
5	100 hrs	30 min	8.11E+70	4.73E+05
6	100 hrs	60 min	7.67E+60	4.11E+05
7	1000 hrs	1 min	2.49E+152	9.82E+05
8	1000 hrs	5 min	1.32E+129	8.39E+05
9	1000 hrs	10 min	1.25E+119	7.77E+05
10	1000 hrs	20 min	1.18E+109	7.15E+05
11	1000 hrs	30 min	1.62E+103	6.79E+05
12	1000 hrs	60 min	1.53E+93	6.17E+05
13	10 hrs	1 min	6.27E+87	5.71E+05
14	10 hrs	5 min	3.32E+64	4.27E+05
15	10 hrs	10 min	3.14E+54	3.66E+05
16	10 hrs	20 min	2.97E+44	3.04E+05
17	10 hrs	30 min	4.06E+38	2.67E+05
18	10 hrs	60 min	3.84E+28	2.06E+05
19	1 hr	1 min	3.14E+55	3.66E+05
20	1 hr	5 min	1.66E+32	2.22E+05
21	1 hr	10 min	1.57E+22	1.60E+05
22	1 hr	20 min	1.49E+12	9.81E+04
23	1 hr	30 min	2.04E+6	6.19E+04
24	5 hr	1 min	1.18E+78	5.09E+05
25	5 hr	5 min	6.28E+54	3.66E+05
26	5 hr	10 min	5.94E+44	3.04E+05
27	5 hr	20 min	5.62E+34	2.42E+05
28	5 hr	30 min	7.68E+28	2.06E+05
29	5 hr	60 min	7.27E+18	1.44E+05
30	30 min	1 min	5.94E+45	3.04E+05
31	30 min	5 min	3.15E+22	1.60E+05
32	30 min	10 min	2.98E+12	9.81E+04
33	30 min	20 min	2.81E+3	3.62E+04

Nine copper-constantan T-type thermocouples (M-23, Physitemp Instruments Inc., Clifton, NJ) are used to record the temperature in the tissue before, during, and after laser irradiation. The thermocouples are inserted into the tissue through the top lid of the water bath. The tips of the thermocouples are located in the plane of the fiber axis (Figure 6.1).

The distribution of the thermocouples in the tissue in relation to the fiber axis is shown in Figure 6.2.

Once the tissue temperature is approximately 37°C, the tissue is irradiated with a 25W 980 nm diode laser system (AOC25, Applied Optronics, South Plainfield, NJ) set at 4.0 W for 5, 10, and 15 minutes. Temperature is recorded during the irradiation and cooling at least until the temperature is below approximately 50°C to ensure that no coagulation occurs after the temperature recordings are stopped. Three experiments were performed per irradiation time (9 experiments in total). After the cooling down period, the optical fiber is removed from the tissue and the location of the distal point of the fiber in the tissue is marked. The tissue slabs are then removed from the water bath. The dimensions of the gross anatomical coagulation zone are measured with a ruler. The positions of the coagulation boundary along the three columns of thermocouples are recorded (see Figure 6.2). These measurements are compared with the predictions obtained with the pairs of Arrhenius equation parameters listed in table 6.1.
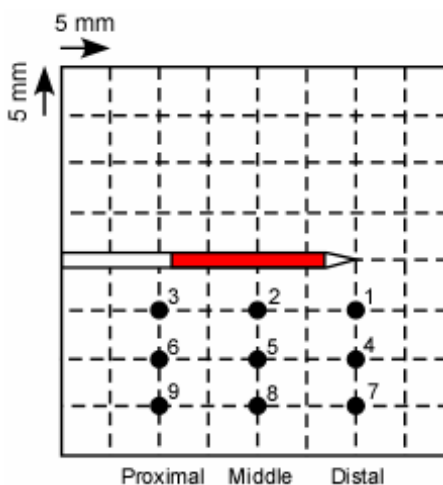
Figure 6.2: The thermocouple distribution during laser heating experiments in ex-vivo porcine tissue. This is the top view of the water bath.
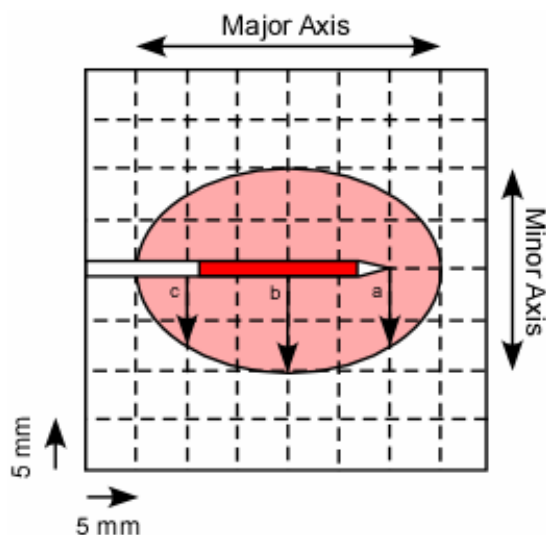
Figure 6.3: The elliptical coagulation zone around the fiber including the major and minor axis. The boundary of the coagulation zone is measured along each column (a, b, c) of thermocouples.

6.4.3 Results

Typical temperature curves recorded during the 5, 10, and 15 minutes laser irradiation experiments are shown in Figures 6.4-6.6. Typical coagulation zones during the 5, 10, and 15 minutes laser irradiation experiments are shown in Figures 6.7-6.9. The position of the coagulation boundaries along the three columns of thermocouples are given in Table 6.2. Typical predicted coagulation curves calculated with the Arrhenius equation from the temperature recordings are shown in Figure 6.10. The final predicted coagulation amount for all experiments except the first experiment at five minutes (not included due to an experimental problem) and at all thermocouple locations are listed in Table 6.3-6.10.

6.5 Determination of the Arrhenius equation parameters

To determine which set of Arrrhenius equation parameter pairs give the best prediction, the following three conditions based on the position of the coagulation boundaries listed in Table 6.2 were imposed:

Condition 1: For all three experiments at 10 minutes and the first experiment at 15 minutes, thermocouples 7,8,and 9 should give 0% coagulation. Pairs which showed less than 1% coagulation for these thermocouples were assumed to satisfy the criterion. Only pairs 1 through 12 satisfy the condition.

Condition 2: For the second and third experiment at 5 minutes, thermocouples 1 and 2 should give 100% coagulation. Pairs which showed more than 99% coagulation for these thermocouples were assumed to satisfy the criterion. This condition eliminates pairs 5,6, and 12. Only pairs 1 through 4 and 7 through 11 remain. According to Table 6.2, 100% coagulation should also be observed at the location of thermocouple 3. Thermocouple 3 was not included in condition 2 because there was a problem with the temperature measurement.

Condition 3: For the first experiment at 10 minutes, thermocouples 4, 5, and 6 should give 0% coagulation. According to Table 6.2, the positions of these thermocouples are outside the coagulation zone. A value of 90% coagulation was selected to satisfy this condition to take into account positioning and measurement errors. This condition eliminates pairs 1, 2, 3 and 7 through 10. Only pairs 4 and 11 remain.
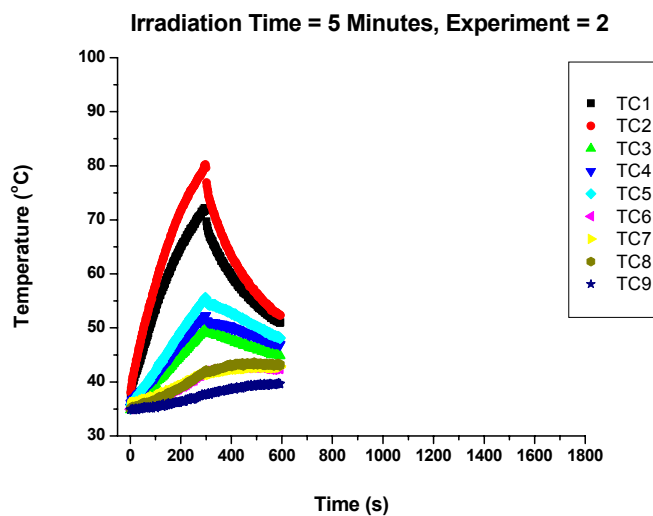
Figure 6.4: Temperature measured during laser irradiation in ex-vivo porcine fibro-fatty tissue at 980 nm, 4 W, and 5 minutes
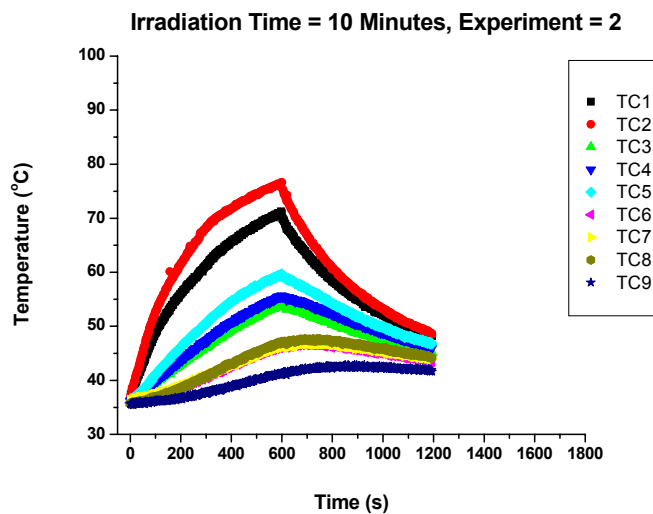
Figure 6.5: Temperature measured during laser irradiation in ex-vivo porcine fibro-fatty tissue at 980 nm, 4 W, and 10 minutes
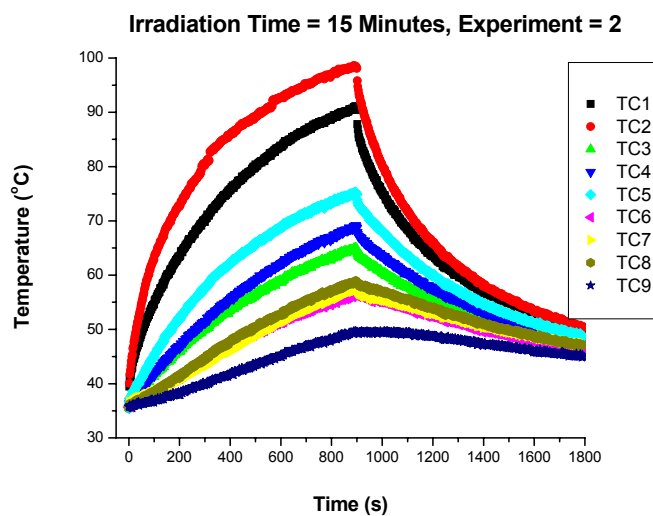
Figure 6.6: Temperature measured during laser irradiation in ex-vivo porcine fibro-fatty tissue at 980 nm, 4 W, and 15 minutes
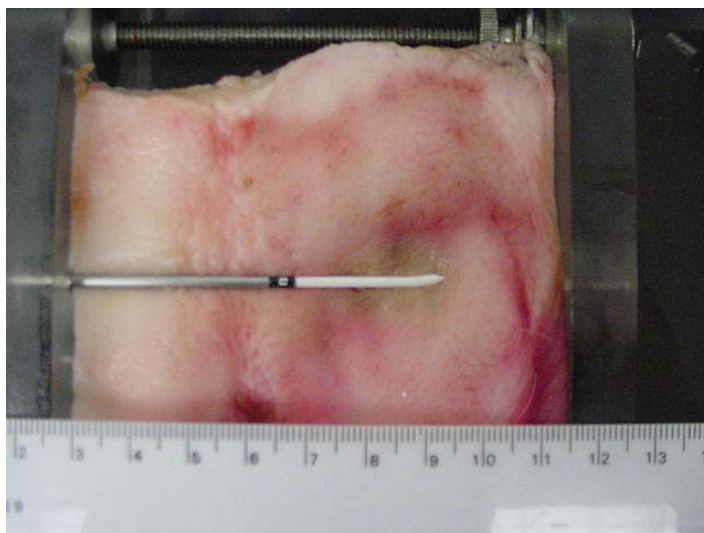
Figure 6.7: Ex-vivo porcine fibro-fatty tissue irradiated after 5 minutes with a 980 nm diode laser at 4.0 W coupled to an Indigo cylindrical diffusing tip optical fiber
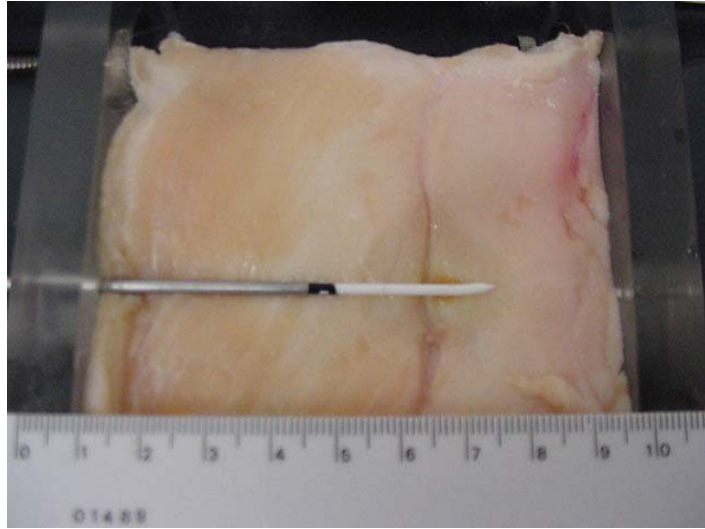
Figure 6.8: Ex-vivo porcine fibro-fatty tissue irradiated after 10 minutes with a 980 nm diode laser at 4.0 W coupled to an Indigo cylindrical diffusing tip optical fiber
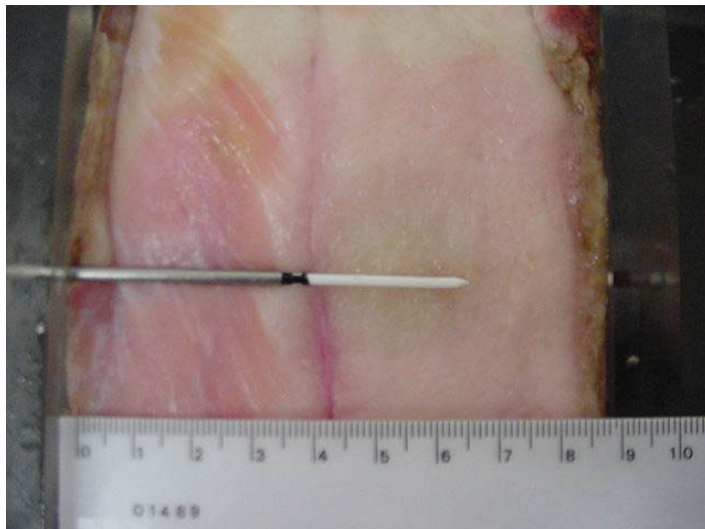
Figure 6.9: Ex-vivo porcine fibro-fatty tissue irradiated after 15 minutes with a 980 nm diode laser at 4.0 W coupled to an Indigo cylindrical diffusing tip optical fiber

10 Min, Exp.1 - A=1.62x10^{103} ; E$_a$=6.79x10^5
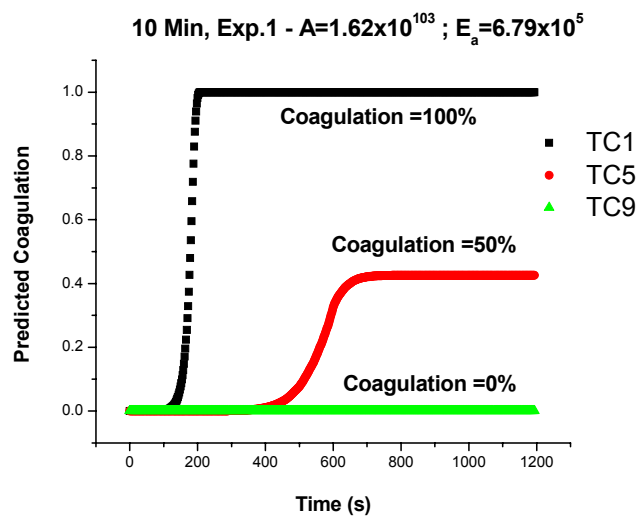
Figure 6.10: The predicted coagulation in ex-vivo porcine fibro-fatty tissue during the first laser irradiation experiment at 4.0 W for ten minutes using the Arrhenius equation with pair #11.

Table 6.2: The coagulation boundary dimensions induced after laser irradiation in ex-vivo porcine fibro-fatty mammary chain tissue

Exp Time (minutes)	Exp Run	Coagulation Boundary Dimensions (mm)		
		Distal (a)	Middle (b)	Proximal (c)
5	1	8	9	7
	2	9	8	4
	3	8	8	7
10	1	5	6	6
	2	8	12	9
	3	11	12	9
15	1	11	12	11
	2	11	15	11
	3	13	14	9

Table 6.3: The predicted coagulation in ex-vivo porcine mammary chain tissue for the second experiment at 5 minutes irradiation time using the Arrhenius equation for the 33 pairs obtained from steps1-2. The coagulation was predicted for all nine temperature measurements.

Predicted Coagulation; Irradiation = 5 min; Experiment 2								
Arrhenius Pairs	**Thermocouples**							
	1	**2**	**3**	**4**	**5**	**6**	**7**	**8**	**9**
1	1	1	0.0001	0.0007	0.0123	0	0	0	0
2	1	1	0.0002	0.0007	0.0071	0	0	0	0
3	1	1	0.0002	0.0008	0.0056	0	0	0	0
4	0.9927	1	0.0002	0.0008	0.0045	0	0	0	0
5	0.8925	1	0.0002	0.0007	0.0036	0	0	0	0
6	0.4985	0.9999	0.0003	0.0007	0.0029	0	0	0	0
7	1	1	0	0.0001	0.0042	0	0	0	0
8	1	1	0	0.0001	0.0016	0	0	0	0
9	1	1	0	0.0001	0.0009	0	0	0	0
10	1	1	0	0.0001	0.001	0	0	0	0
11	1	1	0	0.0001	0.0008	0	0	0	0
12	0.9724	1	0	0.0001	0.0006	0	0	0	0
13	1	1	0.0019	0.0075	0.0546	0.0001	0.0001	0.0001	0
14	1	1	0.0029	0.0081	0.034	0.0003	0.0002	0.0003	0
15	0.9011	1	0.0024	0.0058	0.0196	0.0003	0.0003	0.0004	0.0001
16	0.53	0.994	0.003	0.0061	0.0165	0.0005	0.0005	0.0006	0.0002
17	0.3051	0.8535	0.003	0.0058	0.0136	0.0007	0.0006	0.0008	0.0002
18	0.1216	0.3586	0.0039	0.0063	0.0119	0.0013	0.0012	0.0014	0.0006
19	1	1	0.0238	0.0566	0.1794	0.003	0.0027	0.0035	0.0007
20	0.8474	0.9993	0.0398	0.0666	0.1293	0.012	0.0113	0.013	0.0051
21	0.511	0.8316	0.0512	0.0737	0.1167	0.0221	0.0213	0.0234	0.0122
22	0.2591	0.3905	0.0659	0.0818	0.1067	0.0403	0.0396	0.0415	0.0285
23	0.1774	0.229	0.0777	0.0887	0.104	0.0575	0.0571	0.0585	0.0466
24	1	1	0.0045	0.0153	0.0863	0.0002	0.0002	0.0003	0
25	0.9902	1	0.0048	0.0116	0.0388	0.0006	0.0005	0.0007	0.0001
26	0.7791	1	0.0059	0.0123	0.0327	0.0011	0.001	0.0012	0.0003
27	0.4041	0.8976	0.0074	0.0132	0.0282	0.002	0.0018	0.0022	0.0008
28	0.2285	0.5886	0.0077	0.0125	0.0237	0.0025	0.0024	0.0027	0.0011
29	0.0966	0.2029	0.01	0.014	0.0215	0.0047	0.0046	0.0049	0.0028
30	1	1	0.0575	0.116	0.2827	0.0108	0.0098	0.0122	0.0032
31	0.762	0.972	0.1001	0.1424	0.2203	0.0439	0.0424	0.0463	0.0243
32	0.451	0.6285	0.1275	0.1569	0.202	0.0789	0.0777	0.0812	0.0561
33	0.2613	0.2973	0.169	0.1816	0.1976	0.1436	0.1432	0.1449	0.1281

Table 6.4: The predicted coagulation in ex-vivo porcine mammary chain tissue for the third experiment at 5 minutes irradiation time using the Arrhenius equation for the 33 pairs obtained from steps1-2. The coagulation was predicted for all nine temperature measurements. There was a problem with the temperature recording in thermocouple 3.

Arrhenius Pairs	Thermocouples								
	1	**2**	**3**	**4**	**5**	**6**	**7**	**8**	**9**
1	1	1	0.0001	0.0042	0.0444	0	0	0	0
2	1	1	0.0001	0.0029	0.0189	0	0	0	0
3	1	1	0.0002	0.0026	0.0133	0	0	0	0
4	1	1	0.0002	0.0022	0.0094	0	0	0	0
5	0.9866	1	0.0002	0.0019	0.007	0	0	0	0
6	0.7061	0.9999	0.0002	0.0017	0.0051	0	0.0001	0.0001	0
7	1	1	0	0.0011	0.0243	0	0	0	0
8	1	1	0	0.0005	0.0067	0	0	0	0
9	1	1	0	0.0003	0.0031	0	0	0	0
10	1	1	0	0.0004	0.0031	0	0	0	0
11	1	1	0	0.0003	0.0022	0	0	0	0
12	0.9998	1	0	0.0003	0.0016	0	0	0	0
13	1	1	0.0015	0.0252	0.125	0.0001	0.0002	0.0003	0
14	1	1	0.0025	0.0192	0.0605	0.0004	0.0005	0.0007	0.0001
15	0.9787	1	0.0021	0.012	0.0315	0.0005	0.0005	0.0007	0.0001
16	0.6825	0.9941	0.0027	0.0111	0.024	0.0008	0.0009	0.0011	0.0003
17	0.4077	0.854	0.0028	0.0097	0.0188	0.001	0.0011	0.0013	0.0004
18	0.1559	0.3585	0.0037	0.0093	0.0151	0.0017	0.0018	0.0021	0.0009
19	1	1	0.0211	0.1141	0.2738	0.0048	0.0055	0.0073	0.0014
20	0.9195	0.9993	0.0379	0.0999	0.1646	0.0162	0.0173	0.0205	0.0079
21	0.5811	0.8302	0.0502	0.0982	0.1384	0.0277	0.0289	0.0325	0.0168
22	0.2832	0.3873	0.0659	0.0974	0.1186	0.0465	0.0476	0.0509	0.0346
23	0.1872	0.2267	0.0781	0.0989	0.1113	0.0632	0.0639	0.0666	0.0527
24	1	1	0.0037	0.0439	0.1729	0.0004	0.0005	0.0008	0.0001
25	0.9995	1	0.0043	0.0239	0.062	0.001	0.0011	0.0015	0.0003
26	0.8992	1	0.0054	0.0221	0.0475	0.0016	0.0018	0.0023	0.0006
27	0.5112	0.898	0.007	0.0209	0.0374	0.0027	0.0029	0.0035	0.0012
28	0.2875	0.5885	0.0074	0.0185	0.03	0.0033	0.0036	0.0042	0.0017
29	0.1136	0.2018	0.0099	0.0184	0.0253	0.0058	0.006	0.0067	0.0037
30	1	1	0.0528	0.2002	0.3851	0.0159	0.0176	0.0224	0.0058
31	0.8255	0.9715	0.0982	0.1873	0.2583	0.0549	0.0572	0.0642	0.0334
32	0.4862	0.6246	0.1275	0.1853	0.2231	0.0909	0.0929	0.0993	0.0681
33	0.2686	0.2952	0.1701	0.193	0.2055	0.1515	0.1524	0.1559	0.1373

Table 6.5: The predicted coagulation in ex-vivo porcine mammary chain tissue for the first experiment at 10 minutes irradiation time using the Arrhenius equation for the 33 pairs obtained from steps1-2. The coagulation was predicted for all nine temperature measurements.

Predicted Coagulation; Irradiation = 10 min; Experiment 1								
Arrhenius Pairs	**Thermocouples**							
	1	**2**	**3**	**4**	**5**	**6**	**7**	**8**	**9**
1	1	1	1	1	1	0.0025	0.0007	0.0011	0
2	1	1	1	0.999	0.9664	0.0021	0.0008	0.0012	0
3	1	1	1	0.9387	0.7786	0.002	0.0008	0.0012	0
4	1	1	0.9723	0.6785	0.4916	0.002	0.0009	0.0013	0.0001
5	1	1	0.8328	0.458	0.3204	0.0017	0.0008	0.0012	0.0001
6	1	1	0.4766	0.225	0.1621	0.0017	0.0009	0.0012	0.0001
7	1	1	1	1	1	0.0005	0.0001	0.0002	0
8	1	1	1	1	0.9944	0.0003	0.0001	0.0001	0
9	1	1	1	0.9834	0.7934	0.0002	0	0.0001	0
10	1	1	1	0.9005	0.6268	0.0002	0.0001	0.0001	0
11	1	1	0.9961	0.7063	0.4261	0.0002	0.0001	0.0001	0
12	1	1	0.8573	0.3866	0.2174	0.0002	0.0001	0.0001	0
13	1	1	1	1	1	0.0202	0.0082	0.0122	0.0005
14	1	1	0.9999	0.972	0.9112	0.0189	0.01	0.0135	0.0013
15	1	1	0.9107	0.6517	0.5431	0.0129	0.0077	0.0099	0.0014
16	1	1	0.5949	0.3671	0.3103	0.013	0.0086	0.0106	0.0022
17	1	1	0.3737	0.2281	0.1982	0.012	0.0085	0.0102	0.0025
18	1	0.9994	0.1696	0.1135	0.1051	0.0127	0.0099	0.0114	0.004
19	1	1	1	1	0.9996	0.1219	0.0741	0.0944	0.0138
20	1	1	0.9276	0.8046	0.7717	0.1311	0.1012	0.1165	0.0392
21	1	1	0.6664	0.552	0.5401	0.142	0.1201	0.1324	0.0626
22	0.9612	0.9295	0.3941	0.3482	0.351	0.1563	0.1429	0.1512	0.0982
23	0.6332	0.6042	0.2919	0.2727	0.2771	0.1691	0.1608	0.1663	0.1283
24	1	1	1	1	1	0.0384	0.0176	0.025	0.0015
25	1	1	0.992	0.8787	0.7912	0.0257	0.0153	0.0196	0.0028
26	1	1	0.8359	0.5994	0.5243	0.0259	0.0172	0.0212	0.0043
27	1	1	0.5026	0.3381	0.3052	0.0269	0.0198	0.0233	0.0068
28	1	1	0.3104	0.2141	0.1992	0.0252	0.0197	0.0226	0.008
29	0.9504	0.8663	0.1474	0.1144	0.1124	0.0278	0.0238	0.0261	0.013
30	1	1	1	0.9999	0.9994	0.231	0.1595	0.1927	0.0423
31	1	1	0.8895	0.8003	0.7895	0.2646	0.2264	0.2479	0.1216
32	0.9985	0.995	0.6329	0.5752	0.5788	0.2882	0.2654	0.2795	0.1868
33	0.6249	0.6169	0.4297	0.4176	0.4227	0.3305	0.3226	0.3281	0.2873

Table 6.6: The predicted coagulation in ex-vivo porcine mammary chain tissue for the second experiment at 10 minutes irradiation time using the Arrhenius equation for the 33 pairs obtained from steps1-2. The coagulation was predicted for all nine temperature measurements.

Predicted Coagulation; Irradiation = 10 min; Experiment 2								
Arrhenius Pairs	**Thermocouples**							
	1	**2**	**3**	**4**	**5**	**6**	**7**	**8**	**9**
1	1	1	0.0108	0.0604	0.6681	0.0001	0.0001	0.0001	0
2	1	1	0.0071	0.0291	0.2553	0.0001	0.0001	0.0002	0
3	1	1	0.006	0.0213	0.1547	0.0001	0.0002	0.0003	0
4	1	1	0.0051	0.0157	0.0923	0.0002	0.0002	0.0003	0
5	0.9999	1	0.0042	0.012	0.062	0.0002	0.0002	0.0003	0
6	0.9268	1	0.0037	0.0091	0.037	0.0003	0.0003	0.0004	0
7	1	1	0.0031	0.0273	0.67	0	0	0	0
8	1	1	0.0013	0.0087	0.1794	0	0	0	0
9	1	1	0.0008	0.0043	0.0739	0	0	0	0
10	1	1	0.0009	0.0044	0.0598	0	0	0	0
11	1	1	0.0007	0.0033	0.0393	0	0	0	0
12	1	1	0.0006	0.0024	0.0225	0	0	0	0
13	1	1	0.0583	0.1936	0.8138	0.0014	0.0018	0.0025	0.0001
14	1	1	0.0416	0.1037	0.3834	0.0029	0.0034	0.0044	0.0005
15	0.9998	1	0.0255	0.0561	0.1819	0.0027	0.0031	0.0038	0.0006
16	0.9207	1	0.0229	0.044	0.1156	0.0037	0.0041	0.0049	0.001
17	0.6884	0.9898	0.0198	0.035	0.0813	0.0041	0.0045	0.0052	0.0013
18	0.316	0.6578	0.0186	0.0287	0.0535	0.0058	0.0062	0.0069	0.0024
19	1	1	0.2275	0.4389	0.8657	0.0268	0.0304	0.0376	0.0056
20	0.9965	1	0.1918	0.2895	0.4958	0.0573	0.0616	0.0692	0.023
21	0.8567	0.986	0.1867	0.2502	0.3699	0.0811	0.0854	0.0921	0.043
22	0.517	0.6796	0.1846	0.2195	0.2768	0.1137	0.1173	0.122	0.0786
23	0.3574	0.4364	0.1876	0.2085	0.2399	0.1399	0.1426	0.1457	0.1118
24	1	1	0.0972	0.2726	0.8569	0.0039	0.0046	0.0063	0.0004
25	1	1	0.0503	0.1091	0.3307	0.0054	0.0061	0.0076	0.0011
26	0.9937	1	0.0453	0.0861	0.2179	0.0074	0.0083	0.0098	0.002
27	0.7981	0.9958	0.042	0.0695	0.144	0.0104	0.0113	0.0129	0.0038
28	0.5321	0.8829	0.0369	0.0565	0.1041	0.0115	0.0123	0.0137	0.0049
29	0.2353	0.4169	0.0363	0.0485	0.0727	0.0165	0.0174	0.0186	0.0092
30	1	1	0.3713	0.5934	0.9144	0.072	0.0797	0.0941	0.0203
31	0.9797	0.9998	0.3394	0.4388	0.6042	0.156	0.164	0.1762	0.0844
32	0.7667	0.8973	0.3351	0.3909	0.4769	0.2145	0.2208	0.2291	0.151
33	0.4794	0.528	0.3487	0.3677	0.3941	0.3002	0.3032	0.3063	0.2674

Table 6.7: The predicted coagulation in ex-vivo porcine mammary chain tissue for the third experiment at 10 minutes irradiation time using the Arrhenius equation for the 33 pairs obtained from steps1-2. The coagulation was predicted for all nine temperature measurements.

Predicted Coagulation; Irradiation = 10 min; Experiment 3								
Arrhenius Pairs	**Thermocouples**							
	1	**2**	**3**	**4**	**5**	**6**	**7**	**8**	**9**
1	1	1	0.4776	1	0.9422	0.001	0.0004	0.0006	0
2	1	1	0.1737	0.9379	0.4767	0.0011	0.0005	0.0007	0
3	1	1	0.1071	0.7021	0.291	0.0012	0.0006	0.0008	0.0001
4	1	1	0.0657	0.4131	0.1684	0.0012	0.0007	0.0009	0.0001
5	1	1	0.0449	0.26	0.1103	0.0012	0.0006	0.0008	0.0001
6	1	1	0.0278	0.1269	0.062	0.0012	0.0007	0.0009	0.0002
7	1	1	0.4332	1	0.9724	0.0001	0	0.0001	0
8	1	1	0.1056	0.9892	0.4216	0.0001	0	0.0001	0
9	1	1	0.0441	0.7416	0.1801	0.0001	0	0	0
10	1	1	0.0371	0.5636	0.1382	0.0001	0	0.0001	0
11	1	1	0.0249	0.3699	0.0887	0.0001	0	0.0001	0
12	1	1	0.0147	0.1811	0.0478	0.0001	0	0.0001	0
13	1	1	0.6779	1	0.9679	0.0117	0.0057	0.008	0.0006
14	1	1	0.3008	0.8449	0.5667	0.0135	0.0079	0.0102	0.0015
15	1	1	0.1433	0.4487	0.2759	0.01	0.0063	0.0079	0.0016
16	1	1	0.094	0.245	0.1675	0.0109	0.0074	0.009	0.0024
17	1	1	0.0675	0.1543	0.114	0.0104	0.0074	0.0088	0.0028
18	0.9864	0.9315	0.0463	0.0824	0.0701	0.0117	0.009	0.0103	0.0043
19	1	1	0.787	0.9974	0.9604	0.0957	0.0612	0.0763	0.0155
20	1	1	0.442	0.6786	0.603	0.1197	0.0912	0.1051	0.0423
21	1	0.9998	0.338	0.4625	0.4381	0.1358	0.1118	0.1241	0.0661
22	0.8346	0.8181	0.2618	0.3096	0.3114	0.1542	0.137	0.1463	0.1016
23	0.5117	0.5171	0.232	0.2542	0.2596	0.1686	0.1566	0.1632	0.131
24	1	1	0.7442	1	0.9753	0.0246	0.013	0.0176	0.0018
25	1	1	0.2661	0.6961	0.4757	0.0199	0.0125	0.0157	0.0031
26	1	1	0.1792	0.4299	0.307	0.0217	0.0147	0.0179	0.0048
27	1	1	0.1224	0.2426	0.1935	0.024	0.0176	0.0207	0.0074
28	0.9998	0.9953	0.0904	0.158	0.1353	0.0232	0.0179	0.0205	0.0086
29	0.7092	0.6338	0.0659	0.0922	0.0881	0.0268	0.0223	0.0246	0.0137
30	1	1	0.8612	0.9964	0.9745	0.1966	0.1379	0.1651	0.0467
31	1	1	0.5628	0.7122	0.6854	0.2538	0.2116	0.2335	0.1282
32	0.9726	0.9669	0.4551	0.5233	0.5258	0.2845	0.2553	0.2711	0.1929
33	0.5645	0.575	0.3879	0.4041	0.411	0.3306	0.3182	0.3252	0.2907

Table 6.8: The predicted coagulation in ex-vivo porcine mammary chain tissue for the first experiment at 15 minutes irradiation time using the Arrhenius equation for the 33 pairs obtained from steps1-2. The coagulation was predicted for all nine temperature measurements. There was a problem with the temperature recording in thermocouple 9.

Predicted Coagulation; Irradiation = 15 min; Experiment 1								
Arrhenius Pairs	**Thermocouples**							
	1	**2**	**3**	**4**	**5**	**6**	**7**	**8**	**9**
1	1	0.9983	1	1	0.0067	0.1794	0.0089	0.0001	1
2	1	0.7229	1	1	0.0052	0.0753	0.0066	0.0001	1
3	1	0.4771	1	1	0.0047	0.0514	0.0058	0.0002	1
4	1	0.2816	1	0.999	0.0043	0.0352	0.0052	0.0002	1
5	1	0.1842	1	0.9663	0.0037	0.0257	0.0044	0.0003	1
6	1	0.1006	1	0.6983	0.0035	0.0179	0.004	0.0004	1
7	1	0.9999	1	1	0.0014	0.1061	0.0021	0	1
8	1	0.7234	1	1	0.0008	0.0294	0.001	0	1
9	1	0.3579	1	1	0.0005	0.0136	0.0006	0	1
10	1	0.2703	1	1	0.0006	0.013	0.0008	0	1
11	1	0.174	1	1	0.0005	0.0094	0.0007	0	1
12	1	0.0914	1	0.9801	0.0005	0.0063	0.0006	0	1
13	1	0.9985	1	1	0.0462	0.41	0.0566	0.0018	1
14	1	0.7544	1	1	0.0389	0.1994	0.0447	0.0037	1
15	1	0.4033	1	0.9877	0.0255	0.1027	0.0286	0.0035	1
16	1	0.2438	1	0.7999	0.0246	0.0751	0.0268	0.005	1
17	1	0.1643	1	0.5611	0.022	0.0574	0.0237	0.0055	1
18	1	0.0983	0.9728	0.2743	0.0222	0.0442	0.0233	0.008	0.9047
19	1	0.9943	1	1	0.2275	0.6617	0.2517	0.0347	1
20	1	0.735	1	0.9894	0.2211	0.4173	0.2319	0.0781	1
21	1	0.5521	1	0.8451	0.2289	0.3504	0.235	0.113	0.9998
22	0.9882	0.4037	0.8588	0.5631	0.2406	0.3033	0.243	0.1612	0.8642
23	0.7606	0.345	0.5728	0.4267	0.2531	0.2889	0.254	0.1995	0.6077
24	1	0.9987	1	1	0.0831	0.5133	0.0987	0.0048	1
25	1	0.644	1	0.9998	0.0503	0.1949	0.0563	0.007	1
26	1	0.4281	1	0.96	0.0485	0.1445	0.0529	0.0099	1
27	1	0.2689	1	0.7043	0.048	0.1098	0.0511	0.0142	1
28	1	0.187	0.9993	0.4733	0.0439	0.0865	0.046	0.0159	0.9909
29	0.9791	0.1201	0.703	0.236	0.0462	0.071	0.0474	0.0235	0.647
30	1	0.9963	1	1	0.3918	0.79	0.4193	0.0947	1
31	1	0.8004	1	0.9763	0.4063	0.5792	0.4158	0.2138	1
32	0.9999	0.6445	0.9801	0.8091	0.4232	0.5146	0.4269	0.2965	0.9815
33	0.7619	0.5328	0.6565	0.5864	0.462	0.4902	0.4622	0.4123	0.6905

Table 6.9: The predicted coagulation in ex-vivo porcine mammary chain tissue for the second experiment at 15 minutes irradiation time using the Arrhenius equation for the 33 pairs obtained from steps1-2. The coagulation was predicted for all nine temperature measurements.

Predicted Coagulation; Irradiation = 15 min; Experiment 2								
Arrhenius Pairs	**Thermocouples**							
	1	**2**	**3**	**4**	**5**	**6**	**7**	**8**	**9**
1	1	1	1	1	1	0.1244	0.1703	0.5107	0.0009
2	1	1	0.9942	1	1	0.0563	0.0728	0.1993	0.0011
3	1	1	0.8915	1	1	0.04	0.0503	0.1267	0.0012
4	1	1	0.6209	0.9996	1	0.0287	0.035	0.0801	0.0013
5	1	1	0.4207	0.9768	1	0.0215	0.0259	0.0557	0.0013
6	1	1	0.2171	0.7228	1	0.0157	0.0184	0.0356	0.0014
7	1	1	1	1	1	0.0645	0.0998	0.4415	0.0001
8	1	1	0.9999	1	1	0.0191	0.0277	0.1132	0.0001
9	1	1	0.9251	1	1	0.0092	0.0129	0.0485	0.0001
10	1	1	0.7905	1	1	0.0091	0.0124	0.0418	0.0001
11	1	1	0.5784	1	1	0.0067	0.009	0.0284	0.0001
12	1	1	0.3087	0.9919	1	0.0047	0.0061	0.0173	0.0001
13	1	1	1	1	1	0.3351	0.4031	0.7419	0.0122
14	1	1	0.9655	1	1	0.1749	0.203	0.3662	0.0154
15	1	1	0.6573	0.99	1	0.0937	0.1067	0.1835	0.0119
16	1	1	0.3952	0.8068	0.9999	0.0718	0.0797	0.1247	0.0134
17	1	1	0.258	0.5652	0.9791	0.0564	0.0617	0.0913	0.0131
18	0.9999	1	0.1402	0.275	0.638	0.0452	0.0482	0.0644	0.0153
19	1	1	1	1	1	0.6263	0.6766	0.8684	0.1124
20	1	1	0.865	0.9896	1	0.4209	0.4443	0.5573	0.1525
21	1	1	0.6569	0.8463	0.9882	0.3624	0.3759	0.4453	0.1786
22	0.9626	0.9974	0.4583	0.567	0.7439	0.3162	0.3223	0.3572	0.2092
23	0.7019	0.8205	0.375	0.4307	0.5267	0.2991	0.3021	0.3217	0.2328
24	1	1	1	1	1	0.4421	0.5112	0.8127	0.0266
25	1	1	0.8826	0.9999	1	0.1787	0.2021	0.3334	0.0236
26	1	1	0.6342	0.9627	1	0.1384	0.153	0.2338	0.0266
27	1	1	0.3889	0.7067	0.9922	0.1096	0.1183	0.1655	0.0306
28	1	1	0.2607	0.4744	0.869	0.0883	0.094	0.1247	0.0304
29	0.912	0.9973	0.1523	0.2371	0.4409	0.0743	0.0772	0.0933	0.0363
30	1	1	1	1	1	0.7744	0.8099	0.9303	0.2367
31	1	1	0.8831	0.9767	0.9999	0.5946	0.6116	0.6935	0.3262
32	0.9986	1	0.7066	0.8125	0.9344	0.5325	0.5407	0.5868	0.3746
33	0.734	0.7962	0.5544	0.5901	0.6468	0.4999	0.5019	0.5167	0.4438

Table 6.10: The predicted coagulation in ex-vivo porcine mammary chain tissue for the third experiment at 15 minutes irradiation time using the Arrhenius equation for the 33 pairs obtained from steps1-2. The coagulation was predicted for all nine temperature measurements.

Predicted Coagulation; Irradiation = 15 min; Experiment 3									
Arrhenius Pairs	**Thermocouples**								
	1	**2**	**3**	**4**	**5**	**6**	**7**	**8**	**9**
1	1	1	1	1	1	0.0372	0.3194	0.2908	0.0008
2	1	1	0.9957	1	1	0.0211	0.1265	0.1176	0.0009
3	1	1	0.9076	1	1	0.0166	0.083	0.0782	0.001
4	1	1	0.6503	1	1	0.0131	0.0546	0.0521	0.0011
5	1	1	0.4481	1	1	0.0105	0.0389	0.0374	0.0011
6	1	1	0.2352	1	1	0.0085	0.0259	0.0253	0.0012
7	1	1	1	1	1	0.0131	0.2292	0.1989	0.0001
8	1	1	0.9999	1	1	0.0049	0.0594	0.0525	0.0001
9	1	1	0.9305	1	1	0.0026	0.0264	0.0236	0.0001
10	1	1	0.8041	1	1	0.0029	0.0239	0.0217	0.0001
11	1	1	0.5964	1	1	0.0023	0.0167	0.0153	0.0001
12	1	1	0.3247	1	1	0.0018	0.0107	0.0099	0.0001
13	1	1	1	1	1	0.1538	0.5797	0.5569	0.0103
14	1	1	0.9749	1	1	0.0957	0.2783	0.2719	0.0134
15	1	1	0.6915	1	1	0.0554	0.1406	0.139	0.0105
16	1	1	0.4239	1	1	0.0466	0.0988	0.0989	0.0122
17	1	1	0.2783	0.9983	0.9829	0.0386	0.0739	0.0744	0.0121
18	1	1	0.1503	0.7675	0.655	0.0341	0.0544	0.0553	0.0144
19	1	1	1	1	1	0.4343	0.7803	0.776	0.1005
20	1	1	0.8857	1	1	0.3294	0.4912	0.4964	0.1435
21	1	1	0.6794	0.9968	0.99	0.3044	0.4012	0.4077	0.1723
22	0.9999	0.9998	0.4707	0.7839	0.7499	0.2859	0.3334	0.339	0.2063
23	0.8874	0.8824	0.3816	0.5452	0.5287	0.2819	0.308	0.3121	0.2317
24	1	1	1	1	1	0.2333	0.6756	0.6582	0.0227
25	1	1	0.9048	1	1	0.1077	0.2615	0.2586	0.021
26	1	1	0.6681	1	1	0.091	0.1879	0.188	0.0242
27	1	1	0.4148	0.9995	0.9939	0.079	0.1374	0.1389	0.0285
28	1	1	0.2781	0.946	0.881	0.067	0.1058	0.1075	0.0287
29	1	0.9999	0.1603	0.5149	0.4515	0.0619	0.0828	0.0845	0.0352
30	1	1	1	1	1	0.6149	0.8752	0.8753	0.2173
31	1	1	0.8979	1	0.9999	0.5172	0.6426	0.6504	0.3158
32	1	1	0.7198	0.9533	0.9374	0.49	0.5556	0.5631	0.37
33	0.8314	0.8318	0.559	0.6539	0.6468	0.4867	0.5063	0.5101	0.4436

In summary, the three conditions are satisfied only by the following final two pairs:

- Pair #4; A=5.92x10^{76}; E$_a$=5.09x10^5 (t$_{50}$=100 hrs at 50°C, t$_{50}$=20 min at 60°C)

- Pair #11; A=1.62x10^{103}; E$_a$=6.79x10^5 (t$_{50}$=1000 hrs at 50°C, t$_{50}$=30 min at 60°C)

The frequency factor and the activation energy are proportional to the entropy and enthalpy, respectively. These constants separately do not give any physical insight into the reaction of tissue from native to coagulation. However, these constants can be used together to derive the first order reaction rate of achieving coagulation:

$$k = A \cdot e^{\frac{-E_a}{RT}}$$
Eq.6.4

where k is the reaction rate. Figure 6.11 gives the reaction rate for temperatures between 50 and 70 ^{o}C using the above resultant Arrhenius constant pairs and equation 6.4. Figure 6.12 gives the time values for 50% denaturation between 50 and 70 ^{o}C when using the reaction rates in figure 6.11. The time values in figure 6.12 validate the reaction rates obtained for the above resultant pairs. The reaction rates for pair #4 and #11 at 50 ^{o}C are 1.93x10^{-6} and 1.93x10^{-7} s^{-1}, respectively, while those at 60 ^{o}C are 5.77x10^{-4} and 3.85x10^{-4}, respectively. The reaction rates obtained by equation 6.4 show that the kinetics at 50 ^{o}C are not sufficient to reach coagulation within a practical duration.

6.6 Discussion

The goal of our LITT procedure is to induce a 3 cm thermal lesion encompassing 1 cm diameter breast tumor plus a surrounding 1 cm thick rim of healthy tissue. The optical-thermal model uses the Arrhenius equation to calculate the amount of photocoagulation. There are no published values of the Arrhenius parameters (activation energy and frequency factor) for the coagulation of ex-vivo fibro-fatty tissue. One of the

difficulties in finding values for these parameters is the extremely wide range of values for the frequency factor (10^{40} to 10^{120} s^{-1}). In addition, it is difficult to select initial values of the frequency factor and activation energy because there is no direct correlation between these parameters and experimental observations. To overcome these difficulties, we developed a method that starts with an assumption of the coagulation times at selected temperatures. A relatively narrow range of coagulation times can be assumed based on experimental observations. Combined with temperature and coagulation measurements, this approach produces a relatively narrow range of the activation energy (5×10^5 to 7×10^5 J mol^{-1}). A much wider range is found for the frequency factor (5.92×10^{76} to 1.62×10^{103} s^{-1}). Even though the variability of the frequency factor appears to be excessive at first sight, an analysis of the Arrhenius equation shows that it simply reflects the uncertainty on the value of the activation energy. According to equation 6.1, assuming a constant value of the damage integral, a change ΔE_a in the activation energy at a given temperature is equivalent to multiplying the frequency factor by: $e^{\frac{-\Delta E_a}{RT_c}}$. For instance, for $T_c = 60^{\circ}C$ and $\Delta E_a = 0.5\times10^5$ J mol^{-1}, the frequency factor is multiplied by 1.4×10^{-8}. This example shows that two Arrhenius pairs with slightly different activation energies that predict the same percentage of coagulation will have a difference of several orders of magnitude in the frequency factor.

The comparison of measured coagulation zones with predictions obtained from temperature measurements combined with the values of the Arrhenius parameters derived using our approach produced two final pairs of coefficients. Improvement in the experimental method could help further reduce the range of the experimentally derived coefficients. In our experiments, coagulation was induced at fixed laser power for three

different irradiation times. The limitation of this approach is that the temperature distributions were similar. A better approach may be to vary the laser power and keep the irradiation time constant (Zhu *et al* 2002). Varying the laser power will produce a larger difference in the temperature and coagulation response. These differences, in turn, should produce larger differences in the predictions obtained with the different Arrhenius pairs, which should make it easier to identify the pair that matches the experimental conditions.

Our study also showed that precise positioning of the thermocouples and optical fiber is critical. If the thermocouples are not located in the expected position, there will be a discrepancy between the predicted and measured coagulation. This problem was observed in several of our experiments. For instance, the first experiment at five minutes did not produce useful information probably because of the misplacement of the thermocouples. In several experiments (second and third experiments at 10 minutes), the prediction obtained for thermocouple 3 did not match the measured coagulation.
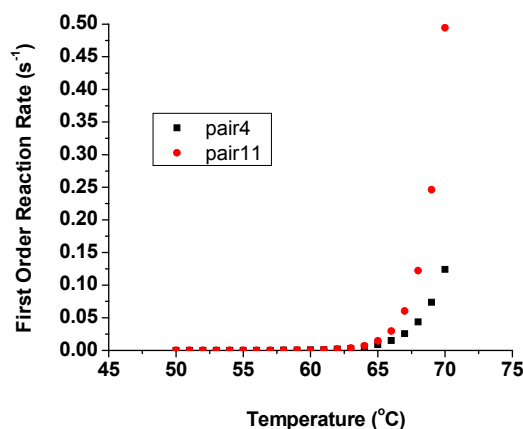

Figure 6.11: The first order reaction rate of coagulation using pair #4 and pair #11 for temperatures between 50 and 70 ^{o}C (323-343 K)

Figure 6.12: The first order reaction rate of coagulation using pair #4 and pair #11 for temperatures between 50 and 70 $^{\circ}$C (323-343 K)

Another limitation of the experimental approach is that coagulation boundaries were measured in ex-vivo tissue by gross anatomical observations. Gross anatomical observation is commonly used to measure coagulation boundaries induced by laser irradiation (Kangasniemi *et al* 2004, Janda *et al* 2003, Prudhomme *et al* 2003, Wohlgemuth *et al* 2001, Robinson *et al* 1998, Tobin and Waldow 1996, Mumtaz *et al* 1996, Muschter *et al* 1995, Muschter and Hofstetter 1995, Harries *et al* 1994). In some of the cases, especially those at lower irradiation times, the coagulation boundaries were not clearly visible as a result of the low output power used. This may result in inaccurate measurements of the boundary dimensions. Histological examination may provide more accurate measurements. Other methods to determine tissue damage may include the use of non-invasive imaging techniques (Purdie *et al* 2000) or measuring the birefringence change in denatured collagen (Thomsen and Pearce 1989). In addition, coagulation and cell death should ideally be assessed on tissue that was treated *in-vivo* to take into

account the effect of blood flow and other physiological effects that are not observed *in-vitro* (Zhu *et al* 2002).

The frequency factor and activation energy of the Arrhenius equation parameters for the quantification of cell death through hyperthermia has been obtained for different cell types. However, hyperthermia and photocoagulation, being different thermal processes, will have different parameters. Therefore, we could not use the parameters taken from cell death studies to properly predict the coagulation or structural protein denaturation in tissue (Bauer and Henle 1979). Other groups have derived Arrhenius parameters from experiments where the tissue was heated to temperatures greater than 50^oC. In each of these cases, the measured or assumed temperatures for selected durations and the extent of thermal damage at the site of the temperature measurements were incorporated in the Arrhenius equation to solve for the parameter pairs. Takata *et al* (1977) determined the values for ex-vivo porcine skin to be $A=9.4 \times 10^{104}$ s^{-1} ; $E_a=6.7 \times 10^5$ J mol^{-1} by visually measuring the extent of skin burns and the peak temperatures induced at the location of the burn (Pearce and Thomsen 1995). Maitland and Walsh (1997) determined the values for collagen from rat tail tendons to be $A=1.93 \times 10^{56}$ s^{-1} ; $E_a=3.70 \times 10^5$ J mol^{-1} by subjecting thin tendons to different temperatures that were constant for different durations. The coagulation percentage was assumed to be proportional to the linear birefringence. The parameters used by Germain *et al* (2001) for predicting thermal damage in liver ($A=2.69 \times 10^{103}$ s^{-1} ; $E_a=6.52 \times 10^5$ J mol^{-1}) was obtained by assuming coagulation times for two different temperatures. The parameters found by Purdie *et al* (2000) for thermal damage in rabbit thigh tumors ranged from 2.0×10^{112} to 3.08×10^{116} s^{-1} for the frequency factor and 7.14×10^5 to 7.26×10^5 J mol^{-1} for the activation energy.

These values were found by correlating the thermal damage in the tissue to the change in blood flow measured with dynamic contrast enhanced computed tomography. The pairs deduced by our study are within the range of these values (pair #11, $A=1.617 \times 10^{103}$ s^{-1} ; $E_a=6.79 \times 10^5$ J mol^{-1}).

6.7 Summary and conclusion

In this chapter, we obtained the Arrhenius equation constants that will predict the thermal coagulation induced in ex-vivo porcine mammary chain fibro-fatty tissue during LITT. A method was developed to obtain these parameters by comparing the values predicted by the Arrhenius equation with those experimentally observed in ex-vivo porcine fibro-fatty tissue after laser irradiation at 5, 10, and 15 minutes. Thirty-three activation energy – frequency factor pairs, deduced by assuming different 50% coagulation times at 50 and 60°C, were used with the temperature measurements from the laser irradiation experiments in ex-vivo porcine tissue to predict the coagulation. The pairs that most closely matched the conditions set by the experimental observed coagulation were selected. The final pairs were the following:

a) $A=5.92 \times 10^{76}$ s^{-1} ; $E_a=5.09 \times 10^5$ J mol^{-1}

b) $A=1.62 \times 10^{103}$ s^{-1} ; $E_a=6.79 \times 10^5$ J mol^{-1}

The reaction rates calculated by using the above resultant pairs show that the kinetics at 50 ^{o}C is not sufficient to achieve coagulation. In the future, initial temperature of 60 and 70 ^{o}C or 60 and 65 ^{o}C, in which coagulation is surely achieved, should be used initially to determine our initial Arrhenius equation parameters.

7. VALIDATION AND APPLICATION OF THE OPTICAL THERMAL MODEL

7.1. Aims

The purpose of the investigations described in this chapter is:

a)   To validate the optical-thermal by comparing the predicted values to measurements recorded during laser heating experiments in *ex-vivo* porcine mammary chain tissue, and

b)   To predict the laser parameters necessary to coagulate a 3 cm diameter volume of tissue in the human breast using the optical-thermal model.

7.2 Thermal model validation

7.2.1 Purpose

The purpose of these investigations is to validate the optical-thermal model. This will be done by:

a)   Comparing the temperature distribution calculated using the thermal model for *ex-vivo* porcine mammary chain fibro-fatty tissue with temperatures measured during laser irradiation (Salas *et al* 2004), and

b)   Comparing the coagulation zone predicted by the coagulation model for *ex-vivo* porcine mammary chain fibro-fatty tissue with those observed after laser irradiation (Salas *et al* 2004).

7.2.2 Laser irradiation experiments in *ex-vivo* porcine tissue

Ex-vivo porcine mammary chain tissue was used for the validation of the optical-thermal model. The pig tissue was obtained from the University of Miami Division of Veterinary Resources and consisted of a top, thin layer of skin, a 1.0-1.5 cm thick layer of mammary gland tissue, and a bottom, muscle layer. Two 90 x 90 x 10 mm samples were excised from each tissue.

The experimental set-up has been described in previous publications (Salas *et al* 2004). The two pig samples were placed on a lab jack inside a water bath. These samples were oriented such that the skin layers are facing away from each other. An optical fiber is inserted into the top tissue sample through the side of the water bath. The top lid is placed on the water bath, compressing the tissue sample enough such that there is no movement during the laser heating experiments (Figure 7.1). Fifteen T-type copper-constantan thermocouples (MT-23, Physitemp Instruments Inc, Clifton, NJ) are inserted into the tissue sample through the top lid of the water bath (Figure 7.2). These thermocouples are placed 5, 10, and 15 mm from the fiber axis.

The tissue was heated with either a 980 nm diode laser system (AOC25, Applied Optronics Inc., South Plainfield, NJ) coupled to an REM Series B diffusing tip optical fiber (outer diameter = 1.7 mm, light-emitting length = 24 mm) (CardioFocus, Marlborough, MA), a 940 nm diode laser system (Medilas D SkinPulse, Dornier MedTech, Kennesaw, GA) coupled to an H-6111-2 diffusing tip optical fiber (outer diameter = 0.9 mm, light-emitting length = 20 mm) (Dornier Medical Systems Inc., Kennesaw, GA), or an 830 nm diode laser system (Indigo830, Ethicon Endo-Surgery, Inc., Cincinnati, OH) coupled to an Indigo diffusing tip optical fiber (outer diameter = 1.8

mm, light-emitting length = 16 mm) (Ethicon Endo-Surgery, Inc., Cincinnati, OH). Both the emission pattern of the Indigo and Dornier fibers are given in section 3.2. The emission pattern out of the REM fiber is similar to that of the Indigo fiber. The irradiation time of each experiment was ten minutes. The 980 nm radiation was delivered at 3.2 W and the 830 and 940 nm at 4.0 W. The temperature measured by each thermocouple was recorded during the irradiation time and for ten minutes after the laser is turned off. The top tissue was then removed from the water bath and sliced in half along the fiber axis. The coagulation zone induced in the tissue was quantified by measuring the long and short axis of the elliptical region of tissue discoloration with a ruler. The thermal responses at each wavelength are shown in Figures 7.3 and 7.4.
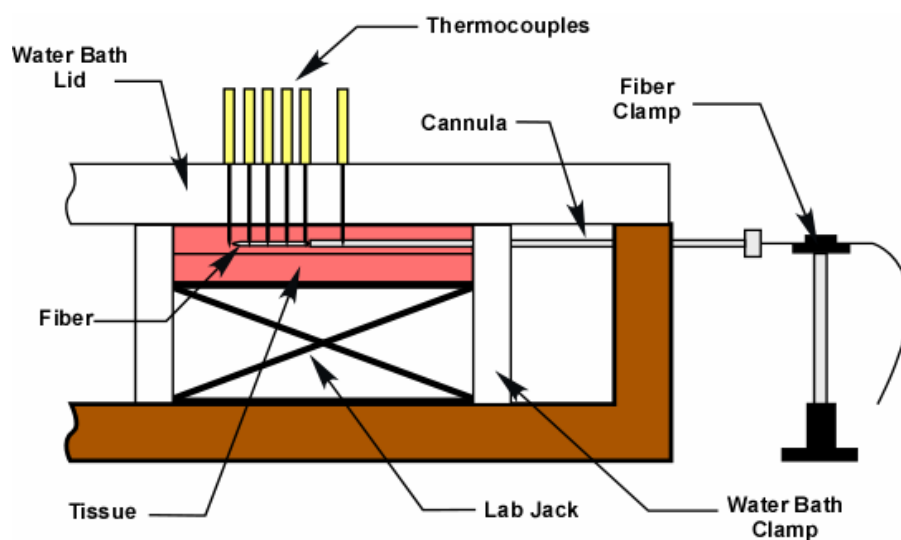

Figure 7.1: Experimental set-up for the laser irradiation of ex-vivo porcine mammary chain fibro-fatty tissue at 830, 940, and 980 nm
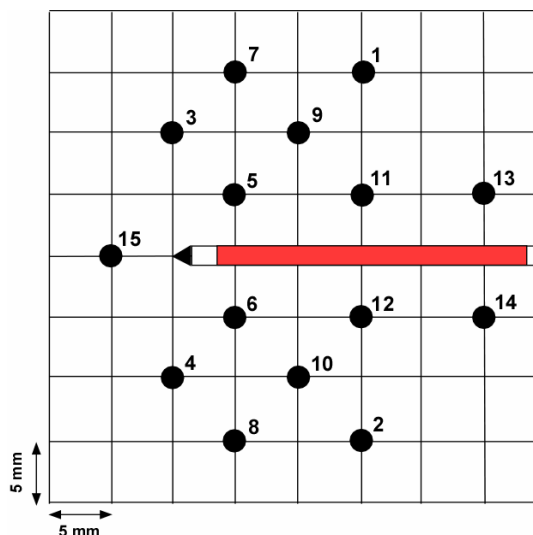
Figure 7.2: Thermocouple distribution during laser irradiation of ex-vivo porcine mammary chain fibro-fatty tissue at 830, 940, and 980 nm

7.2.3. Comparison of calculated and measured temperatures

To validate the model, the temperatures recorded by selected thermocouples were used. Three thermocouples at 5 (TC 12), 10 (TC 10), and 15 (TC 2) mm were chosen at 980 nm. One thermocouple at 5 mm was chosen at 830 nm (TC 6) and 940 nm (TC 5). A MATLAB program was written to calculate the temperature for these thermocouples using equations 4.38. The input parameters of the program are given in Table 7.1. The program calculates the temperature during ten minutes of laser irradiation.

The thermal model was designed for tissue samples with boundaries at constant temperature located far away from the laser source. Due to the small tissue thickness used in the experiments, the boundary conditions of the optical-thermal model do not apply. In addition, there are uncertainties in the position of the thermocouples and in the value of the effective attenuation coefficients. A preliminary analysis showed that these potential sources of error produce an overestimation of the temperature (Figure 7.4). The

optical-thermal model was therefore validated by finding if there is a set of input parameters μ_{eff}, b, and y (see Table 7.1) that provide a good agreement between the model and the experiments. The model will be considered valid if these values of μ_{eff}, b, and y are within the expected uncertainty.

Table 7.1: The input parameters for the optical-thermal model

Input Parameters For The Optical-Thermal Model					
				Values	
Input Parameters	Description	830 nm	940 nm	980 nm	
k (W mm^{-1} ^{o}C^{-1})	Thermal conductivity of the tissue	0.00064	0.00064	0.00064	
α (mm^2 s^{-1})	Thermal diffusivity of the tissue	0.154	0.154	0.154	
b (mm)	Outer radius of the spherical domain	10-50	10-50	10-50	
μ_{eff} (mm^{-1})	Effective attenuation coefficient	0.10-0.50	0.10-0.50	0.10-0.50	
a=r_s (mm)	Radius of the fiber tip	0.90	0.45	0.85	
P_tip (W)	Power emitted out of the fiber tip	3.2	4.0	4.0	
L_tip (mm)	Light-emitting length of the fiber tip	16	20	24	
x (mm)	Location of the thermocouple along the x-axis (fiber axis) in reference to the center of the diffusing tip	0.7-4.3	5	5	
y (mm)	Location of the thermocouple along the x-axis (fiber axis) in reference to the center of the diffusing tip	5-15	5	5	
N	Number of spheres comprising the diffusing tip	51	51	51	

(a.)
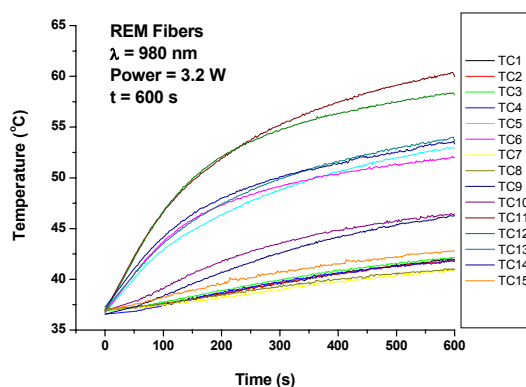
(b.)
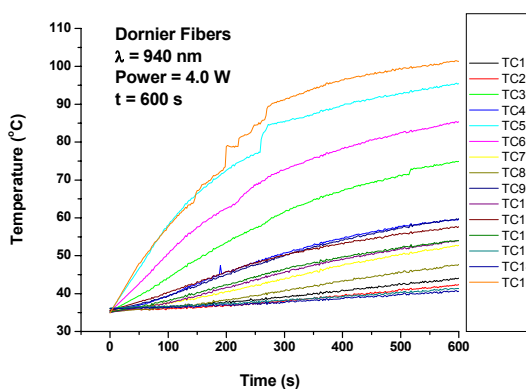
(c.)
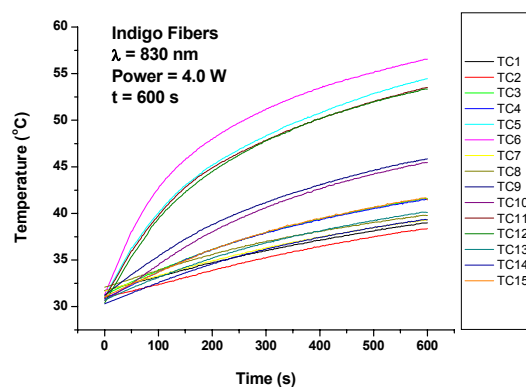
Figure 7.3: The temperature measured from 15 thermocouples during laser irradiation at (a) 980 nm with an REM diffusing tip fiber at 3.2 W, (b) 940 nm with a Dornier diffusing tip fiber at 4.0 W, and (c) 830 nm with an Indigo diffusing tip fiber at 4.0 W.

(a.)
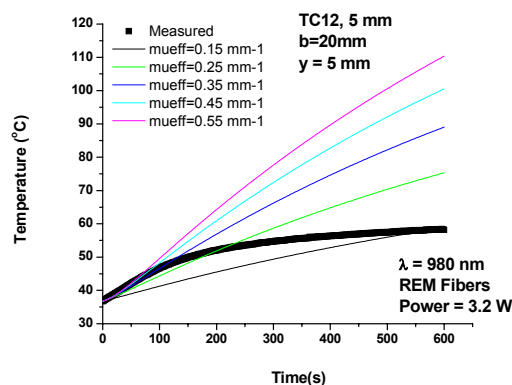
(b.)
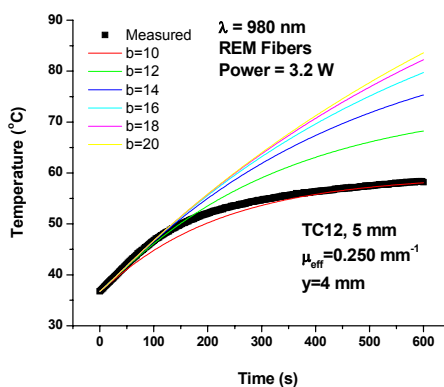
(c.)
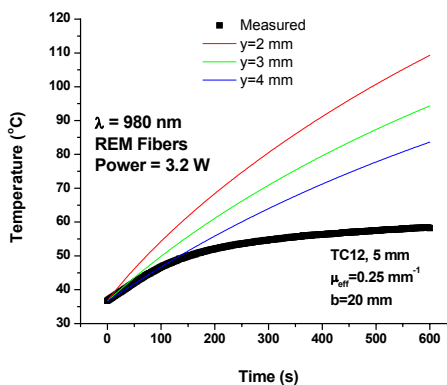
Figure 7.4: The effect of (a) the effective attenuation coefficient "μ_{eff}", (b) the outer radius "b", and (c) the position of the thermocouple (distance from the fiber axis) "y" on the temperature predicted by the optical thermal model. These simulations show that small variations in the parameters μ_{eff}, y, and b produce large variations in the predicted temperatures.

7.2.4 Thermal model validation results

The calculated and measured temperatures for the selected thermocouples are compared in Figures 7.5-7.9. The results are summarized in Table 7.2. For each thermocouple, the analysis finds values of the parameters μ_{eff}, b, and y that are within the expected uncertainties and at the same time provide a close agreement between the predicted and measured temperatures.

<u>Table 7.2:</u> The measured and simulation-derived values of μ_{eff}, y, and b for laser irradiation experiments at 830, 940, and 980 nm.

Input Parameters Of The Optical-Thermal Model					
Wavelength	μ_{eff} (mm^{-1})		y (mm)		b (mm)
(nm)	Measured	Model	TC Position	Model	Model
980	0.466	0.340	5	4	9
980	0.466	0.340	10	8	12.5
980	0.466	0.340	15	12	15
830	0.238	0.300	5	4	9
940	0.370	0.330	5	4	11

<u>Figure 7.5:</u> Comparison of the calculated and measured temperature for ex-vivo porcine mammary chain fibro-fatty tissue irradiated with a 980 nm diode laser system coupled to an REM B-series diffusing tip optical fiber. The temperature was measured 5 mm from the fiber axis.

Figure 7.6: Comparison of the calculated and measured temperature for ex-vivo porcine mammary chain fibro-fatty tissue irradiated with a 980 nm diode laser system coupled to an REM B-series diffusing tip optical fiber. The temperature was measured 10 mm from the fiber axis.

Figure 7.7: Comparison of the calculated and measured temperature for ex-vivo porcine mammary chain fibro-fatty tissue irradiated with a 980 nm diode laser system coupled to an REM B-series diffusing tip optical fiber. The temperature was measured 15 mm from the fiber axis.
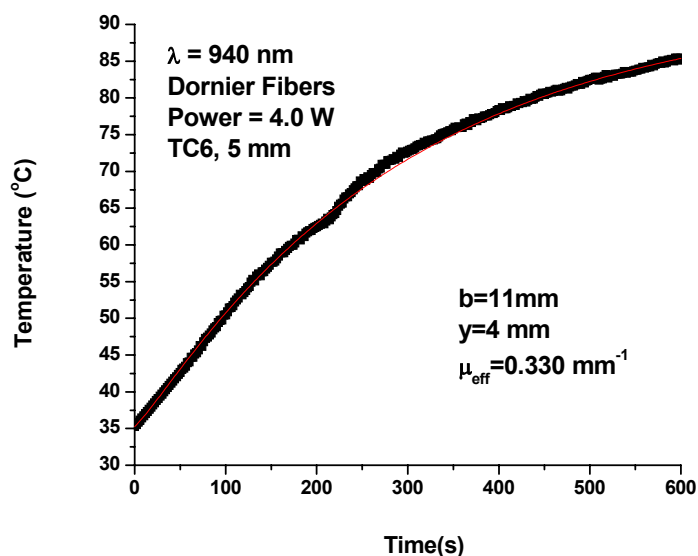
Figure 7.8: Comparison of the calculated and measured temperature for ex-vivo porcine mammary chain fibro-fatty tissue irradiated with a 940 nm diode laser system coupled to a Dornier H-6111-2 diffusing tip optical fiber. The temperature was measured 5 mm from the fiber axis.
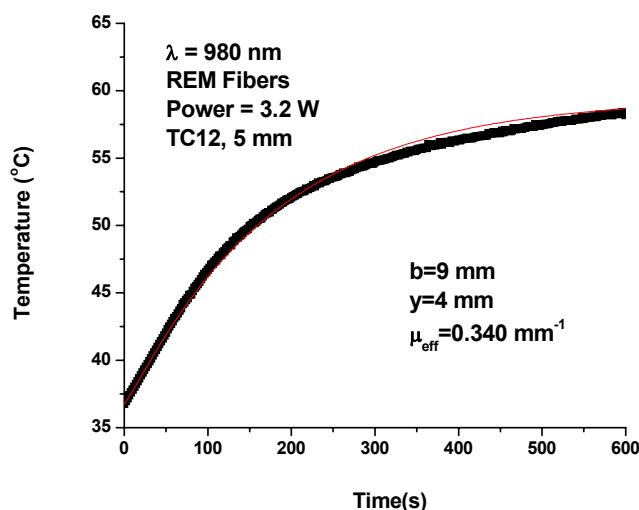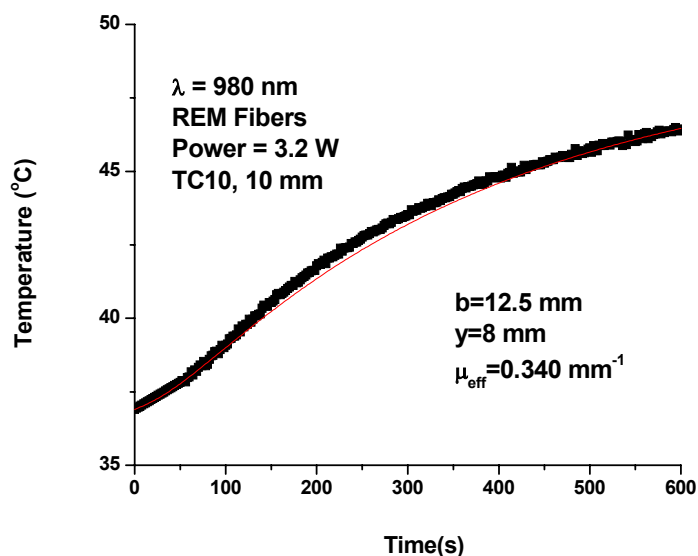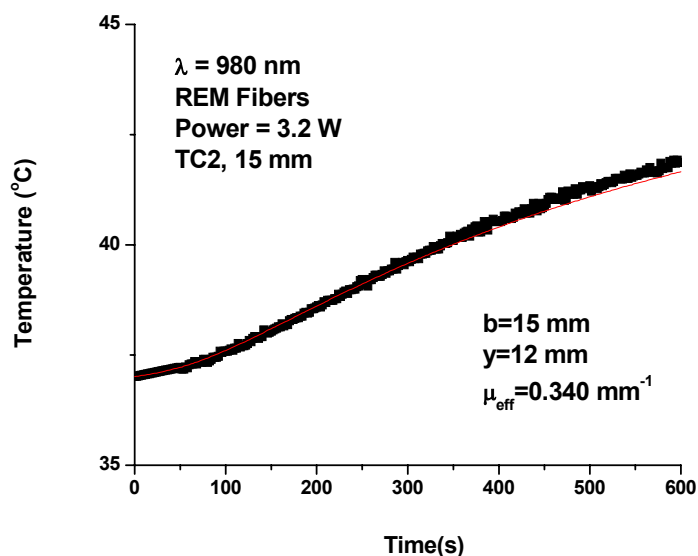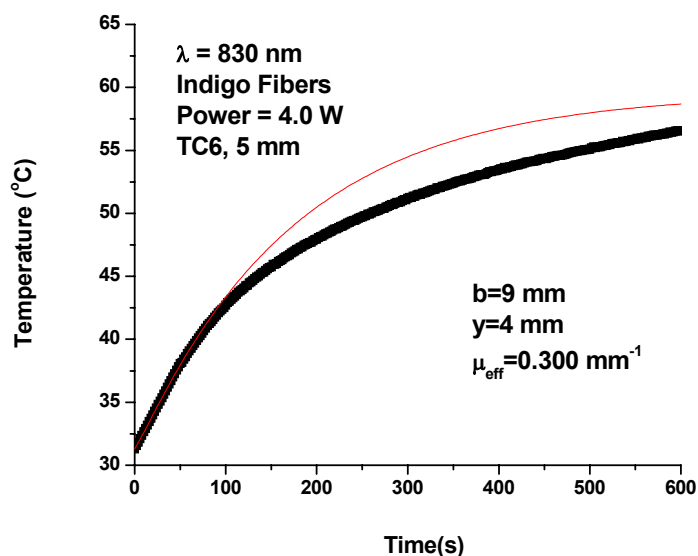

Figure 7.9: Comparison of the calculated and measured temperature for ex-vivo porcine mammary chain fibro-fatty tissue irradiated with an 830 nm diode laser system coupled to an Indigo diffusing tip optical fiber. The temperature was measured 5 mm from the fiber axis.

7.2.5 Discussion

Prior to adjusting the input parameters to account for uncertainties in the values of μ_{eff} and y and differences in the boundary conditions between the model and the experimental system, the thermal model overestimated the temperatures produced during laser irradiation in *ex-vivo* porcine tissue. These differences are expected first because the thermal model was designed with the assumption that the tissue boundaries are far enough from the fiber tip that they have no effect on temperature distribution. In the experiments, however, the thickness of the tissue samples was only approximately 10 mm. This thickness is on the same order as the heat diffusion length $((\alpha t)^{0.5}=9.6$ mm when t=10 min). The assumption that the boundaries have no effect on the temperature is therefore not valid. The temperature will be lower than predicted by the model since the surface temperature of the tissue is maintained at 37 ^{o}C in the experimental set-up. However, the simulations show that the value of "b" can be adjusted to compensate for this discrepancy.

According to the preliminary analysis, the temperature in the short time period was less than the measured temperatures for all effective attenuation coefficients within the range tested (Figure 7.4a). This can be attributed to the positioning error of the thermocouple tip. This error may be due to bending or tilting of the thermocouple probe or to movement of the thermocouple during irradiation. Again, the simulations showed that this error can be accounted for by adjusting the value of the input parameter "y". In all cases, the value of "y" obtained from the simulations was between 1 and 3 mm of the expected position of the thermocouple.

Another potential source of error is that the thermocouples used in our experiments consist of copper and constantan wires encased in a stainless steel shaft. The high thermal conductivity and high optical absorption of the stainless steel shaft can produce measurement errors. Ideally, future work should be performed with thermocouples with a Teflon shaft rather than stainless steel or with optical temperature probes.

The effective attenuation coefficients that give the best match between the model and the experiments at 980, 940, and 830 nm were approximately 0.340, 0.330, and 0.300 mm^{-1}, respectively. The effective attenuation coefficients measured with the single integrating sphere optical property measurement system (see chapter 5) were 0.466, 0.370, and 0.238 mm^{-1}, respectively The relative difference at 830, 940, and 980 nm is 26, 11, and 26 %, respectively. These relative errors are within an acceptable range.

Altogether these findings show that the model provides reliable values of the temperature during LITT in fibro-fatty tissue as long as accurate values of the input parameters are entered in the model. In particular, the simulations suggest that the condition on the outer boundary can have a significant effect on the temperature distribution (Figure 7.10).

7.2.6. Summary and Conclusion

The purpose of these investigations was to validate the optical-thermal model by comparing simulated temperatures to temperatures measured during laser irradiation experiments in *ex-vivo* porcine mammary chain tissue. The results show that once differences in the boundary conditions and uncertainties in the position of the thermocouples and the effective attenuation coefficients are taken into account, the

predictions of the model are in excellent agreement with the measurements. The results also suggest that tissue samples of larger thickness (>4mm) should be used in experiments to avoid that the boundary conditions affect the temperature response.

7.3 Coagulation model validation

7.3.1 Method

The coagulation model was validated by comparing the observed coagulation in *ex-vivo* porcine mammary chain tissue with the predictions of the Arrhenius equation using the frequency factor (A)-activation energy (ΔE) pairs selected in chapter 6:

a) Pair #4: $A = 5.92 \times 10^{76}$ s^{-1}; $\Delta E = 5.09 \times 10^{5}$ J mol^{-1}

b) Pair #11: $A = 1.62 \times 10^{103}$ s^{-1}; $\Delta E = 6.79 \times 10^{5}$ J mol^{-1}
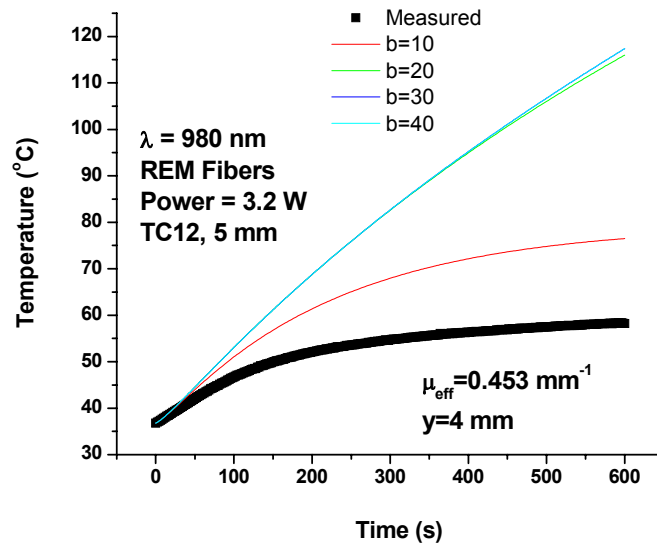
Figure 7.10: Comparison between the simulated temperatures as a function of time for different "b" values and the measured temperature during laser irradiation in ex-vivo porcine tissue at 980 nm with an REM B-series diffusing tip fiber. When b >25 mm, the predicted temperature remains unchanged.

The comparison was made using temperature and coagulation data obtained from five laser irradiation experiments (see section 7.2.2). The dimensions of the observed elliptical coagulation zones are given in Table 7.3. A MATLAB program was written to calculate the coagulation in tissue using the temperature measurements recorded during laser irradiation experiments and the Arrrhenius equation (eq. 4.41). This program calculates the coagulation for all 15 thermocouples used in the experiments. The final coagulation after irradiation was compared to the observed coagulation. The location in the tissue where the simulation predicts approximately 100% (within the coagulation zone), 50% (boundary of the coagulation zone), and 0% (outside the coagulation zone) should match the dimensions of the measured coagulation.

Table 7.3: The grossly observed elliptical coagulation zone dimensions in ex-vivo porcine mammary chain fibro-fatty tissue after laser irradiation for ten minutes.

Grossly Observed Elliptical Coagulation Dimensions			
Experiment	Wavelength and Power	Major Axis (cm)	Minor Axis (cm)
1	980 nm, 4.8 W	2.0	1.8
2	980 nm, 4.8 W	3.0	1.75
3	980 nm, 6.4 W	3.0	2.4
4	980 nm, 6.4 W	3.5	2.0
5	940 nm, 4.0 W	3.0	2.5

7.3.2 Results

The measured and predicted coagulation zones in ex-vivo porcine tissue for each experiment are given in Figures 7.11-7.15. The measured and calculated coagulation zones fit fairly well for both Arrhenius equation pairs. However, for thermocouple locations near the boundaries, there was better agreement with pair #4 than with pair #11. Therefore, pair #4 (A = 5.92 x 10^{76} s^{-1}; ΔE = 5.09 x 10^5 J mol^{-1}) is the final choice.
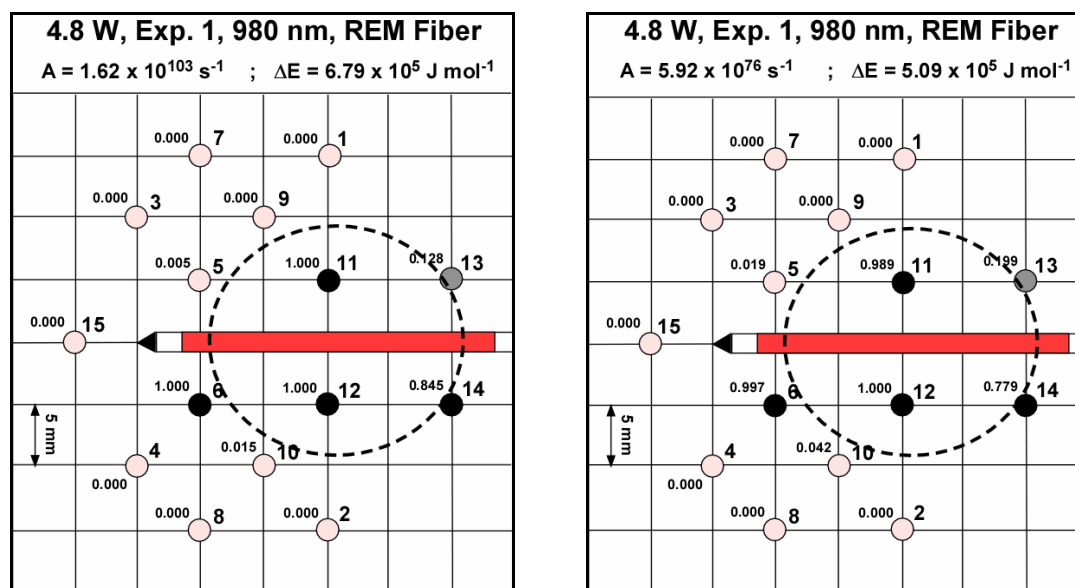
Figure 7.11: The calculated and measured coagulation in ex-vivo porcine mammary chain fibro-fatty tissue during laser irradiation at 980 nm with an REM B-series diffusing tip fiber and 4.8 W (Experiment 1 in Table 7.3). The dotted lines show the measured coagulation zone. The numbers show the calculated percentage of coagulation at each thermocouple location. White dots: <10% coagulation, grey dots: 10%<coagulation<50%, and black dots: >50% coagulation.
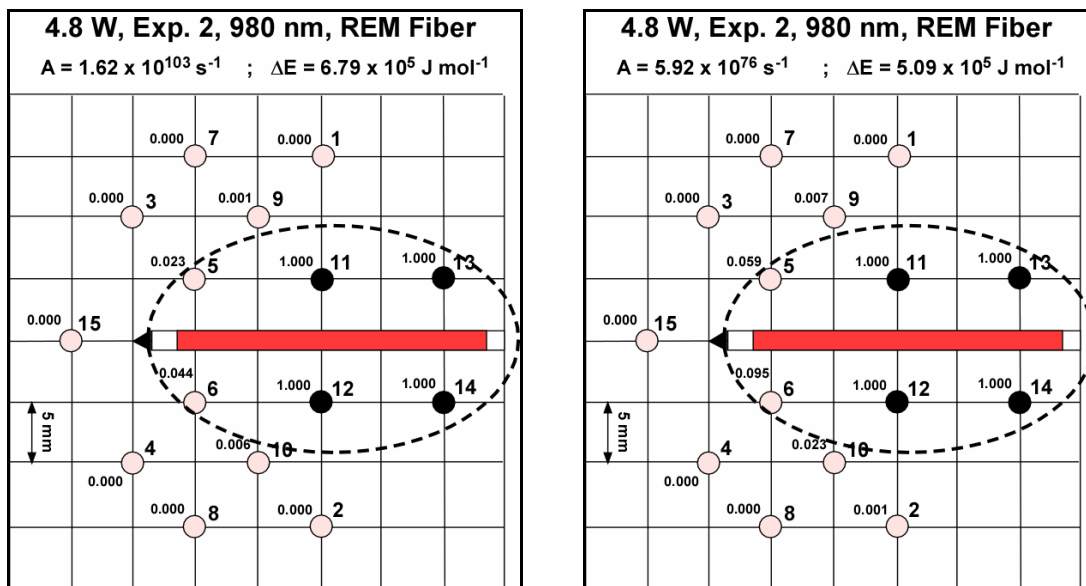
Figure 7.12: The calculated and measured coagulation in ex-vivo porcine mammary chain fibro-fatty tissue during laser irradiation at 980 nm with an REM B-series diffusing tip fiber and 4.8 W (Experiment 2 in Table 7.3). The dotted lines show the measured coagulation zone. The numbers show the calculated percentage of coagulation at each thermocouple location. White dots: <10% coagulation, grey dots: 10%<coagulation<50%, and black dots: >50% coagulation.
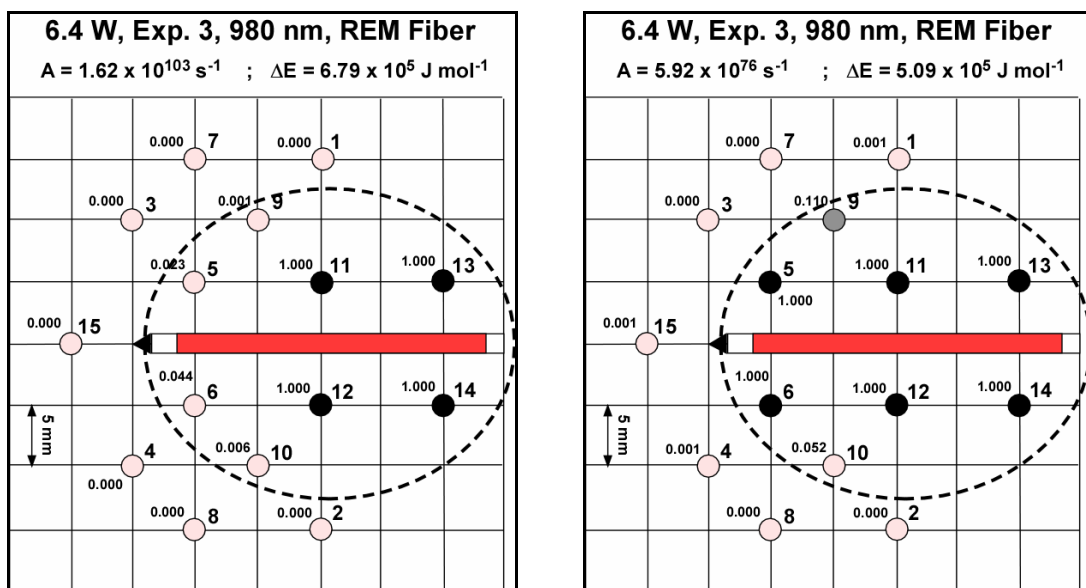
Figure 7.13: The calculated and measured coagulation in ex-vivo porcine mammary chain fibro-fatty tissue during laser irradiation at 980 nm with an REM B-series diffusing tip fiber and 6.4 W (Experiment 3 in Table 7.3). The dotted lines show the measured coagulation zone. The numbers show the calculated percentage of coagulation at each thermocouple location. White dots: <10% coagulation, grey dots: 10%<coagulation<50%, and black dots: >50% coagulation.
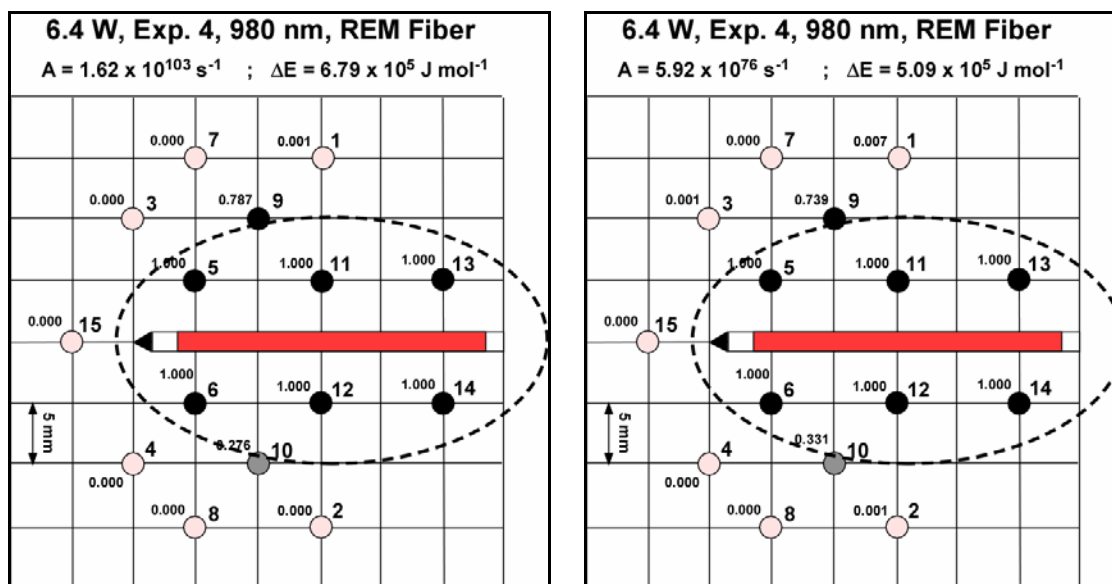
Figure 7.14: The calculated and measured coagulation in ex-vivo porcine mammary chain fibro-fatty tissue during laser irradiation at 980 nm with an REM B-series diffusing tip fiber and 6.4 W (Experiment 4 in Table 7.3). The dotted lines show the measured coagulation zone. The numbers show the calculated percentage of coagulation at each thermocouple location. White dots: <10% coagulation, grey dots: 10%<coagulation<50%, and black dots: >50% coagulation.
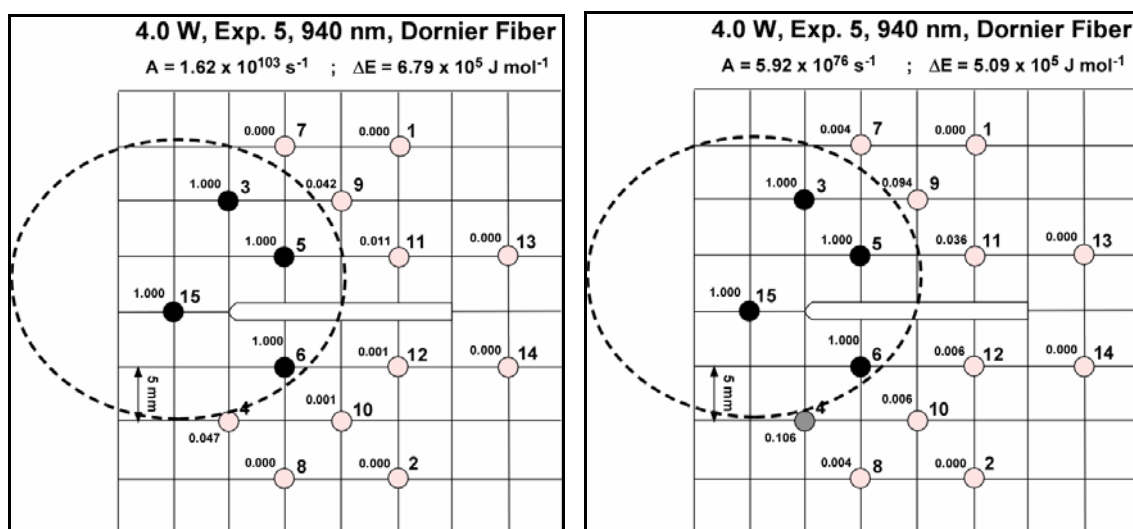
Figure 7.15: The calculated and measured coagulation in ex-vivo porcine mammary chain fibro-fatty tissue during laser irradiation at 940 nm with a Dornier H-6111-2 diffusing tip fiber and 4.0 W (Experiment 5 in Table 7.3). The dotted lines show the measured coagulation zone. The numbers show the calculated percentage of coagulation at each thermocouple location. White dots: <10% coagulation, grey dots: 10%<coagulation<50%, and black dots: >50% coagulation.

7.3.3 Summary and conclusion

The predicted and measured coagulation volumes are in good agreement. In all but one case (TC 6, experiment 1), the locations where the model predicts 100% coagulation are within the actual laser-induced coagulation zone. Therefore, the coagulation model does not overestimate the actual coagulation zone. In all cases, the boundary of the predicted coagulation zone was within ± 2.5 mm from the actual boundary. This difference is within the uncertainty of the position of the thermocouple and the optical fiber. Overall, the experiments show that the prediction of the coagulation model when $A = 5.92 \times 10^{76}$ s^{-1} and $\Delta E = 5.09 \times 10^5$ J mol^{-1} is in good agreement with the coagulation zones produced with LITT in *ex-vivo* porcine tissue.

7.4 Application of the optical-thermal model

7.4.1 Purpose

The optical-thermal model was designed to calculate the temperature and coagulation distribution in the breast during laser interstitial thermotherapy with a diffusing tip optical fiber. In this section, the model will be applied to determine the laser parameters (wavelength, power, duration) necessary to treat a 3 cm diameter volume of breast tissue that includes a 1 cm diameter tumor plus a 1 cm thick surrounding rim of healthy tissue while avoiding vaporization and carbonization.

7.4.2 Method

Ideally, the following criteria must be achieved to successfully coagulate a 3 cm diameter volume:

a) The temperature should not reach 100 °C (boiling point of water) at the fiber surface

b) The temperature at 15 mm away from the fiber axis should reach 65 °C. According to the coagulation model, this temperature is expected to produce coagulation in the breast.

Under these criteria, simulations were performed to determine the following parameters:

a) the power needed to produce coagulation at 10 and 15 mm from the fiber axis while keeping the fiber surface temperature below 100 °C for 10, 20, and 30 minute irradiation times, and

b) the power required to produce coagulation at 10 and 15 mm from the fiber axis while avoiding vaporization at the fiber surface for 10, 20, and 30 minute irradiation times

The simulations assume irradiation with an Indigo diffusing tip optical fiber (fiber diameter = 0.9 mm, light-emitting length = 16 mm). The input parameters are given in Table 7.4. These values were calculated for values of the effective attenuation coefficient ranging from 0.10 to 0.50 mm^{-1}. The effective attenuation coefficient for breast tissue is within this range. According to a preliminary analysis, as long as the value of "b" is greater than 30 mm, this parameter has a negligible effect on the temperature distribution. Therefore, a "b" value of 40 mm was chosen, which corresponds to a breast thickness of 80 mm.

7.4.3 Temperature distribution when the peak temperature is 100 $^{\circ}$C

The optical power necessary to achieve a temperature of 100 $^{\circ}$C at the fiber tip (y=0.9 mm) was calculated for effective attenuation coefficients ranging from 0.10 to 0.50 mm^{-1} in increments of 0.05 mm^{-1}. Since the temperature increase is directly proportional to the power emitted by the fiber tip, the temperature at the fiber surface was first calculated for an output power of 1.0 W. The power, P_{100}, that produces 100 $^{\circ}$C at the fiber tip was then calculated using the following equation:

$$P_{100} = \left(\frac{100 - 37}{T_{1W} - 37} \right), \qquad \text{Eq. 7.1}$$

where T_{1W} is the temperature in $^{\circ}$C produced at 1.0 W. The power was calculated for time t=600, 1200, and 1800 s. The temperature distribution produced with this power was then calculated for each value of the effective attenuation coefficient (Figure 7.16).

The results show that in all cases, the temperature at 15 mm, and even at 10 mm, is well below the coagulation temperature (<50 $^{\circ}$C). This finding suggests that the desired coagulation volume cannot be produced when the laser power is selected to produce a peak temperature below the boiling temperature of water (100 $^{\circ}$C). Figure 7.17 also shows that when the laser power is selected to produce the same temperature at the fiber surface, the value of the effective attenuation coefficient does not have a significant effect on the temperature distribution. The maximum difference in temperature produced by varying the effective attenuation coefficient between 0.1 and 0.5 mm^{-1} was less than 2 $^{\circ}$C (Figure 7.16).

Table 7.4: The input parameters used for the application of the optical-thermal model

Input Parameters	Values
k	0.00064 W mm^{-1} ^{o}C^{-1}
α	0.154 mm^2 s^{-1}
b	40 mm
μ_{eff}	0.10 – 0.50 mm^{-1}
a=r_s	0.90 mm
P_tip	Variable
L_tip	16 mm
x	0 mm
y	0.9, 10, and 15 mm
N	51

7.4.4 Temperature distribution when the peak temperature is below the vaporization threshold

The same technique as in the previous section was used to calculate the laser power required to produce a temperature of 65 ^{o}C at 15 mm from the fiber axis for values of the effective attenuation coefficient ranging from 0.10 to 0.50 mm^{-1}. The temperature distribution as a function of the distance from the optical fiber obtained with this laser power was then calculated. We then verified that the temperature at the surface of the fiber is below the vaporization threshold. The equivalent temperature for vaporization can be calculated using the following relation:

$$\Delta T_{eq} = \Delta T_{vap} + \frac{H}{c}, \qquad \text{Eq. 7.2}$$

where ΔT_{eq} is the equivalent temperature increase leading to vaporization, ΔT_{vap} is the temperature increase required to reach the vaporization temperature, H is the latent heat of vaporization, and c is the specific heat. We assumed that the vaporization temperature is equal to 100 ^{o}C and used the specific heat (c=4.18 kJ kg^{-1} ^{o}C^{-1}) and latent heat of

vaporization of water (H=2240 kJ kg^{-1}). With these values, we find ΔT_{eq}=598 ^{o}C. The results of these simulations (Figure 7.17) show that for a treatment time of 10 min (t=600s), coagulation can be produced at 15 mm without inducing vaporization as long as the effective attenuation coefficient is less than 0.3 mm^{-1}. When the treatment time is 15 or 30 min, coagulation can be achieved without producing vaporization for all values of the effective attenuation coefficient.

7.4.5 Discussion

The goal of our proposed treatment is to treat small tumors of the breast up to 1 cm in diameter plus a 1 cm thick rim of surrounding healthy tissue using laser interstitial thermotherapy within 30 minutes. The optical-thermal model was applied to determine the laser parameters (output power, irradiation time, optical fiber characteristics, wavelength) necessary to treat the target breast tissue volume without producing boiling or vaporization. According to our results, coagulation cannot be achieved at 15 mm and even at 10 mm from the fiber axis when the power is below the power necessary to reach the boiling temperature (100°C).

On the other hand, the simulations show that desired coagulation volume can be achieved without producing vaporization. When the treatment time is limited to ten minutes, the effective attenuation coefficient must be below 0.30 mm^{-1} to avoid vaporization. For longer treatment times, coagulation is achieved without vaporization independent of the value of the effective attenuation coefficient. However, to confirm these findings, a refined version of the model that takes into account the phase change must be developed. The current version of the optical thermal model predicts that the

temperature continues to increase even when the vaporization temperature (100 ^{o}C) is reached. The model therefore overestimates the temperature, especially at regions near the fiber tip.

When the phase change is taken into account, the thermal response becomes non-linear. The principle of linear superposition of spherical sources can therefore no longer be used to calculate the temperature produced by a cylindrical diffusing tip. Future refined versions of the model must calculate the light distribution produced by the entire cylindrical diffusing tip and solve the heat equation with the corresponding three-dimensional heat source term.

The optical-thermal model does not take into account the effect of blood flow. During *in-vivo* laser irradiation, until blood vessels are coagulated, blood flow will act as a heat sink. The blood supply of the tumor and surrounding healthy tissue may affect the temperature response. The magnitude of this effect remains to be investigated. If necessary, future versions of the model should account for blood perfusion.

Our simulations also suggest that similar temperature distributions are produced for a wide range of values of the effective attenuation coefficient when the power is adjusted to produce 65 ^{o}C at 15 mm. This finding suggests that the wavelength has a minimal effect on the treatment outcome if the power is properly adjusted.

(a.)
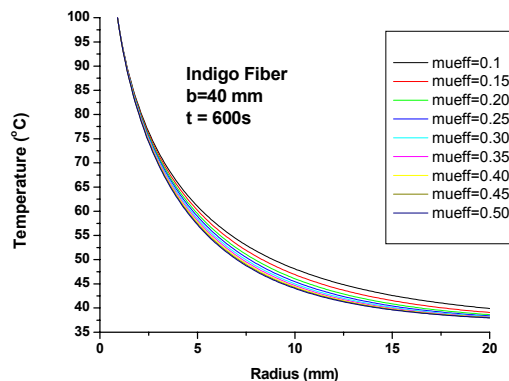
(b.)
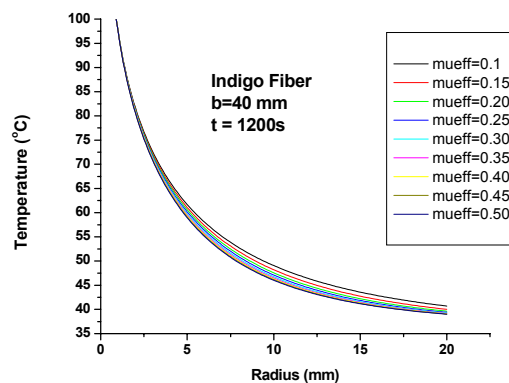
(c.)
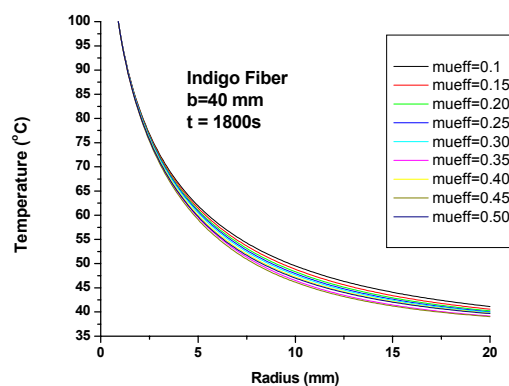
Figure 7.16: The temperature as a function of the distance from the center of the fiber axis for attenuation coefficients ranging from 0.10 to 0.50 mm^{-1} and at time = (a) 600, (b), 1200, and (c) 1800 s when the temperature at the fiber surface reaches 100 ^{o}C.

(a.)
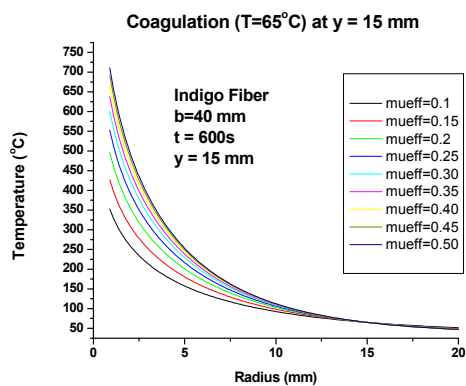
(b.)
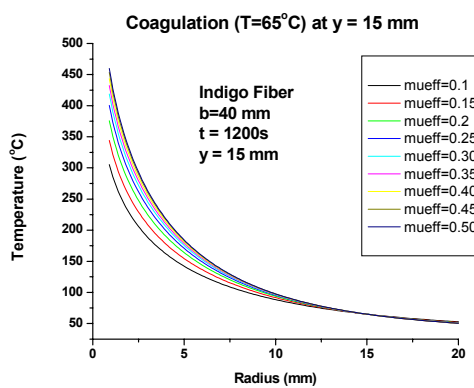
(c.)
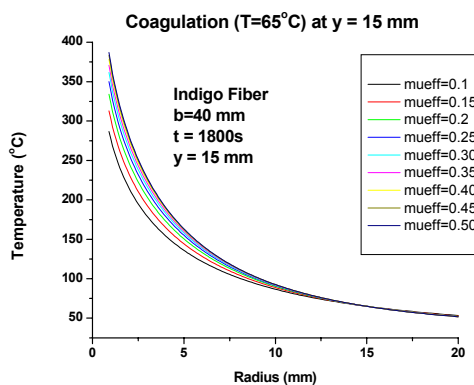
<u>Figure 7.17:</u> The temperature as a function of the distance from the center of the fiber axis for attenuation coefficients ranging from 0.10 to 0.50 mm^{-1} and at time = (a) 600, (b), 1200, and (c) 1800 s when the temperature reaches 65 ^{o}C at 15 mm from the fiber axis.

7.4.6 Summary and conclusion

The optical thermal model was applied to determine the laser parameters necessary to treat a 3 cm diameter volume of breast tissue. The results show that neither the 830, 940, nor 980 nm wavelength can induce a 3 cm diameter coagulation volume in the tissue within 30 minutes without exceeding 100 ^{o}C at the fiber surface. On the other hand, the desired coagulation can be produced in 15 min without causing vaporization or carbonization. The model suggests that this outcome can produced for a range of wavelengths as long as the power is selected accordingly. According to the optical-thermal model, with the *in-vivo* breast optical properties obtained by Cubeddu *et al* (2000), the power necessary to achieve the desired coagulation volume is 13.2 W at 10 min and 6.1 W at 20 min at 830 nm and 10.41 W at 10 min and 4.52 W at 20 min at 940 and 980 nm. Even though the model needs to be refined to take into account the phase change and potential effect of blood flow during *in-vivo* treatments, the application example demonstrates how the model can be used to derive optimal treatment parameters for LITT of breast cancer once accurate values of the optical properties are available.

8. SUMMARY AND FUTURE WORK

Breast cancer is the most common cancer in women in the United States according to the American Cancer Association. Up to the mid 1980's, mastectomy, the total removal of the mammary gland and axillary lymph nodes, was the sole treatment for all stages of malignant breast tumors. With advances in mammography and ultrasound, lumpectomy, the removal of only the tumor plus a surrounding area of healthy tissue, became the method of choice for small tumors. Advances in imaging and diagnostics allow earlier detection of tumors. Several minimally-invasive treatments are currently being explored as alternatives to lumpectomy for treatment of small, local tumors. These techniques include focused ultrasound, cryotherapy, radiofrequency heating, and laser interstitial thermotherapy (LITT).

Laser interstitial thermotherapy has the potential to treat different tumor sizes by adjusting the laser parameters (output power, wavelength, irradiation time, and fiber tip emission). Previous preliminary studies have focused on demonstrating the feasibility of LITT for tumors in the breast using a non-optimized delivery system. The purpose of this project was to develop a delivery system optimized for LITT of small tumors of the breast. The proposed approach is to combine laser interstitial thermotherapy with stereotactic imaging for fiber guidance and treatment monitoring and to use cylindrical diffusing tip optical fibers. The goals of the dissertation were:

a)   Design of a fiber insertion system for cylindrical diffusing tip optical fibers

www.manaraa.com

b)   Design and validation of an optical-thermal model to select optimal laser parameters for coagulation of 1 cm tumor plus a surrounding 1 cm thick rim of healthy tissue

A fiber insertion system compatible with a Fischer Imaging Mammotest / Mammovision Plus high resolution stereotactic digital X-ray biopsy system (Fischer Imaging Corp., Denver, CO) was designed. The fiber insertion system guides the fiber into the tumor site in similar fashion to the insertion of the biopsy needle. The feasibility of the insertion system was tested on a model of the breast.

An optical-thermal model was developed to determine the laser parameters necessary to treat a 3 cm diameter volume of breast tissue comprised of a 1 cm tumor surrounded by a 1 cm thick rim of healthy tissue. The optical-thermal model consists of a radiation model, a thermal model, and a coagulation model. The radiation model predicts the distribution of absorbed laser energy within the tissue during laser irradiation as a function of the optical properties of the tissue and the laser parameters. The thermal model predicts the temperature distribution produced by this absorbed energy. The coagulation model uses the Arrhenius equation to predict the volume of coagulation from this temperature distribution.

The model was validated using *ex-vivo* porcine mammary chain tissue. A single integrating sphere optical property measurement system and an inverse Monte Carlo algorithm were developed to measure the optical properties of *ex*-vivo porcine tissue at 830, 940, and 980 nm. An experimental method was developed to determine the parameters of the Arrhenius model (frequency factor (A) and activation energy (E_a)).

The optical-thermal model was validated by comparing the predicted temperature and coagulation to results of laser irradiation experiments in ex-vivo porcine mammary chain tissue at 830, 940, and 980 nm. There was excellent agreement between the predicted and measured temperature and coagulation volumes. These experiments demonstrate that the proposed optical-thermal model can be used to predict the temperature distribution and coagulation volume during LITT.

The model was applied to determine the laser parameters necessary to treat a 3 cm diameter volume of breast tissue. The simulations show that the desired coagulation volume cannot be achieved without exceeding 100 $^{\circ}$C at the fiber surface. However, it can be induced without producing vaporization. Using published values of the optical properties of the breast, the model predicts that coagulation can be produced without vaporization in 10 min with 10.4 W at 980 and 940 nm and 13.2 W at 830 nm. The same outcome can be achieved in 20 min with 4.5 W at 980 and 940 nm and 6.1 W at 830 nm.

The long-term goal of the project is to develop a treatment algorithm for LITT of breast cancer that can be tested clinically on patients. Before clinical testing can be started, a final prototype of the fiber insertion system suitable for clinical use must be designed and the position accuracy must be evaluated. The current version of the optical-thermal model provides a set of laser parameters that can be used for initial clinical testing. However, based on our findings, the following refinements and additional experiments are suggested to help confirm that these parameters are optimal:

a) Measurement of the effective attenuation coefficient of healthy and cancerous human breast tissue *in-vitro* and, if possible, *in-vivo*.

b)   Improvement of the *ex-vivo* experimental set up that was used to simulate LITT in *ex-vivo* porcine mammary chain tissue. The system must be modified to allow use of thicker tissue, more precise positioning of the diffusing tip, and temperature recordings using probes that have a lesser effect on the temperature distribution.

c)   Confirmation of the values of the Arrhenius equation parameters in human breast tissue using an improved experimental protocol that produces different coagulation volumes by varying the power instead of the irradiation time.

d)   Refinement of the thermal model to take into account the latent heat of vaporization, the geometry of the breast, and potential effect of blood flow.

REFERENCES

Akimov A, Seregin VE, Rusanov KV, Tyurina EG, Glushko TA, Nevzorov VP, Nevzorova OF, Akimova EV; "Nd:YAG Interstitial Laser Thermotherapy in the Treatment of Breast Cancer"; *Lasers in Surgery and Medicine* 22:257-267, 1998

Akimov A, Seregin VE, Rusanov KV, Tyurina EG, Glushko TA, Nevzorov VP, Nevzorova OF, Akimova EV; "Nd:YAG Interstitial Laser Thermotherapy in the Treatment of Breast Cancer"; *Lasers in Surgery and Medicine*, 22:257-267, 1997

Allred DC; "Biologic Characteristics Of Ductal Carcinoma In Situ"; *Ductal Carcinoma In Situ Of The Breast*, Silverstein MJ, Recht A, Lagios MD, eds.; ch.5, p.37-48, Lippincott-Williams & Wilkins, Philadelphia, 2002

Arnfield MR, Mathew RP, Tulip J, McPhee MS; "Analysis Of Tissue Optical Coefficients Using An Approximate Equation Valid For Comparable Absorption And Scattering"; *Physics in Medicine and Biology* vol.37, no.6, p.1219-1230, 1992

Autiero M, Liuzzi R, Riccio P, Roberti G; "Determination Of The Concentration Scaling Law Of The Scattering Coefficient Of Water Solutions Of Intralipid At 832 nm By Comparison Between Collimated Detection Measurements and Monte Carlo Simulations"; *Lasers in Surgery and Medicine* 36:414-422, 2005

Basu S, Ravi B, Kant R; "Interstitial Laser Hyperthermia, a New Method in the Management of Fibroadenoma of the Breast: A Pilot Study"; *Lasers in Surgery and Medicine*, vol.25, p.148-152, 1999

Bauer KD, Henle KJ; "Arrhenius Analysis Of Heat Survival Curves From Normal And Thermotolerant CHO Cells"; *Radiation Research* 78, p.251-263, 1979

Baum M, Saunders C, Meredith S; *Breast Cancer: A Guide For Every Woman*, Oxford University Press, Oxford, New York, 1994

Benson SRC, Blue J, Judd K, Harman JE; "Ultrasound Is Now Better Than Mammography For The Detection Of Invasive Breast Cancer"; *American Journal Of Surgery*, 188, p.381-385, 2004

Bevilacqua, F, Marquet P, Coquoz O, Depeursinge C; "Role Of Tissue Structure In Photon Migration Through Breast Tissues"; *Applied Optics* vol.36, no.1, p.44-51, 1997

Bloom KJ, Dowlat K, Assad L; "Pathologic changes after interstitial laser therapy of infiltrating breast carcinoma"; *The American Journal of Surgery* 182, p. 384-388, 2001

Bown SG; "Phototherapy of Tumors"; *World J. Surgery* 7: 700-709, 1983

Boyle P; "Breast Cancer Control: Signs Of Progress, But More Work Required"; *The Breast*, vol.14, p.429-438, 2005

Caleffi M, Filho DD, Borghetti K, Graudenz M, Littrup PJ, Freeman-Gibb LA, Zannis VJ, Schultz MJ, Kaufman CS, Francescatti D, Smith JS, Simmons R, Bailey L, Henry CA; "Cryoablation Of Benign Breast Tumors: Evolution Of Technique And Technology"; *The Breast*, vol.13, p.397-407, 2004

Cheong W-F, Prahl SA, Welch AJ; "A Review Of The Optical Properties Of Biological Tissues"; *IEEE Journal Of Quantum Electronics*, vol.26, no.12, p.2166-2185, 1990

Chin LC, Whelan WM, Vitkin IA; "Perturbative Diffusion Theory Formalism For Interpreting Temporal Light Intensity Changes During Laser Interstitial Thermal Therapy"; *Physics in Medicine and Biology*, 52(6), p.1659-1674, 2007

Choukeife JE, L'Huillier JP; "Measurements Of Scattering Effects Within Tissue-like Media At Two Wavelengths Of 632.8 nm and 680 nm"; *Lasers in Medical Science* 14:286-296, 1999

Cubeddu R, D'Andrea C, Pifferi A, Taroni P, Torricelli A, Valentini G, "Effects Of The Menstrual Cycle On The Red And Near-Infrared Optical Properties Of The Human Breast", *Photochemistry and Photobiology*, vol.72, no.3, p.383-391, 2000

Derbyshire GJ, Bogen DK, Unger M; "Thermally Induced Optical Property Changes In Myocardium at 1.06 μm"; *Lasers in Surgery and Medicine*, vol.10, p.28-34, 1990

Diaz SH, Nelson JS, Wong BJF; "Rate Process Analysis Of Thermal Damage In Cartilage"; *Physics in Medicine and Biology* 48, p.19-29, 2003

Dossing H, Bennedbaek FN, Hegedüs L; "Beneficial Effect Of Combined Aspiration And Interstitial Laser Therapy In Patients With Benign Cystic Thyroid Nodules: A Pilot Study"; *The British Journal Of Radiology*, vol.79, p.943-947, 2006

Dowlatshahi K, Fan M, Shekarloo M, Bloom KJ, Gould VE. Stereotaxic Interstitial Laser Therapy of Early-Stage Breast Cancer. The Breast Journal 1996; 2:304-311

Dowlatshahi K, Fan M, Gould VE, Bloom KJ, Amjad A. Stereotactically Guided Laser Therapy of Occult Breast Tumors. Archives of Surgery 2000; 135:1345-1352

Dowlatshahi K, Dieschbourg JJ, Bloom KJ; "Laser Therapy Of Breast Cancer With 3-Year Follow-Up"; *Breast Journal*, 10(3), p.240-243, 2004

Dowlatshahi K, *et al*; US Patent #6603988 B2; August 05, 2003

Dowlatshahi K; US Patent #5222953; June 29,1993

Drakaki E, Psycharakis S, Makropoulou, Serafetinides AA; "Optical Properties And Chromophore Concentration Measurements In Tissue-Like Phantoms"; *Optics Communications* 254, p.40-51, 2005

Driver I., Feather JW, King PR, Dawson JB; "The Optical Properties Of Aqueous Suspensions Of Intralipid, A Fat Emulsion"; *Physics in Medicine and Biology* vol.34, no.12, p.1927-1930, 1989

Durduran T, Choe R, Culver JP, Zubkov L, Holboke MJ, Giammarco J, Chance B, Yodh AG; "Bulk Optical Properties Of Healthy Female Breast Tissue"; *Physics in Medicine and Biology*, vol.47, p.2847-2861, 2002

Edström P; "Examination Of The revised Kubelka-Munk Theory: Considerations Of Modeling Strategies"; *Journal of Optical Society of America A*, vol.24, no.2, p.548-556, 2007

Elliott RL, Rice PB, Suits JA, Ostrowe AJ, Head JF; "Radiofrequency Ablation Of A Stereotactically Localized Nonpalpable Breast Carcinoma"; *The American Surgeon*, vol.8, no.1, p.1-5, 2002

Evans III WP; "Stereotactic Core Breast Biopsy"; *Diseases Of The Breast*, Harris JR, Morrow M, Lippman ME, Hellman S, eds., ch6.3, p.144-151, Lippincott-Raven, Philadelphia, 1996

Fantini S, Walker SA, Franceschini MA, Kaschke M, Schlag PM, Moesta KT; "Assessment Of The Size, Position, And Optical Properties Of Breast Tumors In Vivo By Noninvasive Optical Methods", *Applied Optics*, vol.37, no.10, p.1982-1989, 1998

Farina B, Saponaro S, Pignoli E, Tomatis S, Marchesini R; "Monte Carlo Simulation Of Light Fluence In Tissue In A Cylindrical Diffusing Fibre Geometry"; *Physics in Medicine and Biology*, vol.44, p.1-11, 1999

Flock ST, Wilson BC, Patterson MS; "Total Attenuation Coefficients And Scattering Phase Functions Of Tissues And Phantom Materials At 633 nm"; *Medical Physics*, vol.15, no.5, p.835-841, 1987

Flock ST, Jacques SL, Wilson BC, Star WM, van Gemert MJC; "Optical Properties Of Intralipid: A Phantom Medium For Light Propagation Studies"; *Lasers in Surgery and Medicine* 12:510-519, 1992

Gardner CM, Jacques SL, Welch AJ; "Light Transport In Tissue: Accurate Expressions For One-Dimensional Fluence Rate And Escape Function Based Upon Monte Carlo Simulation"; *Lasers in Surgery and Medicine*, vol.18, p.129-138, 1996

Germain D, Chevallier P, Laurent A, Savart M, Wassef M, Saint-Jalmes H; "MR Monitoring Of Laser-Induced Lesions Of The Liver In A Low-Field Open Magent: Temperature Mapping and Lesions Size Prediction"; *Journal of Magnetic Resonance Imaging* 13:42-49, 2001

Germer CT, Roggan A, Ritz JP, Isbert C, Albrecht D, Müller G, Buhr HJ; "Optical Properties Of Native And Coagulated Human Liver Tissue And Liver Metastases In The Near Infrared Range"; *Lasers in Surgery and Medicine*, vol.23, p.194-203, 1998

Gianfelice D, Khiat A, Amara M, Belblidia A, Boulanger Y; "MR Imaging-Guided Focused Ultrasound Surgery Of Breast Cancer: Correlation Of Dynamic Contrast-Enhanced MRI With Histopathologic Findings"; *Breast Cancer Research And Treatment*, vol.82, p.93-101, 2003

Gupta S, Bhawna, Goswami P, Agarwal A, Pradhan A; "Experimental And Theoretical Investigation Of Fluorescence Photobleaching And Recovery In Human Breast Tissue And Tissue Phantoms"; *Applied Optics*, vol.43, no.5, p.1044-1052, 2004

Hale GM, Querry MR; "Optical Constants of Water in the 200 nm to 200 m Wavelength Region"; *Applied Optics*, vol.12, p.555, 1973

Hall-Craggs MA; "Interventional MRI Of The Breast: Minimally Invasive Therapy"; *European Radiology*, vol.10, p.59-62, 2000

Harries SA, Amin Z, Smith MEF, Lees WR, Cooke J, Cook MG, Scurr JH, Kissin MW, Bown SG; "Interstitial Laser Photocoagulation As A Treatment For Breast Cancer"; *British Journal of Surgery* vol.81, p.1617-1619, 1994

Hayashi T, Kashio Y, Okada E; "Hybrid Monte Carlo-Diffusion Method For Light Propagation In Tissue With A Low-Scattering Region"; *Applied Optics*, vol.42, no.16, p.2888-2896, 2003

Hayashi AH, Silver SF, van der Westhuizen NG, Donald JC, Parker C, Fraser S, Ross AC, Olivotto IA; "Treatment of Invasive Breast Carcinoma With Ultrasound-Guided Radiofrequency Ablation"; *American Journal Of Surgery*, 185, p.429-435, 2003

He X, Bischof JC; "The Kinetics Of Thermal Injury In Human Renal Carcinoma Cells"; *Annals of Biomedical Engineering* vol.33, no.4, p.502-510, 2005

Heiskala J, Nissilä I, Neuvonen T, Järvenpää S, Somersalo E; "Modeling Anisotropic Light Propagation In A Realistic Model Of The Human Head"; *Applied Optics*, vol.44, no.11, p.2049-2057, 2005

Heisterkamp J, van Hillegersberg R, Sinofsky E, Ijzermans JNM; "Heat-Resistant Cylindrical Diffuser for Interstitial Laser Coagulation: Comparison With the Bare-Tip Fiber in a Porcine Liver Model"; *Lasers in Surgery and Medicine*, vol.20, p.304-309, 1997

Hourdakis CJ, Perris A; "A Monte Carlo Estimation Of Tissue Optical Properties For Use In Laser Dosimetry"; *Physics In Medicine and Biology*, 40:351-364, 1995

Huston TL, Simmons RM; "Ablative Therapies For The Treatment Of Malignant Diseases Of The Breast"; *American Journal Of Surgery*, 189, p.694-701, 2005

Iizuka M, Vitkin IA, Kolios MC, Sherar MD; "The Effects Of Dynamic Optical Properties During Interstitial Laser Photocoagulation"; *Physics in Medicine and Biology*, vol.45, p.1335-1357, 2000

Ishimaru A; *Wave Propagation And Scattering In Random Media*; IEEE Press, Oxford University Press, 1997

Izzo F, Thomas R, Delrio P, Rinaldo M, Vallone P, DeChiara A, Botti G, D'Aiuto G, Cortino P, Curley SA; "Radiofrequency Ablation In Patients With Primary Breast Carcinoma"; *Cancer*, vol.92, no.8, p.2036-2044, 2001

Jacques SL, Wang L; "Monte Carlo Modeling Of Light Transport In Tissues"; *Optical-Thermal Response Laser-Irradiated Tissue*; Welch AJ, van Gemert MJC, eds., ch.4, p.73-100, Plenum Press, New York, 1995

Janda P, Sroka R, Mundweil B, Betz CS, Baumgartner R, Leunig A; "Comparison Of Thermal Tissue Effects Induced By Contact Application Of Fiber Guided Laser System"; *Lasers in Surgery and Medicine*, vol.33, p.93-101, 2003

Jarlman O, Berg R, Andersson-Engels S, Svanberg S, Pettersson H; "Laser Transillumination Of Breast Tissue Phantoms Using Time-Resolved Techniques"; *European Radiology*, 6, p.387-392, 1996

Kacher DF, Jolesz FA; "MR Imaging-Guided Breast Ablative Therapy"; *Radiologic Clinics of North America*, vol.42, p.947-962, 2004

Kangasniemi M, McNichols RJ, Bankson JA, Gowda A, Price RE, Hazle JD; "Thermal Therapy Of Canine Cerebral Tumors Using A 980 nm Diode Laser With MR Temperature-Sensitive Imaging Feedback"; *Lasers in Surgery and Medicine*, vol.35, p.41-50, 2004

Kaufman CS, Bachman B, Littrup PJ, Freeman-Gibb LA, White M, Carolin K, Francescatti D, Stocks LH, Smith JS, Henry CA, Bailey L, Harness JK, Simmons R; "Cryoablation Treatment Of Benign Lesions With 12-Month Follow-Up"; *American Journal Of Surgery*, vol.188, p.340-348, 2004

Key H, Davies ER, Jackson PC, Wells PNT; "Optical attenuation characteristics of breast tissues at visible and near-infrared wavelengths"; *Phys. Med. Biol.* Vol.36, No. 5, p.579-590, 1991

Key H, Davies ER, Jackson PC, Wells PNT; "Monte Carlo Modeling Of Light Propagation In Breast Tissue"; *Physics in Medicine and Biology* vol.36, no.5, p.591-602, 1991

Kopans DB; "Imaging Analysis Of Breast Lesions"; *Diseases Of The Breast*, JR Harris, M Morrow, ME Lippman, and CK Osborne, eds.; ch.12, p.123-147, Lippincott-Williams & Wilkins, Philadelphia, 2000

Laufer J, Simpson R, Kohl M, Essenpreis M, Cope M; "Effect Of Temperature On The Optical Properties Of *Ex-Vivo* Human Dermis And Subdermis"; *Physics in Medicine and Biology*, vol.43, p.2479-2489, 1998

Lippman ME; "Why Study Ductal Carcinoma In Situ"; *Ductal Carcinoma In Situ Of The Breast*, MJ Silverstein, A Recht, MD Lagios, eds.; ch.2, p.12-16, Lippincott-Williams & Wilkins, Philadelphia, 2002

Liu Q, Zhu C, Ramanujam N; "Experimental Validation Of Monte Carlo Modeling Of Fluorescence In Tissues In The UV-Visible Spectrum"; *Journal of Biomedical Optics*, vol.8, no.2, p.223-236, 2003

Ma N, Gao X, Zhang XX; "Two-Layer Simulation Model Of Laser-Induced Interstitial Thermo-Therapy"; *Lasers in Medical Science*, vol.18, p.184-189, 2004

Mack MG, Straub R, Eichler K, Söllner O, Lehnert T, Vogl TJ; "Breast Cancer Metastases In Liver: Laser-Induced Interstitial Thermotherapy − Local Tumor Control Rate And Survival Data"; *Radiology*, vol.233, no.2, p.400-409, 2004

Magrab EB; *An Engineer's Guide To MATLAB*; Prentice Hall, Upper Saddle River, NJ, 2000

Maitland DJ, Walsh JT; "Quantitative Measurements Of Linear Birefringence During Heating Of Native Collagen"; *Lasers in Surgery and Medicine*, vol.20, p.310-318, 1997

McKenzie AL; "Physics of Thermal Processes In Laser-Tissue Interaction"; *Physics in Medicine and Biology*, vol.35, no.9, p.1175-1209, 1990

McPherson K, Steel CM, Dixon JM; "Breast Cancer − Epidemiology, Risk Factors, and Genetics"; *BMJ* vol.321, p.624-628, 2000

Miller OE, Sant AJ; "Incomplete Integratig Sphere"; *JOSA* vol.48, no.11, 828-831, 1958

Minhaj A, Manns F, Milne P, Denham DB, Salas N, Nose I, Damgaard-Iversen K, Parel JM, Robinson DS; "Laser Interstitial Thermotherapy (LITT) Monitoring Using High-Resolution Digital Mammography: Theory and Experimental Studies"; *Physics in Medicine and Biology*, vol.47, p.2987-2999, 2002

Moes CJM, van Gemert MJC, Star WM, Marijnissen JPA, Prahl SA; "Measurements And Calculations Of The Energy Fluence Rate In A Scattering And Absorbing Phantom At 633 nm"; *Applied Optics* vol.28, no.12, p.2292-2296, 1989

Mohammed Y and Verhey JF; "A Finite Element Method Model To Simulate Laser Interstitial Thermotherapy In Anatomical Inhomogeneous Regions"; *Biomedical Engineering Online*, vol.4, no.2, p.1-16, 2005

Molland JG, Donnellan M, Janu NC, Carmalt HL, Kennedy CW, Gillett DJ; "Infiltrating Lobular Carcinoma – A Comparison Of Diagnosis, Management, and Outcome With Infiltrating Duct Carcinoma"; *The Breast*, vol.13, p.389-396, 2004

Morrow M, Schnitt SJ, Harris JR; "Ductal Carcinoma *in situ* and Microinvasive Carcinoma"; *Diseases Of The Breast*, Harris JR, Morrow M, Lippman ME, and Osborne CK, eds.; ch.27, p.377-381, Lippincott-Williams & Wilkins, Philadelphia, 2000

Morrow M, Schnitt SJ; "Lobular Carcinoma *In Situ*"; *Diseases Of The Breast*, JR Harris, M Morrow, ME Lippman, and CK Osborne, eds.; ch.26, p.377-381, Lippincott-Williams & Wilkins, Philadelphia, 2000

Mumtaz H, Hall-Craggs MA, Wotherspoon A, Paley M, Buonaccorsi G, Amin Z, Wilkinson I, Kissin M, Davidson T, Taylor I, Bown SG; "Laser Therapy for Breast Cancer: MR Imaging and Histopathologic Correlation"; *Radiology*, vol.200, p.651-658, 1996

Muschter R, Hessel S, Jahnen P, Yalavac H, Hofstetter A. Evaluation of Different Laser Wavelengths And Application Systems For LITT. In: G. Muller, A. Roggan, eds. Laser Induced Interstitial Thermotherapy. Bellingham, WA: SPIE Optical Engineering Press, p.212-223, 1995

Muschter R, Hofstetter A. Interstitial Laser Therapy Outcomes In Benign Prostatic Hyperplasia. Journal of Endourology 1995; (9)2: 129-135

Nikfarjam M, Christophi C; "Interstitial Laser Thermotherapy For Liver Tumours"; *British Journal of Surgery*, vol.90, p.1033-1047, 2003

Niemz M; *Laser-Tissue Interactions: Fundamentals and Applications*; Berlin, Heidelberg: Springer-Verlag, 1996

Nilsson AMK, Sturesson C, Liu DL, Andersson-Engles S; "Changes In Spectral Shape Of Tissue Optical Properties In Conjunction With Laser-Induced Thermotherapy"; *Applied Optics* vol.37, no.7, p.1256-1267, 1998

Orr C-S and Eberhart RC; "Overview of Bioheat Transfer"; *Optical-Thermal Response Laser-Irradiated Tissue*; Welch AJ, van Gemert MJC, eds., ch.11, p.367-384, Plenum Press, New York, 1995

Osborne MP; "Breast Development and Anatomy"; *Diseases Of The Breast*, Harris JR, Morrow M, Lippman ME, and Hellman S, eds.; ch.1, p.1-13, Lippincott-Raven Publishers, New York, Philadelphia, 1996

Özişik MN; *Heat Conduction*; John Wiley & Sons, New York, 1980

Page DL, Rogers LW, ; "Biologic Characteristics Of Ductal Carcinoma In Situ"; *Ductal Carcinoma In Situ Of The Breast*, Silverstein MJ, Recht A, Lagios MD, eds.; ch.5, p.37-48, Lippincott-Williams & Wilkins, Philadelphia, 2002

Papaioannou T, Preyer NW, Fang Q, Brightwell A, Carnohan M, Cottone G, Ross R, Jones LR, Marcu L; "Effects Of Fiber-Optic Probe Design And Probe-To-Target Distance On Diffuse Reflectance Measurements Of Turbid Media: An Experimental And Computational Study At 337 nm"; *Applied Optics* vol.43, no.14, p.2846-2858, 2004

Pearce J, Thomsen S; "Rate Process Analysis Of Thermal Damage"; *Optical-Thermal Response of Laser Irradiated Tissue*; Welch A.J., van Gemert M.J.C., eds., ch. 17, p.561-609, Plenum Press, New York, London, 1995

Pecot C; "Stereotactically Guided Opotic Fibier Insertion For Mammographic Thermal Ablative Therapy (MAMTAT)"; a senior design project report submitted to the Department of Biomedical Engineering, University of Miami, Coral Gables, FL as a requirement for the Bachelor of Science degree, April 2002

Peters VG, Wyman DR, Patterson MS, Frank GL; "Optical Properties Of Normal And Diseased Human Breast Tissues In The Visible And Near Infrared"; *Physics in Medicine and Biology*, vol.35, no.9, p.1317-1334, 1990

Pfleiderer SOR, Freesmeyer MG, Marx C, Kühne-Heid R, Schneider A, Kaiser WA; "Cryotherapy Of Breast Cancer Under Ultrasound Guidance: Initial Results and Limitations"; *European Radiology*, vol.12, p.3009-3014, 2002

Pickering JW, Moes CJM, Sterenborg HJCM, Prahl SA, van Gemert MJC; "Two Integrating Spheres With An Intervening Scattering Sample"; *J. Opt. Soc. Am. A*, vol.9 no.4, p.621-631, 1992

Pickering JW, Prahl SA, van Wieringen N, Beek JF, Sterenborg HJCM, van Gemert MJC; "Double-Integrating-Sphere System For Measuring The Optical Properties Of Tissue"; *Applied Optics*, vol.32, no.4, p.399-410, 1993

Pickering JW, Posthumus P, van Gemert MJC; "Continuous Measurement Of The Heat-Induced Changes In The Optical Properties (at 1,064 nm) Of Rat Liver"; *Lasers in Surgery and Medicine*, vol.15, p.200-205, 1994

Prahl SA, van Gemert MJC, Welch AJ; "Determining The Optical Properties Of Turbid Media By Using The Adding-Doubling Method"; *Applied Optics*, vol.32, no.4, p.559-568, 1993

Prahl SA; "The Adding-Doubling Method"; *Optical-Thermal Response of Laser-Irradiated Tissue*, AJ Welch and MJC van Gemert, eds., ch.5, p.101-129, Plenum Press, New York, 1995

Prapavat V, Roggan A, Walter J, Beuthan J, Klingbeil U, Muller G; "In Vitro Studies and Computer Simulations to Assess the Use of a Diode Laser (850 nm) for Laser-Induced Thermotherapy (LITT)" *Lasers in Surgery and Medicine*, 18:22-33, 1996

Prudhomme M, Mattéi-Gazagnes M, Fabbro-Peray P, Puche P, Chabalier J-P, Delacrétaz G, François-Michel LFM, Godlewski G; "MRI Thermodosimetry In Laser-Induced Interstitial Thermotherapy"; *Lasers in Surgery and Medicine*, vol.32, p.54-60, 2003

Purdie TG, Lee TY, Iizuka M, Sherar MD; "Dynamic Contrast Enhancecd CT Measurement Of Blood Flow During Interstitial Laser Photocoagulation: Comparison With An Arrhenius Damage Model"; *Physics in Medicine and Biology* 45, p.1115-1126, 2000

Robinson DS, Parel JM, Denham DB, Gonzalez-Cirre X, Manns F, Milne PJ, Schachner RD, Herron A, Comander J, Hauptmann G, "Interstitial Laser Hyperthermia Model Development for Minimally Invasive Therapy of Breast Carcinoma"; *J Am Coll Surg* 1998; 3:284-292

Robinson DS, Parel JM, Denham DB, Manns F, Gonzalez-Cirre X, Schachner R, Herron A, Burdette E; "Stereotactic Uses Beyond Core Biopsy: Model Development for Minimally Invasive Treatment of Breast Cancer Through Interstitial Laser Hyperthermia"; *The American Surgeon* 1996; 62:117-118

Ritz JP, Lehmann KS, Zurbuchen U, Wacker F, Brehm F, Isbert C, Germer CT, Buhr HJ, Holmer C; "Improving Laser-Induced Thermotherapy Of Liver Metastases – Effects Of Arterial Microembolization And Complete Blood Flow Occlusion"; *European Journal of Surgical Oncology*, vol.33, no.5, p.608-615, 2007

Ritz JP, Roggan A, Isbert C, Müller G, Buhr HJ, Germer CT; "Optical Properties Of Native And Coagulated Porcine Liver Tissue Between 400 and 2400 nm"; *Lasers in Surgery and Medicine*, vol.29, p.205-212, 2001 **(a)**

Ritz JP, Roggan A, Germer CT, Isbert C, Müller G, Buhr HJ; "Continuous Changes In The Optical Properties Of Liver Tissue During Laser-Induced Interstitial Thermotherapy"; *Lasers in Surgery and Medicine*, vol.28, p.307-312, 2001 **(b)**

Roggan A, Dörschel K, Minet O, Wolff D, Müller G; "The Optical Properties Of Biological Tissue In The Near Infrared Wavelength Range - Review And Measurements"; *Laser-Induced Interstitial Thermotherapy*, Muller G., Roggan A., eds., p.10-44, SPIE Optical Engineering Press, Bellingham, WA, 1995

Sakorafas GH; "Breast Cancer Surgery: Historical Evolution, Current Status, and Future Perpectives"; *Acta Oncologica*, vol.40, no.1, p.5-18, 2001

Salas N; *Studies of Thermal Laser Tissue Interactions During Experimental Laser Interstitial Thermotherapy For Breast Cancer*; A thesis submitted to the Department of Biomedical Engineering, University of Miami as requirement for the Masters of Science degree; August 2001

Salas N**,** Manns F, Parel JM, Milne PJ, Figueroa M, Denham DB, Robinson DS; "Experimental Laser Interstitial Thermotherapy In Ex-Vivo Porcine Tissue At 940 nm"; *Lasers in Surgery: Advanced Characterization, Therapeutics, and Systems XII*; Anderson RR, et al., eds.; SPIE Proceedings vol. 4609, p.398-403, 2002

Salas N, Manns F, Parel JM, Milne P, Denham DB, Robinson DS; "Predictions Of Tissue Denaturation During Experimental Laser Interstitial Thermotherapy For Breast Tumors"; *Lasers in Surgery: Advanced Characterization, Therapeutics, and Systems XIII*; LS Bass, *et al.*, ed.; Proc. SPIE Vol.4949, p.444-449, 2003

Salas N, Manns F, Milne PJ, Denham DB, Minhaj AM, Parel JM, Robinson DS, "Thermal Analysis Of Laser Interstitial Thermotherapy In Ex-Vivo Fibro-Fatty Tissue Using Exponential Functions", *Physics in Medicine and Biology* **49**(9), 1609-1624, 2004

Schnitt SJ, Connolly JL; "Pathology Of Benign Breast Disorders"; *Diseases Of The Breast*, Harris JR, Morrow M, Lippman ME, and Osborne CK, eds.; ch.9, p.75-93, Lippincott-Williams & Wilkins, Philadelphia, 2000

Schnitt SJ, Guidi AJ; "Pathology and Biological Markers Of Invasive Breast Cancer"; *Diseases Of The Breast*, Harris JR, Morrow M, Lippman ME, and Osborne CK, eds.; ch.30, p.425-470, Lippincott-Williams & Wilkins, Philadelphia, 2000

Scutt D, Manning JT, Whitehouse GH, Leinster SJ, Massey CP; "The Relationship Between Breast Asymmetry, Breast Size, and The Occurrence Of Breast Cancer"; *British Journal Of Radiology* vol.70, p.1017-1021, 1997

Shafirstein G, Bäumler W, Lapidoth M, Ferguson S, North PE, Waner M; "A New Mathematical Approach To The Diffusion Approximation Theory For Selective Photothermolysis Modeling And Its Implication In Laser Treatment Of Port-Wine Stains"; *Lasers in Surgery and Medicine*, vol.34, p.335-347, 2004

Shah N, Cerussi A, Eker C, Espinoza J, Butler J, Fishkin J, Hornung R, Tromberg B; "Noninvasive Functional Optical Spectroscopy Of Human Breast Tissue"; *PNAS*, vol.98, no.8, p.4420-4425, 2001

Smith LF, Henry-Tillman R, Mancino AT, Johnson A, Jones MP, Westbrook KC, Harms S, Klimberg VS; "Magnetic Resonance Imaging-Guided Core Needle Biopsy And Needle Localized Excision Of Occult Breast Lesions"; *American Journal Of Surgery*, 182, p.414-418, 2001

Smith WJ; *Modern Optical Engineering, third edition*; McGraw-Hill, New York, 2000

Splinter R, Svenson RH, Littmann L, Tuntelder JR, Chuang CH, Tatsis GP, Thompson M; "Optical Properties Of Normal, Diseased, And Laser Photocoagulated Myocardium At The Nd:YAG Wavelength"; *Lasers in Surgery and Medicine*, vol.11, p.117-124, 1991

Steger AC, Lees WR, Walmsley K, Bown SG; "Interstitial Laser Hyperthermia: A New Approach to Local Destruction Of Tumors"; *British Medical Journal*, vol.299, p. 362-365, 1989

Tavassoli FA; *Pathology of the Breast, 2nd edition*; Appleton&Lange, Stamford, CT, 1999

Thomsen S, Pearce JA; "Changes in Birefringence As Markers Of Thermal Damage In Tissues"; *IEEE Transactions on Biomedical Engineering*, vol.36, no.12, 1989

Thomsen S, Tatman D; "Physiological and Pathological Factors Of Human Breast Disease That Can Influence Optical Diagnosis"; *Advances In Optical Biopsy And Optical Mammography*, Alfano R, ed.; Annals of the New York Academy of Sciences, vol. 838, New York, p.171-193, 1998

Thomsen S; "Identification of Lethal Thermal Injury at the Time of Photothermal Treatment"; *Laser-Induced Interstitial Thermotherapy*, Muller G., Roggan A., eds., p.459-467, SPIE Optical Engineering Press, Bellingham, WA, 1995

Tobin KM, Waldow SM; "Effects Of Interstitial Heating On The RIF-1 Tumor Using An Nd:YAG Laser With Multiple Fibers"; *Lasers in Surgery and Medicine*, vol.19, p.216-223, 1996

Tromberg BJ, Shah N, Lanning R, Cerussi A, Espinoza J, Pham T, Svaasand L, Butler J; "Non-invase In Vivo Characterization Of Breast Tumors Using Photon Migration Spectroscopy"; *Neoplasia*, vol.2, no.1-2, p.26-40, 2000

Troy T, Page DL, Sevick-Muraca EM; "Optical Properties Of Normal And Diseased Breast Tissues: Prognosis For Optical Mammography"; *Journal of Biomedical Optics*, 1(3), p.342-355, 1996

Tuchin V; *Tissue Optics: Light Scattering Methods And Instruments For Medical Diagnosis*; SPIE Press, Bellingham, WA, 2000

van Staveren HJ, Moes CJM, van Marle J, Prahl SA, van Gemert MJC; "Light Scattering In Intralipid 10% In The Wavelength Range Of 400-1100 nm"; *Applied Optics* vol.30, no.31, p.4507-4514, 1991

van Veen RLP, Sterenborg HJCM, Marinelli AWKS, Menke-Pluymers M; "Intraoperatively Assessed Optical Properties Of Malignant And Healthy Breast Tissue Used To Determine The Optimum Wavelength Of Contrast For Optical Mammography"; *Journal of Biomedical Optics*, vol.9, no.6, p.1129-1136, 2004

Venta LA, "Image-Guided Biopsy Of Nonpalpable Breast Lesions"; *Diseases Of The Breast*, JR Harris, M Morrow, ME Lippman, and CK Osborne, eds.; ch.13, p.149-164, Lippincott-Williams & Wilkins, Philadelphia, 2000

Verhey JF, Mohammed Y, Ludwig A, Giese K; "Implementation Of A Practical Model For Light And Heat Dsitribution Using Laser-Induced Thermotherapy Near To A Large Vessel"; *Physics in Medicine and Biology*, 48, p.3595-3610, 2003

Vogl THJ, Straub R, Zangos S, Mack MG, Eichler K; "MR-Guided Laser-Induced Thermotherapy (LITT) Of Liver Tumours: Experimental And Clinical Data"; *International Journal of Hyperthermia*, vol.20, no.7, p.713-724, 2004

Welch AJ; "The Thermal Response Of Laser Irradiated Tissue"; *IEEE Journal of Quantum Electronics*; vol. QE-20, no.12, p.1471-1481, 1984

Welch AJ, van Gemert MJC, Star WM, Wilson BC; "Definitions And Overview Of Tissue Optics"; *Optical-Thermal Response Laser-Irradiated Tissue*; Welch AJ, van Gemert MJC, eds., ch.2, p.15-46, Plenum Press, New York, 1995

Welch AJ, Gardner CM; "Monte Carlo Model For Determination Of The Role Of Heat Generation In Laser-Irradiated Tissue"; *Journal of Biomechanical Engineering*, vol.119, p.489-495, 1997

Wilson BC; "Measurement OF Tissue Optical Properties: Methods and Theories"; *Optical-Thermal Response of Laser-Irradiated Tissue*, AJ Welch and MJC van Gemert, eds., ch.8, p.233-303, Plenum Press, New York, 1995

Wohlgemuth WA, Wamser G, Reiss T, Wagner T, Bohndorf K. In Vivo Laser-Induced Interstitial Thermotherapy of Pig Liver With a Temperature-Controlled Diode Laser and MRI Correlation. Lasers in Surgery and Medicine 2001; 29:374-378

Wu F, Wang Z-B, Cao Y-De, Chen W-Z, Bai J, Zou J-Z, Zhu H; "A Randomised Clinical Trial Of High-Intensity Focused Ultrasound Ablation For The Treatment Of Patients With Localised Breast Cancer"; *British Journal of Cancer*, vol.89, p.2227-2233, 2003

Xu T, Zhang C, Wang X, Zhang L, Tian J; "Measurement And Analysis Of Light Distribution In Intralipid-10% at 650 nm"; *Applied Optics* vol.42, No.28, p.5777-5784, 2003

Yang L, Miklavcic SJ; "Theory Of Light Propagation Incorporating Scattering And Absorption In Turbid Media"; *Optics Letters*, vol.30, no.7, p.792-794, 2005

Yaroslavsky AN, Schulze PC, Yaroslavsky IV, Schober R, Ulrich F, Schwarzmaier H-J; "Optical Properties Of Selected Native and Coagulated Human Brain Tissues *In Vitro* In The Visible And Near Infrared Spectral Range"; *Physics in Medicine and Biology*, vol.47, p.2059-2073, 2002

Zhang L-S, Zhang L, Zhang C-P, Qi S-W, Xu T, Tian J-G; "Measurements Of Absorption And Anisotropy Coefficients Of The Fat Emulsion Intralipid-10%"; *Chinese Physics Letters* vol.21, issue 12, p.2517-2520, 2004

Zhu D, Luo Q, Zhu G, Liu W; "Kinetic Thermal Response and Damage in Laser Coagulation Of Tissue"; *Lasers in Surgery and Medicine* 31: 313-321, 2002

APPENDIX A: MONTE CARLO MODEL

The following is the MATLAB program code for finding the absorbed photons in the tissue when irradiated with an isotropic point source using a Monte Carlo algorithm:

```
% Nelson Salas, Jr.
% Monte Carlo Model For Point Source
% Biomedical Optics and Laser Laboratory
% Dept of Biomedical Engineering, University of Miami

%  Program Description
%  This program will calculate the amount of absorbed photons within the tissue
%  during laser irradiation from a point source using the Monte Carlo
%  algorithm

% Clearing the variables from the previous run
clear;

%  Setting loop so that the program will run continuously until I tell it
%  to stop
permission='y';

while permission=='y'

   % Setting the dimensions of the tissue sample in millimeters
   % The tissue samples used are approximately 90x90x20 mm
   x_limit=100;  % The x_limit is half the size since the middle is considered zero
   y_limit=100;   % The y_limit is half the size since the middle is considered zero
   z_limit=200;  % The z_limit is the full size

   % The program will ask for the optical properties of the sample and the laser
parameters
   mua=input('What is the absorption coefficient of your sample? ');  % The absorption
coefficient of the tissue sample
   mus=input('What is the scattering coefficient of your sample? ');  % The scattering
coefficient of the tissue sample
   anis_coeff=input('What is the anisotropy coefficient of your sample? ');  % The
anisotropy coefficient of the tissue sample
   ref_tissue=1.40;  % The refractive index of the tissue sample
   ref_acrylic=1.50;  % The refractive index of the acrylic top lid and clamp
   ref_aluminum=1.39; % The refractive index of the aluminum lab jack
   ref_water=1.33;  % The refractive index of the water in the water bath
```

```
point_power=4.0/18;

% Creating the array that saves the weight of the photons as a function
% of the radius
tissue_abs_weight=zeros(3001,2);
tissue_abs_weight(1:3001,1)=0:0.01:30;

% Starting the Monte Carlo simulation
% Need to establish a random number generator
rand('state',sum(100*clock));

% photon is the amount of photons enetering into the tissue
for photon=1:10000

   % Initializing the weight of the photon prior to launching
   weight=1.0;

   % Launching of the photon
   % The launch will occur for now from a point source located at the
   % proximal edge of the fiber tip.  We will only be looking at the
   % fluence in the tissue grid from one source.
   % The fiber will go along the z-axis of the tissue
   x=0;   % The original position of the photon in the x-direction
   y=0;   % The original position of the photon in the y-direction
   z=100;   % The original position of the photon in the z-direction

   % The initial defletion and azimuthal angle of travel from the
   % isotropic point source will have equal probability for all angles
   % since it is isotropic
   deflection_angle=2*pi*rand;  % The deflection angle of scatter
   azimuthal_angle=2*pi*rand;  % The azimuthal angle of scatter

   % The Directional cosines prior to launching
   % In this revision, the deflection angle has the same meaning, but
   % the launch azimuthal angle is the angle from the positive y-axis
   % rather than the rotation.
   mux=sin(deflection_angle)*sin(azimuthal_angle);
   muy=cos(azimuthal_angle);
   muz=cos(deflection_angle)*sin(azimuthal_angle);

   % Photon movement in the tissue sample
   % The photon will keep moving in the tissue, changing direction at each
   % step and reflecting off the boundaries until the weight reduces to zero.
   % A hit at the boundary of the tissue sample does not mean
   % that the photon completely escapes
```

```
while weight~=0  % Keeps the photons going until it is eliminated

    % Stepsize path of the photon
    s=-log(rand)/(mua+mus);

    %Movement of the photon
    %New direction of the photons into the tissue
    x_prime=x+mux*s;  % Movement in the x-direction
    y_prime=y+muy*s;  % Movement in the y-direction
    z_prime=z+muz*s;  % Movement in the z-direction

    % Photon interaction at the boundaries
    % Making sure that the photon continues til it ends within the
    % boundaries of the tissue
    while x_prime>x_limit|x_prime<-x_limit|y_prime>y_limit|y_prime<-
y_limit|z_prime>z_limit|z_prime<0

        % At Reflection or Transmission at the boundaries, the same photon will be
        % followed until its weight has decreased below a certain value and does
        % not survive the roulette
        % This program has to account for reflections off either one or multiple
        % boundaries.
        k=0;  % k is the variable that sends the program to a specific case upon
reaching a boundary
        % Setting the path length between the original position and the boundary
        % before exiting the tissue for each axis
        if x_prime<-x_limit
            s_escape_x=(-x_limit-x)/mux;  % The distance from the initial photon
location to the x axis boundary
        elseif x_prime>x_limit
            s_escape_x=(x_limit-x)/mux;
        else
            s_escape_x=10000;
        end
        if y_prime<-y_limit
            s_escape_y=(-y_limit-y)/muy;  % The distance from the initial photon
location to the y axis boundary
        elseif y_prime>y_limit
            s_escape_y=(y_limit-y)/muy;
        else
            s_escape_y=10000;
        end
        if z_prime<0
            s_escape_z=-z/muz;  % The distance from the initial photon location to the z
axis boundary
        elseif z_prime>z_limit
```

```
            s_escape_z=(z_limit-z)/muz;
        else
            s_escape_z=10000;
        end
        % Which boundary will hit first is determined by which path length is
        % shortest to its boundary
        if (s_escape_x<s_escape_y)&(s_escape_x<s_escape_z), k=1; end
        if (s_escape_y<s_escape_x)&(s_escape_y<s_escape_z), k=2; end
        if (s_escape_z<s_escape_x)&(s_escape_z<s_escape_y), k=3; end

        % k is the case for each condition
        switch k

            % If the photon goes beyond the positive or negative x boundaries
            case 1
            % According to the configuration of the tissue, the
            % boundaries of the tissue at the x-axes are with water,
            % n=1.33

                if mux>=0
                    theta_boundary_tissue=acos(mux);
                else
                    theta_boundary_tissue=pi-acos(mux);
                end
                critical_angle_water=asin(ref_water/ref_tissue);  % The critical angle at
the acrylic/tissue boundary
                if theta_boundary_tissue<critical_angle_water

theta_boundary_water=asin((ref_tissue/ref_water)*sin(theta_boundary_tissue));
                end
                y=y+muy*s_escape_x;
                z=z+muz*s_escape_x;
                % If the angle out of the tissue is normal to the surface, the reflection
equation will be dividing by zero
                % In this case, both boundaries would be with the
                % water from the water bath
                if theta_boundary_tissue==0
                    weight=weight*((ref_tissue-ref_water)^2/(ref_tissue+ref_water)^2);
                elseif theta_boundary_tissue<critical_angle_water
                    % If the angle in the tissue is less than the
                    % critical angle, the weight will be
                    % incremented by the loss due to reflection at
                    % the boundary, else the light should be
                    % totally reflected and there should be no
                    % decrease of the weight
```

```
                weight=weight*(0.5*((sin(theta_boundary_tissue-
theta_boundary_water))^2/(sin(theta_boundary_tissue+theta_boundary_water))^2+(tan(t
heta_boundary_tissue-
theta_boundary_water))^2/(tan(theta_boundary_tissue+theta_boundary_water))^2));
              end
              % Setting the new position for the x-coordinate
              if x_prime>x_limit
                 x_prime=2*x_limit-x_prime;
                 x=x_limit;
              elseif x_prime<-x_limit
                 x_prime=-2*x_limit-x_prime;  % The x_prime is originally negative in
this direction

                 x=-x_limit;
              end
              mux=-mux;  % Changing the direction cosine in the x-axis
              s=s-s_escape_x;  % Changing the path length to the new one after
reflection off the boundary

              % If the photon goes beyond the positive or negative y boundaries
              % According to the configuration of the tissue, the
              % boundaries of the tissue at the y-axes are with the
              % acrylic and the aluminum lab jack
              case 2
                if muy>=0
                   theta_boundary_tissue=acos(muy);
                else
                   theta_boundary_tissue=pi-acos(muy);
                end
                critical_angle_aluminum=asin(1/ref_aluminum);  % The critical angle at
the lab jack aluminum/tissue boundary

theta_boundary_aluminum=asin((ref_tissue/ref_aluminum)*sin(theta_boundary_tissue));
% The angle after crossing the tissue/air boundary

theta_boundary_acrylic=asin((ref_tissue/ref_acrylic)*sin(theta_boundary_tissue));  %
The angle after crossing the lab jack aluminum/tissue boundary
              x=x+mux*s_escape_y;
              z=z+muz*s_escape_y;
              % Setting the new position for the y-coordinate
              if y_prime>y_limit
                 if theta_boundary_tissue==0
                    weight=weight*((ref_tissue-
ref_acrylic)^2/(ref_tissue+ref_acrylic)^2);
                 else
                    weight=weight*(0.5*((sin(theta_boundary_tissue-
theta_boundary_acrylic))^2/(sin(theta_boundary_tissue+theta_boundary_acrylic))^2+(tan
```

```matlab
(theta_boundary_tissue-
theta_boundary_acrylic))^2/(tan(theta_boundary_tissue+theta_boundary_acrylic))^2));
                end
            y_prime=2*y_limit-y_prime;
            y=y_limit;
        elseif y_prime<-y_limit
            if theta_boundary_tissue==0
                weight=weight*(1-(ref_tissue-
ref_aluminum)^2/(ref_tissue+ref_aluminum)^2);
            else
                if theta_boundary_tissue<critical_angle_aluminum
                    weight=weight*(0.5*((sin(theta_boundary_tissue-
theta_boundary_aluminum))^2/(sin(theta_boundary_tissue+theta_boundary_aluminum))^
2+(tan(theta_boundary_tissue-
theta_boundary_aluminum))^2/(tan(theta_boundary_tissue+theta_boundary_aluminum))
^2));
                end
            end
            y_prime=-2*y_limit-y_prime;
            y=-y_limit;
        end
        muy=-muy;  % Changing the direction cosine in the y-axis
        s=s-s_escape_y;

        % If the photon goes beyond the positive or negative y boundaries
        % According to the configuration of the tissue, the
        % boundaries of the tissue at the z-axes are the
        % acrylic clamps.  They are pretty thick.
        % Therefore, all light going into the clamps will
        % get lost.
    case 3
        if muz>=0
            theta_boundary_tissue=acos(muz);
        else
            theta_boundary_tissue=pi-acos(muz);
        end

theta_boundary_acrylic=asin((ref_tissue/ref_acrylic)*sin(theta_boundary_tissue));
        % In this case the step size path of escape is taken from
        % the thickness of the sample minus the
        % actual position (z=thickness)
        x=x+mux*s_escape_z;  % The x coordinate of escape
        y=y+muy*s_escape_z;  % The y coordinate of escape
        if z_prime>z_limit
            if theta_boundary_tissue==0
```

```
                weight=weight*((ref_tissue-
ref_acrylic)^2/(ref_tissue+ref_acrylic)^2);
                else
                weight=weight*(0.5*((sin(theta_boundary_tissue-
theta_boundary_acrylic))^2/(sin(theta_boundary_tissue+theta_boundary_acrylic))^2+(tan
(theta_boundary_tissue-
theta_boundary_acrylic))^2/(tan(theta_boundary_tissue+theta_boundary_acrylic))^2));
                end
                % Setting the new position for the z-coordinate
                % The reflection off the boundary is taken as if the surface
                % of the tissue/glass is specular
                z_prime=2*z_limit-z_prime;
                z=z_limit;
                muz=-muz;  % The direction cosine at the z-axis is reversed upon
reflection off the boundary
                s=s-s_escape_z;
            elseif z_prime<0
                % In this case the step size path of escape is taken from the
                % the original position minus the actual
                % position (z=0)
                if theta_boundary_tissue==0
                    weight=weight*((ref_tissue-
ref_acrylic)^2/(ref_tissue+ref_acrylic)^2);
                else
                weight=weight*(0.5*((sin(theta_boundary_tissue-
theta_boundary_acrylic))^2/(sin(theta_boundary_tissue+theta_boundary_acrylic))^2+(tan
(theta_boundary_tissue-
theta_boundary_acrylic))^2/(tan(theta_boundary_tissue+theta_boundary_acrylic))^2));
                end
                % Setting the new position for the z-coordinate
                z_prime=-z_prime;
                z=0;
                muz=-muz;  % The direction cosine at the z-axis is reversed upon
reflection off the boundary
                s=s-s_escape_z;
            end

        end  % The end to the switch loop

    end  % The end to the while statement to make sure that the photon ends in the
tissue

    % Will calculate the distance r from the point source and will
    % then record the absorbed photon weight at the appropriate
    % volume between the increment boundaries of the spheres around
    % the point source
```

```
        r=sqrt(x_prime^2+y_prime^2+(z_prime-100)^2);
        if r<=30

tissue_abs_weight(round((r+0.005)/0.01)+1,2)=tissue_abs_weight(round((r+0.005)/0.01)
+1,2)+weight*(mua/(mua+mus));
        end
        weight=weight*(mus/(mua+mus));

        %Creating the deflection angle of scatter
        if anis_coeff~=0
          %  mu_angle is the cosine of the angle of scatter
          mu_angle=(1/(2*anis_coeff))*(1+anis_coeff^2-((1-anis_coeff^2)/(1-
anis_coeff+2*anis_coeff*rand))^2);
        else
          mu_angle=2*rand-1;
        end
        deflection_angle=acos(mu_angle);  % The deflection angle of scatter

        %Creating the azimuthal angle of scatter
        azimuthal_angle=2*pi*rand;

        % New Direction Cosines of the photon in the tissue
        % The new direction cosines will be determined even after each step and
        % absorption, with the step including the reflection at the boundaries and
        % the change in the coordinate direction as a result
        % Alternative formulas for the new directional cosines need to be used if
        % the direction cosine in the z-direction is very close to normal for then
        % the formulas would divide by zero

        if abs(muz)>0.9999
          mux_prime=sin(deflection_angle)*cos(azimuthal_angle);
          muy_prime=sin(deflection_angle)*sin(azimuthal_angle);
          muz_prime=(muz*cos(deflection_angle))/abs(muz);
        else
          mux_prime=(sin(deflection_angle)/sqrt(1-
(muz^2)))*(mux*muz*cos(azimuthal_angle)-
muy*sin(azimuthal_angle))+mux*cos(deflection_angle);
          muy_prime=(sin(deflection_angle)/sqrt(1-
(muz^2)))*(muy*muz*cos(azimuthal_angle)+mux*sin(azimuthal_angle))+muy*cos(defl
ection_angle);
          muz_prime=(-sin(deflection_angle)*cos(azimuthal_angle)*sqrt(1-
(muz^2)))+muz*cos(deflection_angle);
        end

        % The directional cosines primes now becomes the directional cosines.
        % It had to be done this way because of all of the directional cosines
```

```matlab
                    % are required to find the new primes
                    mux=mux_prime;
                    muy=muy_prime;
                    muz=muz_prime;

                    % The primes of the axis coordinates must be changed back to their
                    % original name
                    % primes were used because the original prior coordinates need to be
                    % used to find the coordinates of escape
                    x=x_prime;
                    y=y_prime;
                    z=z_prime;

                    % Once the weight is less than 0.001, the program must decide whether to
                    % continue with the same photon one more cycle or consider it totally
                    % absorbed
                    % It seems like the random numbers (upon small investigation) rarely
                    % goes lower than 0.1.
                    % The photon is given a chance of 1 in m
                    m=10;
                    if weight<0.001
                        photon_end=rand;  %  The variable that helps decide if the photon ends
                        if photon_end<=(1/m)
                            weight=m*weight;
                        else
                            weight=0;
                        end
                    end
                end  % When the weight goes down to 0

        end  % When all the photons goes through

    % Recording the data unto a text file
    cd c:\Nelson_Work;
    folder=['MC Spheres mua' num2str(mua) '_mus' num2str(mus) '_g'
num2str(anis_coeff) '0to30_incpt01_NB.txt'];
    kil=fopen(folder,'w');
    tissue_abs_weight_file=tissue_abs_weight';
    for m=1:3001
        for n=1:2
            if n==1
                fprintf(kil,'%4.3f\t',tissue_abs_weight_file(n,m));
            else
                fprintf(kil,'%4.3f\n',tissue_abs_weight_file(n,m));
            end
        end
    end
```

```
        end
        fclose(kil);

        % Putting the array into a graph
        xx1=linspace(0,30,3001);  % The length of the r axis
        plot(xx1,tissue_abs_weight(1:3001,2),'kd');
        xlabel('Radial distance r (mm)');
        ylabel('Photon weight');
        title('Photon weight vs radial distance from point source');

        % Tells the program whether you want the program again or not
        permission=input('Do you want to run the program again (y or n)? ','s');
        if permission~='y'&permission~='n'
            permission=input('Please try again (y or n)? ','s');
        end  % ends the if loop for permission to continue the program

    end  % End for the while loop that runs the entire program
```

APPENDIX B: THERMAL MODEL

The following is the MATLAB program code for finding the temperature in the tissue as a function of the distance from the cylindrical diffusing tip fiber axis using the thermal model.

```
% Light Propogation Model Program
% Nelson Salas, Jr.
% Biomedical Optics and Laser Laboratory
% University of Miami

% Purpose of the program
% The purpose of this program is to calculate the temperature distribution
% in the tissue sample as a function of the distance from the fiber source.
% The cylindrical diffusing tip fiber is represented as a series of spherical sources of
% finite diameter.  The temperature is initially constant throughout the tissue,
% at 37 degrees C.  The source will be a point source of finite diameter 0.9 mm.

% Command to clear the system prior to running the program
clear;

% Getting the parameters of the tissue
r_s=0.9;  % The radius of the spherical source;
L_tip=16;  % The length of the fiber
N=51;  % The number of spherical sources in the fiber tip
a=r_s;  % The radius of the spherical source
b=40;  % The outer tissue boundary radius
x_inc=(L_tip-2*r_s)/(N-1);  % The distance between the center of the spherical sources

% Using the thermal properties of water taken from the Heat Transfer book
% for properties at 320 degrees Kelvin (47 degrees Celsius)
alpha=0.154;  % Thermal diffusivity
k=0.00064;  % Thermal conductivity

% The irradiation time is specified
time_p=600;

% Specification of the effective attenuation coefficient
mu_eff=input('What do you want mu_eff to be? ');

% Specification of the power at the fiber tip
P_tip=input('What do you want the power to be? ');
```

```
% Finding the Power P_s for each spherical source
P_series=0;
for i=-(N-1)/2:(N-1)/2
   P_series=P_series+(1/(1+i^2*((L_tip-2*r_s)^2/(r_s^2*(N-1)^2))));
end
P_s=((P_tip*2*r_s)/L_tip)*(1/P_series);

% Creating the temperature distribution
% Creating the tissue grid
tissue_increment=1.0;

Ti=37;  % The initial tissue temperature
x=0.0;  % Location of thermocouple along the fiber axis
time=time_p;

% creating the array for the tissue temperature
TC_temp(1:192,1)=0.9:0.1:20;
y_count=1;

for y=0.9:0.1:20

   fiber_series=0;

   for x_fiber=-L_tip/2+r_s:x_inc:L_tip/2-r_s
      r=sqrt((x-x_fiber)^2+y^2);
      temp_series=0;
      for m=1:200
         beta=((2*m-1)*pi)/(2*(b-a));
         f_m=(1-exp(-alpha*beta^2*time))*(((-1)^(m+1)*beta*exp(-
mu_eff*b)+mu_eff*exp(-mu_eff*a))/(beta^2*(beta^2+mu_eff^2)));
         g_m=exp(-alpha*beta^2*time)*(exp(alpha*beta^2*time_p)-1)*(((-
1)^(m+1)*beta*exp(-mu_eff*b)+mu_eff*exp(-mu_eff*a))/(beta^2*(beta^2+mu_eff^2)));
         h_m=(cos(beta*(r-a)))/(r*(b-a));
         if time<=time_p
            temp_series=temp_series+f_m*h_m;
         else
            temp_series=temp_series+g_m*h_m;
         end
      end

      fiber_series=fiber_series+temp_series;

   end
```

```
        TC_temp(y_count,2)=Ti+(P_s/((1+mu_eff*r_s)*exp(-
mu_eff*r_s)))*(mu_eff^2/(2*pi*k))*fiber_series;

        y_count=y_count+1;

    end



    % Sending the file to be recorded to a text file
    folder=['Breast_Indigo_vapor_b' num2str(b) '_time' num2str(time) '_mueff'
num2str(mu_eff) '_y0.9to20_rev10-11-07.txt'];
    cd c:\Nelson_Work
    TC_temp_rec=TC_temp';
    wil=fopen(folder,'w');
    for m=1:192
      for n=1:2
        if n==1
          fprintf(wil,'%3.1f\t',TC_temp_rec(n,m));
        else
          fprintf(wil,'%3.2f\n',TC_temp_rec(n,m));
        end
      end
    end
    fclose(wil);
    clear TC_temp TC_temp_rec;
```

APPENDIX C: COAGULATION MODEL

The following is the MATLAB program code for calculating the coagulation in the tissue induced during laser irradiation and heating using the coagulation model:

```
% Approximating Cell Kill Using The Arrhenius Equation For Multiple Thermocouples
% Nelson Salas, Jr.
% Bascom Palmer Eye Institute-Ophthalmic Biophysics Center
% October 25, 2006

% The purpose of this program is to calculate the coagulation percentage
% from the temperature profiles of 15 thermocouples taken during laser
% heating of ex-vivo porcine tissue.

clear;

permission='y';

while permission=='y';

    choice_pair='y';

    % Seeking the file containing the thermocouple data to be analyzed
    file=input('Which file would you like to analyze? ','s');
    cd c:\Nelson_Work;
    temp=load(file);

    % Getting the size of the temperature matrix
    [coag_row,coag_col]=size(temp);

    % Allows you to test multiple pairs for the same file
    while choice_pair=='y'

        % The program will ask for the activation energy and the frequency
        % factor for each pass
        freq_factor=input('What is the frequency factor? ');
        active_E=input('What is the activation energy? ');
        pair_num=input('What is the pair number? ');

        % Initializing the matrices to get the coagulation percentages
        celsius(1:coag_row,1)=temp(1:coag_row,1);
        death(1:coag_row,1)=temp(1:coag_row,1);
```

```matlab
energy(1:coag_row,1)=temp(1:coag_row,1);

% Creating the for loop to analyze each thermocouple
for e=2:coag_col

   % The thermocouple effect removal.
   % The thermocouple is removed by taking the linear fit of the
   % temperature data right after the exponential rise.  The slope
   % and the intercept are used to replace the initial data within
   % this range and bringing down the remaining data.
   p=polyfit(temp(6:26,1),temp(6:26,e),1);

   % Some thermocouples do not have a TC effect and have a delay
   % because of their distance away from the source.  This
   % accounts for that
            if p(1)>0&p(2)>temp(1:e)
            celsius(1:26,e)=temp(1,e)+p(1)*temp(1:26,1);
            celsius(27:coag_row,e)=temp(27:coag_row,e)-p(2)+temp(1,e);
   else
      celsius(1:coag_row,e)=temp(1:coag_row,e);
   end

   % Calculates amount of cell death using Arrhenius
   % Getting the exponential Aexp(-E/RT)
   energy(1:coag_row,e)=freq_factor*exp(-
active_E./(8.32*(celsius(1:coag_row,e)+273)));

   % Getting the integration of the Arrhenius matrix to calculate
   % the coagulation
   total=0;
   for v=1:coag_row
      if v~=1
         y=[energy(v-1,e),energy(v,e)];
         x=[energy(v-1,1),energy(v,1)];
         total=total+trapz(x,y);
         death(v,e)=1-exp(-total);
      else
         death(v,e)=0;
      end
   end
end  % Ends the for loop for the evaluation of each thermocouple

% Writes the coagulation matrix into a text file
necrosis=death';
folder=input('What would you like the coagulation file to be named? ','s');
cd c:\Nelson_Work;
```

```
kil=fopen(folder,'w');
for m=1:coag_row
   for n=1:coag_col
      if n==1
         fprintf(kil,'%4i\t',necrosis(n,m));
      elseif n>1&n<coag_col
         fprintf(kil,'%1.4f\t',necrosis(n,m));
      else
         fprintf(kil,'%1.4f\n',necrosis(n,m));
      end
   end
end
fclose(kil);

% Puts the temperature data in interpolation form for graphing
disp(['The total amount of time in the file is ' num2str(coag_row*2-2) ' seconds']);
choice_temp=input('Would you like to put the temperature data matrix in
interpolation form (y=yes, n=no)? ','s');
while choice_temp~='y'&choice_temp~='n'
   choice_temp=input('You must choose either y for Yes or n for "No"?! ','s');
end
while choice_temp=='y'
      time_temp=input('At what time do you like to analyze the data (in seconds)?
');
      temp_dis=zeros(81,81);
   temp_dis(11,51)=celsius(time_temp*0.5+1,2);
   temp_dis(71,51)=celsius(time_temp*0.5+1,3);
   temp_dis(21,21)=celsius(time_temp*0.5+1,4);
   temp_dis(61,21)=celsius(time_temp*0.5+1,5);
   temp_dis(31,31)=celsius(time_temp*0.5+1,6);
   temp_dis(51,31)=celsius(time_temp*0.5+1,7);
   temp_dis(11,31)=celsius(time_temp*0.5+1,8);
   temp_dis(71,31)=celsius(time_temp*0.5+1,9);
   temp_dis(21,41)=celsius(time_temp*0.5+1,10);
   temp_dis(61,41)=celsius(time_temp*0.5+1,11);
   temp_dis(31,51)=celsius(time_temp*0.5+1,10);
   temp_dis(51,51)=celsius(time_temp*0.5+1,10);
   temp_dis(31,71)=celsius(time_temp*0.5+1,10);
   temp_dis(51,71)=celsius(time_temp*0.5+1,10);

   % Writes the temperature distribution matrix into a file
                  temp_dis=temp_dis';
   temp_file=input('What would you like the temperature interpolation matrix to be
named? ','s');
   nel=fopen(temp_file,'w');
   cd c:\Nelson_work;
```

```
                    for m=1:81
                        for n=1:81
                        if n<81
                        fprintf(nel,'%3.2f\t',temp_dis(n,m));
            else
                        fprintf(nel,'%3.2f\n',temp_dis(n,m));
            end
        end
    end
                fclose(nel);

    % The program asks if you want to do another temperature
    % distribution matrix
    choice_temp=input('Would you like to create another matrix (y=yes, n=no)? ','s');
    while choice_temp~='n'&choice_temp~='y'
        choice_temp=input('You must choose either y for "Yes" or n for "No"! ','s');
    end
  end  % Ends the for loop for the temeprature distribution matrix

    % Creates an interpolation matrix for death and creates a file
    choice_coag=input('Would you like to put death matrix in interpolation form (y=yes,
n=no)? ','s');
    while choice_coag~='y'&choice_coag~='n'
        choice_coag=input('You must choose either y for "Yes" or n for "No"! ','s');
    end
    while choice_coag=='y'
                time_temp=input('At what time do you like to analyze the data (in
seconds)? ');
            coag_dis=zeros(81,81);
    coag_dis(11,51)=death(time_temp*0.5+1,2);
    coag_dis(71,51)=death(time_temp*0.5+1,3);
    coag_dis(21,21)=death(time_temp*0.5+1,4);
    coag_dis(61,21)=death(time_temp*0.5+1,5);
    coag_dis(31,31)=death(time_temp*0.5+1,6);
    coag_dis(51,31)=death(time_temp*0.5+1,7);
    coag_dis(11,31)=death(time_temp*0.5+1,8);
    coag_dis(71,31)=death(time_temp*0.5+1,9);
    coag_dis(21,41)=death(time_temp*0.5+1,10);
    coag_dis(61,41)=death(time_temp*0.5+1,11);
    coag_dis(31,51)=death(time_temp*0.5+1,12);
    coag_dis(51,51)=death(time_temp*0.5+1,13);
    coag_dis(31,71)=death(time_temp*0.5+1,14);
    coag_dis(51,71)=death(time_temp*0.5+1,15);

    % Writes the coagulation distribution matrix into a file
            coag_dis=coag_dis';
```

```
                    coag_file=input('What would you like the death interpolation
matrix to be named (y=yes, n=no)? ','s');
        son=fopen(coag_file,'w');
        cd c:\Nelson_Work;
                        for m=1:81
                            for n=1:81
                            if n<81
                            fprintf(son,'%1.4f\t',coag_dis(n,m));
            else
                            fprintf(son,'%1.4f\n',coag_dis(n,m));
            end
          end
        end
                fclose(son);

        % The program asks if you want to do another coagulation
        % distribution matrix
        choice_coag=input('Would you like to create another matrix (y=Yes, n=No)? ','s');
        while choice_coag~='y'&choice_coag~='n'
          choice_coag=input('You must choose y for "Yes" or n for "No"! ','s');
        end
      end

      % The program checks to see if you want to analyze another pair of
      % constants with the same file
      choice_pair=input('Do you want to analyze the same file with another pair of
Arrhenius equation constants (y=yes, n=no)? ','s');
      while choice_pair~='y'&choice_pair~='n'
        choice_pair=input('Please try again (y=yes, n=no)! ','s');
      end

   end  % Ends the while loop to repeat using another pair of Arrhenius equation
constants

   % The program checks to see if you want to analyze another file
   permission=input('Do you want to analyze the another file (y=yes, n=no)? ','s');
   while permission~='y'&permission~='n'
     permission=input('Please try again (y=yes, n=no)! ','s');
   end

end % Ends the while statement that decides whether a file is to be analyzed or not

disp('Thanks for using the program.  Have a nice day!');
```

APPENDIX D: DERIVATION OF INTEGRATING SPHERE FORMULAS

Utilizing the methods of Miller and Sant (1958), the expression derived by Pickering *et al* (1992) for the diffuse reflectance of the sample irradiated with collimated incident light is the following:

$$\frac{P_{Rcd}}{P_i} = \frac{A_d}{A_t} \frac{\left(1 - \frac{A_h}{A_t}\right) \cdot R \cdot R_d}{1 - \left(1 - \frac{A_h}{A_t}\right) \cdot R - \frac{A_s}{A_t} \cdot R_{d-diff}}, \qquad \text{Eq. D.1}$$

where:

P_{Rcd} : Power detected by an integrating sphere with a baffle (W)

P_i : Incident power on the sample (W)

R : Reflectance of the integrating sphere wall

R_d : Diffuse reflectance of the sample to collimated incident radiation

R_{d-diff} : Diffuse reflectance of the sample to diffuse incident radiation

A_t : Total area of the sphere (cm^2)

A_d : Area of the photosensor (cm^2)

A_h : Total area of the openings, including the sample opening

A_s : Area of the sample opening

The areas represent the spherical caps missing from the integrating sphere due to the presence of the openings. The expression for the area of the spherical cap, A_c, is the following:

$$A_c = \frac{A_t}{2} \cdot \left(1 - \sqrt{1 - \frac{d_c^2}{d_s^2}} \right), \qquad \text{Eq. D.2}$$

where d_s is the sphere diameter and d_c is the diameter of the circular opening in the sphere. According to our experimental set-up, we have $d_s^2 >> d_c^2$ and the term in the square root can be approximated by the first two terms of its Taylor series. The expression of the spherical cap then becomes the following:

$$A_c = \frac{A_t}{4} \frac{d_c^2}{d_s^2}. \qquad \text{Eq. D.3}$$

Substituting Eq. D.3 into Eq. D.1 gives the following:

$$\frac{P_{Rcd}}{P_i} = F \cdot \frac{d_d^2}{4 \cdot d_s^2} \cdot \frac{R_{eff} \cdot R_d}{1 - R_{eff} - \frac{d_{sample}^2}{4 \cdot d_s^2} \cdot R_{d-diff}}, \qquad \text{Eq. D.4}$$

where F is the detected fraction of the power leaving the detector hole of the integrating sphere and R_{eff} is the following:

$$R_{eff} = (1 - \frac{\sum d_i^2}{4 d_s^2}) \cdot R. \qquad \text{Eq. D.5}$$

where $\sum d_i^2$ is the sum of the squares of the diameters of all the sphere openings. Equation D.4 applies for diffuse reflectance measurements that allow the specular reflection off the sample to escape the sphere.

Similar expressions can be derived from Pickering *et al* (1992) for the diffuse transmittance of the sample irradiated with collimated transmittance and the diffuse reflectance of the sample irradiated with diffuse incident light. The expression for the

diffuse transmittance of the sample irradiated with collimated incident light is given by the following:

$$\frac{P_{Tcd}}{P_i} = F \cdot \frac{d_d^2}{4 \cdot d_s^2} \cdot \frac{R_{eff} \cdot T_d}{1 - R_{eff} - \frac{d_{sample}^2}{4 \cdot d_s^2} \cdot R_{d-diff}} \; , \qquad \text{Eq. D.6}$$

where P_{Tcd} is the detected power during diffuse transmittance measurements and T_d is diffuse transmittance, respectively, of the sample irradiated with collimated incident light. Equation D.6 applies for diffuse transmittance measurements that allow the collimated transmittance through the sample to escape the sphere.

The expression for the diffuse reflectance of the sample irradiated with diffuse incident light is given by the following:

$$\frac{P_{Rd}}{P_i} = F \cdot \frac{d_d^2}{4 d_s^2} \cdot \frac{R \cdot (1 - \frac{d_{sample}^2}{4 d_s^2} R_{d-diff})}{1 - R_{eff} - \frac{d_{sample}^2}{4 d_s^2} R_{d-diff}} \; , \qquad \text{Eq. D.7}$$

where P_{Rd} is the detected power during diffuse reflectance measurements of the sample irradiated with diffuse incident light. This expression was derived by Pickering *et al* (1992) for the case when the radiation is diffuse prior to entering the integrating sphere. According to our experimental protocol, collimated incident light strikes the integrating sphere prior to striking the sample. Utilizing the methods of Miller and Sant (1958), eq. D.7 was modified to account for the first reflection of the incident power off the sphere wall and the second reflection of the incident power off the sphere wall and sample prior to reaching the detector:

$$\frac{P_{Rd}}{P_i} = F \cdot \frac{d_d^2}{4d_s^2} \cdot \frac{R \cdot (R_{eff} + \frac{d_{sample}^2}{4d_s^2} R_{d-diff})}{1 - R_{eff} - \frac{d_{sample}^2}{4d_s^2} R_{d-diff}} \cdot \qquad \text{Eq. D.8}$$

As long as the diameter of the sample hole and the value of R_{eff} are the same for the measurements of the diffuse reflectance and transmittance with collimated incident light and the diffuse reflectance with diffuse incident light, the error introduced by the estimation of the calibration factor and other sphere parameters can be minimized by taking the ratio of the measurements:

$$\frac{P_{Rcd}}{P_{Rd}} = \frac{(1 - \frac{\sum d_i^2}{4d_s^2})R_d}{R_{eff} + \frac{d_{sample}^2}{4d_s^2} R_{d-diff}} \cong \frac{R_d}{R}, \qquad \text{Eq. D.9}$$

$$\frac{P_{Tcd}}{P_{Rd}} = \frac{(1 - \frac{\sum d_i^2}{4d_s^2})T_d}{R_{eff} + \frac{d_{sample}^2}{4d_s^2} R_{d-diff}} \cong \frac{T_d}{R}. \qquad \text{Eq. D.10}$$

From equations D.9 and D.10, the diffuse reflectance and transmittance of the sample irradiated with collimated incident light can be solved by the following:

$$R_d \cong R \cdot \frac{P_{Rcd}}{P_{Rd}}, \qquad \text{Eq. D.11}$$

$$T_d \cong R \cdot \frac{P_{Tcd}}{P_{Rd}} = \frac{P_{Tcd}}{P_{Rcd}} \cdot R_d, \qquad \text{Eq. D.12}$$

The relative error in the estimated values of R_d and T_d introduced by the approximation given in equations D.11 and D.12 is always less than 2.5% in our experimental condition.

VITA

Nelson Salas was born in New York City, NY on July 5, 1974 and was raised in Miami, FL since the age of six months. He attended high school at Coral Gables Senior High where he graduated in 1992 from the International Bacculaureate Program. He received a Bachelors of Science in Engineering Sciences with a minor in Biomechanics from the University of Florida, Gainesville, FL in May of 1997. He received a Masters of Science in Biomedical Engineering at the University of Miami, Coral Gables, FL in August of 2001. On September 2000, Nelson Salas received a predoctoral minority fellowship from the National Cancer Institute (National Institutes of Health) to pursue his doctorate in Biomedical Engineering at the University of Miami while continuing his research in the MAMTAT project. In September of 2001, Nelson Salas entered into the doctoral program in the Biomedical Engineering department at the University of Miami, where he received his degree in December of 2007.

Permanent Address: 4147 SW 11 Street, Miami, FL 33134